UNIVERSITÉ DE GENÈVE

Département de Radiologie et Informatique Médicale

FACULTÉ DE MÉDECINE
Pr H. Zaidi

Département d'Informatique

FACULTÉ DES SCIENCES
Pr S. Voloshynovskiy

Strategies for magnetic resonance imaging-guided attenuation correction in whole-body PET-MRI

THÈSE

présentée à la Faculté des sciences de l'Université de Genève
pour obtenir le grade de Docteur ès sciences, mention interdisciplinaire

par

Hossein Arabi
de
Tehran, Iran

Thèse N° 4968

GENÈVE
Service de reprographie de l'Uni Mail
2016

UNIVERSITÉ DE GENÈVE

FACULTÉ DES SCIENCES

Doctorat ès sciences
Mention interdisciplinaire

Thèse de *Monsieur Hossein ARABI*

intitulée :

"Strategies for Magnetic Resonance Imaging-guided Attenuation Correction in Whole-body PET-MRI"

La Faculté des sciences, sur le préavis de Monsieur S. VOLOSHYNOVSKIY, professeur associé et directeur de thèse (Département d'informatique), Monsieur H. ZAIDI, docteur et codirecteur de thèse (Faculté de médecine, Département de radiologie et informatique médicale – Honorary professor, University of Groningen, The Netherlands – Honorary professor University of Southern Denmark, Funen, Denmark), Monsieur K.-O. LOVBLAD, professeur (Faculté de médecine, Département de radiologie et informatique médicale), Madame S. ZIEGLER, professeure (Ludwig-Maximilians-Universität, Munchen, Germany), Monsieur H. AMMARI, professeur (Département de mathématiques, Ecole Polytechnique Fédérale, Zurich, Suisse), et Monsieur R. BOELLAARD, professeur (Nuclear medicine and molecular imaging, University of Groningen, Netherlands), autorise l'impression de la présente thèse, sans exprimer d'opinion sur les propositions qui y sont énoncées.

Genève, le 21 juin 2016

Thèse - 4968 -

Le Doyen

N.B. - La thèse doit porter la déclaration précédente et remplir les conditions énumérées dans les "Informations relatives aux thèses de doctorat à l'Université de Genève".

Summary

Positron emission tomography (PET) has become an invaluable molecular imaging technique for the non-invasive assessment, quantification and appraisal of various biochemical processes *in vivo*. In principle, a PET examination starts with injection of a positron-emitting radiotracer to the patient, then the PET detectors record the number of emitted annihilation photons representing the biodistribution and kinetics of the administered radiopharmaceutical. The downside of this modality is its inability to provide accurate anatomical information for the localization of metabolically active abnodmalities. Combining PET with an anatomical imaging modality such as x-ray computed tomography (CT) or magnetic resonance imaging (MRI) enabled to address the shortcomings of molecular PET imaging. The emergence of hybrid imaging techniques, such as PET/CT and PET/MRI, in clinical practice engendered a number of new clinical and research opportunities while improved the quantitative accuracy and diagnostic confidence of PET findings. Beside the precious anatomical information provided by CT or MRI, additional information such as attenuation properties of body tissues and motion information can be exploited for correction of emission data and quantitative PET image reconstruction. In PET/CT imaging, the data provided by CT images can be utilized to generate an attenuation map at 511-keV for fulfilling the task of attenuation correction of PET data. The major motivation behind combining PET and MRI, besides reducing radiation exposure, is to benefit from the MRI capability to provide superior soft tissue contrast compared to CT. This enables not only to enhance lesion localization but can also be exploited for anatomically-guided partial volume correction in the PET image reconstruction. Moreover, the merits of MRI in terms of providing motion information allow the implementation of motion correction of the PET data in simultaneous PET/MRI acquisition. Additionally, due to the restriction of positron range in the magnetic field, the in-plane PET resolution will be improved particularly for long positron range radionuclides. Undoubtedly, integration of MR/CT and PET imaging modalities introduces new opportunities and maximizes the potentials of molecular imaging in clinical practice; nevertheless, hybrid imaging causes some new limitations and technical challenges that can adversely affect PET image quality and quantification. As opposed to PET/CT imaging, where attenuation correction is relatively straightforward, attenuation correction in PET/MRI is a major challenge due to the lack of sufficient information provided by MR imaging about the attenuation characteristics of biological tissues, such that MR images cannot be directly converted to PET attenuation maps. In addition, MRI suffers from long acquisition time, which is a limiting factor for exploitation in a wide range of clinical applications. Even though MRI can provide superior soft-tissue identification, bone identification remains a signification challenge since bony structures are reflected in a void signal (similar to air) in most conventional MRI sequences. Therefore, proper PET attenuation map generation from MR images is commonly challenged by bone extraction certainty.

The work presented in this dissertation focuses on some of the prevalent challenges encountered in PET/MRI image reconstruction mostly MR-guided photon attenuation correction and bone identification from MR images through further development of current state-of-the-art techniques and the investigation and validation of new algorithms. In particular, this dissertation deals with clinical assessment of MR-guided attenuation correction techniques, improving methods of MR-based attenuation map generation and bone segmentation from MR images in whole-body imaging.

The quantitative accuracy of MRI-based attenuation correction techniques being used in clinical practice were compared using a dataset of clinical cases. The evaluated methods consisted of the 3-class attenuation map implemented on the Ingenuity TF PET/MRI and the 4-class attenuation map similar to the approach used on the Siemens mMR PET/MR. In this study, PET data of 14 clinical cases with malignant tumors were corrected for attenuated photons using 3-class (containing air, lung and soft-tissue) and 4-class (containing air, lung, fat and soft-tissue) attenuation maps. 3-class attenuation map resulted in significant systematic positive bias in the lungs owing to the higher attenuation coefficient used and negative bias in other regions. 4-class attenuation map slightly underestimated tracer uptake in the lungs, however led to even larger negative bias in other body regions.

A new pseudo-CT generation approach was proposed for accurate extraction of bones and estimation of lung attenuation properties. Since lung attenuation value exhibits dramatic variation across patients, patient-specific lung attenuation estimation is a significant issue in whole-body PET attenuation generation. The presented approach aimed to improve the Gaussian process regression (GPR) kernel proposed by Hofmann et al. (J Nucl

Med 2011). To this end, the atlas dataset was sorted on the basis of local normalized cross-correlation to select the most similar image in the atlas dataset for each voxel. For lung tissue, the advantage of the existing correlation between lung volume and corresponding attenuation properties was taken to predict patient-specific lung attenuation coefficients. In case of pathological tissues in the lungs, the lesions were segmented on PET images followed by assignment of soft-tissue attenuation coefficient. The proposed algorithm was compared to the original Hofmann's approach and the 3-class attenuation correction technique implemented on the Philips Ingenuity TF PET/MR. The proposed technique resulted in better overall PET quantification accuracy than both Hofmann's and the 3-class approaches owing to the more accurate extraction of bones and better prediction of lung attenuation coefficients.

In the next study, we compared the accuracy of whole-body bone extraction from MR images exploiting a number of atlas-based segmentation methods. The motivation for this study was to find the most promising approach for the purpose of MR-derived PET attenuation map generation. To this end, a variety of atlas-based segmentation strategies commonly used in the field of medical image segmentation and pseudo-CT generation were implemented and evaluated in terms of whole-body bone segmentation accuracy. Among the various examined methods, voxel-wise atlas fusion approach exhibited promising potential for accurate and reliable bone segmentation.

One of the major challenges of atlas-based methods is the long processing time taken by atlas registration. Thus, a novel method was proposed that consists only one online registration between the target and reference images, regardless of the number of atlas images (N), while for the remaining atlas images, the pre-computed transformation matrices to the reference image are used to align them to the target image. The performance characteristics of the proposed method was evaluated and compared with conventional atlas-based attenuation map generation strategies (direct registration of the entire atlas images). The quantitative analysis revealed a good correlation between PET images corrected for attenuation using the proposed method and the corresponding CT images. The computational time was reduced by a factor 1/N at the expense of a modest decrease in quantitative accuracy.

MRI-guided radiation therapy treatment planning is also challenged by the lack of a direct link between MRI voxel intensities and electron density. A two-step (segmentation and fusion) atlas-based algorithm was proposed focusing on bone tissue identification to create a pseudo-CT image from conventional MRI sequences. In the first step, bone segmentation of the target image is optimized through local weighted atlas voting. The obtained bone map is then used to assess the quality of deformed atlases to perform voxel-wise weighted atlas fusion. A dosimetric evaluation of volumetric modulated arc therapy photon treatment plans calculated using the different pseudo-CT images was carried out. The proposed method generates accurate pseudo-CT images from conventional Dixon MRI sequences with improved bone extraction accuracy. The approach is promising for potential use in PET attenuation correction and MRI-only or hybrid PET/MRI-guided radiation therapy treatment planning.

In the next study, a number of strategies have been developed for MRI-guided attenuation correction were quantitatively evaluated and compared. These methods include three generic attenuation correction methods of standard 3-class MR segmentation-based, advanced atlas-registration-based and emission-based approaches in the context of brain time-of-flight (TOF) PET/MRI. A robust atlas-registration based AC method, which employs local weighted fusion of atlases based on their morphological similarity to target MR image, was compared with MRI-guided maximum likelihood reconstruction of activity and attenuation (MLAA) algorithm. The accuracy of bone prediction and quantification of the PET tracer uptake were assessed to evaluate the performance of the different AC strategies. The 3-class attenuation map led to significant underestimation of the PET tracer uptake, while the MLAA-AC method was unable to remarkably reduce quantification errors. On the other hand, the proposed atlas-AC method provided the most accurate attenuation maps in terms of bone prediction accuracy, and thus the lowest quantification bias.

The Shape-based averaging (SBA), which is a proven method of atlas fusion scheme, was proposed for the purpose of whole-body bone segmentation from MR images. The performance of SBA method was improved through incorporation of local regularisation to maximize bone segmentation accuracy. The improved method was used to generate PET attenuation map and its performance was evaluated in terms of radiotracer uptake recovery. The quantitative evaluation of PET images corrected for attenuation using the proposed pseudo-CTs revealed a good correlation with PET images corrected for attenuation using the corresponding reference CT images.

Résumé

La tomographie par émission de positons (TEP) est devenue une technique d'imagerie moléculaire inestimable pour l'évaluation non-invasive, la quantification et l'évaluation des divers processus biochimiques in vivo. En principe, un examen TEP commence par l'injection d'un radiotraceur émettant des positrons pour le patient, les détecteurs TEP enregistrent le nombre de photons d'annihilation émis, représentant la biodistribution et la cinétique du produit radiopharmaceutique administré. L'inconvénient de cette modalité est son incapacité de fournir des informations anatomiques précises pour la localisation des lésions métaboliquement actives.

La combinaison de TEP avec une modalité d'imagerie anatomique telle que x-ray tomodensitométrie (TDM) ou l'imagerie par résonance magnétique (IRM) a permis de combler les lacunes de l'imagerie TEP moléculaire. L'émergence des techniques d'imagerie hybrides, tels que le TEP / CT et TEP / IRM, dans la pratique clinique a engendré un certain nombre de nouvelles opportunités cliniques et de recherches tout en améliorant la précision quantitative et la fiabilité du diagnostic des résultats TEP. Outre les informations anatomiques fournies par CT ou IRM, des informations supplémentaires telles que les propriétés d'atténuation des tissus du corps et de l'information de mouvement peut être exploitée pour la correction des données d'émission et pour la reconstruction de l'image TEP. Dans l'imagerie TEP / CT, les données fournies par les images TDM peuvent être utilisées pour générer des cartes d'atténuation à 511 keV pour la correction d'atténuation des données TEP. La principale motivation derrière la combinaison de TEP et IRM, est en plus de réduire l'exposition aux radiations, est de profiter de la capacité de fournir des IRM avec un contraste des tissus mous supérieur à CT. Ceci permet non seulement d'améliorer la localisation des lésions mais peut également être exploitée pour la correction de l'effet de volume partiel anatomiquement guidé dans la reconstruction de l'image TEP. En outre, la fourniture d'informations de mouvement du patient par l'IRM, permet la mise en œuvre de la correction du mouvement des données de TEP dans l'acquisition TEP / IRM simultanée. En raison de la restriction de la gamme de positons dans le champ magnétique, la résolution de TEP dans le plan sera améliorée en particulier pour la gamme de positons radio-isotopes longue. Sans aucun doute, l'intégration des modalités d'imagerie IRM / CT avec TEP introduit de nouvelles possibilités et maximise le potentiel de l'imagerie moléculaire dans la pratique clinique; néanmoins, l'imagerie hybride provoque de nouvelles limites et des défis techniques qui peuvent nuire à la qualité d'image TEP et à la quantification. Contrairement à l'imagerie TEP / CT, où la correction d'atténuation est relativement simple, la correction d'atténuation en TEP / IRM est un défi majeur en raison du manque d'informations suffisantes fournies par l'IRM sur les caractéristiques d'atténuation des tissus biologiques, de telle sorte que les images IRM peuvent ne pas être directement converties en cartes d'atténuation. En outre, l'IRM souffre d'une longue période d'acquisition, ce qui est un facteur limitant pour l'exploitation dans une large gamme d'applications cliniques. Même si l'IRM peut fournir une identification des tissus mous de qualité supérieure, l'identification de l'os reste un défi de signification puisque les structures osseuses sont reflétées dans un signal vide (semblable à l'air) dans la plupart des séquences d'IRM classiques. Par conséquent, une bonne carte d'atténuation générée à partir d'images IRM est généralement contestée par la certitude de l'extraction de l'os.

Le travail présenté dans cette thèse se concentre sur certains des défis prévalents rencontrés en reconstruction d'image TEP / IRM essentiellement la correction d'atténuation guidée par IRM et l'identification des os à partir d'images IRM par le développement des techniques au-delà de l'état de l'art actuelle et la validation de nouveaux algorithmes. En particulier, cette thèse porte sur l'évaluation clinique des techniques de correction d'atténuation guidées par IRM, l'amélioration des méthodes de base-IRM pour la génération des cartes d'atténuation et la segmentation des os à partir d'images IRM dans l'imagerie du corps entier.

La précision quantitative des techniques de correction d'atténuation à base d'IRM utilisé dans la pratique clinique ont été comparées en utilisant un ensemble de données de cas cliniques. Les méthodes évaluées comprenaient la carte d'atténuation 3-classe implémentée sur le système Ingenuity TF TEP / IRM et la carte d'atténuation 4-classe similaire à l'approche utilisée sur le Siemens mMR TEP / MR. Dans cette étude, les données de TEP de 14 cas cliniques de tumeurs malignes ont été corrigées pour les photons atténués à l'aide des cartes d'atténuation 3-classe (contenant de l'air, du poumon et des tissus mous) et des cartes d'atténuation 4-classe (contenant de l'air, du poumon, de la graisse et des tissus mous). La carte d'atténuation 3-classe a entraîné un biais significatif positif dans les poumons en raison du coefficient d'atténuation le plus utilisé et un biais

négatif dans d'autres régions. La carte d'atténuation 4-classe a légèrement sous-estimé l'absorption du traceur dans les poumons, mais a conduit encore à une plus grande polarisation négative dans d'autres régions du corps.

Une nouvelle approche de génération pseudo-CT a été proposée pour l'extraction précise des os et pour l'estimation des propriétés d'atténuation du poumon. Puisque la valeur d'atténuation du poumon présente une variation spectaculaire entre les patients, la valeur d'estimation d'atténuation du poumon spécifique au patient est un problème important dans l'ensemble du corps. L'approche présentée vise à améliorer le processus gaussien régression (GPR) proposé par Hofmann et al. (J Nucl Med 2011). A cet effet, l'ensemble de données de l'atlas a été réglé sur la base de la corrélation locale croisée et normalisée pour sélectionner l'image la plus similaire dans l'ensemble de données d'atlas pour chaque voxel. Pour les tissus pulmonaires, l'avantage de la corrélation existant entre le volume pulmonaire et les propriétés d'atténuation correspondant a été conduit pour prévoir des coefficients d'atténuation du poumon spécifiques au patient. Dans le cas des tissus pathologiques dans les poumons, les lésions ont été segmentés sur les images TEP suivie d'affectation de coefficient d'atténuation des tissus mous. L'algorithme proposé a été comparé à l'approche original d' Hofmann et la technique de correction d'atténuation 3-classe mis en œuvre sur le Philips Ingenuity TF TEP / IRM. La technique proposée a permis une précision de quantification de TEP plus meilleure que celle du Hofmann et de 3 classe ,du fait d'une extraction plus précise des os et une meilleure prédiction des coefficients d'atténuation du poumon.

Dans l'étude suivante, nous avons comparé la précision de l'extraction de l'os du corps entier à partir d'images IRM exploitant un certain nombre de méthodes de segmentation basée sur atlas. La motivation de cette étude était de trouver l'approche la plus prometteuse dans le but de dériver des cartes d'atténuation TEP dérivées par IRM. À cette fin, une variété de stratégies de segmentation basée sur la méthode atlas, qui sont couramment utilisés dans le domaine de l'imagerie médicale essentiellement la segmentation et la génération pseudo-CT, ont été mis en œuvre et évalués en termes de précision de la segmentation des os du corps entier. Parmi ces différentes méthodes examinées, l'approche atlas fusion voxel-sage présentait un potentiel prometteur pour la segmentation précise et fiable de l'os.

L'un des principaux défis de méthodes basées sur l'atlas est le temps de traitement pris par l'enregistrement des atlas. Ainsi, une nouvelle méthode a été proposée qui consiste à une seule inscription en ligne entre les images cibles et de référence, quel que soit le nombre d'atlas images (N), tandis que pour les atlas images restantes, les matrices de transformation pré-calculées à l'image de référence sont utilisées pour les aligner sur l'image cible. Les caractéristiques de performance de la méthode proposée ont été évaluées et comparées avec les stratégies de génération des cartes d'atténuation conventionnelles basées sur atlas (enregistrement direct de l'atlas entier des images). L'analyse quantitative a révélé une bonne corrélation entre les images TEP corrigées pour l'atténuation en utilisant la méthode proposée et les images CT correspondantes. Le temps de calcul a été réduit d'un facteur 1 / N, au détriment d'une légère diminution de la précision quantitative. La planification du traitement de la thérapie des rayonnements guidée par IRM est également contestée par l'absence d'un lien direct entre les intensités de voxels d'IRM et la densité électronique. Deux étapes d'algorithme (segmentation et de fusion) basées sur atlas ont été proposées, concentrées sur l'identification des tissus osseux pour créer une image pseudo-CT à partir des séquences d'IRM classiques. Dans la première étape, la segmentation des os de l'image cible est optimisée grâce au vote de l'atlas pondéré local. La carte de l'os obtenu est ensuite utilisée pour évaluer la qualité des atlas déformés pour effectuer la fusion atlas voxel-sage pondérée. Une évaluation dosimétrique des plans de traitement des photons de thérapie arc volumétrique modulée a été calculée en utilisant les différentes images pseudo-CT. La méthode proposée génère des images précises pseudo-CT à partir de séquences Dixon IRM classiques avec une meilleure précision de l'extraction de l'os. L'approche est prometteuse pour une utilisation potentielle dans la correction d'atténuation TEP et IRM seule ou l'imagerie hybride TEP /IRM guidée par la planification du traitement de la thérapie des radiations.

Dans l'étude suivante, un certain nombre de stratégies développé pour la correction d'atténuation guidée par IRM a été évalué et comparé quantitativement. Ces méthodes comprennent trois méthodes d'approches fondées sur les émissions de segmentation standards de 3 classe MR, l'enregistrement avancé basées sur atlas et les approches basées sur les émissions dans le contexte du temps de vol du cerveau (TOF) PET / IRM. Une méthode robuste d'enregistrement atlas AC, qui emploie la fusion pondérée locale d'atlas en fonction de leur similitude morphologique pour cibler l'image MR, a été comparée à la reconstruction du maximum de vraisemblance de l'atténuation et de l'activité guidée par IRM 'Maximum Likelihood reconstruction of Attenuation and Activity (MLAA)'. La précision de la prédiction de l'os et la quantification de l'absorption du traceur ont été évaluées pour la performance des différentes stratégies de la correction d'atténuation AC. La carte d'atténuation 3-classe a

conduit à une sous-estimation importante de l'absorption du traceur, alors que la méthode ERMR-AC a été incapable de réduire remarquablement les erreurs de quantification. D'autre part, la méthode atlas-AC proposée a fourni des cartes d'atténuation les plus précises en termes de la précision de la prédiction de l'os, et donc un biais de quantification le plus bas.

La moyenne en fonction de forme 'Shape-Based Averaging (SBA)', qui est une méthode éprouvée de de la fusion atlas, a été proposée dans le but de la segmentation des os de l'ensemble du corps depuis des images IRM. La performance de la méthode SBA a été améliorée par incorporation de la régularisation locale pour maximiser la précision de la segmentation des os. La méthode améliorée a été utilisée pour générer des cartes d'atténuation TEP et sa performance a été évaluée en termes de récupération de l'absorption du radiotraceur. L'évaluation quantitative des images TEP corrigées pour l'atténuation, en utilisant le projet de pseudo-CT, a révélé une bonne corrélation avec les images TEP corrigées pour l'atténuation en utilisant comme référence des images CT correspondantes.

To My Parents

Papers included in this dissertation

This dissertation is based on a number of studies submitted and reported in the following peer-reviewed original journal articles. Published articles are reprinted by the kind permission of the referred publisher.

1. **Arabi H**, Rager O, Alem A, Varoquaux A, Becker M and Zaidi H "Clinical assessment of MRI-guided 3-class and 4-class attenuation correction in PET/MR" Mol Imaging Biol Vol. 17, No. 2, pp 264-276 (2015).

2. Mehranian A, **Arabi H** and Zaidi H "Magnetic resonance imaging-guided attenuation correction in PET/MRI: Challenges, solutions and opportunities" Med Phys Vol. 43, No. 3, pp 1130-1155 (2016).

3. **Arabi H** and Zaidi H "MRI-guided attenuation correction in whole-body PET/MRI using a sorted atlas approach" Med Imag Anal Vol. 31, No. July, pp 1-15 (2016).

4. Mehranian A, **Arabi H** and Zaidi H "Quantitative analysis of MRI-guided attenuation correction methods in time-of-flight brain PET/MRI" Neuroimage Vol. 130, pp 123-133 (2016).

5. **Arabi H** and Zaidi H "One registration multi atlas-based pseudo-CT generation for attenuation correction in PET/MRI" Eur J Nucl Med Mol Imaging Vol. 43, No. 11, pp 2021-2035 (2016).

6. **Arabi H**, Koutsouvelis N, Rouzaud M, Miralbell R and Zaidi H "Atlas-guided generation of pseudoCT images for hybrid PET-MRI and MR-only based radiotherapy treatment planning" Phys Med Biol Vol. 61, No. 17, pp 6531-6552 (2016).

7. **Arabi H** and Zaidi H "Whole-body bone segmentation from MRI for PET/MRI attenuation correction using shape-based averaging" Med Phys Vol. 43, No. 11, pp 5848-5861 (2016).

8. **Arabi H** and Zaidi H "Comparison of atlas-based techniques for whole-body bone segmentation" Med Image Anal Vol. 36, pp 98–112 (2017).

Contents

Chapter 1

Introduction

I. Introduction

Positron Emission Tomography (PET), as a powerful molecular imaging modality, benefits from the high sensitivity of detecting underlying electron-positron annihilation, allowing the use of relatively little exogenous material [1]. The recent technical advancements in the field of biomedical engineering have led to remarkable improvement of molecular imaging techniques for the quantitative evaluation and examination of biological processes *in vivo* [2]. In addition, the development of new drugs and biomarkers has attracted much attention aiming at the early detection and treatment of life threatening diseases. PET radiotracers are commonly made of naturally occurring compounds specifically radiolabeled to participate into certain biochemical processes. A wide range of radiotracers and molecular imaging probes labeled with positron emitting radionuclides can be imaged on PET scanners due to their relatively high sensitivity and spatial resolution compared to single-photon emission computed tomography (SPECT). This outstanding merit of a specific PET has made it an invaluable tool in clinical oncology for the diagnosis, staging, restaging, monitoring of response to treatment and radiation therapy treatment planning. Besides, PET can be used for assessing neurodegenerative and cardiovascular diseases [3]. PET measures the spatial (and possibly temporal) distribution of radiotracer. PET radiotracers emit positrons, which travel a certain distance determined by their kinetic energy, before annihilation into two annihilation photons travelling in virtually opposite directions. The annihilation photon are then recorded in coincidence by the PET scanner's detectors. PET images depict the spatial distribution of the tracer in various organs/tissues depending on the characteristics of the tracer. The provided functional and metabolic information is useful but PET inherently lacks anatomical details. Therefore, there is a need to combine PET with high-resolution anatomical information provided by other imaging modalities, such as x-ray computed tomography (CT) and magnetic resonance imaging (MRI), to improve the interpretation of PET images through anatomical mapping of the metabolic abnormalities.

Nowadays, hybrid PET/CT imaging is regarded as the method of choice in clinical practice owing to its potential to overcome the shortcomings of standalone PET imaging and to enable the synergy of combined functional and anatomical imaging [4]. X-ray CT provides tomographic images of the underlying tissues and structures based on their attenuation properties through transmission scanning. The detailed anatomical information provided by CT images in hybrid PET/CT imaging allows for accurate localization of radiotracer uptake in PET images as well as improving PET^s quantitative accuracy through CT-based attenuation correction (CTAC) of PET data [5]. Since the underlying principle of CT image formation is based on the photon-electron interaction, CT numbers are directly related to photon attenuation properties of tissues. Therefore, CT images can be converted into PET attenuation maps through simple conversion to the photon energy of 511 keV to correct the PET data for attenuation. MRI is also able to provide required anatomical details for combination with the molecular images provided by PET. The capability of MR imaging to achieve high spatial resolution images with superior soft-tissue contrast compared with CT has paved the way for combined PET/MRI to become the method-of-choice in clinical oncology to assess brain, soft-tissue neoplasms, lesions in the pelvis and head and neck regions (Fig. 1). The underlying principle of MR imaging is based on proton density and relaxation time properties of tissues exited by radiofrequency signals inside an external magnetic field. Therefore, MRI, as opposed to CT imaging, does not contribute additional radiation exposure to patients, which may play an important role in the pediatric population, serial studies and adaptive radiation therapy planning [6]. In addition, the complementary functional information provided by multiparametric MR, such as diffusion weighted imaging, dynamic contrast-enhanced MRI, fMRI and MR spectroscopy can contribute precious clinical and research information [7]. Simultaneous PET/MRI data acquisition also provides an opportunity to correct forpartial volume effect in PET images and the concurrent assessment of functional and molecular processes [8]. In addition, performing PET acquisition within the magnetic field generated by MRI can reduce the positron range of the radionuclide in the direction perpendicular to the magnetic field, which improves PET's spatial resolution, particularly for radiotracers using high range positions [9]. Uncertainties in activity distribution estimation caused by moving organs during PET acquisition degrades significantly the effective spatial resolution and impairs the quantitative accuracy of PET. Simultaneous PET/MR imaging can overcome this issue through employing motion deformation fields generated by MR imaging to reconstruct motion-compensated PET images [10].

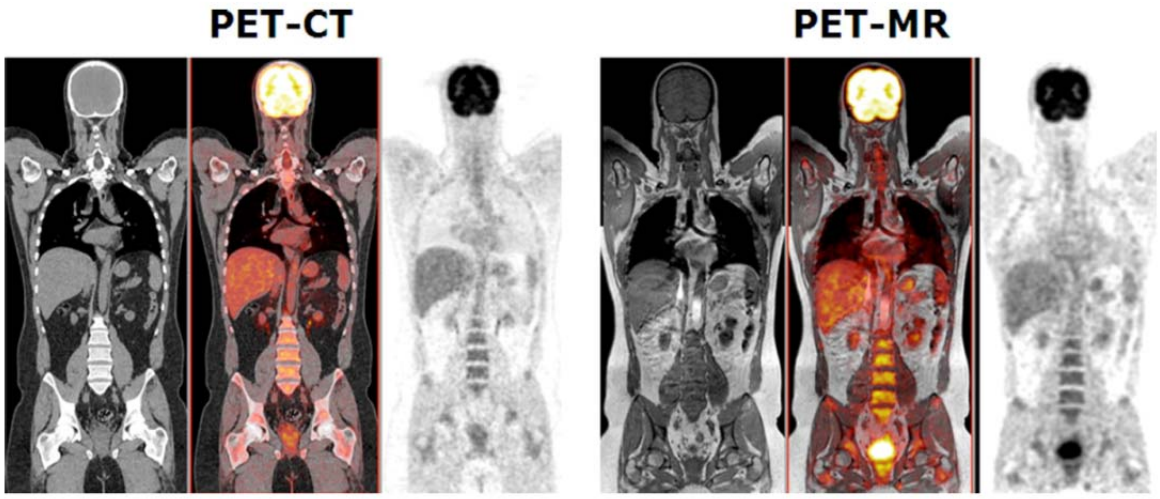

Figure. 1 Representative clinical PET/CT (left) and PET/MR (right) whole-body images of the same patient acquired sequentially (60 min time difference) on two combined systems (Siemens Biograph Hirez TrueV and Philips Ingenuity TF PET/MRI, respectively) following injection of 370 MBq of ^{18}F-FDG. Reprinted with permission from [11].

Despite the fact that integration of MR and PET imaging provides precious advantages and interesting clinical avenues, MRI suffers from relatively long data acquisition time, compared to CT, especially when complementary MR sequences are required [12]. Motion tracking and supplementary MR sequences are only effective with fast data acquisition. Above all, in hybrid PET/MRI, PET attenuation correction should be performed using MR images. As opposed to CT images, MR image intensities indicate hydrogen proton density, relaxation time properties of tissues and the selected pulse timing parameters rather than the electron density required for PET attenuation correction. Hence, MR intensities contain no or little information about the photon attenuation properties of the tissues and therefore there is no unique global mapping to convert MR images to PET attenuation maps. Moreover, bony structures, an important tissue type in attenuation maps owing to high density and photon stopping power, exhibit no or very faint signals in images acquired with conventional MR sequences. Low levels of water content in bony structures and short transverse relaxation time cause bone to be projected void on MR images very similar to air. Due to this effect, distinguishing between bony structures and air is difficult when using conventional MR sequences [13]. To overcome the issue of bone identification on MR images, ultra-short echo time (UTE) MR pulse sequences have been proposed which can distinguish bony structures to some extent [14]. However, UTE pulse sequences are timing-consuming and susceptible to magnetic field inhomogeneities. The drawbacks of UTE sequence has restricted its application to brain imaging (single bed position) and therefore this technique is not yet clinically feasible in whole-body MRI-based attenuation correction (MRAC) of PET data [15]. Apart from bony structures, lung tissue, exhibiting weak signal, cannot be well distinguished in conventional MR sequences. Therefore, estimation of lung attenuation value from MR images is a significant challenge in MRI-guided whole-body attenuation map generation. Employing UTE techniques can be effective for the detection and visualization of lung parenchyma. However, these techniques suffer from lung acquisition time which greatly limits their application in whole-body imaging [16]. Recent commercial PET/MRI systems being used in clinical setting employ MRI segmentation-based approaches as the standard attenuation correction method [13, 17]. In principle, these methods segment MRI into a number of tissue-classes followed by assignment of predefined constant linear attenuation coefficients at 511-keV to each tissue class. For example, the Philips Ingenuity TF PET/MR (Philips Healthcare, Cleveland, Ohio, USA) uses a 3-class attenuation map obtained from segmentation of a T1-weighted MR sequence into air, lung and soft-tissue followed by assignment of attenuation coefficients (air: 0 cm^{-1}, lung: 0.022 cm^{-1}, soft-tissue: 0.096 cm^{-1}) [18]. Conversely, the approach used on the Siemens mMR PET/MR (Siemens Healthcare, Erlangen, USA) system generates a 4-class attenuation map by performing segmentation of a Dixon MR sequence [19] including fat in addition to the above referenced tissues classes [13, 20]. The following attenuation coefficients are then assigned to each tissue class (air: 0 cm^{-1}, lung: 0.018 cm^{-1}, fat: 0.086 cm^{-1}, soft-tissue: 0.096 cm^{-1}). Segmentation approaches ignore inter/intra-patient heterogeneity of attenuation coefficients in different tissue classes by assigning predefined uniform attenuation coefficient to each tissue class. However, above all, due to

the fact that both bony structures and air cavities appear void and cannot be well differentiated when using conventional MR sequences (with fast acquisition times), these tissue classes are often ignored and replaced by soft-tissue, which can lead to significant bias in PET tracer uptake quantification [21, 22].

Due to the significant contribution of bony structures to photon attenuation and to account for their presence in PET attenuation maps, other techniques of attenuation map generation based on atlas registration [23], external transmission sources [24] and PET emission data [25] have been revisited and found practical application in PET/MRI.

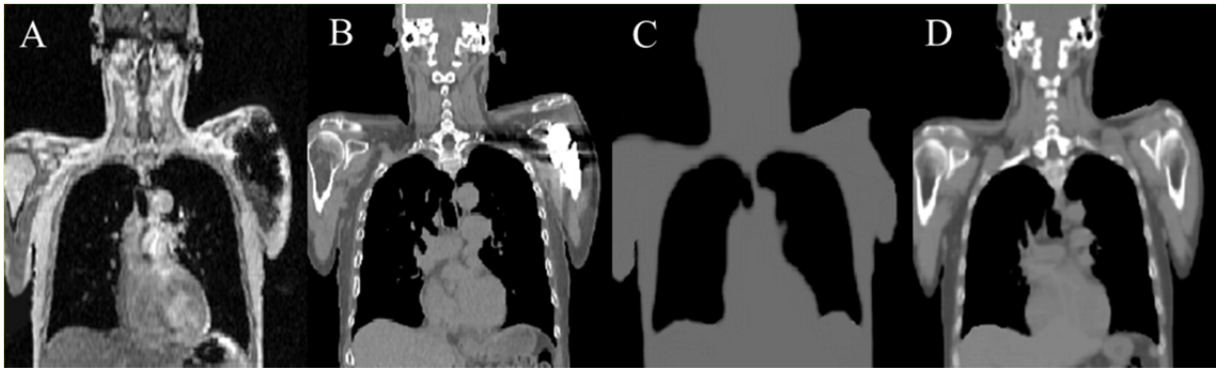

Figure 2. A) IP Dixon MR image, one of the conventional sequences used for attenuation map generation, B) the corresponding aligned CT image C) 3-class attenuation map generated by the Philips Ingenuity TF PET/MR (Philips Healthcare, Cleveland, Ohio, USA). D) Pseudo-CT attenuation map generated using an atlas-based approach.

In principle, atlas-based or registration approaches start with spatially aligning a pre-defined spatial distribution of coefficients or atlas database created using similar image type to a target MRI dataset. Atlas registration-based approaches involve aligning a co-registered MRI-CT atlas dataset to the MR image of the patient to generate a pseudo CT image or by employing machine learning techniques to create a mapping function that predicts a pseudo CT image. These methods proved promising to solve MRI-guided attenuation map generation challenge, particularly in brain imaging where internal organs/tissues are fixed to the skull base and head motion is mostly rigid, thus leading to an acceptable registration between the atlas dataset and different subject images [26]. Regarding whole-body imaging, due to the large axial field-of-view, moving organs such as the lungs, non-rigid motion of the body and substantial anatomical differences between patients, accurate registration is rarely possible. Therefore, the majority of atlas-based methods are applied and evaluated in the context of brain imaging [27]. However, atlas-based approaches have been recently revisited in whole-body imaging thanks to the availability of advanced registration algorithms and image processing techniques (Figure 2) [28]. Recent advances in PET detector technology enabled the introduction of fast signal formation and time-of-flight (TOF) PET capability in clinical PET/CT and PET/MRI systems. This capability helps to improve lesion detectability and image quality, as well as to reduce acquisition time and/or patient's administered activity [29]. TOF PET capability opens the opportunity to derive patient-specific attenuation maps in PET/MRI. Hence, the uncertainties associated with segmentation-based methods can be avoided. In order to find a surrogate for CT attenuation map, transmission-based approaches directly measuring attenuation coefficients using external positron-emitting sources that operate in a simultaneous transmission and emission acquisition have been explored. In the case of TOF imaging, the TOF information can then be used to separate transmission from emission data. This method suffers from the low count statistics of transmission scanning limited by emission scan time per bed position and additional patient dose [30]. However, emission-based approaches do not require external transmission sources to simultaneously estimate activity and attenuation by relying on TOF emission data. Despite promising results achieved by simultaneous activity and attenuation estimation methods, these approaches suffer from high level of noise, uncertainty in bone estimation, great dependency on radiotracer distribution and TOF resolution as well as activity-attenuation cross-talk [31].

Hybrid imaging systems, in particular PET/MRI, have triggered special interest during the last decade in clinical and research settings. The combination of anatomical information from MRI with molecular information provided by PET has introduced new opportunities in the clinical utility of PET and also triggered an emerging paradigm toward multi-modality and multi-parametric imaging. A number of active research groups in both

academic and corporate settings are focusing their efforts on addressing key limiting factors of PET/MR imaging to create new innovative approaches in multimodal molecular imaging.

In this dissertation, we focused mainly on MRI-guided PET attenuation map generation using atlas-based techniques. To this end, whole-body imaging was addressed since there is a need for more accurate attenuation map containing bony structures and proper estimation of lung attenuation maps. Moreover, whole-body attenuation map generation with separate bone class is not yet clinically feasible using the UTE sequence owing to its prohibitively long acquisition time. Despite the need for bone segmentation from MR images in whole-body imaging, this issue has not received much attention in the literature.

II. Aim and outline of thesis

In the work presented in this dissertation, we aimed at addressing major challenges encountered in PET/MRI imaging specifically MR-guided photon attenuation correction and bone identification from MR images through further development of current state-of-the-art techniques and the investigation and validation of new algorithms. Along these lines, we summarize the aims of this thesis in the following items:

i) Assessment of quantitative accuracy of MRI-based attenuation correction techniques being used in clinical practice in order to discover and address the major shortcomings of available methods.

ii) The development and evaluation of robust and accurate atlas-based methods aiming at generation of μ-maps for the purpose of PET/MR attenuation correction task and MR-alone radiation therapy planning particularly for whole-body imaging.

iii) The development and evaluation of accurate whole-body bone segmentation from MR images using methods of atlas-based segmentation.

In chapter 2, the early and latest state-of-the-art developments, innovations and strategies in PET/MRI attenuation correction were reviewed where some of the methods presented in this thesis are also included. Quantitative PET imaging involves a certain steps of data corrections among which attenuation correction is an essential part. Thus, to improve the quantitative accuracy of hybrid PET/MR imaging, robust and novel strategies are required to be developed and evaluated for deriving accurate attenuation maps. An extensive and comprehensive review of available methods together with their advantages and drawbacks for addressing the challenges of MR-based attenuation correction is presented in this chapter. Moreover, a discussion over future prospects, potential clinical applications and their commercial feasibilities are also discussed.

In chapter 3, the quantitative accuracy of MRI-based attenuation correction techniques being used in clinical practice were compared using a dataset of clinical cases. The evaluated methods consist of the 3-class attenuation map implemented on the Ingenuity TF PET/MRI and the 4-class attenuation map similar to the approach used on the Siemens mMR PET/MR while taking the CT-based attenuation corrected PET images as standard of reference. The standard uptake value (SUV) metric was used to assess the accuracy of radiotracer uptake recovery for volumes of interest in various organs/tissues and malignant lesions. These two scanners were chosen for this study because they are widely used in clinical practice and the evaluation of their performances allows us for further improvement of the strategies.

The clinicaly active PET/MR attenuation correction strategies, particularly for whole-body imaging, suffer from a separate bone tissue class which leads to significant underestimation of activity recovery in PET images. Moreover, patient-specific lung attenuation estimation is ignored in these strategies. In chapter 4, a new pseudo-CT generation approach was proposed for accurate extraction of bones and estimation of lung attenuation properties. The presented approach aimed to improve the Gaussian process regression (GPR) kernel proposed by Hofmann *et al.* (J Nucl Med 2011). The atlas dataset was sorted on the basis of local normalized cross-correlation to select the most similar image in the atlas dataset for each voxel. For lung tissue, the advantage of the correlation between lung volume and corresponding attenuation properties was taken to predict patient-specific lung attenuation coefficients. Moreover, in case of pathological tissues in the lungs, the lesions were segmented on PET images followed by assignment of soft-tissue attenuation coefficient. The proposed algorithm was compared to Hofmann's approach and the 3-class attenuation correction technique implemented on the Philips Ingenuity TF PET/MR.

Since bony structures play key role in accuracy of whole-body attenuation map generation, in chapter 5, we compared the accuracy of whole-body bone extraction from MR images exploiting a number of atlas-based segmentation methods. The motivation for this study was to find the most promising approach for the purpose of MR-derived PET attenuation map generation. To this end, a variety of atlas-based segmentation strategies, which are commonly used in the field of image segmentation and pseudo-CT generation, were implemented and evaluated in terms of whole-body bone segmentation accuracy.

One of the major challenges of atlas-based method of segmentation and attenuation map generation is the long processing time taken by of atlas registration. In chapter 6, a novel method was proposed that involves only one online registration between the target and reference images, regardless of the number of atlas images (N), while for the remaining atlas images, the pre-computed transformation matrices to the reference image are used to align them to the target image. The performance characteristics of the proposed method was evaluated and compared with conventional atlas-based attenuation map generation strategies (direct registration of the entire atlas images). The proposed algorithm was capable of generating promising attenuation maps.

Generation of μ-map from MR images not only can be used for the task of PET/MR attenuation correction but also for MR-alone radiation therapy planning. Radiation therapy treatment planning is challenged by the lack of a direct link between MRI voxel intensities and electron density. In chapter 7, a novel two-step (segmentation and fusion) atlas-based algorithm was proposed focusing on bone tissue identification to create a pseudo-CT image from conventional MRI sequences. In the first step, bone segmentation of the target image is optimized through local weighted atlas voting. The obtained bone map is then used to assess the quality of deformed atlases to perform voxel-wise weighted atlas fusion. A dosimetric evaluation of volumetric modulated arc therapy photon treatment plans calculated using the different pseudo-CT images was carried out using CT images as reference.

Quantitative PET/MR imaging is markedly challenged by the accuracy of attenuation maps derived from MR images for the task of attenuation correction. In chapter 8, a number of strategies have been developed for MRI-guided attenuation correction were quantitatively evaluated and compared. These methods include three generic attenuation correction methods of standard 3-class MR segmentation-based, advanced atlas-registration-based and emission-based approaches in the context of brain time-of-flight (TOF) PET/MRI. A clinical set of brain images examined by MRI and 18F-FDG PET/CT were reconstructed using different attenuation maps derived from MRI, namely standard 3-class MR-segmentation, atlas-based and emission-based AC methods. 3-class attenuation maps were generated from T1-weighted MRI images with background air, fat and soft-tissue classes followed by assignment of predefined constant linear attenuation coefficients. A robust atlas-registration based AC method, which employs local weighted fusion of atlases based on their morphological similarity to the target MR image, was compared with recently proposed MRI-guided maximum likelihood reconstruction of activity and attenuation (MLAA) algorithm. The accuracy of bone prediction and quantification of PET tracer uptake were assessed to evaluate the performance of the different AC strategies with respect to the reference CT and PET/CT images.

In chapter 9, we evaluate the performance of shape-based averaging (SBA) technique for whole-body bone segmentation from MRI in the context of MRI-guided attenuation correction (MRAC) in hybrid PET/MRI. In this study, we aimed to enhance the performance of the SBA scheme through combination with statistical atlas fusion techniques. The SBA method was proposed to be combined with simultaneous truth and performance level estimation (STAPLE) and the selective and iterative method for performance level estimation (SIMPLE). Moreover, a fast and efficient shape comparison-based atlas selection scheme was developed and incorporated into the SBA method. The performance of the proposed methods was assessed using a clinical dataset of PET/CT and MR images of 21 patients. The evaluation was performed based on the accuracy of extracted whole-body bones, fragmentation, and computational time achieved by the different methods. The majority voting (MV) atlas fusion scheme was also evaluated as a conventional and commonly used method. MRI-guided attenuation maps were generated using the different segmentation methods. Thereafter, quantitative analysis of attenuation corrected PET images was performed using CT-based attenuation correction as standard of reference.

Chapter 10 provides a conclusion of this work and discusses prospective development in this field. Further improvement of the works presented in this dissertation and their future applications are also discussed in this chapter.

References

[1] L. Fass, "Imaging and cancer: a review," *Molecular oncology,* vol. 2, pp. 115-152, 2008.

[2] D. A. Torigian, H. Zaidi, T. C. Kwee, B. Saboury, J. K. Udupa, Z.-H. Cho*, et al.*, "PET/MR imaging: technical aspects and potential clinical applications," *Radiology,* vol. 267, pp. 26-44, 2013.

[3] J. F. Valliant, "A bridge not too far: Linking disciplines through molecular imaging probes.," *J Nucl Med,* vol. 51, pp. 1258-1268, August 1, 2010 2010.

[4] O. Israel, M. Mor, D. Gaitini, Z. Keidar, L. Guralnik, A. Engel*, et al.*, "Combined functional and structural evaluation of cancer patients with a hybrid camera-based PET/CT system using F-18 FDG.," *J Nucl Med,* vol. 43, pp. 1129-1136, 2002.

[5] R. Bar-Shalom, N. Yefemov, L. Guralnik, D. Gaitini, A. Frenkel, A. Kuten*, et al.*, "Clinical performance of PET/CT in evaluation of cancer: Additional value for diagnostic imaging and patient management.," *J Nucl Med,* vol. 44, pp. 1200-1209, 2003.

[6] J. Brunt, "Computed tomography–magnetic resonance image registration in radiotherapy treatment planning," *Clinical Oncology,* vol. 22, pp. 688-697, 2010.

[7] A. R. Padhani and K. A. Miles, "Multiparametric Imaging of Tumor Response to Therapy 1," *Radiology,* vol. 256, pp. 348-364, 2010.

[8] C. C. Meltzer, P. E. Kinahan, P. J. Greer, T. E. Nichols, C. Comtat, M. N. Cantwell*, et al.*, "Comparative evaluation of MR-based partial-volume correction schemes for PET.," *J Nucl Med,* vol. 40, pp. 2053-2065, Dec 1999.

[9] J. Cal-González, J. Herraiz, S. España, P. Corzo, J. J. Vaquero, M. Desco*, et al.*, "Positron range estimations with PeneloPET," *Phys Med Biol,* vol. 58, p. 5127, 2013.

[10] S. Y. Chun, T. G. Reese, J. Ouyang, B. Guerin, C. Catana, X. Zhu*, et al.*, "MRI-based nonrigid motion correction in simultaneous PET/MRI," *Journal of Nuclear Medicine,* vol. 53, pp. 1284-1291, 2012.

[11] H. Zaidi and A. Del Guerra, "An outlook on future design of hybrid PET/MRI systems.," *Med Phys,* vol. 38, pp. 5667-5689, 2011.

[12] G. K. von Schulthess and P. Veit-Haibach, "Workflow considerations in PET/MR imaging," *Journal of Nuclear Medicine,* vol. 55, pp. 19S-24S, 2014.

[13] A. Martinez-Moller, M. Souvatzoglou, G. Delso, R. A. Bundschuh, C. Chefd'hotel, S. I. Ziegler*, et al.*, "Tissue classification as a potential approach for attenuation correction in whole-body PET/MRI: Evaluation with PET/CT data.," *J Nucl Med,* vol. 50, pp. 520-526, Apr 2009.

[14] V. Keereman, Y. Fierens, T. Broux, Y. De Deene, M. Lonneux, and S. Vandenberghe, "MRI-based attenuation correction for PET/MRI using ultrashort echo time sequences.," *J Nucl Med,* vol. 51, pp. 812-818, May 2010.

[15] A. Aitken, D. Giese, C. Tsoumpas, P. Schleyer, S. Kozerke, C. Prieto*, et al.*, "Improved UTE-based attenuation correction for cranial PET-MR using dynamic magnetic field monitoring," *Medical physics,* vol. 41, p. 012302, 2014.

[16] K. Zeimpekis, G. Delso, F. Wiesinger, P. Veit-Haibach, G. von Schulthess, and R. Grimm, "Investigation of 3D UTE MRI for lung PET attenuation correction," *Journal of Nuclear Medicine,* vol. 55, pp. 2103-2103, 2014.

[17] Z. Hu, N. Ojha, S. Renisch, V. Schulz, I. Torres, D. Pal*, et al.*, "MR-based attenuation correction for a whole-body sequential PET/MR system," in *IEEE Nuclear Science Symposium & Medical Imaging Conference*, 25-31 October 2009, Orlando (FL), USA, 2009, pp. 3508-3512.

[18] V. Schulz, I. Torres-Espallardo, S. Renisch, Z. Hu, N. Ojha, P. Börnert*, et al.*, "Automatic, three-segment, MR-based attenuation correction for whole-body PET/MR data.," *Eur J Nucl Med Mol Imaging,* vol. 38, pp. 138-152, 2011.

[19] W. T. Dixon, "Simple proton spectroscopic imaging.," *Radiology,* vol. 153, pp. 189-194, Oct 1984.

[20] G. Delso, S. Furst, B. Jakoby, R. Ladebeck, C. Ganter, S. G. Nekolla*, et al.*, "Performance measurements of the Siemens mMR integrated whole-body PET/MR scanner.," *J Nucl Med,* vol. 52, pp. 1914-1922, Dec 2011.

[21] I. Bezrukov, H. Schmidt, F. Mantlik, N. Schwenzer, C. Brendle, B. Schölkopf*, et al.*, "MR-Based Attenuation Correction Methods for Improved PET Quantification in Lesions Within Bone and Susceptibility Artifact Regions," *Journal of Nuclear Medicine,* vol. 54, pp. 1768-1774, October 1, 2013 2013.

[22] O. Jinsong, C. Se Young, Y. Petibon, A. A. Bonab, N. Alpert, and G. El Fakhri, "Bias Atlases for Segmentation-Based PET Attenuation Correction Using PET-CT and MR," *Nuclear Science, IEEE Transactions on,* vol. 60, pp. 3373-3382, 2013.

[23] M. Hofmann, B. Pichler, B. Schölkopf, and T. Beyer, "Towards quantitative PET/MRI: a review of MR-based attenuation correction techniques," *Eur J Nucl Med Mol Imaging,* vol. 36, pp. 93-104, 2009.

[24] P. Mollet, V. Keereman, E. Clementel, and S. Vandenberghe, "Simultaneous MR-compatible emission and transmission imaging for PET using time-of-flight information.," *IEEE Trans Med Imaging,* vol. 31, pp. 1734-1742, 2012.

[25] A. Salomon, A. Goedicke, B. Schweizer, T. Aach, and V. Schulz, "Simultaneous reconstruction of activity and attenuation for PET/MR.," *IEEE Trans Med Imaging,* vol. 30, pp. 804-813, 2011.

[26] N. Burgos, M. Cardoso, M. Modat, S. Pedemonte, J. Dickson, A. Barnes*, et al.*, "Attenuation Correction Synthesis for Hybrid PET-MR Scanners," in *Medical Image Computing and Computer-Assisted Intervention – MICCAI 2013*. vol. 8149, K. Mori, I. Sakuma, Y. Sato, C. Barillot, and N. Navab, Eds., ed: Springer Berlin Heidelberg, 2013, pp. 147-154.

[27] N. Burgos, M. J. Cardoso, K. Thielemans, M. Modat, S. Pedemonte, J. Dickson*, et al.*, "Attenuation Correction Synthesis for Hybrid PET-MR Scanners: Application to Brain Studies," *Medical Imaging, IEEE Transactions on,* vol. 33, pp. 2332-2341, 2014.

[28] H. R. Marshall, J. Patrick, D. Laidley, F. S. Prato, J. Butler, J. Théberge*, et al.*, "Description and assessment of a registration-based approach to include bones for attenuation correction of whole-body PET/MRI," *Medical physics,* vol. 40, p. 082509, 2013.

[29] M. Conti, "Focus on time-of-flight PET: the benefits of improved time resolution.," *Eur J Nucl Med Mol Imaging,* vol. 38, pp. 1147-1157, 2011.

[30] P. Mollet, V. Keereman, J. Bini, D. Izquierdo-Garcia, Z. A. Fayad, and S. Vandenberghe, "Improvement of attenuation correction in time-of-flight PET/MR imaging with a positron-emitting source," *Journal of Nuclear Medicine,* vol. 55, pp. 329-336, 2014.

[31] A. Mehranian, H. Arabi, and H. Zaidi, "Quantitative analysis of MRI-guided attenuation correction techniques in time-of-flight brain PET/MRI," *NeuroImage,* vol. 130, pp. 123-133, 2016.

Chapter 2

Vision 20/20: Magnetic resonance imaging-guided attenuation correction in PET/MRI: Challenges, solutions and opportunities

Abolfazl Mehranian, Hossein Arabi and Habib Zaidi

Medical Physics, Vol. 43, No. 3, pp 1130-1155 (2016)

Abstract

Attenuation correction is an essential component of the long chain of data correction techniques required to achieve the full potential of quantitative PET imaging. The development of combined PET/MRI systems mandated the widespread interest in developing novel strategies for deriving accurate attenuation maps with the aim to improve the quantitative accuracy of these emerging hybrid imaging systems. The attenuation map in PET/MRI should ideally be derived from anatomical MR images; however, MRI intensities reflect proton density and relaxation time properties of biological tissues rather than their electron density and photon attenuation properties. Therefore, in contrast to PET/CT, there is a lack of standardized global mapping between the intensities of MRI signal and linear attenuation coefficients at 511 keV. Moreover, in standard MRI sequences, bones and lung tissues do not produce measurable signals owing to their low proton density and short transverse relaxation times. MR images are also inevitably subject to artifacts that degrade their quality, thus compromising their applicability for the task of attenuation correction in PET/MRI. MRI-guided attenuation correction strategies can be classified in three broad categories; (i) segmentation-based approaches, (ii) atlas-registration and machine learning methods, and (iii) emission/transmission-based approaches. This paper summarizes past and current state-of-the-art developments and latest advances in PET/MRI attenuation correction. The advantages and drawbacks of each approach for addressing the challenges of MR-based attenuation correction is comprehensively described. The opportunities brought by both MRI and PET imaging modalities for deriving accurate attenuation maps and improving PET quantification will be elaborated. Future prospects and potential clinical applications of these techniques and their integration in commercial systems will also be discussed.

I. Introduction

Hybrid positron emission tomography/magnetic resonance imaging (PET/MRI) has emerged as a new imaging modality enabling concurrent morphological and molecular characterization of different organs/tissues and physiopathological conditions. Over the last decade, tremendous efforts have been directed toward addressing the challenges faced by PET/MRI systems from two perspectives: (i) instrumentation and conceptual system design and (ii) improvement of quantitative performance to achieve at least comparable accuracy to standard PET/computed tomography (CT) systems where CT-based attenuation correction (CTAC) is the standard procedure. With the advent of solid-state photodetectors, the challenge of mutual compatibility between PET and MRI subsystems has now been reasonably addressed, paving the way toward fully integrated clinical time-of-flight (TOF) PET/MR systems [1-3]. However, accurate attenuation correction (AC) of PET data has remained a major challenge in PET/MRI [4, 5]. A number of active research groups have focused on the development of innovative techniques for deriving accurate attenuation maps to improve the quantitative accuracy of PET/MR imaging. During the last decade, significant progress has been achieved in this field as thoroughly appraised in previous reviews by Hofmann *et al.* [6], Bezrukov *et al.* [4] and many others [7-9].

In this article, we examine the challenges and recent technical advances in the rapidly evolving field of attenuation correction in PET/MRI. Overall, AC methods in PET/MRI can be categorized into three main classes: (i) segmentation-based approaches, which segment MR images into different tissue classes and assign predefined attenuation coefficients to each class, (ii) atlas-based and machine learning techniques in which a co-registered MR-CT atlas dataset is used to derive a pseudo-CT image and/or to learn a mapping function that predicts the pseudo-CT image from patient-specific MR image and (iii) the recently revisited emission- and transmission-based methods, in which the attenuation map is estimated from TOF emission or transmission data. We discuss the challenges and technical considerations involved for attenuation map generation in PET/MRI and provide a detailed overview of MRI-guided attenuation correction (MRAC) methods with special emphasize on their pros and cons. A possible scenario of future developments and opportunities is also provided.

In PET/MRI, the attenuation map at 511 keV should ideally be derived from the acquired MR images. However, contrary to x-ray CT, MRI signals are not correlated with electron density and photon attenuating properties of tissues, but rather to proton density and magnetic relaxation properties. Therefore, there is no unique global mapping technique to convert MRI intensities to attenuation coefficients. Similar to early transmission-based AC methods [10], the most straightforward way to derive attenuation maps in PET/MRI is to classify MR images for segmentation of different tissue classes and assign proper linear attenuation coefficients (LACs) to each tissue class. However, lung tissues and cortical bones, which are two important tissue types in attenuation maps, exhibit low signals on images acquired using conventional MR pulse sequences. Therefore, the lungs, bones and air pockets, which also produce a low MR signal intensity, cannot be well differentiated from each other for the generation of MRI segmentation-based attenuation maps. Ultra-short echo time (UTE) pulse sequences have also been investigated for the detection and visualization of bones [11, 12] as well as lung parenchyma [13]. However, UTE MRI is prohibitively timing-consuming and sensitive to magnetic field inhomogeneities and, as such, it is not yet clinically feasible for whole-body MRAC of PET data. However, substantial progress has been recently achieved in accelerated sub-Nyquist MRI acquisitions using parallel MRI and compressed sensing techniques, which are particularly suited for UTE data acquisition [14, 15].

In contrast to PET/CT, in whole-body PET/MRI scans, the arms are positioned down mainly because of patient comfort and support as well as coil positioning constraints. However, the limited transaxial field-of-view (FOV) of MRI scanners (45-50 cm) can result in the truncation of the arms and shoulders in the acquired MRI images[16] compared to the larger useful transaxial FOV of PET scanners (60-70 cm). The generation of attenuation maps from truncated MR images is another challenge in terms of deriving complete attenuation maps in whole-body scans. In patients with metallic implants, such as titanium prosthesis or dental fillings, the main magnetic field around the implants is usually locally distorted producing expansive signal voids with peripheral areas of high intensity known as blooming or magnetic susceptibility artifacts [17]. These artifacts are more pronounced in fast GRE MRI sequences, often used for MRAC, due to the lack of 180º refocusing radio-frequency (RF) pulses. The void artifacts can be miss-segmented or lead to inaccurate LAC prediction by atlas-based learning techniques.

A further challenge arises from the attenuation and scattering of annihilation photons by MRI RF coils in integrated or insert-based PET/MRI systems as well as other attenuating objects present in the PET FOV

including patient's bed and patient positioning aids. In whole-body MRI imaging, integrated body coils are usually used for receiving MRI signals. Moreover, to improve signal-to-noise ratio, without compromising acquisition time, flexible surface RF coils or head and neck coils are employed during scanning. Similar to bony structures, short T_2 materials do not provide measurable signals in conventional MRI sequences and therefore remain invisible. The presence of such attenuating material, especially flexible coils that can be placed in arbitrary positions and orientations, can locally affect PET quantification and must therefore be included in the attenuation map. Several other challenges and problems specific to each category of MRAC methods are discussed in the following section together with recent advances in the field.

II. Strategies for MRI-guided attenuation correction in PET/MRI

In this section, a comprehensive overview of the outlined AC strategies is elaborated with special emphasize on current state-of-the art techniques. For the sake of completeness, earlier contributions discussed in previous reviews are also briefly covered. Table 1 summarizes the major contributions for each category of methods highlighting the working principles and required data for implementation, major advantages and findings, limitations, performance and reported quantitative accuracy.

II.A Segmentation-based methods

The attenuating tissues in the body consist mainly of soft tissues, adipose (fat) tissue, lungs, air cavities (sinuses, abdominal air pockets) and cortical and spongy bones. Each tissue class has different intra/inter-patient attenuation coefficients at 511 keV as summarized in Table 2. In segmentation-based MRAC methods, the aim is to segment MR images into (at least) the above-mentioned 6 tissue classes[18] and to assign representative, or if possible, patient-specific, linear attenuation coefficients to each tissue class.

1) Brain Imaging

In brain PET imaging, the cortical bones of skull substantially contribute to the attenuation and scattering of annihilation photons. For accurate PET quantification, the bones must therefore be accounted in the MRAC map. Otherwise if substituted by soft tissue, the tracer uptake might be underestimated by up to 25% in cortical regions and 5-10% in central regions of the cranium, as recently reported by Anderson *et al.* [19]. In a comparative study, Teuho *et al* [20] also reported the largest underestimations (11% to 17%) in the temporal cortex and orbito-frontal cortex by ignoring the bones.

One of the earliest segmentation-based MRAC studies was reported by Zaidi *et al.* [21] where T1-weighted MR images were segmented into air, brain tissue, skull and nasal sinuses using a supervised fuzzy C-means clustering. Later, Wagenknecht *et al.* [22, 23] proposed an automatic tissue segmentation approach using neural network and prior knowledge about brain's anatomical regions. MR segmented regions showed a high correspondence with the CT segmented regions, however, the authors reported that this technique might result into mis- or over-segmentation of bones in the presence of abnormal anatomy or pathology. Since 2010, ultrashort echo time (UTE) MRI-based methods were then explored for bone visualization and direct segmentation of bones in brain studies. Catana *et al.* [11] and Keereman *et al.* [12] independently proposed a dual-echo UTE MRI sequence to derive 3-class attenuation maps including air, soft tissue and bones. Despite the promising results, the authors showed that UTE-based bone classification is still subject to over or under-segmentation of bones, especially at bone/air or soft-tissue air interfaces due to diamagnetic susceptibility effects.

The combination of UTE and Dixon sequences for bone detection and fat separation in order to generate a 4-class PET attenuation map was proposed by Berker *et al.* [25]. The resulting 4-class attenuation maps exhibited a high visual similarity to reference CTAC maps and over 80% of voxels in 6 studied patients were correctly classified. Using a trimodality PET/CT-MR system, Delso *et al.* [45] recently reported that the UTE segmented bones produce an acceptable overlap with reference CT bones over the skull, however, segmentation errors increase at the base of the skull, air interfaces eyeballs and dental arch mainly due to susceptibility and motion effects. They concluded that bone segmentation errors can degrade the reconstructed PET images. Overall, post-processing and segmentation procedures are required for bone extraction in UTE-based approaches, leading to significant differences in the obtained results.

Table 1. Overview of MRI-guided attenuation correction strategies in PET/MRI.

Category	Body region	Technique and data	Tissue classes (attenuation values)	Key advantages of the method/findings of study	Limitations	Quantification errors
Segmentation-based methods (Sec. II. A)	**Brain**	Segmentation of T_1W MRI using supervised fuzzy C-means clustering[21]	Brain tissue (0.099 cm^{-1}), skull (0.14 cm^{-1}), nasal sinuses (0.054 cm^{-1}) and air (0 cm^{-1})	Inclusion of bones	Semi-automatic segmentation of bones	2.4% bias using 10 patients in comparison to transmission μ-maps
		Neural network-based segmentation of MP-RAGE MRI[22, 24]	Air (0 cm^{-1}), brain tissue (0.096 cm^{-1}), skull (0.146 cm^{-1}) and mastoid process (0.054 cm^{-1})	Fully automatic, knowledge-based	Mis- or over-segmentation of bones in the presence of abnormal anatomy or pathology	–6.1% to 2.7% bias in cortical regions and –7.0% to 5.6% for subcortical regions using 4 patients
		Segmentation of dual-echo UTE MRI using region-growing and thresholding [12]	Air (0 cm^{-1}), soft tissue (0.096 cm^{-1}) and bones (0.12 cm^{-1})	Direct segmentation of bones	Long acquisition time (6 min), mis-segmentation at air tissue interfaces	Average 5% error in brain tissues of 5 PET/CT/MRI patients
		Segmentation of dual-echo UTE MRI using morphological closing and arithmetical operations [11]	Air (0 cm^{-1}), soft tissue (0.096 cm^{-1}) and bones (0.136 to 0.180 cm^{-1})	Direct segmentation of bones, 3.3 min acquisition time	Poor spatial resolution of UTE data, mis-segmentation at air tissue interfaces	Bone LACs of 0.143 cm^{-1} and 0.151 cm^{-1} resulted in best bias variability trade-off in quantification
		Segmentation of triple-echo UTE MRI using thresholding and morphological filtering [25]	Air (0 cm^{-1}), soft tissue (0.1 cm^{-1}), fat (0.09 cm^{-1}) and bones (0.172 cm^{-1})	Direct segmentation of bones and inclusion of fat	Bone misclassifications at paranasal sinuses	Over 80% of bone voxels were correctly classified in 6 studied patients
		Segmentation of Dixon fat and water MRI [19]	Air, soft tissue fat	Radial variation of quantification errors when bones are ignored	Presence of metal-induced artifacts in MRAC maps	SUV bias of 25% in cortical regions and 5–10% in central regions of the brain (19 patients)
	Whole-body	Segmentation of 3D T1 SPGR MRI using deformable shape modeling and thresholding [16]	Air, lungs and soft tissue	Fast, fully automatic	Bone/air and lung segmentation challenging, truncation artifacts … etc	<10% SUV bias in malignant soft tissue lesions w.r.t CTAC, –12% bias in a pelvis lesion (15 patients)
		Segmentation of 2-point Dixon MRI [26]	Air, lungs and soft and fat tissue	Inclusion of fat tissue, fast	Same as above	−8% SUV bias in bone lesions (35 patients)
		Phase-field-based segmentation and mapping of 2-point Dixon MRI[27]	Continuous fat/water (0.086-0.1 cm^{-1}), lungs and air	Continuous fat and water LACs	Same as above	Mean SUV bias of 10% in the liver and –2% in malignant lesions (16 patients)
Atlas-based segmentation, registration and machine learning methods (Sec. II. B)	**Brain (without UTE)**	Patch-based Gaussian process regression and atlas registration[28]	Continuous	Robust to miss-registration errors	Very time consuming (Gaussian process regression)	Mean SUV bias of 3% for predefined regions of interest wrt CTAC
		Voxel-wise classification of air/bone from MRI without atlas registration using random forest method[29]	Binary	No need for atlas registration, time efficient	Susceptible to presence of artifacts in MR image	Dice values of 0.83±0.08 and 0.98±0.01 for air and bone, respectively

		Voxel-wise atlas fusion using LNCC as image similarity measure[30]	Continuous	Very robust to miss-registration errors	Time consuming (40 atlas registrations are required)	Relative absolute error of 5% for the full head wrt CTAC
		Patch-based pseudo CT generation without using deformable atlas registrations[31]	Continuous	No need for atlas registration, time efficient	-	Dice values of 0.84±0.02 for bone volume
	Brain (with UTE)	Pseudo-CT generation by including spatial information into Gaussian mixture regression[32]	Continuous	Robust pseudo-CT generation using UTE sequence	Requires four UTE images with different echo times and flip angles	Mean absolute prediction deviation of 130±18 HU with spatial information
		Patient specific bone attenuation coefficient estimation based on UTE[33]	Continuous bone, air (0 cm^{-1}), fat (0.092 cm^{-1}) and soft-tissue (0.1 cm^{-1})	Patient-specific bone attenuation coefficient	Requiring UTE and Dixon sequences	Dice values of 0.75±0.05 across 98 subjects for bone and 0.60±0.08 for sinus air cavities
		Patch-based pseudo-CT generation via Bayesian framework[34]	Continuous	No atlas registration and segmentation required	–	PET pseudo-CT AC exhibited correlation coefficient of 0.99 w.r.t PET-CTAC
	Whole-body	Gaussian process regression and atlas registration[35]	Continuous	Robust to miss-registration errors	High computational time	In regions of normal physiologic uptake, the average bias was 8 ± 8% and for lesions was 6 ± 5%
		Gaussian process regression and tissue segmentation[36]	Continuous bone, lung (0.024 cm^{-1}), fat (0.0856 cm^{-1}), non-fat (0.1007 cm^{-1}) and fat/soft-tissue mixture (0.0988 cm^{-1})	Robust to metal induced artifact in MR images	–	SUV bias of 24 ± 6% for lesions near bone and 0.6 ± 11.1% for lesions affected by MR susceptibility artifacts
		Most similar single atlas registration[37]	Continuous	Very time efficient (only one atlas registration)	Lack of multi-atlas consensus	SUV bias in bony regions ranging from -3% to 4% and -2.1% to 2.6% for lean tissue
		Improved Gaussian process regression with sorted atlas registration[38]	Continuous	Very robust to miss-registration errors, patient-specific lung LACs	High computational time	Up to 4% lung SUV bias (14 patients
Emission- and transmission-based methods (Sec. II. C)		Attenuation estimation using consistency conditions of TOF Radon transform[39]	Continuous	Estimation of attenuation sinogram and analytical reconstruction	ACFs are determined up to a constant scaling factor	–
	Whole-body	Maximum likelihood reconstruction of attenuation and activity (MLAA) only TOF EM data[40]	Continuous	Patient-specific LACs	Estimated LACs should be corrected for a missing scale factor	–
		MRI-guided MLAA using anatomical regions[41]	Discrete LACs (depending on the number of MR regions)	Reduced noise and cross-talks in estimated mu maps	Unsolved scale factor, MRI mis-segmentation errors, limited tissue heterogeneity	Bias of -6% in the lungs, -10% in bones, -3% in soft tissues (only 1 patient)
		MLAA using MR-constrained Gaussian mixture models[42]	Continuous, mean LACs of lungs, fat, soft tissue and bones: 0.027, 0.086, 0.097,	Solved the scale problem, robust to MRI-segmentation errors	Selection of regularization parameters, registration of a	Bias of -4% in the lungs, -10% in bones and -5.0% in soft tissues/lesions (5 patients)

	0.104 cm^{-1}		bone probability map	
Attenuation estimation from transmission data acquired in simultaneous transmission and TOF PET scanning[43]	Continuous, mean LACs of lungs and soft tissue: 0.019 cm^{-1} and 0.098 cm^{-1}, respectively	Patient-specific LACs with simultaneous transmission and emission scanning	External transmission source is required, imperfect separation of transmission and emission data results in scaling the LACs, increased radiation dose	~10% in the lungs and soft tissues and ~15% in bones (5 patients)
Attenuation estimation from transmission and emission[44]	Continuous	Solved the scale problem and improved performance	External transmission source is required, increased radiation dose	–

Table 2. Attenuation coefficients at 511-keV of different biological tissues. [7]

Tissue	Linear attenuation coefficient (cm^{-1})
Lung	0.018–0.03
Adipose tissue	0.086–0.093
Soft tissue	0.094–0.100
Spongious bone	0.110
Cortical bone	0.130–0.172

2) Whole-body imaging

Contrary to brain imaging, bone segmentation in whole-body imaging is more challenging, especially the vertebra where the bones are spongy and contain tissues with a moderate MR intensity. The application of UTE MRI sequences for whole-body bone segmentation is not feasible yet since it is time-consuming for routine clinical usage, as a typical 5 to 7 bed-position whole-body scan would take from 30 to 45 mins [12, 46].

Current whole-body MRAC methods rely on the segmentation of MR images into 3- or 4-tissue classes, where bones are substituted by soft-tissue. In an early work, Hu *et al.* [16, 47] and Schulz *et al.* [48] implemented a 3-class attenuation map on the Ingenuity TF PET/MR system [49] by segmenting MR images of a 3-min 3D T1-weighted gradient/spin echo sequences into background air, lungs and soft-tissue. The clinical assessment of this technique indicated an overall underestimation of tracer uptake by up to 10% in malignant lesions [16], while an overall bias of <7% in most malignant lesions was reported [48]. To include fat as 4th tissue class, Martinez-Moeller *et al.* [26] used a Dixon sequence for the separation of fat and water. In their study, a mean standardized uptake value (SUV) error of about −8% was found for bone lesions compared to reference CTAC PET images. Hence, the authors concluded that this SUV bias is clinically irrelevant. In a follow-up study, Eiber *et al.* [50] also demonstrated that there is no statistically significant difference between PET/MRI and PET/CT for the anatomical localization of PET positive lesions. A mixture of fat and soft tissues was investigated by Hoffmann *et al.* [35] as an additional tissue class, leading to mean absolute SUV errors of 8% and 14% in lesions and regions of normal uptake, respectively. In the same spirit, Wollenweber *et al.* [27] recently proposed a continuous fat/water (CFW) method allowing for continuous variation of fat and soft attenuation coefficients in the range of 0.086 - 0.1 cm^{-1}. Their quantitative analysis showed that the CFW and 4 discrete-class MRAC methods result in mean SUV errors of 10.4% and 5.7% in the liver and 1.7%, and –1.6% in malignant lesions, respectively.

To evaluate the importance of bones in whole-body MRAC maps, as the 5th tissue class (in addition to air, lung, fat and soft tissue classes), Hofmann *et al.* [35] substituted bones in CTAC maps of 11 PET/CT patients by soft tissue. Their results demonstrated that the substitution of bones with soft-tissue results in mean SUV errors of 4% in soft-tissues adjacent to bones and 3% in soft-tissue lesions. A similar study was conducted by Samarin *et al.* [51] showing an underestimation of tracer uptake by 11% and 3% in osseous and soft-tissue lesions

adjacent to bones, respectively. Aznar *et al.* also showed that the assignment of spongeous bone LACs (0.13 cm^{-1}) to all bones resulted in <5% quantification bias in soft tissue and bone lesions [52]. For sclerotic and osteolytic spine lesions, mean SUV underestimations of 16% and 7%, respectively, were reported.

Ouyang *et al.* [53] assessed PET quantification accuracy of 3-, 4- and 5-tissue class MRAC methods using PET/CT datasets and demonstrated that as the number of tissue classes increases, absolute quantification errors in different tissue classes, except the lungs, decrease. Using Monte Carlo simulation studies, Keereman *et al. [9, 18]* also concluded that at least 6-tissue classes (air, lung, soft tissue, fat, spongious and cortical bones) should be identified in MRAC maps to reduce quantification errors to less than 5%. Similarly, Akbarzadeh *et al.* [54] confirmed that the accuracy of segmentation-based MRAC improves as the number of tissue classes increases.

Accurate segmentation of different tissue classes is also of high importance, especially in the presence of noise and partial volume effect in clinical MR images. Keereman *et al.* [18] evaluated the effect of errors in the segmentation of lungs and cortical bones due to high level of noise and partial volume effect. They found that up to 20% misclassification of bone as soft tissue or 10% misclassification of lung as air yielded errors below 5%. It has also been reported that the mis-segmentation of air cavities in the head [55] and soft-tissue in the abdomen [56] can noticeably affect the visual interpretation of PET images. Catana *et al.* [11] reported that substituting the internal air cavities with soft-tissue can introduce large overestimations (>20%) in adjacent structures. Choi *et al.* [57] showed that the mis-segmentation of brain ventricles as air in the 3-class UTE-based MRAC maps resulted in significant underestimation of binding potential ratio in 16 patients suspected to have Parkinson disease. More recently, Brendle *et al.* [58] evaluated the frequency and impact of tissue misclassifications, caused by MR image artifacts on PET quantification and interpretation. An analysis of 100 PET/MRI studies revealed 276 identified artifacts affecting 21% of PET-avid lesions located mostly around metal implants (16%), in the lungs (19%), and outer body contours (31%). The quantitative analysis showed that attenuation artifacts led to significant SUV changes in areas with misclassification of air as soft tissue (i.e, metal artifacts) and soft tissue as lung. Ladefoged *et al.[59]* showed that inpainting regions miss-classified as air, owing to the presence metal artifacts, with soft-tissue increased mean and maximum SUVs averaged in the corrected regions across all patients by 52%±11% and 28%±11%, respectively.

3) Segmentation of non-attenuation corrected PET images

The segmentation of non-attenuation corrected (NAC) PET images has also been revisited in the context of PET/MRI [60]. Chang *et al.* [61] proposed a semi-automated iterative PET segmentation method for whole-body ^{18}F-FDG imaging to identify 3 tissue classes (i.e. background air, lung, and soft tissues). However, tissue classification from NAC PET images is generally limited to radiotracers that distribute throughout the body, such as ^{18}F-FDG, and probably will not work for specific (non-FDG) PET tracers. These techniques have been extensively employed to reduce truncation and metal artifacts in MRI-derived attenuation maps, as discussed in the following sections.

II. B Atlas-based segmentation, registration and machine learning methods

To predict attenuation coefficients on a continuous scale or segment bone tissue class, current methods rely on either a number of atlases or template registration to the target subject or the use of machine learning techniques to train a classifier or mapping function to segment MR images or convert them into pseudo-CT images. An appraisal of the different atlas-based approaches with special emphasis on latest developments and advances in brain and whole-body imaging is given below.

1) Atlas-based and machine learning methods in brain imaging

Template-based attenuation map generation is commonly performed through nonlinear warping of a template of normal subjects to the target patient [62]. Templates are usually created by taking the average of multiple co-registered brain attenuation maps to represent mean attenuation coefficients and anatomical variability of a given population [63]. Wollenweber *et al.* [64] evaluated the performance of template-based AC compared to 3-class segmentation-based method in head imaging and concluded that template-based AC provides adequate PET quantification compared to methods that do not account for bone.

Template-based approaches rely on a single anatomical template transformation which may suffer from registration errors or inter-patient anatomical variability. The concept of utilizing consensus on multiple atlas

registration helps to minimize non-systematic registration errors. Hofmann *et al.* [28] proposed a method combining prior knowledge available in the multiple aligned atlas dataset with pattern recognition to generate patient-specific attenuation maps in brain imaging. A Gaussian process regression (GPR) is utilized to predict the substitute CT value for each voxel based on robust measurement of intensity similarity and spatial closeness of patches of voxels between the target image and atlas dataset to minimize the impact of miss-registration. Basically, methods relying on multiple atlas alignment outperform template-based or single atlas alignment methods owing to the uncorrelated error cancelation and power of consensus on multiple aligned atlases [65, 66].

In a comparative study, Uh *et al.* [65] demonstrated that the method proposed by Hofmann [28] may not be able to provide significant improvement compared to other atlas methods, such as arithmetic average of aligned CT atlas images, questioning its relevance given its high computation time (~271 min for a single study). To increase the robustness of atlas-based methods to miss-registration errors, Burgos *et al*. [30] developed synthetic CTs through a multi-atlas information propagation scheme for brain imaging where the MRI-derived patient's morphology is locally matched to the aligned dataset of MRI-CT pairs using a robust local image similarity measure based on local normalized cross-correlation (LNCC) criterion. The local matching through morphological similarity enables the algorithm to find local matches and similar anatomy across the atlas dataset. Using CT images as reference, the obtained pseudo-CT images were compared to a segmentation-based method using an UTE MRI sequence and to a simplified atlas-based method resulting in mean relative errors of 0.2%, –11.8% and 0.8%, respectively. Examples of ground truth CT, proposed pseudo-CT, best-atlas CT [30], UTE CT and difference images are presented in Figure 1.

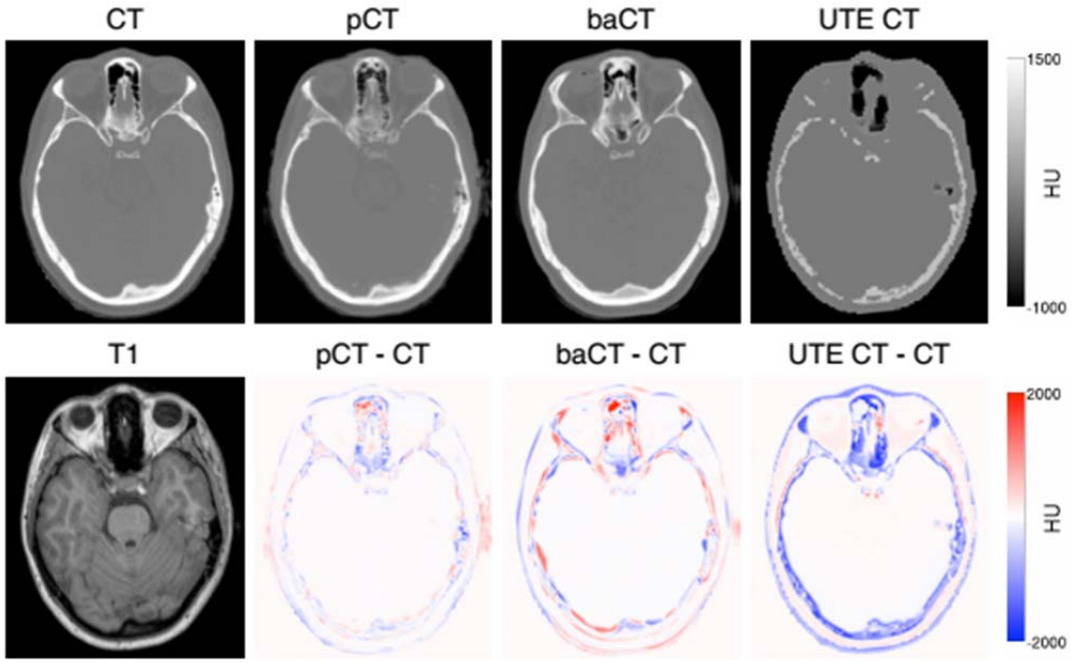

Figure 1. Top row (from left to right): The acquired CT, the pseudo-CT generated by the proposed method, the best atlas CT (baCT) and the UTE CT. Bottom row (from left to right): the acquired T1, the difference between pCT and CT, the difference between baCT and CT, and the difference between UTE CT and CT. Reprinted with permission from Burgos *et al.*[30]

Izquierdo-Garcia *et al.* [67] presented an approach for AC of brain PET data using Statistical Parametric Mapping 8 software (SPM8) taking advantage of both segmentation and atlas-derived features. Anatomic MR images of 15 subjects were first segmented into 6 distinct tissue classes, and then non-rigidly co-registered using a diffeomorphic approach to generate an MR-CT pair template. Thereafter, for a given subject, a similar procedure is carried out to co-register the target MR image to the template and the pseudo-CT image is constructed by applying the inverse transformations. In fact, the incorporated segmentation part enriched the available information in MR images allowing for a more accurate registration outcome. The quantitative analysis of the corresponding reconstructed PET images revealed mean relative errors of 3.9±5.0% and 2.7±2.3% for voxelwise and region of interest-based analysis, respectively.

To generate head attenuation maps for PET AC without using atlas registration or head template Chan *et al.* [29] proposed a voxelwise classification method for bone/air segmentation from MR images using random forest classifier fed by a bag of features, such as gradient and local image context extracted from structural MR and uncorrected PET images. The same idea was evaluated by Yang *et al.* [68] utilizing conditional random field and image fusion based on dual-tree complex wavelet transform and extracted features from uncorrected PET and T1-weighted MR image. These methods were developed to eliminate the atlas registration step from the process of pseudo-CT generation to save computation time. However, a comparative study enabling to evaluate the performance of these methods against conventional atlas-based approaches is lacking.

In the context of PET/MRI-guided radiation therapy planning, Sjölund *et al.* [69] developed a surrogate CT generation approach using a deformable registration algorithm, known as the Morphon, enhanced with a certainty mask enabling to tailor the influence of certain regions in the registration. Furthermore, for the atlas fusion part, the collection of deformed atlas CTs is iteratively registered to their joint mean to build a more similar pseudo-CT to the target CT. Andreasen *et al.* [31] proposed a patch-based pseudo-CT generation approach using T1-weighted MR images without using deformable atlas registrations. In this method, a database is created with patches of voxels extracted from MR images together with their corresponding Hounsfield unit values from aligned CT images. Given the query MR image, patches of voxels are extracted and compared to the database patches based on MR intensity similarity. A comparison between the proposed method and Gaussian mixture regression based on dual UTE scans [70] and multi-atlas information propagation using T1-weighted scans *[30, 71]* demonstrated a competitive performance and promising potential for use in MRI-only or PET/MRI-guided radiation therapy planning of brain malignancies.

2) UTE machine learning and atlas-based segmentation in brain imaging

The capability of UTE sequences to provide additional information to ease the detection of bones along with machine learning techniques to classify new observations can potentially yield promising results in terms of attenuation map determination for brain imaging. Johansson *et al.[70]* developed a Gaussian mixture regression algorithm trained with features derived from 2 UTE sequences and spatial information on a voxel-by-voxel basis to predict continuous LACs of the head [32]. They concluded that the inclusion of spatial information enhanced the accuracy of the estimated pseudo-CT, particularly in small complicated anatomical regions, such as the inner ear and post-nasal cavities. Ribeiro *et al.* [72] developed a feed forward neural network algorithm to predict non-linearly the attenuation coefficients based on patches of voxels extracted from 2 UTE sequences and a template-based AC map of 10 transmission PET scans.

In brain imaging, UTE MRI segmentation is subject to artifacts and under- or over-segmentation of bones [45]. The high level of noise and weak bone signal (low signal to noise ratio) are the main drawbacks of UTE imaging. To address this issue, many researchers used complimentary information present in an atlas or template. Poynton *et al.* [73] employed a probabilistic air/soft-tissue/bone atlas from T1-weighted, dual-echo UTE and co-registered CT images of 13 patients used to train a classifier that calculates the posterior class probability of each tissue class. The results showed an improvement over UTE-based segmentation, especially in the sinus and inferior regions of the skull. Delso *et al.* [74] proposed a similar approach for improved bone segmentation of UTE images using certain empirical rules to reduce the impact of mis-registration errors, metal artifacts and partial volume effects in MRI/CT training datasets. The methods described so far required a template or atlas registration to compensate the uncertainty of bone identification in UTE images. Roy *et al.* [34] proposed a patch-based method to obviate the need for atlas registration through matching the patches of voxels extracted from the target MR image to the reference dataset. Then, corresponding patches from the atlas database of CT images are combined via a Bayesian framework.

Juttukonda *et al.* [33] demonstrated a correlation between bone intensities in MR and CT images to assign patient-specific bone attenuation coefficients. The scatter plot derived from 97 subjects, where each point represents the intensity of bone tissue in UTE images versus CT number, suggested a strong sigmoid relationship (R^2=0.95). The proposed pseudo-CT generation required dual echo UTE and two-point Dixon image acquisitions, where bony structures were extracted via thresholding of the R2 image generated from the UTE echo 1 and 2 images, which resulted in mean Dice coefficients of 0.75 ± 0.1 across 98 subjects for bone and 0.6 ± 0.1 for sinus air cavities.

3) Whole-body imaging

The variability and complexity of the human anatomy and the high level of noise and partial volume effect in MR sequences used for attenuation correction make the direct segmentation of bones from MR images a challenging task. Furthermore, application of UTE sequences for whole-body imaging is not yet customary owing to the long acquisition time and susceptibility to artifacts when using a large FOV. Therefore, the use of atlas registration for prediction of bone tissue is common practice in whole-body MRI-guided attenuation generation.

Due to the large field-of-view, anatomical variability and moving organs atlas alignment errors are more pronounced in whole-body imaging. To alleviate this issue, Hofmann *et al.* [34] proposed a combination of atlas registration and pattern recognition method similar to the one described earlier for brain imaging [28] where a 4-class MRI segmentation-based attenuation map (air, lung, water and fat) was used to augment the robustness of GPR. Arabi and Zaidi [38] further improved the robustness of Hofmann's method to non-systematic registration bias and anatomical abnormalities by exploiting a method to locally sort atlas images based on their similarity to the target image. In this way, the atlas images with locally gross misalignment errors would be discarded from training and pseudo-CT generation process. Yet, the high computational time required for elaborating and training the GPR is thought to be the major drawback of this method.

A time efficient scheme was proposed by Marshall *et al.* [37] which required only one online image registration to incorporate bone tissue in whole-body attenuation maps. A database of 121 CT images was created to match the target MRI via weighted heuristic measures to find the most similar CT in terms of body geometry before the atlas registration step. The similarity metrics consist of factors such as sex, weight, age, fat to lean tissue ratio lung volume. Then the most similar CT in the atlas database was non-rigidly aligned to the target subject. MRI-based attenuation correction ignoring bone (standard 4-class attenuation map) resulted in relative errors ranging from −37% to −8% in VOIs containing bone while the inclusion of bone reduced these errors to −3% to 4%. Paulus *et al.* [75] used a template of major body bones including left and right femur and hip, spine and skull to be registered to the target MR image separately. For the rest of the body, routine Dixon MRI-based segmentation AC was performed to generate a 4-class attenuation map. This method is also time efficient since it requires just one template registration.

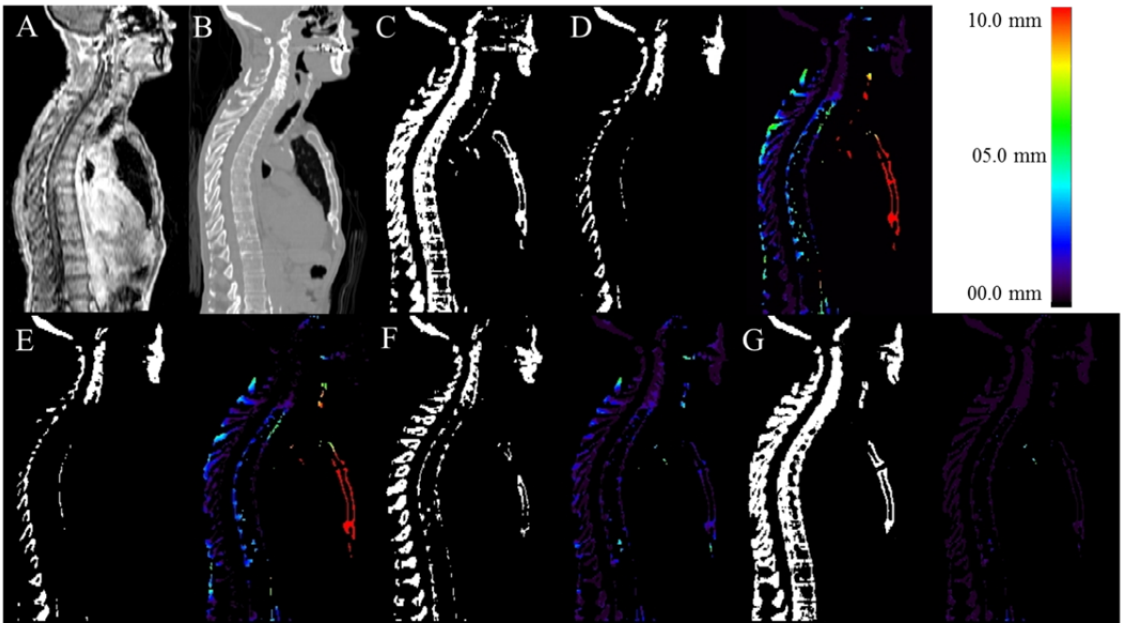

Figure 2. Representative slice of bone segmentation from MR image along with corresponding error distance map. (A) In-phase MR image, (B) corresponding CT image, (C) binary image of reference bone, (D) Hofmann's method [34], (E) arithmetic mean of whole aligned dataset, (F) global weighting atlas fusion, and (G) local weighting atlas fusion. Reprinted with permission from Arabi and Zaidi [66].

More recently, Arabi and Zaidi [66] implemented and compared a wide range of atlas-based attenuation map generation and bone segmentation methods of whole-body MR images. The accuracy of extracted bones was

evaluated for different algorithms using PET/CT and MR Dixon images of 23 clinical studies, This included Hofmann's method,[34] arithmetic mean of whole aligned atlas dataset,[65] single template,[76] most similar atlas,[37] global[77] and local weighting atlas fusion strategies[30]. Local weighting atlas fusion strategies based on standard image similarity measures such as the mean square distance and LNCC outperformed other methods. A representative slice of extracted whole-body bone along with error distance map obtained using the aforementioned methods is illustrated in Figure 2.

Since existing MRI-based attenuation map generation approaches are not specifically designed for pediatric patients, Bezrukov *et al.* [78] assessed the impact of inter- and intra-patient variability of attenuation coefficients and anatomy. The quantitative accuracy of MRI-based attenuation correction based on an approach developed by the same authors [36] was evaluated using an adult and pediatric atlas on PET data of pediatric patients. The use of a dedicated atlas for pediatric patients resulted in improved attenuation map prediction and reduced inter-patient bias variability.

So far, atlas-based pseudo-CT generation methods exhibited superior performance compared to conventional segmentation-based methods in both whole-body and brain imaging. Multi-atlas registration followed by local weighting atlas fusion resulted in promising pseudo-CT images and acceptable PET quantification. However, atlas-based methods may fail in cases with abnormal anatomy and in the presence of implants which are very unlikely to be present in atlas databases. Exploiting advanced segmentation and image processing techniques together with atlas-based methods can address this issue to provide more patient specific attenuation maps. On the other hand, although the UTE MR sequence is able to extract bone signal, the high level of noise and presence of artifacts greatly influence its performance and application. Moreover, its long acquisition time limits its usage to only brain or small axial field-of-view (e.g. head and neck) imaging. However, the capability of the UTE sequence to provide patient-specific bone extraction makes it a valuable technique. Reducing its acquisition time and artifacts may render this approach the method of choice in the future, even in whole-body imaging studies.

II.C Emission- and transmission-based methods

With advances in PET detector technology, TOF PET capability has been introduced in clinical PET/CT and PET/MRI systems, with the aim of improving image quality through the higher signal to noise ratio and enhanced lesion detectability. Following the resurfacing of TOF-PET, transmission- and emission-based methods have been revisited for deriving patient-specific attenuation maps in PET/MRI. In the following, we briefly review current state-of-the-art algorithms proposed so far for attenuation estimation.

1) Attenuation estimation using consistency conditions

Early attempts focused on the direct estimation of attenuation coefficients from emission data without using any estimate of the activity map based on the Helgason-Ludwig consistency conditions for emission data [79]. These conditions state that, in the absence of noise, a given emission data can only arise under certain attenuation conditions, or conversely for a given attenuation map; only certain emission data are possible. Based on the range of consistency conditions of the TOF attenuated Radon transform, Defrise *et al.* [39] recently showed that attenuation correction factors can be determined from TOF-PET data up to a constant scaling factor. They demonstrated that for all LORs containing activity, emission data determine the angular and radial derivatives of the Radon transform of the attenuation map. Rezaei *et al.* [80] extended this work to 3D TOF PET and only made use of the radial derivatives to estimate the attenuating volume. Li *et al.* [81] recently improved upon this approach by incorporating prior MR sinograms into the maximum a posteriori estimation of the attenuation sinogram from TOF emission data.

2) Attenuation estimation from only emission data

Emission-based estimation of attenuation coefficients was first proposed by Censor *et al.* [82] where an algebraic reconstruction technique was used to simultaneously reconstruct attenuation and activity maps. Nuyts *et al.* [83] further refined the concept of simultaneous maximum likelihood reconstruction of activity and attenuation (MLAA), in which the activity and attenuation were alternatively reconstructed using an MLEM and a scaled gradient ascent algorithm. The MLAA algorithm had limited success owing to: (i) inherent cross-talk artifacts, i.e. the propagation of activity features into the attenuation map and vice versa, (ii) the limitations of activity

support, i.e. the LORs that are out of the support of activity distribution (those without prompt coincidences) provide no information about the attenuation, and (iii) count statistics, which determine the level of noise in the estimated attenuation and activity maps. To reduce the cross-talk and noise artifacts, Nuyts *et al.* imposed Gaussian tissue preference and Gibbs smoothness priors on the attenuation estimation.

With the advent of TOF PET/MRI scanners, Salomon *et al.* [41] imposed the inherent spatial constraint of TOF on activity estimation and MR anatomical information on attenuation map estimation within the MLAA algorithm. Thereby, the noise and cross-talk artifacts were substantially reduced. As reported earlier by the same authors, the incorporated TOF information enables the reduction of cross-talk artifacts [84]. Moreover, in their modified MLAA algorithm, the attenuation coefficients were estimated over many anatomical regions obtained from the segmentation of MRI. However, the segmentation of anatomical MR images is subject to errors, especially between bones and air in paranasal sinuses, or soft tissue close to the ribs and vertebrae.

Rezaei *et al.* [40] also demonstrated that TOF can suppress cross-talk in the MLAA algorithm, consequently stabilizing the joint estimation problem. In addition, consistent with theoretical findings reported earlier [39], they found that the reconstructed activity maps are globally scaled, while the attenuation maps show a position-dependent scaling. Later, Rezaei *et al.* [85], proposed a maximum likelihood algorithm that jointly estimates the activity distribution and the attenuation correction factors (MLACF). This method avoids the reconstruction of the attenuation map and is robust to errors in the detector pair sensitivities. Since MLACF does not estimate the attenuation map, the authors suggested using prior knowledge about the tracer distribution to correct for the scale problem. Bal *et al.* [86] studied the scale corrected MLACF algorithm using 57 FDG-PET/CT brain studies in comparison with the CTAC method serving as reference. They concluded that MLACF-based reconstruction can provide images that are both qualitatively and quantitatively equivalent to CT-based reconstructions.

Recently, Mehranian and Zaidi [87] proposed an MRI-guided MLAA algorithm for AC in whole-body PET/MR imaging. The algorithm imposes MRI spatial and CT statistical constraints on the estimation of attenuation maps using a constrained Gaussian mixture model (GMM) and Markov random field smoothness prior. Contrary to Salomon *et al.* [41], they employed Dixon water and fat MR images, which were segmented into 4 known tissue classes, including outside air, lung, fat and soft-tissue and an unknown MR low-intensity class corresponding to air cavities, cortical bone and susceptibility artifacts. The estimation of attenuation coefficients over the unknown/known classes was regularized using a mixture of Gaussians. It was demonstrated that the modified MLAA algorithm effectively suppresses noise, cross-talk and scaling problems of the joint estimation problem. In a companion clinical study [42], the same authors showed that the 4-class MRAC and their proposed MLAA-AC methods resulted in average SUV errors of –5.4% and –3.5% in lungs and –18.4% and –10.2% in bones, respectively. Despite the promise of MLAA-AC, a recent study pertaining to brain PET/MRI demonstrated that this approach has some limitations for this particular application and is actually outperformed by sophisticated atlas-based AC algorithms which provided the most accurate attenuation maps, and thus the lowest PET quantification bias [88].

3) Attenuation estimation from emission and transmission data

Clinthorne *et al.* [89] reported the first study of joint maximum likelihood (ML) reconstruction of attenuation and activity images from emission and transmission data. However, these methods had a limited success as the transmission data are contaminated with emission data and vice versa.

Based on the capability of TOF technology in the separation of emission and transmission data [90], Mollet *et al.* [91] implemented a simultaneous transmission and emission acquisition on the Philips Ingenuity TF PET/MRI scanner [49] using an annulus-shaped transmission source. Despite the promising results, a companion study of 5 PET/MRI clinical datasets demonstrated that the limited TOF resolution of current PET scanners does not allow for perfect separation of transmission data from emission data [43] , which in turn results in non-uniformly scaled attenuation coefficients.

As demonstrated by Rezaei *et al. [40]*, the MLAA algorithm can estimate both activity and attenuation maps up to a scaling factor, which depends on the initial guess of the activity and attenuation maps. Furthermore, it was emphasized that the emission data do not provide information about the attenuation along the LORs located out-of-activity support. Panin *et al.* [44] proposed to make use of simultaneous emission and rotating rod sources transmission TOF data acquisition to stabilize the solution and solve the scaling and out-of-activity support problems. Similarly, Watson [92] proposed to use sparse line sources for transmission scanning in combination

with emission data. It was concluded that the use of supplemental transmission data can significantly improve the accuracy of the estimated LACs in truncated regions as well as the quantitative performance of the emission-only MLAA algorithm. More recently, Rothfuss *et al.* [93] studied the feasibility of using the inherent background radiation of LSO crystals as transmission sources, where TOF information is employed to separate emission and LSO transmission data. The utilization of this additional information has pertinent implications when combined with emission data to stabilize and improve the MLAA algorithm.

4) Attenuation estimation from scattered coincidences

For the task of estimating activity and attenuation distributions from emission data of locally accumulating radiotracers, the projections that are out of the support of the activity distribution (i.e. those without prompt coincidences but intersecting the patient's body) do not directly provide information about photon attenuation. However, these LORs might contain scattered coincidences that can provide additional information about attenuation they have experienced. Recently, Conti *et al.* [94] demonstrated that scattered coincidences can be used to reconstruct activity distributions using TOF and energy information. Sun and Pistorius [95] proposed a generalized scatter reconstruction algorithm to extract the activity distribution using both true and scattered coincidences by considering the limited energy resolution of PET detectors used in clinical practice. More recently, Berker *et al.* [96] proposed a scatter-to-attenuation backprojection to reconstruct PET attenuation coefficients from scattered-photon energies in the range 248–478 keV. Their simulation results suggested that the attenuation map can be derived in the case of perfect spherical symmetry of attenuation and activity distributions as well as attenuation outside of the activity support.

III. Challenges and potential solutions

The previous section focused on the various strategies followed to derive attenuation maps for PET attenuation correction using the information provided by MR images. However, a number of limitations and challenges, arising mostly from the inherent characteristics and constraints of MRI, have a significant impact on the accuracy of attenuation map derivation and PET quantification. Body truncation, metal and respiratory artifacts, MR coils attenuation, and patient-specific attenuation characteristics are among the most important challenging tasks. The technical aspects of these issues and the strategies developed to address them are discussed in the following sections.

III.A MRI truncation compensation

The MRI transaxial FOV is limited owing to the deterioration of the homogeneity of the main magnetic field (B0) and linearity of gradient field, especially at the edge of the FOV. Therefore, the truncation of body organs at the edge of the FOV can occur in obese patients, which if not compensated for, can adversely affect MRAC of PET data [97]. Schramm *et al.* [98] reported that arm truncation artifacts in 19 PET/MRI patient datasets led to an average SUV underestimation of less than 6% for VOIs defined in the trunk, while over the arms the errors were in the range 16% to 57%. Overall, three general approaches have been proposed to compensate for MRI FOV truncation including: PET image segmentation, emission-based and pure MRI-based approaches.

1) PET image segmentation

Hu *et al.* [16] proposed to compensate for truncation artifacts of 3-class MRAC attenuation maps using the body contour delineated from uncorrected PET images. To better delineate the body contour, Delso *et al.* [97] proposed to segment PET images preliminary corrected for attenuation using truncated attenuation maps. Schramm *et al.* [98] followed a similar approach and employed a 3D contour identification using an automatically determined threshold. Using a TOF PET/MRI system, Qian *et al.* [99] demonstrated that the segmentation of NAC TOF PET images results in more accurate body contour delineation. However, thresholding-based separation of body contour and background air, even when using NAC TOF PET images, is sensitive to intensity variations and threshold selection. Blaffert *et al.* [100] compared threshold-based and gradient-based segmentation of body contour. They concluded that gradient-based segmentation results in better separation of the arms from the body and, thus leading to more accurate truncation compensation (Figure 3).

However, they found that the correction of truncated breasts is still challenging since in most NAC TOF PET images, air-breast tissue contrast is lower than air-to-arms tissue contrast.

2) Emission-based truncation compensation

Nuyts *et al.* [101] proposed to compensate the missing part of the MRI-derived attenuation map from non-TOF emission data using a constrained MLAA algorithm. The authors evaluated this method using five artificially truncated ^{18}F-FDG PET/CT studies and demonstrated that SUV underestimation errors were reduced from 20% to 7% for all voxels with SUVs larger than 1. In the MRI-guided MLAA algorithms described in Ref. [87], the authors suggested to segment the uncorrected or preliminary corrected PET images to identify the truncated regions in MR images. However, as mentioned earlier, the performance of the MLAA algorithm is dependent on the tracer biodistribution. For specific tracers with local uptake, emission-based techniques might have limited success.

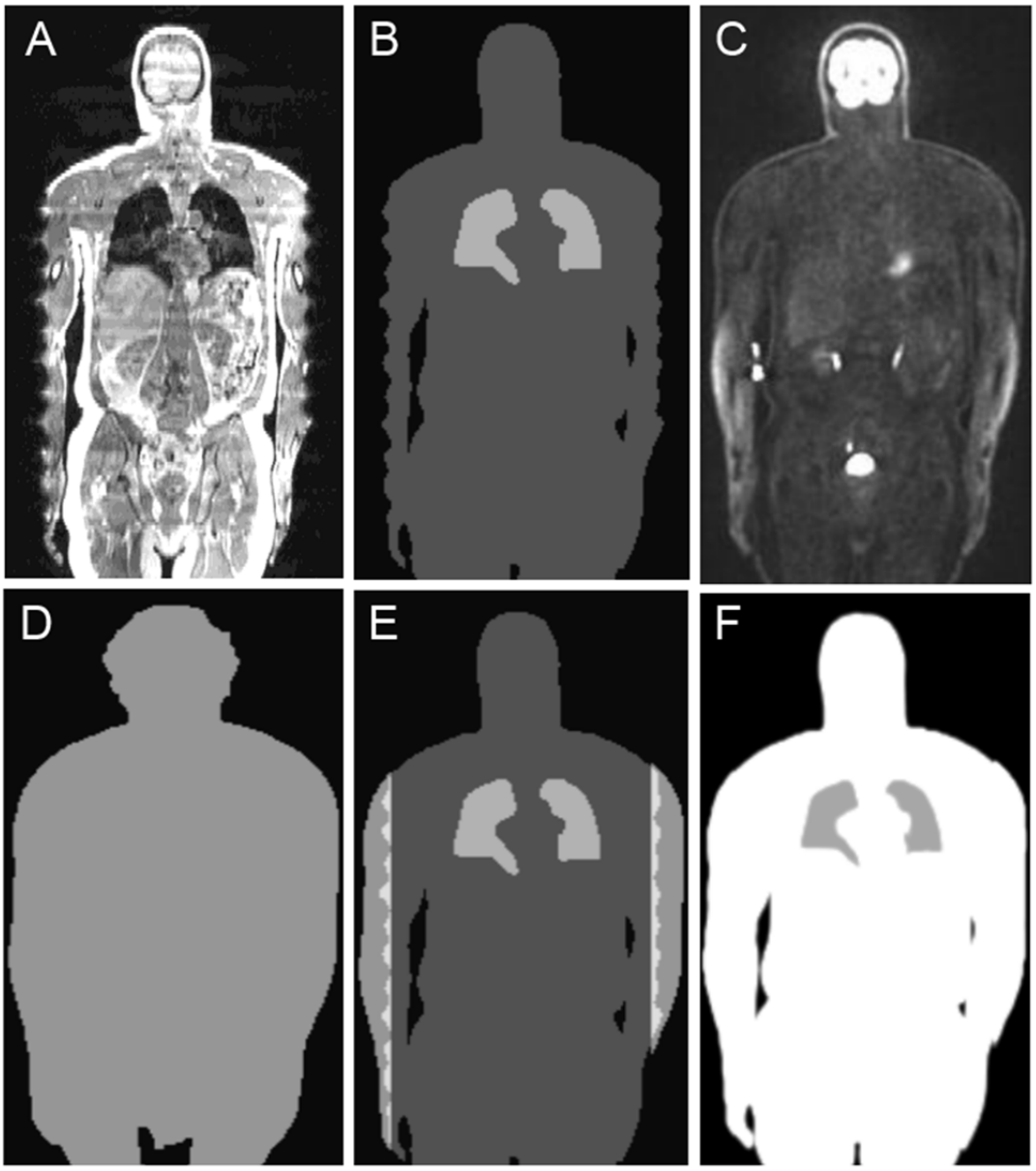

Figure 3. PET/MRI truncation compensation using PET segmentation. (**A**) truncated T1-weighted MR image, (**B**) 3-class MRAC map, (**C**) NAC TOF PET image, (**D**) body contour derived from segmentation of NAC TOF PET image, (**E**) overlap of the attenuation map and the identified truncation regions, and (**F**) final truncation compensated attenuation map. Adapted with permission from Blaffert *et al.* [100]

3) Extended FOV MRI

The B0 inhomogeneities and gradient nonlinearities at the edges of the MRI transaxial FOV usually result in geometrically distorted or truncated body contours. To address these effects, Blumhagen *et al.* [102] proposed a method to extend the FOV using B0 homogenization with gradient enhancement (HUGE). The distortion artifacts outside the normal MRI FOV was noticeably reduced by this approach without any hardware modifications. The authors compared the performance of the HUGE algorithm with the MLAA algorithm using PET/MRI clinical studies [103]. Applying the HUGE method extended the FOV of the Dixon MRI from 50 to 60 cm, but at the expense of increased MRI data acquisition time. Overall, both truncation compensation methods improved the accuracy of derived attenuation maps with a trade-off of increased scanning time using the HUGE method and increased post-processing time using the MLAA algorithm. The main advantage of HUGE over MLAA is that MRI-based FOV extension is independent of tracer distribution and kinetics.

III.B MR susceptibility and respiratory artifact reduction

Void signal caused by metallic implants (blooming artifacts) can give rise to segmentation errors in segmentation-based MRAC methods as well as imperfect LAC prediction when using atlas-based learning techniques. It has been reported that the resulting erroneous attenuation map can lead to substantial SUV underestimation by about 50% in the case of hip prosthesis [36] and >100% in dental filling cases [104]. The correction of MR susceptibility artifacts has been explored using the following approaches.

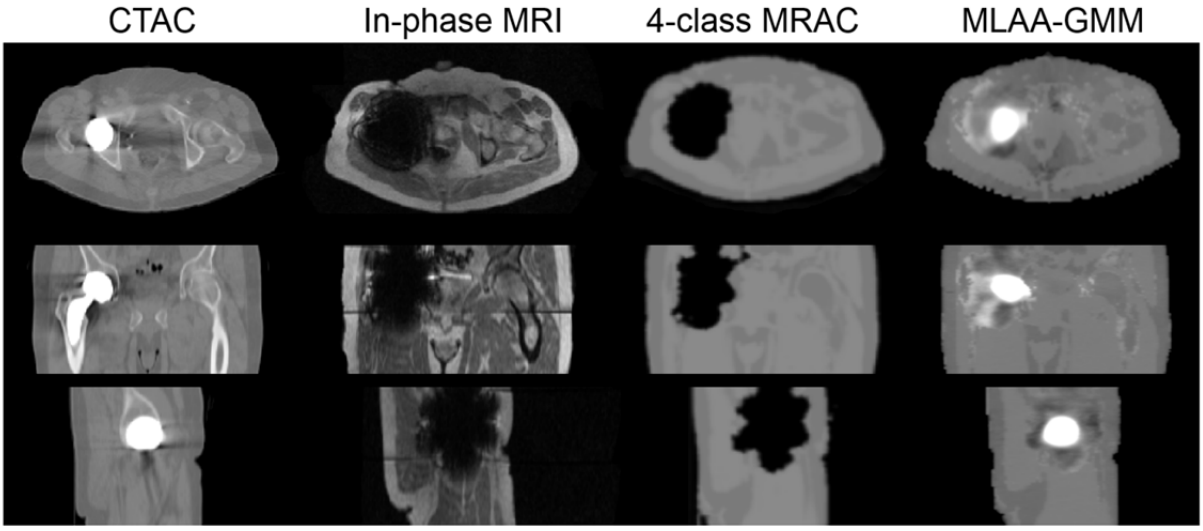

Figure 4. The compensation of metal induced susceptibility artifacts in MRAC maps using the MRI-guided MLAA algorithm described in Ref. [87].

1)Void regions segmentation

Ladefoged *et al.* [105] proposed to semi-automatically segment the signal voids caused by endoprotheses, and to fill them with soft-tissue attenuation coefficients. It was demonstrated that the resulting attenuation maps can substantially reduce the underestimation of the SUVs. Schramm *et al.* [106] proposed an automatic approach to segment the body contour from preliminary attenuation-corrected PET images and T1-weighted MR image. The resulting body contour is filled by soft-tissue, thereby isolated signal voids and particularly the artifacts connecting the background air to soft-tissues and lungs are corrected. The lungs are then segmented using an intensity thresholding approach. Although simple filling of voids by soft-tissue attenuation coefficient is a first-line correction method, the authors reported a residual SUV bias of about −13% on average.

2) Atlas-based registration and emission-based estimation

Bezrukov *et al.* [36] proposed an atlas-based susceptibility artifact correction technique, in which the possible position of artifacts is identified using an atlas of artifact regions. The attenuation coefficients of the identified positions are estimated using an atlas-based registration method. Their results indicated that filling the voids with soft-tissue reduces the quantification errors in lesions located within or near the artifacts from about –50% to –

15%, while accounting for bones in the artifactual regions reduces the errors to <1%. Another approach for proper correction of artifacts that also accounts for the attenuation coefficients of metallic implants is the emission-based estimation of the attenuation coefficients using MLAA type of algorithms. Figure 4 shows the performance of the MLAA-GMM algorithm [87] in terms of estimating attenuation maps at 511 keV of a patient with unilateral hip prosthesis. As shown, the in-phase MR image and the resulting 4-class MRAC attenuation map suffer substantially from the blooming artifacts. The MLAA algorithm, initialized with the 4-class MRAC map, however, is capable of not only filling the void regions in an acceptable way but also estimating the attenuation coefficients of the metallic implant. Therefore, the results demonstrate that emission-based AC methods are promising for proper attenuation correction of PET images in the presence of extensive MR metallic artifacts.

3) Optimized MRI data acquisition

The dephasing of MR signal caused by metallic implants can be partially avoided using spin-echo and UTE sequences. In spin-echo sequences, 180° refocusing RF pulses are applied to reverse the dephasing induced by magnetic field inhomogeneity, while in UTE sequences, the MR signal is sampled immediately after RF excitation, so that the magnetization does not have enough time to be dephased. [17, 107] Several techniques have also been developed for minimizing metal artifacts for fast spin-echo sequences, such as slice encoding for metal artifact correction (SEMAC) and multi-acquisition with variable resonance image combination (MAVRIC) [17, 108]. Recently, Burger *et al.* [109, 110] utilized diagnostic MAVRIC images to compensate for dental metal artifacts induced in Dixon-based attenuation maps They demonstrated that accurate attenuation maps can be derived using this technique, yet at the expanse of a considerably increased acquisition time.

Respiratory phase mismatch between PET and MRI/CT attenuation maps is known to be another source of error in PET quantification. Owing to this mismatch, white-band banana artifacts usually occur around the heart and liver dome in PET images due to undercorrection for attenuation [111]. It has been shown that these artifacts result in errors of up to 24% in tracer uptake of liver tumors [112]. Methodologies for the correction of this type of artifacts can be classified into two categories which are briefly discussed below.

4) 4D attenuation map generation

Buerger *et al.* [112] explored the possibility of deriving 4D MRAC maps for AC of respiratory gated PET data. Respiratory synchronized MRI acquisitions were used to gate PET data acquisition and to derive motion vector fields. The gated data were then reconstructed using their corresponding phase-matched attenuation maps with respect to a reference respiratory phase. Since 4D MRI acquisition is time-consuming, Fayad *et al.* [113] proposed to derive motion fields from gated non-attenuation corrected PET images and to generate 4D MRI attenuation maps from end-expiration static MRI volumes. They demonstrated the potential of using 4D NAC PET images to derive 4D MRAC attenuation maps from a single static MRI volume.

5) Emission-based attenuation/motion estimation

Recently, Mehranian and Zaidi [114] investigated the potential of emission-based estimation of lung attenuation coefficients of 4-class MRAC attenuation maps. They demonstrated that the proposed constrained MLAA algorithm can compensate for respiratory-phase mismatch as well as lung mis-segmentation errors, thus improving SUV quantification of liver and lung lesions. Rezaei and Nuyts [115] proposed a joint reconstruction and registration framework of gated PET data. In this framework, the gated PET activity and attenuation images are jointly reconstructed using the MLAA algorithm and registered to a reference frame using Demons registration algorithm. Using simulations, the authors demonstrated that this approach reduces the inter-frame registration error between activity and attenuation maps.

III.C MR coils and other attenuating devices

Besides patient's body, several other objects such as RF coils, patient bed and patient positioning and immobilization devices can contribute to photon attenuation and scattering in the FOV of PET/MRI systems. Ignoring surface RF coils in the attenuation map may lead to tracer underestimation of 19% [116] and 15.5% [117] in brain and whole-body PET imaging, respectively. Fürst *et al.*[118] reported that the patient's table results in 19% count loss of true coincidences on the integrated Biograph mMR PET/MR system.

The attenuation of fixed objects, such as patient bed, body and rigid coils (i.e. head/neck, spine, torso, … etc) can be measured using transmission sources (^{68}Ge or ^{137}Cs) [119] or CT scans [120] and incorporated into attenuation maps as templates. The patient table and coil templates generated from transmission scans are more accurate than those generated from CT scans owing to the lack of streaking artifacts caused by high-density metallic components [121]. Moreover, the bi-linear energy mapping of CT to attenuation coefficients at 511 keV for non-biological materials might not be valid [116]. In this regard, Paulus *et al.* [122] optimized the bi-linear CT energy mapping procedure of hardware PET/MR components through the calibration of CT numbers of these components using transmission scanning and reported a reduction of SUV bias in the NEMA phantom from 3.1% to −0.5%.

The inclusion of flexible surface coils is more challenging because of their patient-specific application, positioning and orientation. To determine the position of body matrix coil, Paulus *et al.* [123] applied two approaches: (i) cod liver oil capsules were attached to the surface of the coil as MR visible markers and (ii) UTE sequence was employed to image the coil. In the first approach, MR markers were rigidly registered to the same markers in the CT image of the coil using landmark-based registration. In the second approach, UTE images showed only parts of the coil's plastic housing and image registration to CT template was more difficult to achieve. Eldib *et al.* [124] studied several non-rigid registration algorithms to correctly deform CT templates to match MR coil markers. They found that the V-spline registration algorithm produced the most accurate registration compared to B-spline, thin-plate spline and elastic body spline methods. Kartmann *et al.* [117] presented an approach for automatic localization of multiple RF surface coils in whole-body PET/MRI. In this approach, different marker patterns were used to distinguish multiple partly overlapping RF surface coils. Non-rigid B-spline registration was used to register the corresponding markers on the CTAC template to the identified MR markers. The presented algorithm reliably reduced PET quantification errors due to overlooking the coils in the attenuation maps from 15.5% to 4.3%. Figure 5 shows the MR imaging setup of a subject with three overlapping RF surface coils together with coil CT templates overlaid on the 4-class MARC map [117].

Another approach for estimating the attenuation of MR invisible objects present in the FOV of PET/MRI scanners is to use emission- or transmission-based methods. In a simulation study, Nuyts *et al.* [101] demonstrated that the MLAA algorithm not only compensated for MR truncation artifacts but also retrieved 6 rods placed in the front of a torso phantom. In an experimental study, Rezaei *et al.* [40] showed that the MLAA algorithm can partially estimate the patient table. These approaches are promising; however, their robustness still needs to be characterized in different situations using large clinical databases.The standard coils currently employed on clinical MRI systems have not been designed to have low or zero photon attenuation but to provide the maximum signal-to-noise ratio in MR imaging. In PET/MR systems, these coils should be redesigned to have low photon attenuation without compromising their performance. Saha [125] redesigned the whole-body RF coil in a 3T simultaneous PET/MR system with minimal use of high density RF components in the PET FOV, thereby producing a zero PET attenuation whole-body coil. Dregely *et al.* [126] also developed a dedicated breast MR coil for the mMR scanner, in which PET attenuation was reduced by moving the high-density components, such as preamplifiers, away from the imaging FOV. However, to account for the overall photon attenuation and scattering in the coil, a CT-based template of the coil was acquired and co-registered to the coil's position for incorporation in 4-class MRAC maps.

III.D Inter/intra-patient variability of LACs

In segmentation-based Dixon and UTE MRAC methods, constant predefined attenuation coefficients are assigned to each tissue class. Therefore, intra- and inter-patient variability of the attenuation coefficients is ignored, which can lead to non-negligible SUV errors especially in the lungs and bones. Atlas-based machine learning and emission-based AC methods are capable of providing more accurate estimates of patient-specific LACs of lungs and bones using the additional information available in atlas and emission data.

1) Lungs

Among the various tissue classes defined in segmentation-based MRAC methods, the lungs have the largest inter-patient LAC variability with a standard deviation of 0.004 cm^{-1} [18, 48, 127]. In fact, the pulmonary parenchyma and vasculature vary considerably among patients by as much as 30% [128]. As such, different LACs have been assigned to lung tissue class, ranging from 0.018 to 0.035 cm^{-1} [26, 129]. It has been reported

that the assignment of a LAC of 0.024 cm^{-1} to the lungs produces relative errors of 13.5±10.7% [34] and 7.7±3.0% [37]. Conversely, the assignment of a LAC of 0.018 cm^{-1} to the lungs produces PET quantification bias of 1.9±2.3% [26] and –0.5±13.3% [56] in lung lesions and normal lung tissues. A small number of studies have focused on the derivation of patient-specific lung LACs considering lung tissue heterogeneity. The techniques reported so far can be classified into 3 categories: (i) prediction of mean lung LACs from MRI intensity and/or lung volume, (ii) atlas-based registration and learning, and (iii) emission-based estimation of lung LACs.

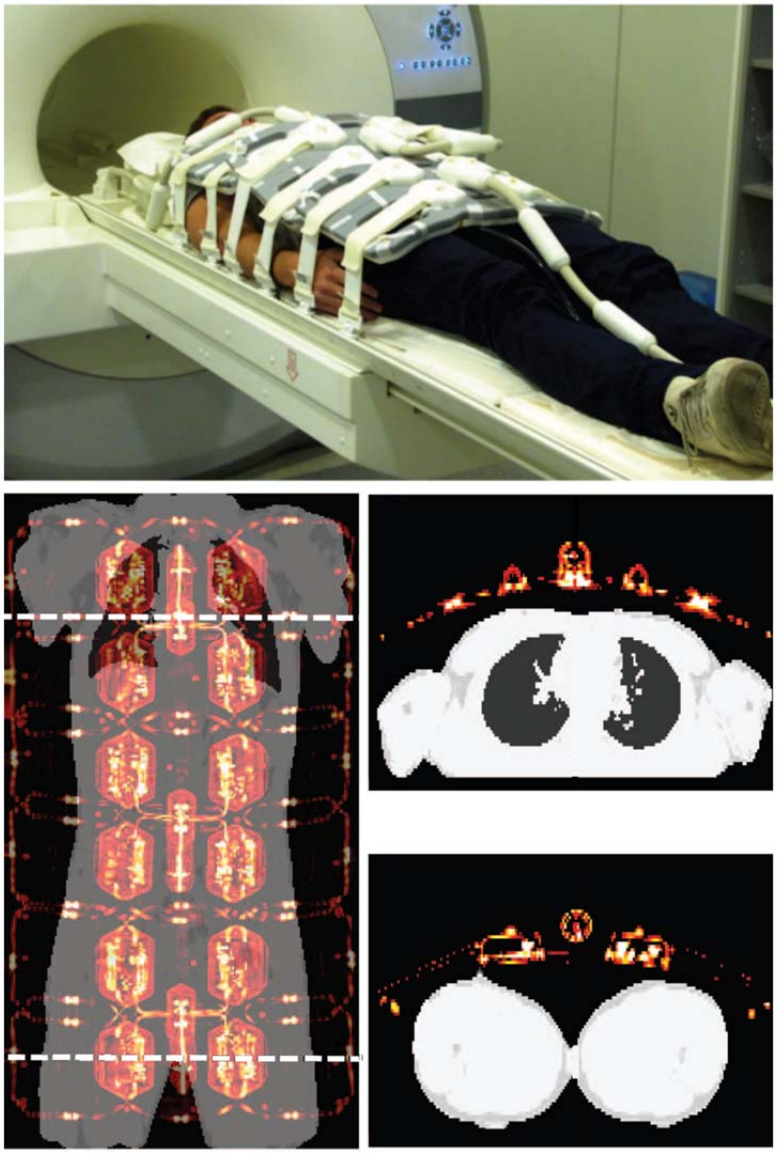

Figure 5. Attenuation correction of flexible RF coils. Top: MR imaging setup of an exemplary volunteer with three overlapping RF surface coils. Bottom: Combined 4-class attenuation map of the volunteer with the registered CT-based attenuation maps of the overlapping RF coils. The dash lines show the axial location of transverse slices. Adapted with permission from Kartmann *et al.* [117].

Marshall *et al.* established a linear mapping function between MRI and CT image intensities to predict the mean of lung LACs [130]. Lonn *et al.* [131] derived a linear relationship between lung volume and mean LACs. Both studies proved the improved performance of these approaches in terms of lung LAC prediction. However, as a general rule, the MRI-to-CT mapping function requires a standardized MRI protocol and is influenced by the presence of respiratory motion, diamagnetic susceptibility and flow-related artifacts, while the volume-to-LAC prediction model does not take into account the impact of other factors, such as gender, age, pathological conditions and body positioning.

Atlas-based registration and machine learning techniques can in principle predict intra-patient variability of lung LACs. In the technique proposed by Hofmann *et al.* [34], local structures of MR images and their corresponding CT atlases are incorporated into a GPR for prediction of LACs. In spite of promising results achieved for soft-tissue and bony structures, this method exhibited large errors in the lungs owing to the insufficient signal produced by the lungs when using conventional MRI sequences. Recently, Arabi and Zaidi [38] embedded the correlation between lung volume and lung mean LACs into the GPR kernels and demonstrated that their improved method reduces the lung SUV bias from 8.9% (using Hofmann's approach) to 4.1%.

Emission-based derivation of lung LACs has also been explored by various groups. Berker *et al.* [132] proposed a constrained TOF-MLAA algorithm for the estimation of mean lung LACs in 5-class MRAC maps (including bone as the 5th class). The results obtained using Monte Carlo simulated PET/CT studies showed a high PET quantification bias, because of out-of-field accidental coincidences.

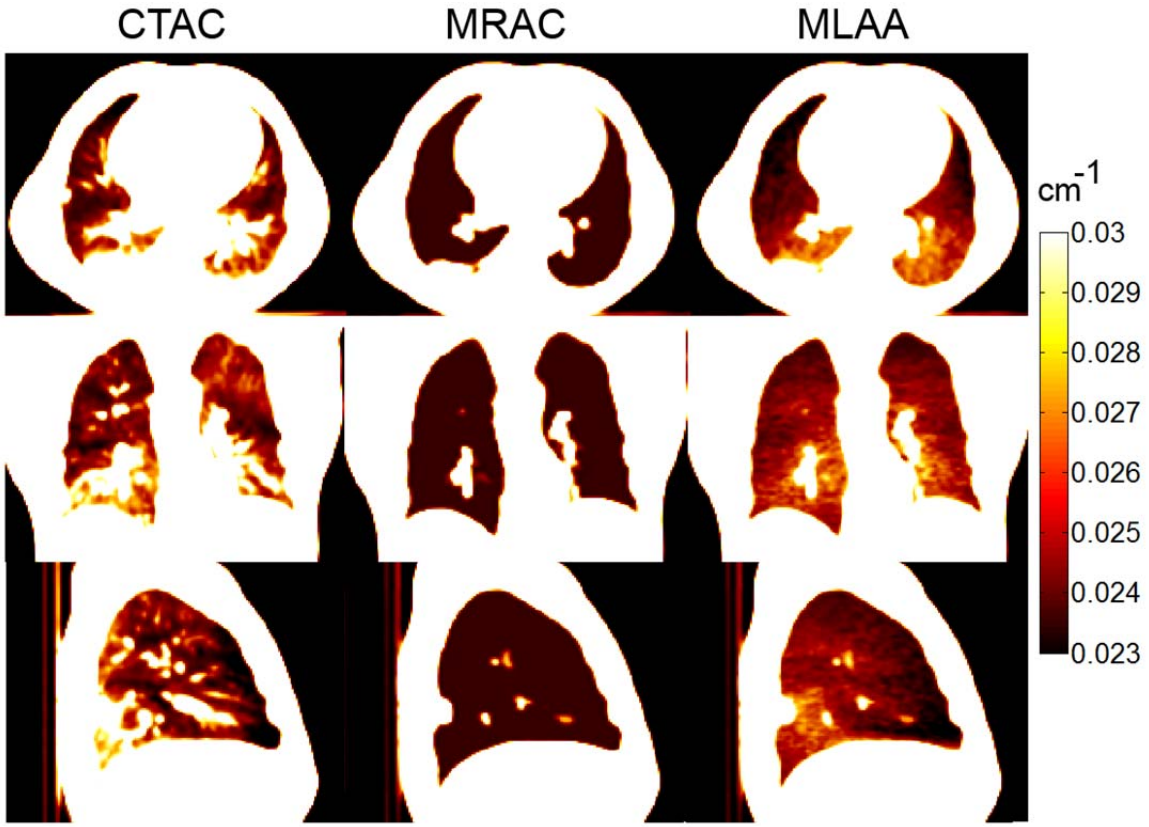

Figure 6. Comparison of the attenuation maps of the standard 4-class MRAC and the MRAC improved by the MLAA algorithm over the lungs with the reference CTAC maps in lung displaying windows. Adapted with permission from Ref [114].

An alternative approach was investigated by Mehranian and Zaidi [114] using an MLAA algorithm constrained by a lung tissue preference prior for patient-specific lung LACs estimation of 19 PET/CT clinical studies. Their results showed that the standard 4-class MRAC method resulted in an average SUV error of –5.2±7.1% in the lungs, while the proposed MLAA algorithm reduced the error to –0.8±6.3%. Figure 6 compares the CTAC, MRAC and MLAA attenuation maps of a patient whose lungs have a congested structure and high density gradients. As shown, the MLAA algorithm can accurately retrieve the lung density gradient in a continuous fashion, thus providing more accurate attenuation correction.

2) Bones

In segmentation-based methods, where bones are segmented as an additional tissue class using either UTE sequences or atlas-based approaches, the selection of appropriate bone tissue LAC is a subject of debate (see Table 2 in Ref [7] for details) as different LACs have been used for the skull (range of 0.116-0.172 cm^{-1}) and

whole-body cortical and spongious bones (range of 0.11-0.15 cm^{-1}). Schleyer *et al.* [133] demonstrated that the assignment of soft-tissue LAC to bones produces a lower SUV error than the assignment of cortical bone LACs, mainly because spongious bones have LACs of around 0.11 cm^{-1} [18].. In brain UTE imaging, Catana *et al.* [11] evaluated the impact of 8 different bone LACs ranging from 0.136 to 0.180 cm^{-1} on PET quantification. Their results suggested that the best bias-variability trade-off in PET quantification was achieved by assigning bone LACs of 0.143 cm^{-1} and 0.151 cm^{-1}, as previously reported in Ref [21].

Atlas-based AC methods can potentially estimate intra-patient variability of bone LACs by for example differentiating cortical bone in the skull from spongy bone in the vertebrae. Making use of the best atlas or local weighting of sorted atlases [30], [36] can in principle capture the inter-patient variability of the predicted bones.

Navalpakkam *et al.* [134] employed a UTE-based machine learning technique to predict continuous bone LACs. Their results showed that assigning a constant LAC value of 0.151 cm^{-1} to bone tissue class resulted in 4.2% SUV overestimation, while the continuously predicted bone LACs resulted in errors of 2.2%. Emission-based approaches are also promising for estimation of patient-specific bone attenuation coefficients. A recent study reported a mean LAC for bone derived from CT images of 5 PET/CT/MRI datasets of 0.118 cm^{-1}, while the MLAA-GMM algorithm estimated a mean value of 0.104 cm^{-1}, which reduced the bias compared to the standard 4-class MRAC method neglecting bone [42].

3)MRI contrast agents

In contrast-enhanced MR imaging, the administration of small molecular weight paramagnetic contrast agents can have an impact on PET attenuation correction in PET/MRI. In experimental phantom studies, Lee *et al.* [135] evaluated the effects of MR contrast agents on PET quantification using different concentrations of Gadolinium-based contrast agents on breast-cancer patients. Their results revealed that clinically relevant concentrations of MRI contrast media (<0.2 mmol) have negligible effects on the interpretation and quantification of PET images.

Lois *et al*. [136] also evaluated the effect of oral and intravenous MRI contrast media on PET quantification in PET/MRI. The results of CT and PET transmission measurements showed that clinically relevant concentrations of MRI contrast media have similar mean linear PET attenuation coefficients as water. Therefore, the administrated contrast agents did not result in noticeable quantification errors in the corresponding PET images. However, it was demonstrated that attenuation map miss-segmentation errors might occur after ingestion of superparamagnetic iron oxide (SPIO)-based contrast agents.

IV. Current trends and opportunities

IV.A Impact of time-of-flight on erroneous attenuation correction

During TOF PET image reconstruction, the image voxels are locally updated, therefore error propagations are reduced in proportion to TOF timing resolution, while in non-TOF PET the propagated errors are proportional to the patient size [137].

Wollenweber *et al.* [138] evaluated the effect of excluding an anterior array surface coil from the MRAC maps on PET quantification using TOF and non-TOF reconstructions. They found that with TOF information, the SUV errors due to neglecting the coil attenuation are slightly reduced from –8.2% to –7.3%. Davison *et al.* [139] evaluated the impact of TOF on reduction of PET quantification errors induced by metal artifact voids in MRAC maps of the TOF PET/MRI SIGNA system (GE Healthcare, Waukesha, WI) with nominal TOF time resolution of <400 ps [140]. It was found that the TOF capability significantly reduces the artifacts. The percentage error reduction with TOF ranged from 21% to 60% for medium-sized artifacts simulated in the maxilla and the sternum, respectively. Another study reported that TOF information improves image quality and diagnostic interpretation of PET images in the presence of attenuation artifacts [141].

Mehranian and Zaidi [142] also studied the impact of TOF PET image reconstruction on the reduction of MRAC attenuation errors. Their results showed that non-TOF MRAC resulted in an average error of –3.4% and –21.8% in the lungs and bones, respectively, whereas the TOF reconstructions reduced the errors to –2.9% and –15.3%, respectively. Simulation studies also showed that as TOF time resolution improves, quantification errors are substantially reduced (Figure 7). It was concluded that MRI-guided attenuation correction should be less of a concern on future TOF PET/MR scanners with improved timing resolution.

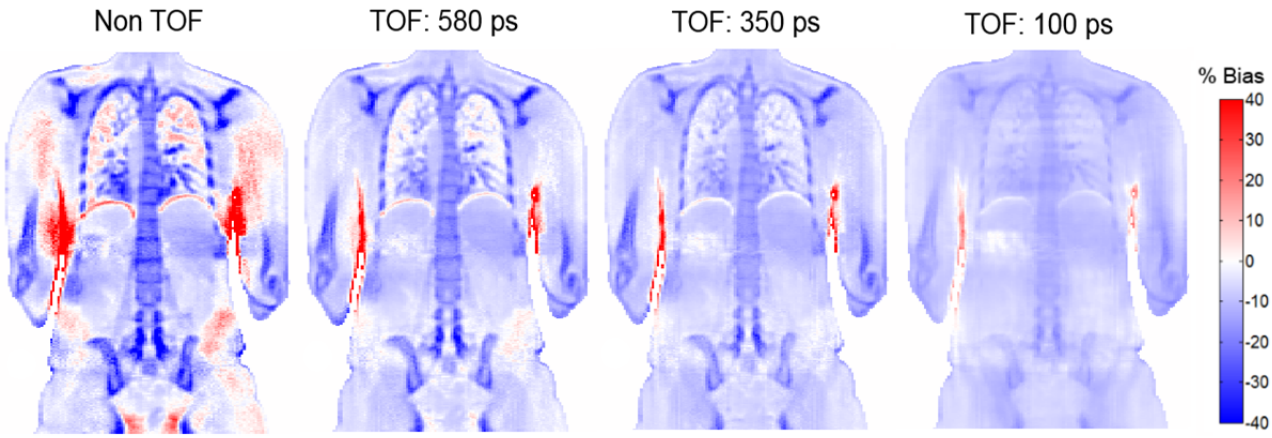

Figure 7. Bias maps between PET image reconstructed by the 4-class MRAC and CTAC maps without TOF and with different TOF resolutions in a whole-body phantom simulated from a clinical study. Adapted with permission from Ref [142].

IV.B Advances in ultrashort and zero echo time MRI

Ultra-short echo time MRI sequences have been developed to depict tissues with low proton density and short T2 relaxation time, such as the lung and cortical bone. However, the acquisition of high-resolution UTE images is time-consuming, typically around 6 mins in 3T brain imaging [12]. The acquisition time can be reduced by acquiring data with a coarser resolution, but this would lead to segmentation and learning errors for the task of attenuation correction. Recent attempts for accelerating UTE data acquisition focus on k-space under-sampling in the context of compressed sensing (CS) and parallel MR imaging (pMRI), or the combination of both [143]. Li *et al.* [144] described a 3D CS UTE sequence with hybrid-radial encoding strategy and demonstrated the feasibility of their technique for achieving an acceleration factor of 10. Hu *et al.* [145] studied the acceleration of UTE scans through k-space sampling optimization. In this work, the angular sampling rate of 3D radial k-space trajectories was reduced from 100% to 25% for a series of UTE sequences with TEs in the range 0.1-2.3 ms. The resulting scan times on the Philips 3T Achieva MRI system were in the range 172-43 sec. They demonstrated that high-quality bone-enhanced images can be generated using the UTE sequence with k-space undersampling as low as 25% (acceleration factor of 4) while preserving bone-air contrast at the cost of a minimal increase of noise level.

Aitken *et al.* [14] proposed to combine CS and sensitivity encoding [146] pMRI for accelerating dual-echo UTE by factors of 2 to16. Their results showed that there is a good agreement between the fully sampled and undersampled maps with undersampling factors of up to 8 (scan time of 53 sec.). For higher acceleration, the contrast between bone and soft tissue was deteriorated leading to bone-air misclassification during the generation of MRAC maps. The sampling pattern in radial UTE sequences; however, does not meet sampling requirements of pMRI techniques, such as SENSE. Therefore, advanced non-Cartesian image reconstruction algorithms are required. Johansson *et al.* [15] studied two non-Cartesian parallel image reconstruction algorithms for the reconstruction of undersampled radial UTE and GRE data of 23 head datasets by factors of 3-30. The authors reported that for acceleration of up to a factor of 5, acceptable pseudo-CT images can be obtained by the reconstruction methods.

Promising advances were recently reported in the development of zero time echo (ZTE) sequences for imaging of short T2 structures in which signal readout starts instantaneously upon excitation leading to a nominal TE of zero. [147] Wiesinger *et al.* [148] investigated a PD-weighted ZTE sequence for visualization and segmentation of the skull. In contrast to dual-echo UTE sequences, which mostly explore T2 time differences, the presented PD-weighted ZTE takes advantage of PD differences. Therefore, it eliminates the application of long T2 suppression methods. The authors studied standard and high-resolution protocols with acquisition times of about 3 and 6 min, respectively. Figure 8 shows a representative high-resolution ZTE and log-scaled images of the head.

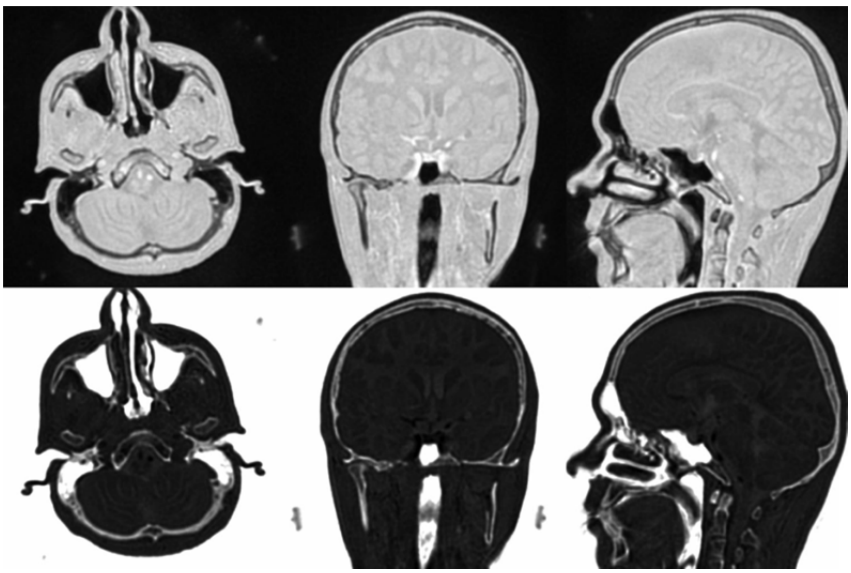

Figure 8. High-resolution zero TE image of the head in linear (Top) and inverse logarithmic (Bottom) scale. Reprinted with permission from Ref [148].

Delso *et al.* [149] evaluated the feasibility of PD-weighted ZTE imaging for skull segmentation of 15 clinical studies acquired on a trimodality PET/CT-MR system. Quantitative evaluation based on the Jaccard distance between ZTE and corresponding CT bone masks showed improved performance of ZTE over dual-echo UTE by achieving overlap distances over the entire head of 38-63% compared to 47-79%. It was found that contrary to UTE, the presence of tendons on bone masks obtained with ZTE was minor. However, they reported remaining mis-classifications at air/tissue interfaces, i.e. nasal cartilage and inner ear as in UTE.

Lung tissues are characterized by low PD and fast decaying signal. Recently, Johnson *et al.*[46] demonstrated the feasibility of free-breathing 3D radial UTE whole lung imaging. Radial undersampling and 8-channel pMRI were used to reduce scan time to 5.5 min. Gibiino *et al.* [150] studied a free-breathing 3D ZTE approach for visualization of lung parenchyma and vessels. They also demonstrated that high-quality images of lung parenchyma free from blurring and eddy-current artifacts can be obtained using ZTE in less than 6 min.

V. Concluding remarks and outlook

V.A Technical aspects of MRI-guided attenuation correction in PET/MRI

The generation of accurate and patient-specific attenuation maps in whole-body PET/MRI is proving to be a challenging task. In this work, we critically reviewed the tremendous efforts carried out during the last decade for developing solutions and algorithms to address these challenges. We categorized the MRAC algorithms into three generic groups: segmentation, atlas registration and learning and emission/transmission-based methods. The principles, algorithmic implementations and recent advances in each category of methods were then elaborated. Each category of techniques has its own advantages and drawbacks from different standpoints and considering the various aspects.

Table 3 (inspired from Ref [8]) compares the general pros, cons and potential of the three category of techniques. Owing to their time-efficacy, simplicity and robustness, segmentation-based MRAC is currently the method of choice implemented on virtually all current commercial PET/MRI scanners. In fact, robustness is one of the main prerequisites for the clinical adoption of an attenuation correction technique to guarantee accurate diagnosis and interpretation of PET findings. Since the introduction and wide adoption of segmentation-based MRAC methods on hybrid clinical PET/MRI systems (Philips Ingenuity and Siemens mMR PET/MRI scanners employ 3-class [49] and 4-class [151] MRAC, respectively), a number of studies have shown that their use on commercial PET/MRI systems provides images with similar or even improved diagnostic accuracy as PET/CT imaging [152, 153]. However, these methods have some limitations and drawbacks, including reduced PET quantification accuracy in lesions located in/close to bones, lungs and in regions presenting with artifacts. Czernin *et al.* [154] demonstrated comparable diagnostic performance of PET/MRI and PET/CT imaging based on clinical assessment of more than 900 patient studies. Since MRI is the modality of choice for providing the anatomical and functional information required by a number of oncological indications, PET/MRI would be a

reasonable option provided the duration of imaging protocols and associated cost are kept to an acceptable level. New insights into disease phenotypes and biology can be provided by the complementary information imparted by hybrid PET/MR imaging. So far, it is becoming clear that PET/MRI presents diagnostic advantages in bone metastases and in prostate cancer, whereas it is outperformed by PET/CT in the assessment of lung nodules [155].

On the other hand, atlas-based and emission-based methods are promising in terms of deriving more accurate attenuation maps, thus improving PET quantification. To provide an overall picture of the performance of these methods, Figure 9 compares the attenuation maps of a representative clinical study produced using the segmentation-based 4-class technique with atlas- and emission-based algorithms as compared to the CT-derived attenuation map serving as reference. As can be seen, atlas- and emission-based AC methods have successfully predicted/differentiated bones and air tissues compared to the standard 4-class segmentation-based method. However, these two methods are still in their infancy and require extensive testing and in-depth clinical assessment to improve their robustness and efficacy. For instance, the performance of atlas registration-based methods depends on the collectivity of the MRI/CT training set and the efficiency of the learning algorithm. The performance of emission-based methods depends on TOF timing resolution and the PET tracer biodistribution. In brain imaging, several studies demonstrated that atlas-based segmentation or registration techniques can properly segment or predict bones [30], [70]. Our ranking of patient specificity of emission-based AC methods for lung and bone LACs is conservative as they are merely based on a few recent [42, 116] studies showing the high potential of these methods for the derivation of lung LACs. However, further studies are required to demonstrate the performance of these AC methods for different tracers, cohorts of patients and TOF resolutions. In fact, the performance of emission-based AC methods in deriving bones should be ranked conservatively based on current studies, since its performance is highly dependent on the TOF resolution, count level and activity distribution. In addition, we conservatively ranked respiratory artifact reduction of emission-based AC methods. Indeed, evaluation and comparison with 4D attenuation correction are needed to demonstrate the potential of emission-based AC methods for this task.

Table 3. Comparison of pros and cons of the different categories of MRAC techniques used in PET/MRI.

	Segmentation-based	Atlas-based	Emission-based
Computation speed	+++	+	–
Simplicity and robustness	+++	+	+
Patient-specificity of lung LACs	–	+	++
Patient-specificity of bone LACs	–	++	++
Specific data requirement	–	+	+
MR truncation compensation	–	–	++
Coil attenuation estimation	–	–	+
MR susceptibility artifact reduction	–	+	++
Respiratory artifact reduction	–	–	+

In whole-body imaging, the combination of segmentation-based and atlas-based registration showed promising performance compared to that achieved by each method alone [36]. The combination of segmentation-based and lung emission-based attenuation correction has also been investigated showing a high potential of emission-based methods in deriving patient-specific lung LACs [114]. The results of comprehensive comparative evaluation studies can be exploited to come up with novel MRAC strategies taking advantage of the benefits of each technique.

MRI transaxial FOV truncation compensation through TOF NAC PET image segmentation or the MLAA algorithm are among the most promising approaches. Further investigation is still required to evaluate the efficiency and computational complexity of the two approaches. The attenuation coefficients of fixed and flexible objects (patient table, body coils, surface coils, … etc) is currently best accounted for using pre-measured attenuation maps of fixed parts and deformable registration of templates for flexible parts [117]. Although emission-based algorithms can in principle estimate such attenuating objects, it remains to be demonstrated whether these techniques can accurately and completely estimate these objects given that they might have partial support of activity. As elaborated in this work, emission-based methods look promising for the correction of metal susceptibility artifacts by estimating the high attenuation coefficients of the metallic implants, which is not feasible using atlas-based registration techniques. On the MRI side, there have been some

promising pulse sequence developments that can mitigate and reduce the extent of metal blooming artifacts. For the compensation of respiratory-phase mismatch between MRAC maps and PET images, two approaches are currently possible: (i) acquisition of 4D attenuation maps and (ii) simultaneous reconstruction of activity and attenuation. Emission-based methods are, however, as computationally intensive as atlas-based registration methods or even more. This further motivates the combination of these advanced methods with fast segmentation-based techniques. However, additional investigation is still required to further improve the accuracy and robustness of these attenuation correction methods to pave the way for their translation into clinical PET/MRI systems.

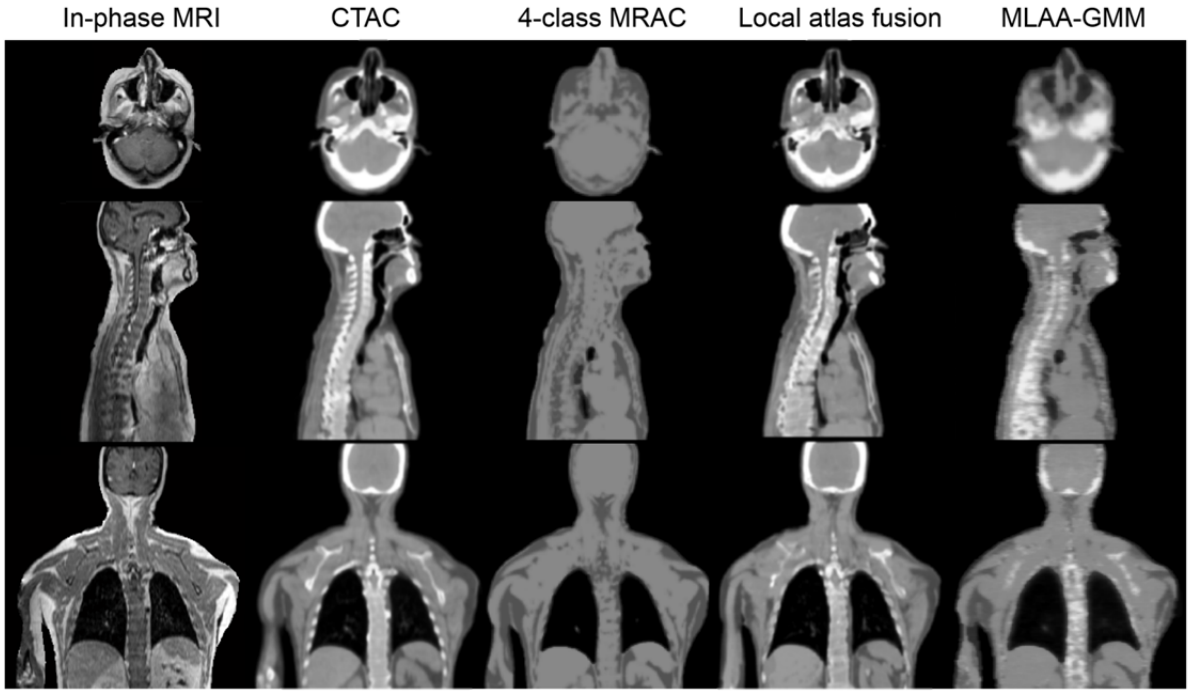

Figure 9. Comparison of the attenuation maps obtained by the 4-class segmentation based method [26], local weighted atlas fusion [38] and an MRI-guided emission based method [87]. Adapted with permission from Mehranian and Zaidi [42].

As an outlook, we believe that potential exciting developments to achieve accurate PET attenuation correction in PET/MRI, thus enabling improved PET quantification, can be broadly summarized in the following items: (i) The most promising attenuation correction methods will likely be achieved by hybrid techniques combining the three categories of MRAC methods to take advantage of the positive aspects of each class of methods. (ii) Technological advances in time-of-flight PET as well as U/ZTE MRI sequences will progressively continue to respectively provide opportunities in mitigating the adverse effects of inaccurate attenuation correction and deriving more accurate attenuation maps.

During the next decade, we shall witness further developments in PET detector technology and translation of digital silicon photomultipliers with new detector modules [156] from laboratory and preclinical settings into the clinical arena, assuring improved TOF capability and thus attenuation correction errors to an acceptable level. In addition, emission-based AC methods, which rely on information available in PET data to estimate attenuation maps, will show more promise as the TOF time resolution of PET scanners improves. With ongoing developments in instrumentation, we believe that a TOF PET time resolution of less than 100 ps might be possible in the future [156, 157]. Thereby, one can anticipate improved robustness and availability of this type of attenuation correction methods in the near future, given their high potential compared to other techniques (Table 3). With ongoing progress in parallel processing technology [158] and feasibility of real-time image reconstruction [159], emission-based AC methods will also be certainly computationally appealing in clinical setting.

There have been remarkable advances in fast MRI data acquisition through parallel MRI and k-space undersampling to make the acquisition time of UTE MRI sequences clinically feasible. Moreover, the same trend was followed by the recent emergence of ZTE MRI sequence with promising characteristics for bone and lung

parenchyma visualization in the context of PET/MRI. Certainly, these pulse sequences will continue to undergo further developments and improvements and will be made available in the clinic not only for attenuation correction but also for musculoskeletal and pulmonary disease evaluation.

V.B Clinical perspectives of PET/MRI attenuation correction

The clinical impact of segmentation-based MRAC methods implemented on current generation PET/MRI scanners has been evaluated in a number of studies in terms of visible artefacts, lesion detectability and quantification accuracy. Overall, there is a growing consensus that ignoring bones and tissue variability of attenuation coefficients in 3- or 4-class attenuation maps do not significantly impair lesion detectability and in general the diagnostic confidence of PET findings [26, 56]. In addition, when PET molecular information is being complemented with MRI functional and morphological information, the number of equivocal findings can be substantially reduced, especially in soft-tissue neoplastic involvements typically encountered in prostate cancer [160], head and neck cancers [153, 161-163] and gynecologic cancer [164]. However, the presence of artifacts in MRAC maps, particularly metal-susceptibility artifacts, can complicate the interpretation of PET findings[56] and even lead to false-positive or false-negative findings [58]. Therefore, similar to artifacts observed in PET/CT imaging, it has been strongly recommended to increase the diagnostic confidence by interpreting MRAC-PET images in conjunction with NAC-PET images. However, as highlighted in the previous sections, advances in TOF PET technology and Z/UTE MRI should enable to reduce or completely eradicate the frequency and the negative impact of these artifacts. Therefore, from a clinical perspective, the impact of artifacts and inaccuracies in attenuation maps is expected to be less of a concern, which might result in the adoption of new guidelines and procedures for PET interpretation.

The success of hybrid PET/MRI depends on the level of confidence revealed by current and future reports on clinical applications being explored where combined PET/MRI provides useful additional information. This might lead in the future to the widespread acceptance of PET/MRI in clinical setting, particularly in neurology and some applications in oncology [165]. However, the quantitative capability of PET imaging in PET/MRI with current AC methods has remained a major concern. Several reports from single-injection, dual-imaging studies demonstrated discrepancies in SUVs between PET/CT and PET/MR data, which were in many instances attributed to differences in the applied attenuation correction methods. The conclusions drawn from these studies should, however, be interpreted with some caution since time-dependent differences in tracer uptake owing to the non-stationary nature of FDG biodistribution were neglected. A number of studies used aligned CT and MR images to correct the same PET data, thus allowing a more straightforward assessment of the accuracy of MRAC in PET/MRI.

In most soft tissue lesions, an average SUV bias of less than 10% has been found to be clinically irrelevant [48]. However, significant differences might be observed in some regions particularly the brain, spine, lungs. Some investigators have suggested that ignoring bone could be acceptable in the abdominal and hip regions[16, 26, 48], but probably not in the thorax.[52, 166] There is a wide range of SUV underestimation for osseous lesions as reported by different groups. The bias was reported to be in the range 5-15% [26, 48] or up to 23% [49] using PET/CT data, whereas simulation studies using an anthropomorphic thorax phantom reported a local bias of up to 17% [18] or even 30% [51]. Overall, results reported so far seem to demonstrate that ignoring bone might not be adequate for quantification of osseous lesions.

The commonly accepted uncertainty in terms of dose calculation accuracy in radiation therapy planning is 5%. CT is commonly used as surrogate to estimate chemical composition. MRI is capable of probing soft-tissue properties with even greater accuracy and, as such, a combination of the information extracted from MRI and generated pseudo-CT images could give a better insight, particularly for particle radiation therapy where the beam range depends strongly on chemical composition [69]. In terms of dosimetric accuracy in radiation therapy treatment planning, the radiation dose distributions computed using generated pseudo-CT images agreed reasonably well with those derived using CT images (within 2%) [31], [61], [167, 168].

Moving from the present to the future will involve tremendous evaluation and further development of the three main classes of attenuation correction strategies discussed in this work both in academic and corporate settings to achieve the best compromise. The assessment and comparison of the various attenuation correction techniques should continue in the context of multicentric clinical trials supported and implemented by manufacturers involving the use of large databases to assure the reproducibility and robustness of the developed

algorithms. The outcomes of these trials will be vital for clinical adoption of the most promising approaches meeting the high-level standards required for their translation into clinical setting.

Acknowledgments

This work was supported by the Swiss National Science Foundation under Grant SNSF 31003A-149957 and the Indo-Swiss Joint Research Programme ISJRP-138866.

References

[1] H. Zaidi and A. D. Guerra, "An outlook on future design of hybrid PET/MRI systems," *Med Phys,* vol. 38, pp. 5667-5689, 2011.

[2] J. A. Disselhorst, I. Bezrukov, A. Kolb, C. Parl, and B. J. Pichler, "Principles of PET/MR imaging," *J Nucl Med,* vol. 55, pp. 2S-10S, 2014.

[3] S. Vandenberghe and P. K. Marsden, "PET-MRI: a review of challenges and solutions in the development of integrated multimodality imaging.," *Phys Med Biol,* vol. 60, pp. R115-54, Feb 21 2015.

[4] I. Bezrukov, F. Mantlik, H. Schmidt, B. Scholkopf, and B. J. Pichler, "MR-Based PET attenuation correction for PET/MR imaging," *Semin Nucl Med,* vol. 43, pp. 45-59, Jan 2013.

[5] H. Zaidi, "Is MR-guided attenuation correction a viable option for dual-modality PET/MR imaging?," *Radiology,* vol. 244, pp. 639-642, 2007.

[6] M. Hofmann, B. Pichler, B. Schölkopf, and T. Beyer, "Towards quantitative PET/MRI: a review of MR-based attenuation correction techniques," *Eur. J. Nucl. Med. Mol. Imaging,* vol. 36, pp. 93-104, 2009/03/01 2009.

[7] G. Wagenknecht, H.-J. Kaiser, F. Mottaghy, and H. Herzog, "MRI for attenuation correction in PET: methods and challenges," *Magn Reson Mater Phy,* vol. 26, pp. 99-113, 2013/02/01 2013.

[8] A. Martinez-Moller and S. G. Nekolla, "Attenuation correction for PET/MR: problems, novel approaches and practical solutions," *Z Med Phys,* vol. 22, pp. 299-310, Dec 2012.

[9] V. Keereman, P. Mollet, Y. Berker, V. Schulz, and S. Vandenberghe, "Challenges and current methods for attenuation correction in PET/MR.," *MAGMA,* vol. 26, pp. 81-98, Feb 2013.

[10] H. Zaidi and B. H. Hasegawa, "Determination of the attenuation map in emission tomography.," *J Nucl Med,* vol. 44, pp. 291-315, 2003.

[11] C. Catana, A. van der Kouwe, T. Benner, C. J. Michel, M. Hamm, M. Fenchel*, et al.*, "Toward implementing an MRI-based PET attenuation-correction method for neurologic studies on the MR-PET brain prototype.," *J Nucl Med,* vol. 51, pp. 1431-1438, Sep 2010.

[12] V. Keereman, Y. Fierens, T. Broux, Y. De Deene, M. Lonneux, and S. Vandenberghe, "MRI-based attenuation correction for PET/MRI using ultrashort echo time sequences," *J Nucl Med,* vol. 51, pp. 812-8, 2010.

[13] K. Zeimpekis, G. Delso, F. Wiesinger, P. Veit-Haibach, G. von Schulthess, and R. Grimm, "Investigation of 3D UTE MRI for lung PET attenuation correction," *J Nucl Med,* vol. 55, p. 2103, 2014.

[14] A. Aitken, C. Kolbitsch, T. Schaeffter, C. Prieto Vasquez, A. Aitken, C. Kolbitsch*, et al.*, "Rapid acquisition of PET attenuation maps from highly undersampled UTE images using sparse-SENSE reconstruction.," in *Proceedings of the 21st Annual Meeting of ISMRM*, Salt Lake City, Utah, 2013, p. 0769.

[15] A. Johansson, A. Garpebring, T. Asklund, and T. Nyholm, "CT substitutes derived from MR images reconstructed with parallel imaging.," *Med Phys,* vol. 41, p. 082302, Aug 2014.

[16] Z. Hu, N. Ojha, S. Renisch, V. Schulz, I. Torres, D. Pal*, et al.*, "MR-based attenuation correction for a whole-body sequential PET/MR system," presented at the IEEE Nuclear Science Symposium and Medical Imaging Conference (NSS/MIC), 2009.

[17] B. A. Hargreaves, P. W. Worters, K. B. Pauly, J. M. Pauly, K. M. Koch, and G. E. Gold, "Metal-induced artifacts in MRI.," *Am J Roentgen,* vol. 197, pp. 547-555, 2011/09/01 2011.

[18] V. Keereman, R. V. Holen, P. Mollet, and S. Vandenberghe, "The effect of errors in segmented attenuation maps on PET quantification," *Med Phys,* vol. 38, pp. 6010-9, Nov 2011.

[19] F. L. Andersen, C. N. Ladefoged, T. Beyer, S. H. Keller, A. E. Hansen, L. Hojgaard*, et al.*, "Combined PET/MR imaging in neurology: MR-based attenuation correction implies a strong spatial bias when ignoring bone," *Neuroimage,* vol. 84, pp. 206-16, Jan 1 2014.

[20] J. Teuho, J. Johansson, J. Linden, V. Saunavaara, T. Tolvanen, and M. Teras, "Specification and estimation of sources of bias affecting neurological studies in PET/MR with an anatomical brain phantom.," *Nucl Instrum Methods Phys Res A,* vol. 734, pp. 179-184, 2014.

[21] H. Zaidi, M. L. Montandon, and D. O. Slosman, "Magnetic resonance imaging-guided attenuation and scatter corrections in three-dimensional brain positron emission tomography," *Med Phys,* vol. 30, pp. 937-48, May 2003.

[22] G. Wagenknecht, E. R. Kops, L. Tellmann, and H. Herzog, "Knowledge-based segmentation of attenuation-relevant regions of the head in T1-weighted MR images for attenuation correction in MR/PET systems," in *Nuclear Science Symposium Conference Record (NSS/MIC), 2009 IEEE*, 2009, pp. 3338-3343.

[23] G. Wagenknecht, H.-J. Kaiser, F. M. Mottaghy, and H. Herzog, "MRI for attenuation correction in PET: methods and challenges," *Magnetic Resonance Materials in Physics, Biology and Medicine,* vol. 26, pp. 99-113, 2013.

[24] E. Rota Kops, G. Wagenknecht, J. J. Scheins, L. Tellmann, and H. Herzog, "Attenuation correction in MR-PET scanners with segmented T1-weighted MR images," in *IEEE Nuclear Science Symposium & Medical Imaging Conference*, 25-31 October 2009, Orlando (FL), USA, 2009.

[25] Y. Berker, J. Franke, A. Salomon, M. Palmowski, H. C. Donker, Y. Temur*, et al.*, "MRI-based attenuation correction for hybrid PET/MRI systems: a 4-class tissue segmentation technique using a combined ultrashort-echo-time/Dixon MRI sequence," *J Nucl Med,* vol. 53, pp. 796-804, 2012.

[26] A. Martinez-Möller, M. Souvatzoglou, G. Delso, R. A. Bundschuh, C. Chefd'hotel, S. I. Ziegler*, et al.*, "Tissue classification as a potential approach for attenuation correction in whole-body PET/MRI: evaluation with PET/CT data," *J Nucl Med,* vol. 50, pp. 520-526, 2009.

[27] S. D. Wollenweber, S. Ambwani, A. R. Lonn, D. D. Shanbhag, S. Thiruvenkadam, S. Kaushik*, et al.*, "Comparison of 4-class and continuous fat/water methods for whole-body, MR-based PET attenuation correction," *IEEE Trans Nuc Sci,* vol. 60, pp. 3391-3398, 2013.

[28] M. Hofmann, F. Steinke, V. Scheel, G. Charpiat, J. Farquhar, P. Aschoff*, et al.*, "MRI-based attenuation correction for PET/MRI: a novel approach combining pattern recognition and atlas registration," *J Nucl Med,* vol. 49, pp. 1875-1883, 2008.

[29] S. L. S. Chan, Y. Gal, R. L. Jeffree, M. Fay, P. Thomas, S. Crozier*, et al.*, "Automated classification of bone and air volumes for hybrid PET-MRI brain imaging," in *2013 International Conference on Digital Image Computing: Techniques and Applications (DICTA)*, 2013, pp. 1-8.

[30] N. Burgos, M. Cardoso, K. Thielemans, M. Modat, J. Schott, J. Duncan*, et al.*, "Attenuation correction synthesis for hybrid PET-MR scanners: Application to brain studies.," *IEEE Trans Med Imaging,* vol. 33, pp. 2332-2341, Jul 17 2014.

[31] D. Andreasen, K. Van Leemput, R. H. Hansen, J. A. Andersen, and J. M. Edmund, "Patch-based generation of a pseudo CT from conventional MRI sequences for MRI-only radiotherapy of the brain," *Med Phys,* vol. 42, pp. 1596-605, Apr 2015.

[32] A. Johansson, A. Garpebring, M. Karlsson, T. Asklund, and T. Nyholm, "Improved quality of computed tomography substitute derived from magnetic resonance (MR) data by incorporation of spatial information-potential application for MR-only radiotherapy and attenuation correction in positron emission tomography," *Acta Oncologica,* vol. 52, pp. 1369-1373, 2013.

[33] M. R. Juttukonda, B. G. Mersereau, Y. Chen, Y. Su, B. G. Rubin, T. L. Benzinger*, et al.*, "MR-based attenuation correction for PET/MRI neurological studies with continuous-valued attenuation coefficients for bone through a conversion from R2* to CT-Hounsfield units," *NeuroImage,* 2015.

[34] S. Roy, W.-T. Wang, A. Carass, J. L. Prince, J. A. Butman, and D. L. Pham, "PET attenuation correction using synthetic CT from ultrashort echo-time MR imaging," *J Nucl Med,* vol. 55, pp. 2071-2077, 2014.

[35] M. Hofmann, I. Bezrukov, F. Mantlik, P. Aschoff, F. Steinke, T. Beyer*, et al.*, "MRI-based attenuation correction for whole-body PET/MRI: Quantitative evaluation of segmentation- and Atlas-based methods.," *J Nucl Med,* vol. 52, pp. 1392-1399, Sep 2011.

[36] I. Bezrukov, H. Schmidt, F. Mantlik, N. Schwenzer, C. Brendle, B. Schölkopf*, et al.*, "MR-based attenuation correction methods for improved PET quantification in lesions within bone and susceptibility artifact regions," *J Nucl Med,* vol. 54, pp. 1768-1774, 2013.

[37] H. R. Marshall, J. Patrick, D. Laidley, F. S. Prato, J. Butler, J. Théberge*, et al.*, "Description and assessment of a registration-based approach to include bones for attenuation correction of whole-body PET/MRI," *Med Phys,* vol. 40, p. 082509, 2013.

[38] H. Arabi and H. Zaidi, "MRI-based pseudo-CT generation using sorted atlas images in whole-body PET/MRI," presented at the IEEE Nuclear Science Symposium and Medical Imaging Conference (NSS/MIC), 2014.

[39] M. Defrise, A. Rezaei, and J. Nuyts, "Time-of-flight PET data determine the attenuation sinogram up to a constant," *Phys Med Biol,* vol. 57, pp. 885-899, Feb 2012.

[40] A. Rezaei, M. Defrise, G. Bal, C. Michel, M. Conti, C. Watson*, et al.*, "Simultaneous reconstruction of activity and attenuation in Time-of-Flight PET," *IEEE Trans Med Imaging* vol. 31, pp. 2224-33, 2012.

[41] A. Salomon, A. Goedicke, B. Schweizer, T. Aach, and V. Schulz, "Simultaneous reconstruction of activity and attenuation for PET/MR," *IEEE Trans Med Imaging,* vol. 30, pp. 804-813, 2011.

[42] A. Mehranian and H. Zaidi, "Clinical assessment of emission- and segmentation-based MRI-guided attenuation correction in whole body TOF PET/MRI.," *J Nucl Med,* vol. 56, pp. 877-883, 2015.

[43] P. Mollet, V. Keereman, J. Bini, D. Izquierdo-Garcia, Z. A. Fayad, and S. Vandenberghe, "Improvement of attenuation correction in time-of-flight PET/MR imaging with a positron-emitting source," *J Nucl Med,* vol. 55, pp. 329-36, Feb 2014.

[44] V. Y. Panin, M. Aykac, and M. E. Casey, "Simultaneous reconstruction of emission activity and attenuation coefficient distribution from TOF data, acquired with external transmission source," *Phys Med Biol,* vol. 58, pp. 3649-69, 2013.

[45] G. Delso, M. Carl, F. Wiesinger, L. Sacolick, M. Porto, M. Hüllner, *et al.*, "Anatomic evaluation of 3-dimensional ultrashort-echo-time bone maps for PET/MR attenuation correction," *J Nucl Med,* vol. 55, pp. 780-785, May 1, 2014 2014.
[46] K. M. Johnson, S. B. Fain, M. L. Schiebler, and S. Nagle, "Optimized 3D ultrashort echo time pulmonary MRI," *Magn Reson Med,* vol. 70, pp. 1241-1250, 2013.
[47] Z. Hu, S. Renisch, B. Schweizer, T. Blaffert, N. Ojha, T. Guo, *et al.*, "MR-based attenuation correction for whole-body PET/MR system," presented at the IEEE Nuclear Science Symposium and Medical Imaging Conference (NSS/MIC), 2010.
[48] V. Schulz, I. Torres-Espallardo, S. Renisch, Z. Hu, N. Ojha, P. Börnert, *et al.*, "Automatic, three-segment, MR-based attenuation correction for whole-body PET/MR data," *Eur. J. Nucl. Med. Mol. Imaging,* vol. 38, pp. 138-152, 2011.
[49] H. Zaidi, N. Ojha, M. Morich, J. Griesmer, Z. Hu, P. Maniawski, *et al.*, "Design and performance evaluation of a whole-body Ingenuity TF PET-MRI system," *Phys Med Biol,* vol. 56, pp. 3091-106, May 21 2011.
[50] M. Eiber, A. Martinez-Möller, M. Souvatzoglou, K. Holzapfel, A. Pickhard, D. Löffelbein, *et al.*, "Value of a Dixon-based MR/PET attenuation correction sequence for the localization and evaluation of PET-positive lesions," *Eur. J. Nucl. Med. Mol. Imaging,* vol. 38, pp. 1691-1701, 2011/09/01 2011.
[51] A. Samarin, C. Burger, S. Wollenweber, D. Crook, I. Burger, D. Schmid, *et al.*, "PET/MR imaging of bone lesions – implications for PET quantification from imperfect attenuation correction," *Eur. J. Nucl. Med. Mol. Imaging,* vol. 39, pp. 1154-1160, 2012/07/01 2012.
[52] M. C. Aznar, R. Sersar, J. Saabye, C. N. Ladefoged, F. L. Andersen, J. H. Rasmussen, *et al.*, "Whole-body PET/MRI: the effect of bone attenuation during MR-based attenuation correction in oncology imaging," *Eur J Radiol,* vol. 83, pp. 1177-83, Jul 2014.
[53] J. Ouyang, C. Se Young, Y. Petibon, A. A. Bonab, N. Alpert, and G. El Fakhri, "Bias atlases for segmentation-based PET attenuation correction using PET-CT and MR," *IEEE Trans Nuc Sci,* vol. 60, pp. 3373-3382, 2013.
[54] A. Akbarzadeh, M. R. Ay, A. Ahmadian, N. Riahi Alam, and H. Zaidi, "MRI-guided attenuation correction in whole-body PET/MR: assessment of the effect of bone attenuation," *Annals of Nuclear Medicine,* vol. 27, pp. 152-162, 2013/02/01 2013.
[55] S. Keller, S. Holm, A. Hansen, B. Sattler, F. Andersen, T. Klausen, *et al.*, "Image artifacts from MR-based attenuation correction in clinical, whole-body PET/MRI," *Magnetic Resonance Materials in Physics, Biology and Medicine,* vol. 26, pp. 173-181, 2013/02/01 2013.
[56] H. Arabi, O. Rager, A. Alem, A. Varoquaux, M. Becker, and H. Zaidi, "Clinical Assessment of MR-Guided 3-Class and 4-Class Attenuation Correction in PET/MR," *Mol Imaging Biol,* vol. 17, pp. 264-76, Apr 2015.
[57] H. Choi, G. J. Cheon, H. J. Kim, S. H. Choi, J. S. Lee, Y. I. Kim, *et al.*, "Segmentation-based MR attenuation correction including bones also affects quantitation in brain studies: an initial result of 18F-FP-CIT PET/MR for patients with parkinsonism," *J Nucl Med,* vol. 55, pp. 1617-22, Oct 2014.
[58] C. Brendle, H. Schmidt, A. Oergel, I. Bezrukov, M. Mueller, C. Schraml, *et al.*, "Segmentation-based attenuation correction in positron emission tomography/magnetic resonance: erroneous tissue identification and its impact on positron emission tomography interpretation," *Invest Radiol,* vol. 50, pp. 339-346, May 2015.
[59] C. N. Ladefoged, A. E. Hansen, S. H. Keller, B. M. Fischer, J. H. Rasmussen, I. Law, *et al.*, "Dental artifacts in the head and neck region: implications for Dixon-based attenuation correction in PET/MR," *EJNMMI Physics,* vol. 2, p. 8, 2015.
[60] Y. C. Tai, K. P. Lin, M. Dahlbom, and E. J. Hoffman, "A hybrid attenuation correction technique to compensate for lung density in 3-D total body PET," *IEEE Trans Nuc Sci,* vol. 43, pp. 323-330, 1996.
[61] T. Chang, R. H. Diab, J. W. Clark, and O. R. Mawlawi, "Investigating the use of nonattenuation corrected PET images for the attenuation correction of PET data," *Med Phys,* vol. 40, p. 082508, 2013.
[62] M.-L. Montandon and H. Zaidi, "Atlas-guided non-uniform attenuation correction in cerebral 3D PET imaging.," *Neuroimage,* vol. 25, pp. 278-286, 2005.
[63] H. Zaidi, M.-L. Montandon, and S. Meikle, "Strategies for attenuation compensation in neurological PET studies.," *Neuroimage,* vol. 34, pp. 518-541, 2007.
[64] S. D. Wollenweber, S. Ambwani, G. Delso, A. H. R. Lonn, R. Mullick, F. Wiesinger, *et al.*, "Evaluation of an atlas-based PET head attenuation correction using PET/CT & MR patient data," *IEEE Trans Nuc Sci,* vol. 60, pp. 3383-3390, 2013.
[65] J. Uh, T. E. Merchant, Y. Li, X. Li, and C. Hua, "MRI-based treatment planning with pseudo CT generated through atlas registration.," *Med Phys,* vol. 41, pp. 051711-8, 2014.

[66] H. Arabi and H. Zaidi, "Comparison of atlas-based bone segmentation methods in whole-body PET/MRI," in *IEEE Nuclear Science Symposium and Medical Imaging Conference (NSS/MIC)*, Seattle, WA, USA, 2014.
[67] D. Izquierdo-Garcia, A. E. Hansen, S. Forster, D. Benoit, S. Schachoff, S. Furst*, et al.*, "An SPM8-based approach for attenuation correction combining segmentation and nonrigid template formation: application to simultaneous PET/MR brain imaging," *J Nucl Med,* vol. 55, pp. 1825-30, Nov 2014.
[68] Z. Yang, J. Choupan, F. Sepehrband, D. Reutens, and S. Crozier, "Tissue classification for PET/MRI attenuation correction using conditional random field and image fusion.," *International Journal of Machine Learning and Computing,* vol. 3, pp. 87-98 2013.
[69] J. Sjölund, D. Forsberg, M. Andersson, and H. Knutsson, "Generating patient specific pseudo-CT of the head from MR using atlas-based regression," *Phys Med Biol,* vol. 60, p. 825, 2015.
[70] A. Johansson, M. Karlsson, J. Yu, T. Asklund, and T. Nyholm, "Voxel-wise uncertainty in CT substitute derived from MRI.," *Med Phys,* vol. 39, pp. 3283-3290, 2012.
[71] N. Burgos, M. J. Cardoso, M. Modat, S. Pedemonte, J. Dickson, A. Barnes*, et al.*, "Attenuation correction synthesis for hybrid PET-MR scanners," in *Medical Image Computing and Computer-Assisted Intervention–MICCAI*, ed: Springer, 2013, pp. 147-154.
[72] A. S. Ribeiro, E. R. Kops, H. Herzog, and P. Almeida, "Hybrid approach for attenuation correction in PET/MR scanners," *Nucl Instrum Methods Phys Res A,* vol. 734, pp. 166-170, 2014.
[73] C. B. Poynton, K. T. Chen, D. B. Chonde, D. Izquierdo-Garcia, R. L. Gollub, E. R. Gerstner*, et al.*, "Probabilistic atlas-based segmentation of combined T1-weighted and DUTE MRI for calculation of head attenuation maps in integrated PET/MRI scanners," *Am J Nucl Med Mol Imaging,* vol. 4, pp. 160-171, 2014.
[74] G. Delso, K. Zeimpekis, M. Carl, F. Wiesinger, M. Hüllner, and P. Veit-Haibach, "Cluster-based segmentation of dual-echo ultra-short echo time images for PET/MR bone localization," *EJNMMI Physics,* vol. 1, pp. 1-13, 2014/06/04 2014.
[75] D. H. Paulus, H. H. Quick, C. Geppert, M. Fenchel, Y. Zhan, G. Hermosillo*, et al.*, "Whole-Body PET/MR Imaging: Quantitative Evaluation of a Novel Model-Based MR Attenuation Correction Method Including Bone," *J Nucl Med,* vol. 56, pp. 1061-6, Jul 2015.
[76] E. Rota Kops and H. Herzog, "Template based attenuation correction for PET in MR-PET scanners," in *IEEE Nuclear Science Symposium Conference Record*, 2008, pp. 3786-3789.
[77] Y. Xia, J. Fripp, S. S. Chandra, R. Schwarz, C. Engstrom, and S. Crozier, "Automated bone segmentation from large field of view 3D MR images of the hip joint.," *Phys Med Biol,* vol. 58, pp. 7375-7390, 2013.
[78] I. Bezrukov, H. Schmidt, S. Gatidis, F. Mantlik, J. F. Schäfer, N. F. Schwenzer*, et al.*, "Quantitative evaluation of segmentation-and atlas-based attenuation correction for PET/MR on pediatric patients," *Journal of Nuclear Medicine,* p. jnumed. 114.149476, 2015.
[79] F. Natterer, "Determination of Tissue Attenuation in Emission Tomography of Optically Dense Media," *Inverse Probl,* vol. 9, pp. 731-736, 1993.
[80] A. Rezaei, J. Nuyts, and M. Defrise, "Analytic reconstruction of the attenuation from 3D time-of-flight PET data," in *IEEE Nuclear Science Symposium and Medical Imaging Conference (NSS/MIC)*, 2012, pp. 2330-2333.
[81] H. Li, G. El Fakhri, and Q. Li, "Direct MAP estimation of attenuation sinogram using TOF PET data and anatomical information," in *Proceedings of Fully 3D Image Reconstruction in Radiology and Nuclear Medicine*, 2013, pp. 404-407.
[82] Y. Censor, D. E. Gustafson, A. Lent, and H. Tuy, "A New Approach to the Emission Computerized Tomography Problem: Simultaneous Calculation of Attenuation and Activity Coefficients," *IEEE Trans Nuc Sci,* vol. 26, pp. 2775-2779, 1979.
[83] J. Nuyts, P. Dupont, S. Stroobants, R. Benninck, L. Mortelmans, and P. Suetens, "Simultaneous maximum a posteriori reconstruction of attenuation and activity distributions from emission sinograms," *IEEE Trans Med Imaging,* vol. 18, pp. 393-403, 1999.
[84] A. Salomon, A. Goedicke, and T. Aach, "Simultaneous reconstruction of activity and attenuation in multi-modal ToF-PET.," in *10th International Meeting on Fully Three-Dimensional Image Reconstruction in Radiology and Nuclear Medicine (Fully3D)*, Beijing, China, 5-10 Sept. 2009, 2009, pp. 339-342.
[85] A. Rezaei, M. Defrise, and J. Nuyts, "ML-reconstruction for TOF-PET with simultaneous estimation of the attenuation factors," *IEEE Trans Med Imaging,* vol. 33, pp. 1563-1572, 2014.
[86] G. Bal, F. Kehren, C. Michel, C. Watson, D. Manthey, and J. Nuyts, "Clinical evaluation of MLAA for MR-PET," *J NUCL MED MEETING ABSTRACTS,* vol. 52, pp. 263-, May 1, 2011 2011.
[87] A. Mehranian and H. Zaidi, "Joint estimation of activity and attenuation in whole-body TOF PET/MRI using constrained Gaussian mixture models.," *IEEE Trans Med Imaging,* vol. 34, pp. 1808-1821, 2015.
[88] A. Mehranian, H. Arabi, and H. Zaidi, "Quantitative analysis of MRI-guided attenuation correction methods in time-of-flight brain PET/MRI.," *Neuroimage,* Vol. 130, pp 123-133 (2016).

[89] N. H. Clinthorne, J. A. Fessler, G. D. Hutchins, and W. L. Rogers, "Joint maximum likelihood estimation of emission and attenuation densities in PET," in *Conference Record of the IEEE Nuclear Science Symposium and Medical Imaging Conference*, 1991, pp. 1927-1932.
[90] W. W. Moses, "Time of flight in PET revisited," *IEEE Trans Nuc Sci,* vol. 50, pp. 1325-1330, 2003.
[91] P. Mollet, V. Keereman, E. Clementel, and S. Vandenberghe, "Simultaneous MR-compatible emission and transmission imaging for PET using time-of-flight information," *IEEE Trans Med Imaging,* vol. PP, pp. 1-1, 2012.
[92] C. C. Watson, "Supplemental transmission method for improved PET attenuation correction on an integrated MR/PET," *Nucl Instrum Methods Phys Res A,* vol. 734, Part B, pp. 191-195, 2014.
[93] H. Rothfuss, V. Panin, A. Moor, J. Young, I. Hong, C. Michel*, et al.*, "LSO background radiation as a transmission source using time of flight," *Phys Med Biol,* vol. 59, pp. 5483-500, 2014.
[94] M. Conti, I. Hong, and C. Michel, "Reconstruction of scattered and unscattered PET coincidences using TOF and energy information," *Phys Med Biol,* vol. 57, pp. N307-17, Aug 7 2012.
[95] H. Sun and S. Pistorius, "A generalized scatter reconstruction algorithm for limited energy resolution PET detectors," in *IEEE Nuclear Science Symposium and Medical Imaging Conference (NSS/MIC)*, 2014.
[96] Y. Berker, F. Kiessling, and V. Schulz, "Scattered PET data for attenuation-map reconstruction in PET/MRI," *Med Phys,* vol. 41, p. 102502, Oct 2014.
[97] G. Delso, A. Martinez-Möller, R. A. Bundschuh, S. G. Nekolla, and S. I. Ziegler, "The effect of limited MR field of view in MR/PET attenuation correction," *Med Phys,* vol. 37, pp. 2804-2812, 2010.
[98] G. Schramm, J. Langner, F. Hofheinz, J. Petr, A. Lougovski, B. Beuthien-Baumann*, et al.*, "Influence and Compensation of Truncation Artifacts in MR-Based Attenuation Correction in PET/MR," *IEEE Trans Med Imaging,* vol. 32, pp. 2056-2063, 2013.
[99] H. Qian, R. M. Manjeshwar, S. Ambwani, and S. D. Wollenweber, "Truncation completion of MR-based PET attenuation maps using time-of-flight non-attenuation-corrected PET images," in *Nuclear Science Symposium and Medical Imaging Conference (NSS/MIC)*, 2012, pp. 2773-2775.
[100] T. Blaffert, S. Renisch, J. Tang, M. Narayanan, and Z. Hu, "Comparison of threshold-based and watershed-based segmentation for the truncation compensation of PET/MR images.," in *Proc. SPIE 8314, Medical Imaging 2012: Image Processing*, 2012, pp. 831403-831403-12.
[101] J. Nuyts, G. Bal, F. Kehren, M. Fenchel, C. Michel, and C. Watson, "Completion of a Truncated Attenuation Image from the Attenuated PET Emission Data," *IEEE Trans Med Imaging,* vol. 32, pp. 237-46, 2013.
[102] J. O. Blumhagen, R. Ladebeck, M. Fenchel, and K. Scheffler, "MR-based field-of-view extension in MR/PET: B0 homogenization using gradient enhancement (HUGE)," *Magn Reson Med,* vol. 70, pp. 1047-57, Oct 2013.
[103] J. O. Blumhagen, H. Braun, R. Ladebeck, M. Fenchel, D. Faul, K. Scheffler*, et al.*, "Field of view extension and truncation correction for MR-based human attenuation correction in simultaneous MR/PET imaging," *Med Phys,* vol. 41, p. 022303, 2014.
[104] C. N. Ladefoged, T. Beyer, S. H. Keller, I. Law, L. Hojgaard, A. Kjær*, et al.*, "PET/MR imaging of head/neck in the presence of dental implants: reducing image artifacts and increasing accuracy through inpainting [abstract]." *Eur J Nucl Med Mol Imaging,* p. OP601, Jan 8 2013.
[105] C. Ladefoged, F. Andersen, S. Keller, J. Löfgren, A. Hansen, S. Holm*, et al.*, "PET/MR imaging of the pelvis in the presence of endoprostheses: reducing image artifacts and increasing accuracy through inpainting," *Eur. J. Nucl. Med. Mol. Imaging,* vol. 40, pp. 594-601, 2013/04/01 2013.
[106] G. Schramm, J. Maus, F. Hofheinz, J. Petr, A. Lougovski, B. Beuthien-Baumann*, et al.*, "Evaluation and automatic correction of metal-implant-induced artifacts in MR-based attenuation correction in whole-body PET/MR imaging," *Phys Med Biol,* vol. 59, pp. 2713-26, Jun 7 2014.
[107] M. J. Lee, S. Kim, S. A. Lee, H. T. Song, Y. M. Huh, D. H. Kim*, et al.*, "Overcoming artifacts from metallic orthopedic implants at high-field-strength MR imaging and multi-detector CT," *Radiographics,* vol. 27, pp. 791-803, May-Jun 2007.
[108] K. M. Koch, J. E. Lorbiecki, R. S. Hinks, and K. F. King, "A multispectral three-dimensional acquisition technique for imaging near metal implants," *Magn Reson Med,* vol. 61, pp. 381-90, Feb 2009.
[109] I. A. Burger, M. C. Wurnig, A. S. Becker, D. Kenkel, G. Delso, P. Veit-Haibach*, et al.*, "Hybrid PET/MR Imaging: An Algorithm to Reduce Metal Artifacts from Dental Implants in Dixon-Based Attenuation Map Generation Using a Multiacquisition Variable-Resonance Image Combination Sequence," *J Nucl Med,* vol. 56, pp. 93-7, Jan 2015.
[110] J. M. Gunzinger, G. Delso, A. Boss, M. Porto, H. Davison, G. K. von Schulthess*, et al.*, "Metal artifact reduction in patients with dental implants using multispectral three-dimensional data acquisition for hybrid PET/MRI," *EJNMMI Physics,* vol. 1, p. 102, 2014.

[111] T. Pan and H. Zaidi, "Attenuation Correction Strategies for Positron Emission Tomography/Computed Tomography and 4-Dimensional Positron Emission Tomography/Computed Tomography," *PET Clinics,* vol. 8, pp. 37-50, 2013.
[112] C. Buerger, A. Aitken, C. Tsoumpas, A. P. King, V. Schulz, P. Marsden*, et al.*, "Investigation of 4D PET attenuation correction using Ultra-short Echo Time MR," in *IEEE Nuclear Science Symposium and Medical Imaging Conference (NSS/MIC)*, 2011, pp. 3558-3561.
[113] H. Fayad, H. Schmidt, C. Wuerslin, and D. Visvikis, "4D attenuation map generation in PET/MR imaging using 4D PET derived motion fields," in *Nuclear Science Symposium and Medical Imaging Conference (NSS/MIC), 2013 IEEE*, 2013, pp. 1-4.
[114] A. Mehranian and H. Zaidi, "Emission-based estimation of lung attenuation coefficients for attenuation correction in PET/MR," *Phys Med Biol,* vol. 60, pp. 4813-33, 2015.
[115] A. Rezaei and J. Nuyts, "Joint registration of attenuation and activity images in gated TOF-PET," in *IEEE Nuclear Science Symposium and Medical Imaging Conference (NSS/MIC)*, 2013, pp. 1-4.
[116] L. R. MacDonald, S. Kohlmyer, C. Liu, T. K. Lewellen, and P. E. Kinahan, "Effects of MR surface coils on PET quantification," *Med Phys,* vol. 38, pp. 2948-2956, 2011.
[117] R. Kartmann, D. H. Paulus, H. Braun, B. Aklan, S. Ziegler, B. K. Navalpakkam*, et al.*, "Integrated PET/MR imaging: Automatic attenuation correction of flexible RF coils," *Med Phys,* vol. 40, p. 082301, 2013.
[118] S. Furst, M. Souvatzoglou, A. Martinez-Moller, M. Schwaiger, S. G. Nekolla, and S. I. Ziegler, "Impact of flexible body surface coil and patient table on PET quantification and image quality in integrated PET/MR," *Nuklearmedizin,* vol. 53, pp. 79-87, 2014.
[119] G. Delso, A. Martinez-Möller, R. A. Bundschuh, R. Ladebeck, Y. Candidus, D. Faul*, et al.*, "Evaluation of the attenuation properties of MR equipment for its use in a whole-body PET/MR scanner," *Phys Med Biol,* vol. 55, p. 4361, 2010.
[120] B. Aklan, D. H. Paulus, E. Wenkel, H. Braun, B. K. Navalpakkam, S. Ziegler*, et al.*, "Toward simultaneous PET/MR breast imaging: Systematic evaluation and integration of a radiofrequency breast coil," *Med Phys,* vol. 40, p. 024301, 2013.
[121] B. Zhang, D. Pal, Z. Hu, N. Ojha, G. Muswick, C.-H. Tung*, et al.*, "Attenuation correction for MR table and coils for a sequential PET/MR system," in *IEEE Nuclear Science Symposium & Medical Imaging Conference*, 25-31 October 2009, Orlando (FL), USA, 2009, pp. 3303-3306.
[122] D. H. Paulus, L. Tellmann, and H. H. Quick, "Towards improved hardware component attenuation correction in PET/MR hybrid imaging.," *Phys Med Biol,* vol. 58, pp. 8021-8040, Nov 21 2013.
[123] D. H. Paulus, H. Braun, B. Aklan, and H. H. Quick, "Simultaneous PET/MR imaging: MR-based attenuation correction of local radiofrequency surface coils," *Med Phys,* vol. 39, pp. 4306-15, Jul 2012.
[124] M. Eldib, J. Bini, C. Calcagno, P. M. Robson, V. Mani, and Z. A. Fayad, "Attenuation correction for flexible magnetic resonance coils in combined magnetic resonance/positron emission tomography imaging," *Invest Radiol,* vol. 49, pp. 63-9, Feb 2014.
[125] S. Saha, "Whole body RF coil design for a simultaneous PET-MR system," in *Joint Annual Meeting ISMRM-ESMRMB*, Milan, Italy, 2014.
[126] I. Dregely, T. Lanz, S. Metz, M. F. Mueller, M. Kuschan, M. Nimbalkar*, et al.*, "A 16-channel MR coil for simultaneous PET/MR imaging in breast cancer," *Eur Radiol,* vol. 25, pp. 1154-61, Apr 2015.
[127] M. Hofmann, B. Schölkopf, I. Bezrukov, and N. D. Cahill, "Incorporating prior knowledge on class probabilities into local similarity measures for intermodality image registration," in *Proceedings of the MICCAI, Workshop on Probabilistic Models for Medical Image Analysis (PMMIA)*, 2009.
[128] R. Karimi, G. Tornling, H. Forsslund, M. Mikko, A. Wheelock, S. Nyren*, et al.*, "Lung density on high resolution computer tomography (HRCT) reflects degree of inflammation in smokers," *Respir Res,* vol. 15, p. 23, 2014.
[129] J. H. Kim, J. S. Lee, I. C. Song, and D. S. Lee, "Comparison of segmentation-based attenuation correction methods for PET/MRI: evaluation of bone and liver standardized uptake value with oncologic PET/CT data," *J Nucl Med,* vol. 53, pp. 1878-82, Dec 2012.
[130] H. R. Marshall, F. S. Prato, L. Deans, J. Théberge, R. T. Thompson, and R. Z. Stodilka, "Variable lung density consideration in attenuation correction of whole-body PET/MRI," *J Nucl Med,* vol. 53, pp. 977-984, June 1, 2012 2012.
[131] A. R. Lonn and S. D. Wollenweber, "Estimation of mean lung attenuation for use in generating PET attenuation maps," in *IEEE Nuclear Science Symposium and Medical Imaging Conference (NSS/MIC)*, 2012, pp. 3017-3018.
[132] Y. Berker, A. Salomon, F. Kiessling, and V. Schulz, "Lung attenuation coefficient estimation using Maximum Likelihood reconstruction of attenuation and activity for PET/MR attenuation correction," in *IEEE Nuclear Science Symposium and Medical Imaging Conference (NSS/MIC)*, 2012, pp. 2282-2284.

[133] P. J. Schleyer, T. Schaeffter, and P. K. Marsden, "The effect of inaccurate bone attenuation coefficient and segmentation on reconstructed PET images," *Nucl Med Commun,* vol. 31, pp. 708-16, Aug 2010.
[134] B. K. Navalpakkam, H. Braun, T. Kuwert, and H. H. Quick, "Magnetic resonance-based attenuation correction for PET/MR hybrid imaging using continuous valued attenuation maps," *Invest Radiol,* vol. 48, pp. 323-32, May 2013.
[135] W. Lee, J.-A. Park, K. M. Kim, I.-O. Ko, I. Lim, J. S. Kim*, et al.*, "Effects of MR contrast agents on PET quantitation in PET-MRI study," *J Nucl Med Meeting Abstracts,* vol. 52, pp. 53-, May 1, 2011 2011.
[136] C. Lois, I. Bezrukov, H. Schmidt, N. Schwenzer, M. Werner, J. Kupferschläger*, et al.*, "Effect of MR contrast agents on quantitative accuracy of PET in combined whole-body PET/MR imaging," *Eur. J. Nucl. Med. Mol. Imaging,* vol. 39, pp. 1756-1766, 2012/11/01 2012.
[137] S. Ahn, L. Cheng, and R. M. Manjeshwar, "Analysis of the effects of errors in attenuation maps on PET quantitation in TOF PET," presented at the IEEE Nuclear Science Symposium Conference Record (NSS/MIC), Seattle, WA, 2014.
[138] S. Wollenweber, G. Delso, T. Deller, D. Goldhaber, M. Hüllner, and P. Veit-Haibach, "Characterization of the impact to PET quantification and image quality of an anterior array surface coil for PET/MR imaging," *Magn Reson Mater Phy,* vol. 27, pp. 149-159, 2014/04/01 2014.
[139] H. Davison, E. E. Ter Voert, F. de Galiza Barbosa, P. Veit-Haibach, and G. Delso, "Incorporation of Time-of-Flight Information Reduces Metal Artifacts in Simultaneous Positron Emission Tomography/Magnetic Resonance Imaging: A Simulation Study," *Invest Radiol,* vol. 50, pp. 423-9, Mar 11 2015.
[140] T. W. Deller, A. M. Grant, M. M. Khalighi, S. H. Maramraju, G. Delso, and C. S. Levin, "PET NEMA performance measurements for a SiPM-based time-of-flight PET/MR system," in *IEEE Nuclear Science Symposium and Medical Imaging Conference (NSS/MIC)*, Seattle, WA, 8-15 November 2014, 2014.
[141] ter Voert E, Delso G, Ahn S, Wiesinger F, Huellner M, and V.-H. P, "The effect of TOF on PET reconstructions in patients with (metal) implants in simultaneous TOF PET/MR scanning," presented at the Radiological Society of North America Scientific Assembly and Annual Meeting Chicago IL, 2014
[142] A. Mehranian and H. Zaidi, "Impact of time-of-flight PET on quantification errors in MRI-based attenuation correction," *J Nucl Med,* vol. 56, pp. 635-41, 2015.
[143] K. G. Hollingsworth, "Reducing acquisition time in clinical MRI by data undersampling and compressed sensing reconstruction.," *Phys Med Biol,* vol. 60, pp. R297-322, Nov 7 2015.
[144] C. Li, J. Magland, and F. Wehrli, "Compressed sensing 3D ultrashort echo time (COMPUTE) imaging," in *Proceedings of the 20th Annual Meeting ISMRM*, 2012.
[145] L. Hu, K.-H. Su, G. C. Pereira, A. Grover, B. Traughber, M. Traughber*, et al.*, "k-space sampling optimization for ultrashort TE imaging of cortical bone: Applications in radiation therapy planning and MR-based PET attenuation correction," *Med Phys,* vol. 41, p. 102301, 2014.
[146] R. Galea, R. G. Wells, C. K. Ross, J. Lockwood, K. Moore, J. T. Harvey*, et al.*, "A comparison of rat SPECT images obtained using (99m)Tc derived from 99Mo produced by an electron accelerator with that from a reactor.," *Phys Med Biol,* vol. 58, pp. 2737-2750, May 7 2013.
[147] M. Weiger, D. O. Brunner, B. E. Dietrich, C. F. Muller, and K. P. Pruessmann, "ZTE imaging in humans," *Magn Reson Med,* vol. 70, pp. 328-32, Aug 2013.
[148] F. Wiesinger, L. I. Sacolick, A. Menini, S. S. Kaushik, S. Ahn, P. Veit-Haibach*, et al.*, "Zero TE MR bone imaging in the head," *Magn Reson Med,* Jan 16 2015.
[149] G. Delso, F. Wiesinger, L. I. Sacolick, S. S. Kaushik, D. D. Shanbhag, M. Hüllner*, et al.*, "Clinical evaluation of zero-echo-time MR imaging for the segmentation of the skull," *J Nucl Med,* vol. 56, pp. 417-422, March 1, 2015 2015.
[150] F. Gibiino, L. Sacolick, A. Menini, L. Landini, and F. Wiesinger, "Free-breathing, zero-TE MR lung imaging.," *MAGMA,* vol. 28, pp. 207-215, Sep 9 2015.
[151] G. Delso, S. Fürst, B. Jakoby, R. Ladebeck, C. Ganter, S. G. Nekolla*, et al.*, "Performance Measurements of the Siemens mMR Integrated Whole-Body PET/MR Scanner," *J Nucl Med,* vol. 52, pp. 1914-1922, 2011.
[152] A. Drzezga, M. Souvatzoglou, M. Eiber, A. J. Beer, S. Furst, A. Martinez-Moller*, et al.*, "First clinical experience with integrated whole-body PET/MR: comparison to PET/CT in patients with oncologic diagnoses," *J Nucl Med,* vol. 53, pp. 845-55, Jun 2012.
[153] M. Becker and H. Zaidi, "Imaging in head and neck squamous cell carcinoma: the potential role of PET/MRI," *Br J Radiol,* vol. 87, p. 20130677, 2014.
[154] J. Czernin, L. Ta, and K. Herrmann, "Does PET/MR imaging improve cancer assessments? Literature evidence from more than 900 patients.," *J Nucl Med,* vol. 55, pp. 59S-62S, June 1, 2014 2014.
[155] C. Spick, K. Herrmann, and J. Czernin, "18F-FDG PET/CT and PET/MRI perform equally well in cancer patients: Evidence from studies in more than 2300 patients.," *J Nucl Med,* p. *in press*, Jan 7 2016.

[156] H. T. van Dam, G. Borghi, S. Seifert, and D. R. Schaart, "Sub-200 ps CRT in monolithic scintillator PET detectors using digital SiPM arrays and maximum likelihood interaction time estimation.," *Phys Med Biol,* vol. 58, pp. 3243-3257, May 21 2013.
[157] K. Doroud, A. Rodriguez, M. C. S. Williams, K. Yamamoto, A. Zichichi, and R. Zuyeuski, "Systematic study of new types of Hamamatsu MPPCs read out with the NINO ASIC.," *Nucl Instr Meth A,* vol. 753, pp. 149-153, 7/21/ 2014.
[158] J.-y. Cui, G. Pratx, S. Prevrhal, and C. S. Levin, "Fully 3D list-mode time-of-flight PET image reconstruction on GPUs using CUDA," *Med Phys,* vol. 38, pp. 6775-6786, 2011.
[159] I. Hong, W. Luk, V. Panin, C. Watson, F. Kehren, and M. Casey, "Real-time PET reconstruction," in *IEEE Nuclear Science Symposium and Medical Imaging Conference (NSS/MIC)*, Seattle, WA, 8-15 November 2014, 2014, p. *in press*.
[160] A. Afshar-Oromieh, U. Haberkorn, H. P. Schlemmer, M. Fenchel, M. Eder, M. Eisenhut*, et al.*, "Comparison of PET/CT and PET/MRI hybrid systems using a 68Ga-labelled PSMA ligand for the diagnosis of recurrent prostate cancer: initial experience," *Eur J Nucl Med Mol Imaging,* vol. 41, pp. 887-897, 2014/05/01 2014.
[161] M. Covello, C. Cavaliere, M. Aiello, M. S. Cianelli, M. Mesolella, B. Iorio*, et al.*, "Simultaneous PET/MR head–neck cancer imaging: Preliminary clinical experience and multiparametric evaluation," *Eur J Radiol,* vol. 84, pp. 1269-1276, 2015.
[162] S. Partovi, A. Kohan, J. L. Vercher-Conejero, C. Rubbert, S. Margevicius, M. D. Schluchter*, et al.*, "Qualitative and quantitative performance of (1)(8)F-FDG-PET/MRI versus (1)(8)F-FDG-PET/CT in patients with head and neck cancer," *Am J Neuroradiol,* vol. 35, pp. 1970-5, Oct 2014.
[163] A. Varoquaux, O. Rager, A. Poncet, B. M. Delattre, O. Ratib, C. D. Becker*, et al.*, "Detection and quantification of focal uptake in head and neck tumours: (18)F-FDG PET/MR versus PET/CT," *Eur. J. Nucl. Med. Mol. Imag,* vol. 41, pp. 462-75, Mar 2014.
[164] S. I. Lee, O. A. Catalano, and F. Dehdashti, "Evaluation of gynecologic cancer with MR imaging, 18F-FDG PET/CT, and PET/MR imaging," *J Nucl Med,* vol. 56, pp. 436-43, Mar 2015.
[165] D. A. Torigian, H. Zaidi, T. C. Kwee, B. Saboury, J. K. Udupa, Z.-H. Cho*, et al.*, "PET/MR Imaging: Technical aspects and potential clinical applications.," *Radiology,* vol. 267, pp. 26-44, 2013.
[166] J. Steinberg, G. Jia, S. Sammet, J. Zhang, N. Hall, and M. V. Knopp, "Three-region MRI-based whole-body attenuation correction for automated PET reconstruction," *Nucl Med Biol,* vol. 37, pp. 227-35, Feb 2010.
[167] J. H. Jonsson, M. M. Akhtari, M. G. Karlsson, A. Johansson, T. Asklund, and T. Nyholm, "Accuracy of inverse treatment planning on substitute CT images derived from MR data for brain. lesions," *Radiat Oncol,* vol. 10, p. 13, 2015.
[168] J. A. Dowling, J. Lambert, J. Parker, O. Salvado, J. Fripp, A. Capp*, et al.*, "An atlas-based electron density mapping method for magnetic resonance imaging (MRI)-alone treatment planning and adaptive MRI-based prostate radiation therapy.," *Int J Radiat Oncol Biol Phys,* vol. 83, pp. e5-11, May 1 2012.

Chapter 3

Clinical Assessment of MR-Guided 3-Class and 4-Class Attenuation Correction in PET/MR

Arabi H, Rager O, Alem A, Varoquaux A, Becker M and Zaidi H

Molecular Imaging and Biology, Vol. 17, No. 2, pp 264-276 (2015)

Abstract

Purpose: We compare the quantitative accuracy of magnetic resonance imaging (MRI)-based attenuation correction (AC) using the 3-class attenuation map (PET-MRAC3c) implemented on the Ingenuity TF PET/MRI and the 4-class attenuation map (PET-MRAC4c) similar to the approach used on the Siemens mMR PET/MR considering CT-based attenuation-corrected PET images (PET-CTAC) as standard of reference.

Methods: Fourteen patients with malignant tumors underwent whole body sequential ^{18}F-FDG PET/CT and PET/MR imaging. A 3-class attenuation map was obtained from segmentation of T1-weighted MR images followed by assignment of attenuation coefficients (air: 0 cm^{-1}, lung: 0.022 cm^{-1}, soft-tissue: 0.096 cm^{-1}), whereas a 4-class attenuation map was derived from a MR Dixon sequence (air: 0 cm^{-1}, lung: 0.018 cm^{-1}, fat: 0.086 cm^{-1}, soft-tissue: 0.096 cm^{-1}). Additional adipose tissue class and inner body air cavities (e.g. sinus and abdomen) were also considered. Different attenuation coefficients were assigned to the lungs since the two techniques were implemented as they were proposed without any modification. SUV_{mean} and SUV_{max} metrics were calculated for volumes of interest in various organs/tissues and malignant lesions. Well established metrics were used for the analysis of SUVs estimated using both PET-MRAC techniques and PET-CTAC including relative error, Spearman rank correlation and Bland and Altman analysis.

Results: PET-MRAC3c and PET-MRAC4c revealed significant underestimation of SUV for normal organs (-17.4±8.5% and -22.0±6.8%, respectively) compared to PET-CTAC. Lesions' SUV presented the same trend with larger underestimation for PET-MRAC4c (-9.2±6.1%) compared to PET-MRAC3c (-3.9±9.0). The different attenuation coefficients assigned to the lungs with both techniques resulted in significant positive bias on PET-MRAC3c (18.6±15.3%) and low negative bias on PET-MRAC4c (-0.5±13.3%). Both approaches yielded the largest differences in and near bony structures. Despite the large bias, there was good correlation between PET-MRAC3c (R=0.97, $p<0.01$) and PET-CTAC, and PET-MRAC4c (R=0.97, $p<0.01$) and PET-CTAC, respectively.

Conclusion: PET-MRAC3c resulted in significant systematic positive bias in the lungs owing to the higher attenuation coefficient used and negative bias in other regions. PET-MRAC4c slightly underestimated tracer uptake in the lungs and lead to even larger negative bias than PET-MRAC3c in other body regions. The presence of artefacts in the MRAC maps might lead to misinterpretation of clinical studies. As such, the attenuation map needs to be checked for artefacts as part of the reading procedure to avoid misinterpretation of SUV measurements.

I. Introduction

The growing clinical and research interest in hybrid PET/MR imaging demonstrate that this technology could provide a major technological breakthrough having the potential to trigger a ground-breaking paradigm shift in clinical diagnostic imaging and revolutionize clinical practice [1]. There are many compelling reasons to combine PET and MRI such as higher soft-tissue contrast compared with CT, the availability of various MRI sequences and the foremost advantage of MRI is the absence of radiation exposure. [2-3]. Therefore, much research efforts are directed toward the development of combined PET/MR systems and addressing related crucial issues such as quantitative imaging [4].

Although the preliminary clinical results obtained using combined PET/MR are promising [5-7], attenuation correction is technically challenging since the MR signal is not correlated with attenuation coefficients of biological tissues. Nevertheless, a number of approaches have been suggested to generate an attenuation map from MR images [8-9]. This includes MR image segmentation techniques [10-12], atlas and machine learning approaches [13-14], the use of special MRI sequences such as ultra-short echo [15-17], and joint estimation of emission and transmission maps through iterative reconstruction of emission data only [18-20].

Segmentation-based methods, the most widely employed techniques, rely on classifying the patient MR image into a number of tissue classes followed by assignment of predefined linear attenuation coefficients. However, ignoring bony structures is the major drawback of these techniques, Since the percentage of bone tissue in the body is relatively low compared to specific body regions/organs such as the head, attenuation correction that neglects bones may be sufficient for most clinical indications [11-12]. Yet, underestimation of tracer uptake by osseous lesions has been reported in a number of studies, typically ranging within 5-8% [11-12, 21] or up to 15% [22] and 23% [23] compared to what is achieved using clinical PET/CT data, whereas simulation studies using an anthropomorphic thorax phantom reported a local bias of up to 17% [24] and even 30% [25]. The average underestimation of tracer uptake in bony structure was reported to vary between 7.8% [11] and 27% [14]. Comparison of segmentation-based attenuation correction methods revealed underestimation of tracer uptake by 15%-16% when using a 3-class attenuation map [26]. These discrepancies can be partially explained by the assignment of different attenuation coefficients for each individual class. For instance, a linear attenuation coefficient of 0.101 cm-1 for soft tissue was used in one study [14] whereas 0.0952 cm-1 was used in another [22, 26].

The Philips Ingenuity TF PET/MR (Philips Healthcare, Cleveland, Ohio, USA) uses a 3-class attenuation map from segmentation of a T1-weighted MR sequence including air, lung and soft-tissue [12, 27]. Conversely, the approach used on the Siemens mMR PET/MR (Siemens Healthcare, Erlangen, USA) system generates a 4-class attenuation map from segmentation of a Dixon MR sequence [28] including fat in addition to the above referenced tissues classes [11, 29]. The above referenced MRAC procedures are widely used in clinical setting. Therefore, the clinical assessment of their performance is commended.

In this work, we compare the 3-class (air, lung, soft-tissue) and the 4-class (air, lung, fat, soft-tissue) approaches implemented on the Ingenuity TF PET/MRI and reported by Martinez-Moller et al. [11] (an approach similar to the technique implemented on the Biograph mMR PET/MR), respectively, using clinical whole-body PET data. PET images corrected for attenuation using coregistered CT images are used as reference for comparison of the standardized uptake values (SUVs).

II. Materials and methods

II.A. PET/CT and PET/MR data acquisition

The study population comprised 14 consecutive patients, 9 men and 5 women (mean age ± SD = 61 ± 7 y), in whom MRI of the head and neck, whole body 18F-FDG PET/MR and whole-body 18F-FDG PET/CT were performed for staging of head and neck malignancies. The study protocol was approved by the institutional ethics committee and all patients gave informed consent to participate in the study. A single injection of ^{18}F-FDG (371±23 MBq) was used.

18F-FDG PET/CT scans were performed on a Biograph 64 True Point scanner (Siemens Healthcare, Erlangen, Germany) After a localization scout scan, an unenhanced CT scan (120 kVp, 180 mAs, 24×1.5 collimation, a pitch of 1.2, and 1 s per rotation) was performed for attenuation correction. PET data acquisition

started 146.2±20 min post-injection with 3 min per bed position for a total of 5-6 beds, resulting in a total acquisition time of 15-18 min.

MRI examinations were performed on the Ingenuity TF PET/MR[27] The so-called atMR whole-body MRI sequence was developed for fast acquisition (<3 min) of the 3-class attenuation map. It consists of a 3D multi-stack spoiled T1-weighted gradient echo sequence with the following parameters: flip angle 10°, TE 2.3 ms, TR 4.1 ms, smallest water–fat shift, 600 mm transverse FOV with a slab thickness of 120 mm, voxel size 1.9×1.9×6 mm3, 12 mm overlap between adjacent stacks [12].The 4-class attenuation map (air, lung, fat and soft-tissue) is derived from a Dixon sequence [11, 30]. The whole body Dixon 3D volumetric interpolated T1-weighted sequence used the following parameters: flip angle 10°, TE1 1.1 ms, TE2 2.0 ms, TR 3.2 ms, 450×354 mm2 transverse FOV, 0.85×0.85×3 mm3 voxel size, and a total acquisition time of 2 min 17 s. It should be noted that the Dixon sequence parameters used in this work are slightly different from what has been used in [9, 29] (TE1 1.17 ms and TR 20 ms), which might result in slightly different fat and water contrast, thus impacting the segmentation results. In-phase images were used for anatomic localization and PET/MR data fusion and registration. The maximum temporal difference between PET/CT and PET/MR scans was less than an hour.

II.B. Attenuation correction

Dixon MR images (in-phase) were deformably registered to the corresponding CT images obtained from the PET/CT scan using the Elastix package (based on the ITK library) [31]. The alignment was performed by employing a combination of rigid and non-rigid registration based on maximum mutual and B-spline transform as described previously [32]. A multiresolution approach with 6 steps from 1/32 to 1/1 along with a stochastic gradient descent optimizer were utilized for coregistration of in-phase MR to CT. 32 histogram bins and 2000 iterations at each resolution achieved good results. The obtained transformation fields were applied to atMR images taking advantage of prior alignment of Dixon and atMR images. It should be noted that the regions located in the vicinity of misalignment errors were disregarded from further analysis.

Subsequently, the coregistered atMR images were used to create a 3-class attenuation map corresponding to air (background), lung, and soft-tissue according to the method implemented on the Ingenuity PET/MR system with the following attenuation coefficients: 0 cm-1 (-1000 HU), 0.022 cm-1 (-770 HU) and 0.096 cm-1 (0 HU) for background, lung and soft-tissue, respectively [33].

Likewise, a 4-class segmentation of MR images (air, lung, fat, and soft-tissue) was carried out using in-phase and fat-only Dixon images. In the first step, the transformation matrices obtained from the registration of in-phase images to the corresponding CT images were applied to register the corresponding fat-only MR images. The external body contour and lungs were determined by applying a 3D snake active contour algorithm [34]. The segmentation was performed through connected-component analysis of the low intensity voxels initiated by manual seeds using the ITK-SNAP image processing software [35]. In the next step, fat masks obtained using histogram-based thresholding of fat-only images [36] were superimposed on the segmented in-phase images to achieve a 4-class segmented image to which the following attenuation coefficients were assigned: air 0 cm-1 (-1000 HU), lung 0.018 cm-1 (-820 HU), fat 0.086 cm-1 (-140 HU) soft-tissue 0.096 cm-1 (0 HU). The procedure followed to derive the 4-class attenuation map was similar to the one proposed by Martinez-Moller et al. [11] deemed to be the basis of the technique implemented on the Siemens mMR although the latter approach seems to be specifically optimized for this scanner configuration using 4-class (with different attenuation coefficients) [29] or 5-class [9] attenuation maps. In the last step, PET/CT patient bed was then added to the 3 and 4-class attenuation maps followed by 3D Gaussian filtering (FWHM of 5 mm). It is worth highlighting that the air gaps in the body (air-filled paranasal sinuses and gastro-intestinal air) were also separately identified and assigned the corresponding attenuation coefficient. Segmentation of air sinus and air gaps in the abdomen was performed using an actour contour technique initialized by manual selection of initial seeds in the air cavities.

II.C. Image reconstruction

Image reconstruction was performed three times for each clinical study: PET images of the PET/CT data corrected for attenuation using CT (PET-CTAC) used as reference, PET attenuation corrected using the 3-class (PET-MRAC3c) and 4-class (PET-MRAC4c) attenuation maps. PET image reconstruction was performed using attenuation weighted, ordered subset-expectation maximization (AW-OSEM) iterative reconstruction algorithm

using default parameters (4 iterations, 8 subsets, and a post-processing Gaussian kernel with a FWHM of 5 mm) on the multimodality workstation (Siemens Healthcare, Hoffman Estates, IL, USA).

II.D. Data analysis

The comparison of PET images corrected for attenuation using the 3 different techniques was performed using volume of interest (VOI)-based analysis. A nuclear medicine physician drew manually the VOIs on regions of normal physiologic uptake and also on areas of abnormally increased activity accumulation (lesions). The VOIs were defined on six regions in the lungs, liver, spleen, cerebellum, 2 bone tissues (cervical vertebrae 6 and dorsal vertebrae 5), aorta (as normal physiologic uptake) and malignant lesions. The differences between the attenuation correction techniques were quantified in terms of changes in the standard uptake value (SUV). The SUVs were calculated by dividing the activity concentration in each VOI by the injected activity divided by body weight (Eq. 1) [37]. For all defined VOIs, mean and max SUVs were measured to assess the strength of correlation between SUVs derived from PET-CTAC and PET-MRAC images separately for different organs and malignant lesions.

$$SUV_{mean(max)} = \frac{Mean(Max)\ VOI\ activity\ (MBq/ml)}{Injected\ dose\ (MBq)} \times \frac{Body\ weight\ (g)}{decay\ factor\ of\ F^{18}} \quad (1)$$

Of the 168 VOIs defined in normal physiologic regions, 146 VOIs were used for further evaluation whereas 22 VOIs were excluded owing to prevalent errors, such as misalignment, metal artefacts, patient movement, and segmentation errors. In addition, of the 35 VOIs defined on malignant lesions, 4 were excluded for subsequent statistical analysis due to the same aforementioned reasons. The number of malignant lesions varied only slightly between the patients (range: 2–4 lesions, mean = 3).

Relative errors between SUVs measured on PET-MRAC3c/PET-MRAC4c and PET-CTAC, used as reference, were computed for SUVmean(max) according to Eq. (2). Subsequently, the average and standard deviation (SD) of relative errors were calculated for each individual VOI over all patients. In addition, the relative error was calculated on a voxel-by-voxel basis to ease the comparative evaluation process.

$$Relative\ error\ (\%) = \frac{MRAC\ (SUV) - Reference\ (SUV)}{Reference\ (SUV)} \times 100\% \quad (2)$$

The Shapiro-Wilk test was used to examine null hypothesis that measured SUVs follow a normally distributed population and the calculated p-values were reported for each individual VOI. Furthermore, the Spearman rank correlation coefficient (ρ) was calculated to assess the correlation between SUVs measured on both PET-MRAC images and PET-CTAC according to Eq. (3).

$$\rho = \frac{\sum_i (M_i - \bar{M})(C_i - \bar{C})}{\sqrt{\sum_i (M_i - \bar{M})^2\ (C_i - \bar{C})^2}} \quad (3)$$

Where M and C are measured SUVs on PET-MRAC and PET-CTAC, respectively, and i is the VOI number. Bland and Altman analysis [38] was used to determine the concordance between SUVs measured on both attenuation corrected images by plotting PET-MRAC against PET-CTAC. Linear mixed models with a random effect on patients for non-normal distributed samples of clustered data were used to calculate the relative difference between SUVs from PET/MR and PET/CT in order to avoid bias from multiple lesions per patient [39-40]. The relative error might be high in regions with low tracer uptake, such as the lungs, whereas the absolute difference is quite insignificant. The absolute difference obtained by subtracting SUVs measured on PET-CTACs and PET-MRAC images were plotted for all organs and lesions.

III. Results

Visual inspection of PET/CT and PET/MR images of the 14 patients in terms of image quality, fusion accuracy, and lesions conspicuity was performed (Supplemental Fig. 1S). In the case of local mismatch or severe effect of deep breathing motion, the VOIs in the vicinity of the mismatch were excluded from further analysis. Three patients were affected by local mismatch in the cerebellum, lungs and liver region and one patient presented with deep breathing motion. VOIs located in the vicinity of the misaligned regions were excluded from analysis. Dental fillings and implants degraded image quality on both PET-CTAC and PET-MRAC images in 8 and 6 patients, respectively, and the ensuing metal artefacts impaired PET quantification, thus leading to considerable changes of tracer uptake (Fig. 1).

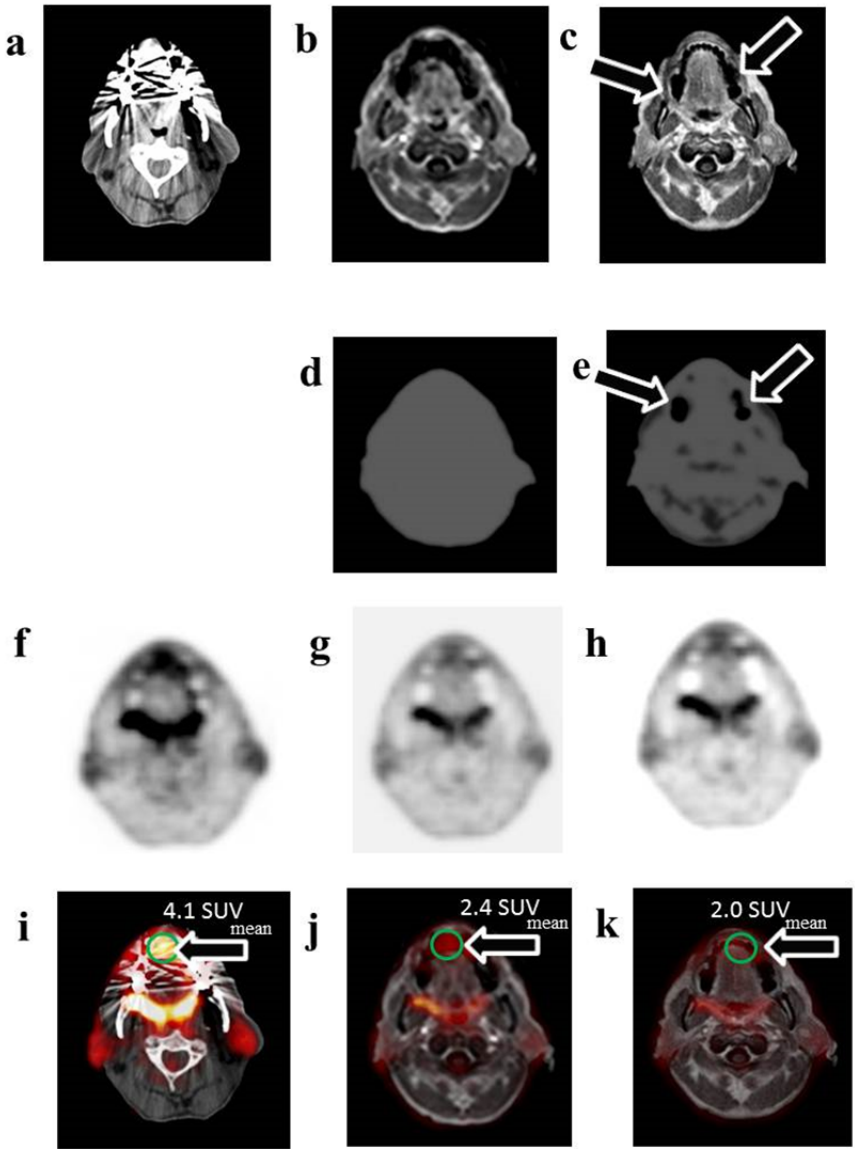

Figure 1. Representative artefacts on PET-CTAC and PET-MRAC images due to the presence of metallic dental implants and their impact on SUV measurements in a patient with a squamous cell carcinoma of the retromolar trigone but no lesion in the floor of the mouth. (A) CT, (B) atMR, (C) Dixon, (D) MRAC3c, (E) MRAC4c, (F) PET-CTAC, (G) PET-MRAC3c, and (H) PET-MRAC4c, (I) fusion of PET-CTAC and CT, (J) fusion of PET-MRAC3c and atMR, (K) fusion of PET-MRAC4c and Dixon. Note that a lesion with high metabolism appears to be present in the floor of the mouth on PET-CT whereas no lesion is seen on PET-MR.

The procedure used to generate the 3-class attenuation map disregards air gaps and areas with no MR signal inside the body which generates an attenuation map where air gaps are filled with soft-tissue (Fig. 1d). On the other hand, the procedure followed to generate the 4-class attenuation map takes air gaps into account; however, MR image degradation due to the presence of metal implants may affect the 4-class attenuation map in most cases as shown in Fig. 1e. Table 1 summarizes the relative errors for SUVmean between PET-MRAC3c/PET-MRAC4c and PET-CTAC images. The statistical significance (p-value) of the Shapiro-Wilk test was also calculated for each VOI (statistical significance level at 0.05).

The relative SUVmean error for VOIs averaged over all organs (considering the 6 VOIs in the lungs as one VOI) is -12±10.7% for PET-MRAC3c and -19.0±7.8% for PET-MRAC4c. Similarly, Fig. 3 shows the relative error between SUVmax estimated using PET images corrected by MRAC3c and MRAC4c compared to the PET-CTAC for different organs. Table 2 provides a summary of these results. The relative SUVmax error for VOIs averaged over all body regions is -9.1±9.6% and -18.4±8.0% for PET-MRAC3c and PET-MRAC4c, respectively.

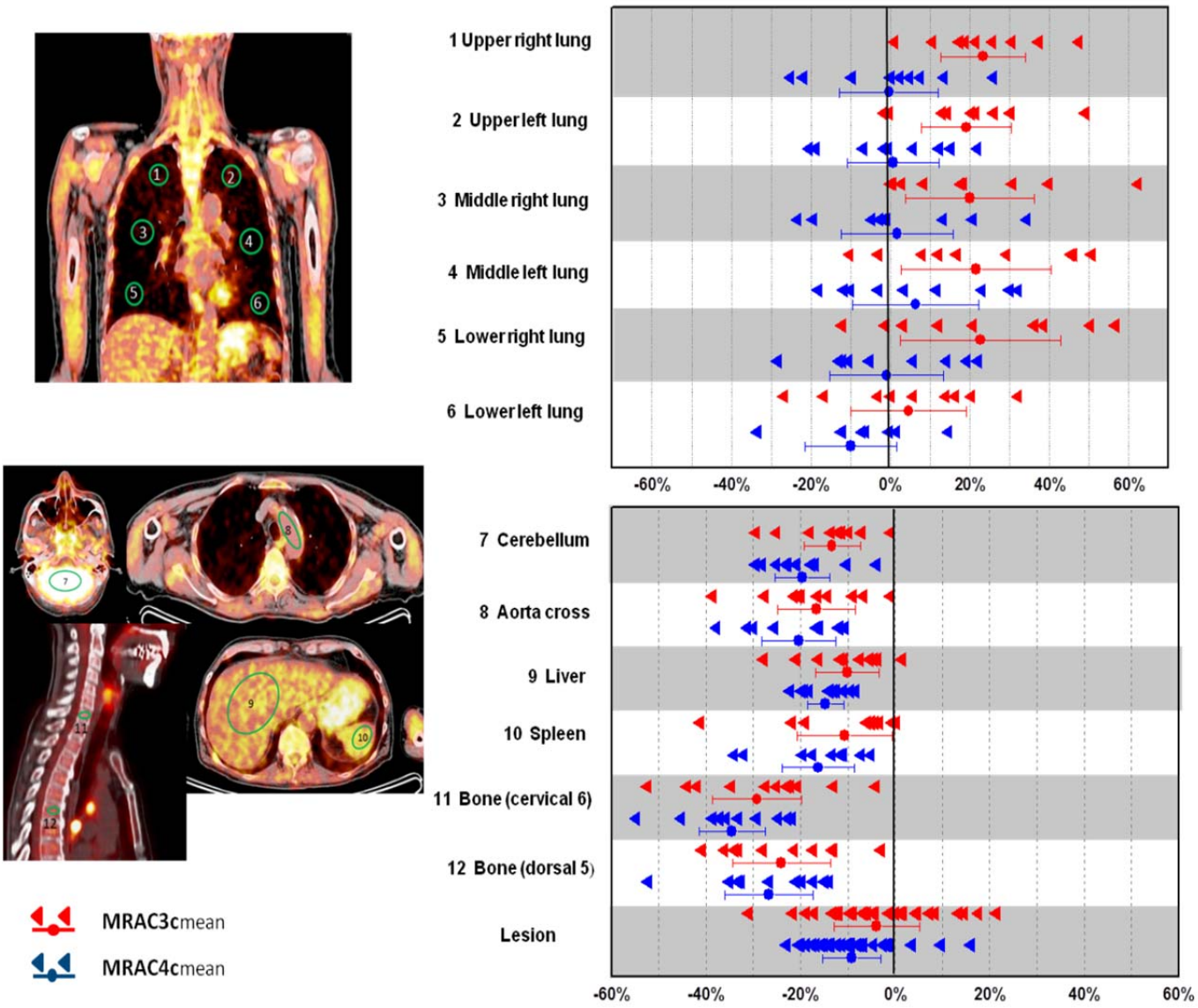

Figure 2. Relative errors between SUVmean estimated using PET images corrected for attenuation using three- (PET-MRAC3c) and four-class (PET-MRAC4c) based MR-guided attenuation correction compared to CT-based attenuation correction (PET-CTAC) for different organs. The dot point and line bar indicate the mean and standard deviation of the results, respectively.

Table 1. Relative errors between SUV_{mean} estimated using PET images corrected for attenuation using three- (MRAC3c) and four-class (MRAC4c) based MR-guided attenuation correction compared to CT-based attenuation correction (CTAC). Shapiro-Wilk test P-value<0.05 are considered statistically significant.

Region	$MRAC3c_{mean}$	P-value	$MRAC4c_{mean}$	P-value
Upper right lung	23.3±10.6	<0.01	-00.4±12.4	0.24
Upper left lung	19.1±11.4	<0.01	00.7±11.6	0.33
Middle right lung	20.0±16.1	<0.01	01.7±14.0	0.29
Middle left lung	21.5±18.9	0.02	06.3±15.8	0.45
Lower right lung	22.6±20.2	0.02	-01.0±14.4	0.21
Lower left lung	04.6±14.5	0.49	-10.0±11.5	0.06
Cerebellum	-13.4±06.0	<0.01	-19.6±05.8	<0.01
Aorta cross	-16.6±08.2	<0.01	-20.4±07.9	<0.01
Liver	-10.2±06.7	<0.01	-14.7±03.4	<0.01
Spleen	-10.7±10.0	0.01	-16.3±07.6	<0.01
Bone (cervical 6)	-29.3±09.4	<0.01	-34.5±07.0	<0.01
Bone (dorsal 5)	-24.1±10.4	<0.01	-26.7±09.3	<0.01
Lesions	-03.9±09.0	0.01	-09.2±06.1	<0.01

Table 2. Relative errors between SUV_{max} estimated using PET images corrected for attenuation using three- (MRAC3c) and four-class (MRAC4c) based MR-guided attenuation correction compared to CT-based attenuation correction (CTAC). Shapiro-Wilk test P-values<0.05 are considered statistically significant.

Region	$MRAC3c_{max}$	P-value	$MRAC4c_{max}$	P-value
Upper right lung	35.3±11.2	<0.01	-02.0±09.6	0.17
Upper left lung	12.9±10.2	<0.01	-04.1±09.8	0.09
Middle right lung	17.6±15.0	<0.01	-00.6±13.5	0.17
Middle left lung	18.5±15.4	0.02	04.5±11.8	0.46
Lower right lung	19.2±15.0	0.01	-04.6±12.1	0.13
Lower left lung	05.9±17.7	0.34	-09.8±13.1	0.07
Cerebellum	-11.5±05.6	<0.01	-17.8±05.5	<0.01
Aorta cross	-10.1±09.8	0.01	-18.6±06.0	<0.01
Liver	-05.8±08.7	0.11	-15.3±07.5	<0.01
Spleen	-06.6±10.8	0.1	-15.7±08.4	<0.01
Bone (cervical 6)	-25.8±07.9	<0.01	-31.8±06.7	<0.01
Bone (dorsal 5)	-22.0±10.4	<0.01	-26.6±8.8	<0.01
Lesions	-03.3±08.0	0.01	-09.0±06.0	<0.01

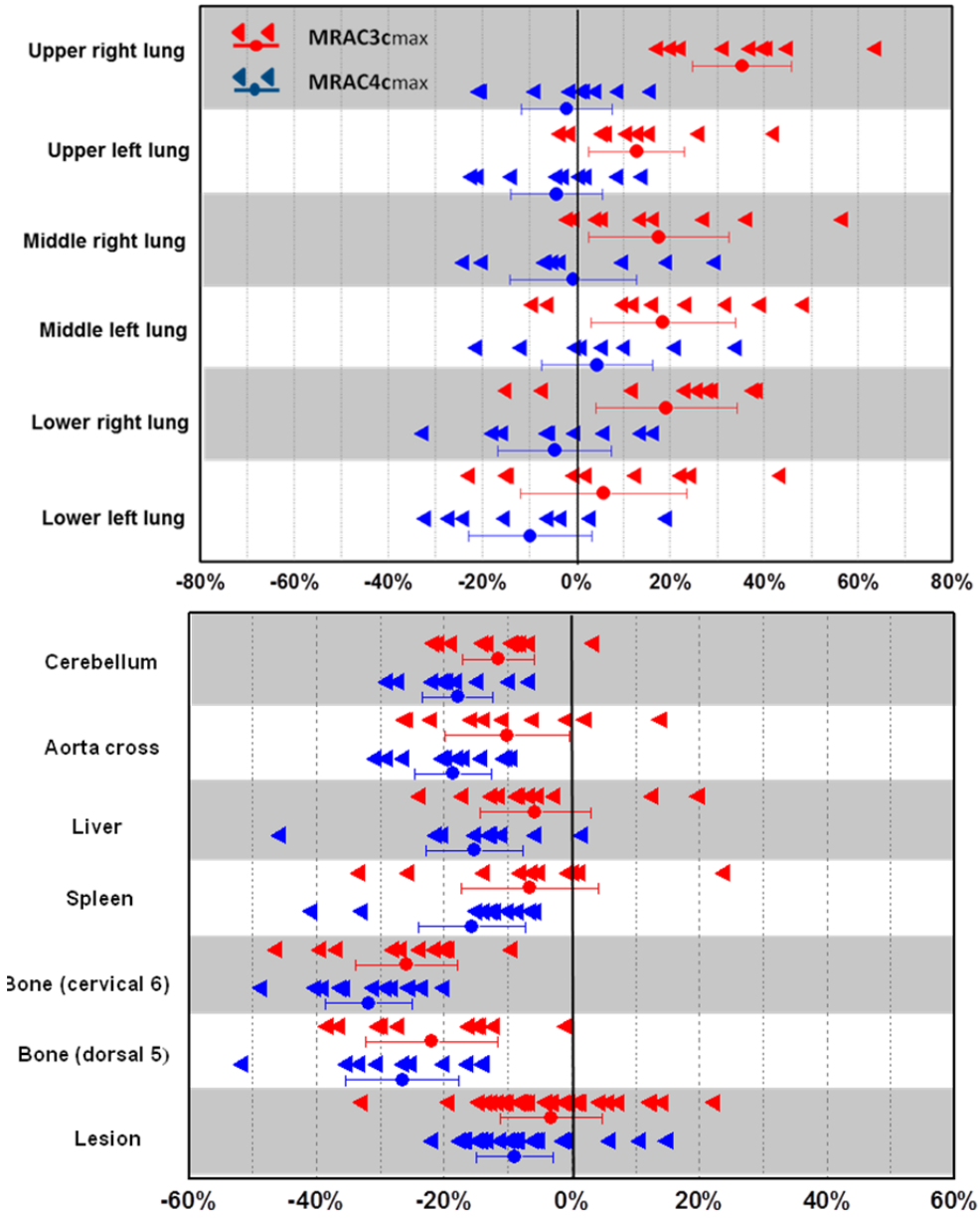

Figure 3. Relative errors between SUVmax estimated using PET images corrected for attenuation using three- (PET-MRAC3c) and four-class (PET-MRAC4c) based MR-guided attenuation correction compared to CT-based attenuation correction (PET-CTAC) for various organs. The dot point and line bar indicate the mean and standard deviation of the results, respectively.

Figs. 4 and 5 show regression plots and Spearman's correlation analysis between SUVmean/SUVmax for different organs and malignant focal uptake estimated using both MRI-guided attenuation correction techniques and the CT-based attenuation correction technique. The Spearman's correlation coefficient for SUVmean metric is equal to 0.97 for both PET-MRAC3c and PET-MRAC4c in normal uptake regions and 0.95 and 0.96 for malignant lesions, respectively.

Bland and Altman concordance analysis for SUVmean and SUVmax corresponding to normal physiologic uptake and malignant focal uptake measured on PET-MRAC3c and PET-MRAC4c are shown in Figs. 6 and 7. The limit of agreement and systematic bias (average difference) are presented in the plot.

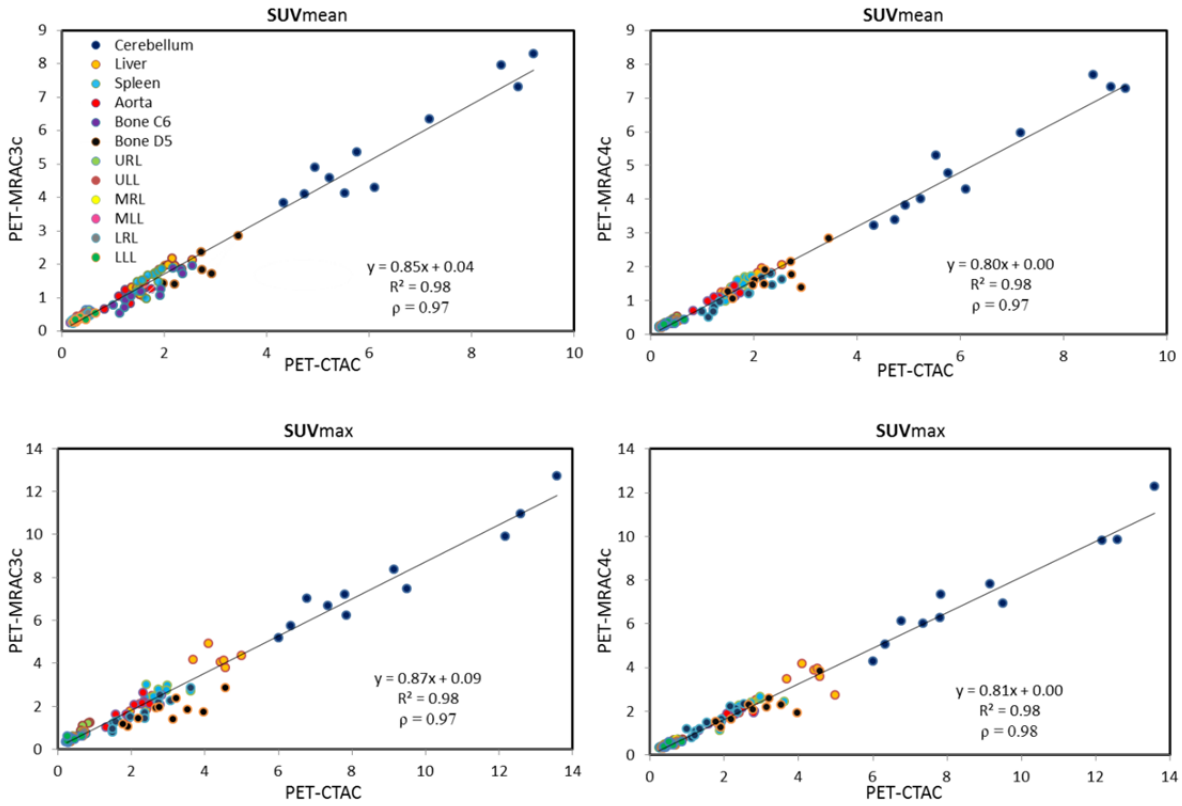

Figure 4. Regression plots between SUVmean/SUVmax estimated using images corrected for attenuation using three- (PET-MRAC3c) and four-class (PET-MRAC4c) based MR-guided attenuation correction and CT-based attenuation correction (PET-CTAC) for various organs.

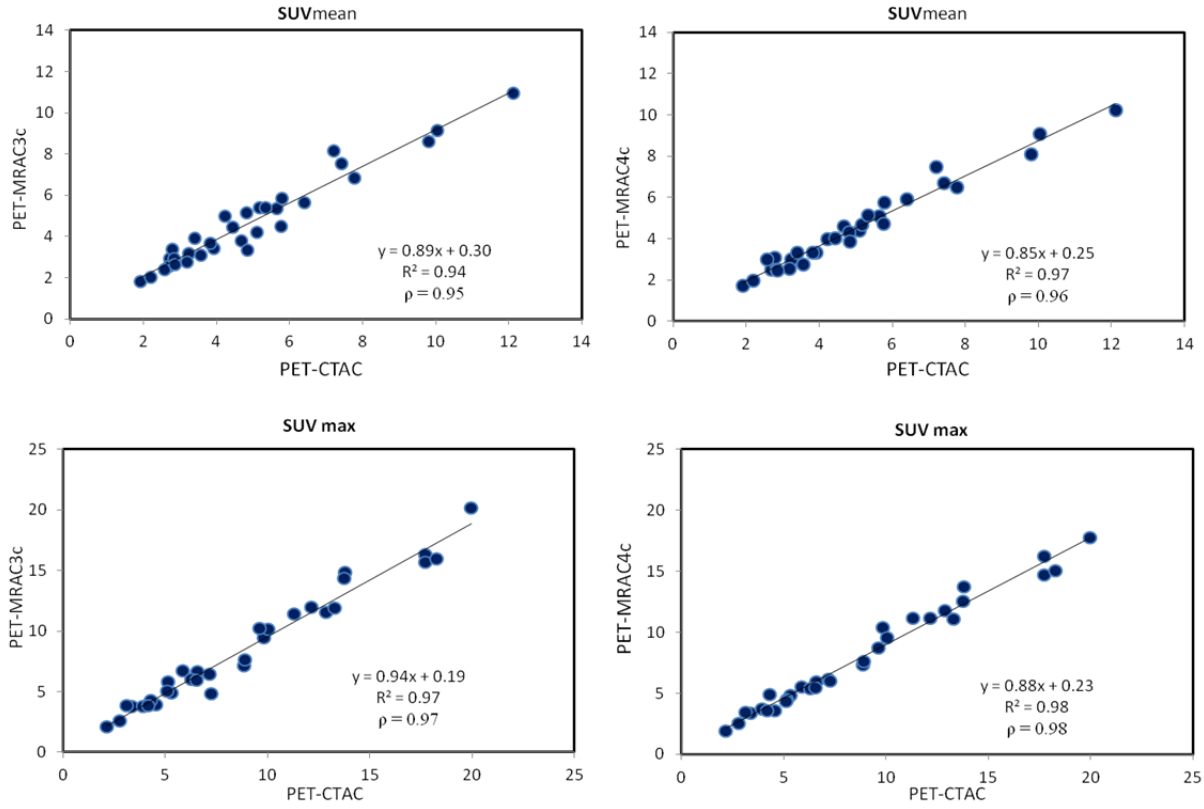

Figure 5. Regression plots between SUVmean/SUVmax estimated using images corrected for attenuation using three- (PET-MRAC3c) and four-class (PET-MRAC4c) based MR-guided attenuation correction and CT-based attenuation correction (PET-CTAC) for malignant lesions.

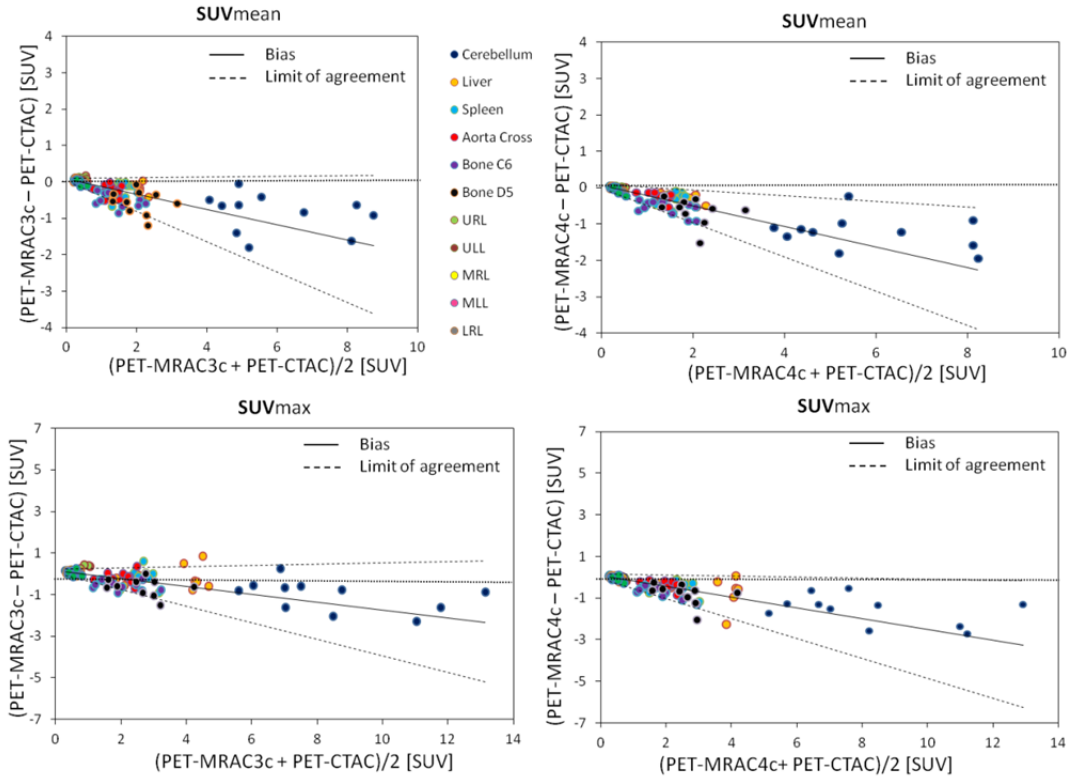

Figure 6. Bland Altman plots of SUVmean/SUVmax measurement for various organs between PET-MRAC3c/PET-MRAC4c and PET-CTAC. Bias and limits of agreements are indicated taking into account the relative systematic SUV underestimation. The oblique lines represent results of regression analysis performed on stepwise curves obtained for individual organs.

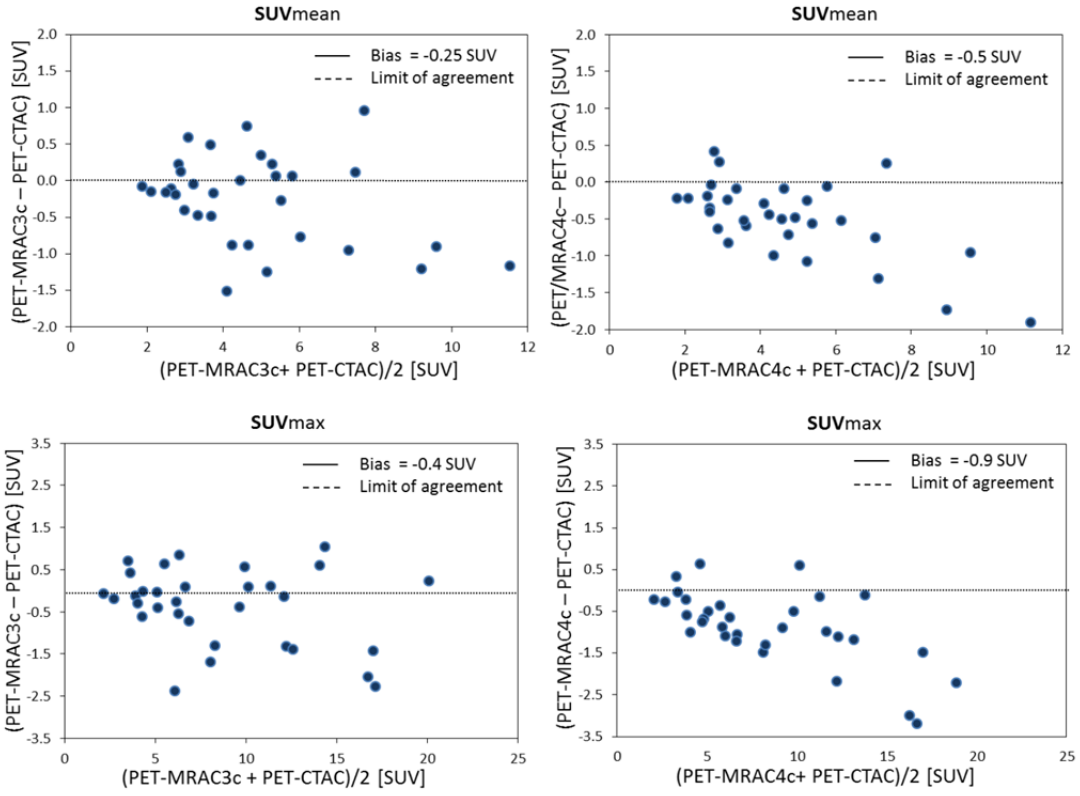

Figure 7. Bland Altman plots of SUVmean/SUVmax measurement for malignant lesions between PET-MRAC3c/PET-MRAC4c and PET-CTAC. Bias and limits of agreements are indicated taking into account the relative systematic SUV underestimation.

IV. Discussion

The 3-class attenuation map discards the air gaps in the inner body and assumes them to be soft-tissue (Fig. 8b top and bottom) whereas the 4-class attenuation map, as implemented in this work, considers the air gaps (Fig. 8c top and bottom). This resulted in noticeable local SUV differences. For instance, the local SUV in the sinus cavities area is 1.4 on PET-MRAC3c, 0.6 SUV on PET-MRAC4c and 0.8 SUV on PET-CTAC (Fig. 8 (top)). Similarly, in Fig. 8 (bottom), the local SUV in the air pocket within the abdomen is 1.42, 0.32 and 0.41 for PET-MRAC3c, PET-MRAC4c and PET-CTAC, respectively. Since the approach used to generate the 3-class attenuation map fills the region located inside the external body contour with soft-tissue, in contrast to the 4-class attenuation map, it is less sensitive to dental filling and metal implant related artifacts (Fig. 2d). Although neglecting air cavities in the inner body might result in considerable local SUV bias, filling the inner body void regions with soft-tissue leads to more accurate attenuation maps in the presence of metal artifacts on MR images which might affect SUV measurements in PET-MR [41].

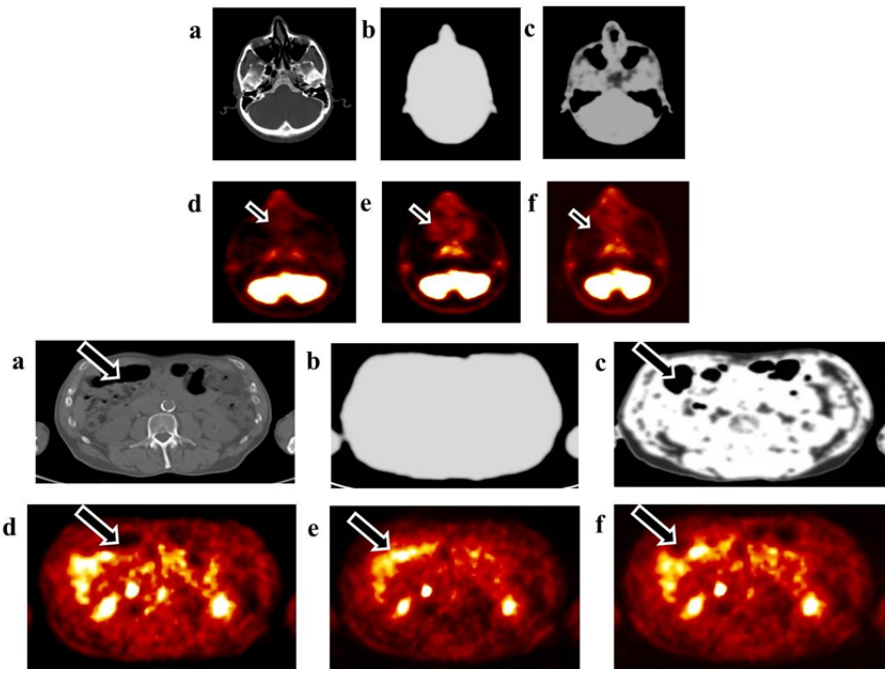

Figure 8. Representative slice showing the impact of neglecting sinus air cavities (top) and air pockets in the abdomen (bottom) in the 3-class attenuation map. (A) CT, (B) MRAC3c attenuation map, (C) MRAC4c attenuation map, (D) PET-CTAC, (E) PET-MRAC3c, and (F) PET-MRAC4c. SUVs measured in sinus cavities and air pockets are 0.80 and 0.41 SUVmean on PET-CTAC, 1.40 and 1.42 SUVmean on PET-MRAC3c, and 0.60 and 0.32 SUVmean on PET-MRAC4c, respectively.

Overall, the relative error for SUVmean in VOIs defined in normal physiologic uptake, except the lungs (figures 3 and 4 and tables 1 and 2), is smaller in the 3-class compared to the 4-class attenuation correction technique. The average error for all organs except the lungs is -17.4±8.46% and -22.0±6.8% for PET-MRAC3c and PET-MRAC4c, respectively. The negative bias observed in the liver, cerebellum and bony regions is consistent with what was reported by Ouyang et al. (-7.4±3.4% for liver and -15.4±10.5% for bone) [22], Schramm et al. (-5±10% for liver) [21], Kim et al. (-12% for liver and -18% for bone) [42] and Hofmann et al. (-30% for bone) [14]. Ouyang et al. reported a 5.6% positive bias in the liver when using a 4-class attenuation map which is inconsistent with our observations. This discrepancy likely stems from the higher soft-tissue attenuation coefficient (1.004 cm-1) used in the above referenced work. The relative error in bony structures was more severe (tables 1 and 2), resulting in over 30% bias owing to neglecting bone in the attenuation correction map [25]. However, the influence of neglecting bone was higher on PET-MRAC4c since bone was mostly replaced with fat tissue owing to partial volume effect in the bone marrow. Our data are in accordance to recently published results which have shown that MRI-guided attenuation mainly underestimates SUV values in areas close to large bony structures [22, 43].

The 3-class technique resulted in a mean relative error of 18.6±15.3% for all VOIs in the lungs while the 4-class method yielded an average error of -0.45±13.3% for SUVmean. Ouyang et al. [22] observed a positive uptake bias in the lungs for the 3-class attenuation map (5.8±14.6%) while Martinez-Moller et al. [11] reported -1.8% bias for the 4-class attenuation map. Since the attenuation coefficients assigned to the lung are 0.022 cm-1 and 0.018 cm-1 in the 3-class and 4-class approaches, respectively, it can be deduced that an attenuation coefficient of 0.018 cm-1 (4-class) approximates better attenuation of the lungs at least for our patients. The Shapiro-Wilk test revealed that the null hypothesis of the test was rejected for all but lower left VOIs in the lung for MRAC3cmean, whereas it was not rejected for the entire lung VOIs for MRAC4cmean. The same trend is observed for SUVmax (table 2) where the null hypothesis was not rejected for MRAC4cmean in the lung region. The standard deviation for both techniques in the lung region was approximately similar which indicates comparable correlation strength with mean values. The density of the lungs varies between patients due to respiratory motion, smoking habits or age [44]. The 3-class and 4-class attenuation correction techniques resulted in -3.9% and -9.2% relative errors for malignant lesions (Fig. 2), respectively. Since most patients included in this study protocol had lesions located in the head and neck region, the characteristics of the bias for lesions follow a similar trend to VOIs located outside the lungs where neglecting bony structures caused underestimation of tracer uptake. None of the patients had lesions in the lungs. Since a positive bias was obtained for VOIs located in the lungs when using PET-MRAC3c whereas a small negative bias was obtained for PET-MRAC4c, the bias for lesions located in the lungs might be different between these two attenuation correction techniques. The Shapiro-Wilk test (Tables 1 and 2) demonstrates that the null hypothesis was rejected for lesions and normal physiologic regions (except the lungs), whereas, the p-values are not statistically significant for the liver and spleen when using MRAC3cmax.

The relative errors for VOIs defined in the lungs were considerably high (tables 1 and 2); however, the absolute differences indicate insignificant errors for both PET-MRAC3c and PET-MRAC4c (Supplemental Figs. 2S-4S). The average absolute SUV differences for all VOIs in the lung region are 0.05 and 0.02 for SUVmean, while they are -0.08 and -0.03 for SUVmax for PET-MRAC3c and PET-MRAC4c, respectively. This is due to the low tracer uptake in the lungs and the noise associated with image reconstruction in low count regions [14]. The maximum absolute difference for VOIs defined in regions of normal physiologic uptake occurred in the cerebellum for both PET-MRAC3c and PET-MRAC4c. A plausible explanation of this negative bias might be that the thickness and density of ignored bony structures (skull) around the cerebellum is significantly higher than in other organs. The same observations were made by Bezrukov et al. [9] and Ouyang et al. [22] reporting a negative SUV bias of up to -12% near bony regions. In contrast, Schramm et al. [21] reported 12% SUV bias in the cerebellum. The average absolute errors for lesions are 0.25 and 0.5 (maximum -2.4) for SUVmean, while they are 0.4 and 0.86 (maximum -3.2) for SUVmax for PET-MRAC3c and PET-MRAC4c, respectively. The lesion located near bony structures resulted in a higher absolute error particularly when using the 4-class attenuation map owing to the misclassification of bone marrow as fat.

The high Spearman's correlation coefficient (ρ=0.97 for both techniques) indicates a statistically significant relationship between SUVs measured on PET-MRAC3c/PET-MRAC4c and PET-CTAC (Fig. 4). However, it should be noted that a significant nonzero correlation coefficient does not imply that these attenuation correction approaches are concordant, since the probability that they deviate from each other remains even in case of strong correlation . Consequently, Bland and Altman analysis was performed to depict by how much the SUVs measured on PET images corrected for attenuation using both approaches are likely to deviate from the SUVs measured on PET-CTAC. Bland and Altman plots indicate that the systematic bias was higher on PET-MRAC3c than PET-MRAC4c for normal physiologic uptake (except the lungs) while SUVmax had lower bias than SUVmean. The systematic bias was higher on PET-MRAC4c than PET-MRAC3c for malignant lesions. It worth mentioning that, in accordance to data published by previous investigators [5], the change in SUV measurements depends on their absolute values. That is, the higher the SUVs, the higher the absolute difference between SUVs measured on PET-MRAC and PET-CTAC images.

V. Conclusion

In this work, we evaluate the quantitative accuracy of the 3-class and 4-class attenuation correction techniques used on hybrid PET/MRI systems. Overall, the quantitative analysis revealed significant underestimation of SUVs in organs presenting with normal physiologic uptake (except the lungs) and malignant lesions by both

PET-MRAC3c and PET-MRAC4c as compared to PET-CTAC. The 3-class technique resulted in overestimation of tracer uptake in the lung whereas the 4-class approach produced insignificant negative bias.This trend is explained by the different attenuation coefficients for lung tissue used by both attenuation correction techniques. The largest differences were observed in bony structures or near massive bones for both approaches. Despite the bias induced by both attenuation correction approaches, there is good correlation between SUVs measured on PET-MRAC images and PET-CTAC. Overall, it was observed that the 3-class attenuation map generates a lower systematic negative bias of tracer uptake; however, the attenuation coefficient assigned to the lung should be adapted. Regardless of the attenuation correction technique used, it is strongly recommended to check the attenuation map as part of the reading procedure for the presence of artifact, which might in some cases induce clinically relevant SUV changes, including metal artifacts, lung and body contour segmentation errors, and miss-alignment issues.

Acknowledgements

This work was supported by the Swiss National Science Foundation under grants SNSF 31003A-135576, SNFN 31003A-149957 and SNSF 320030_135728/1.

Supplementary Material

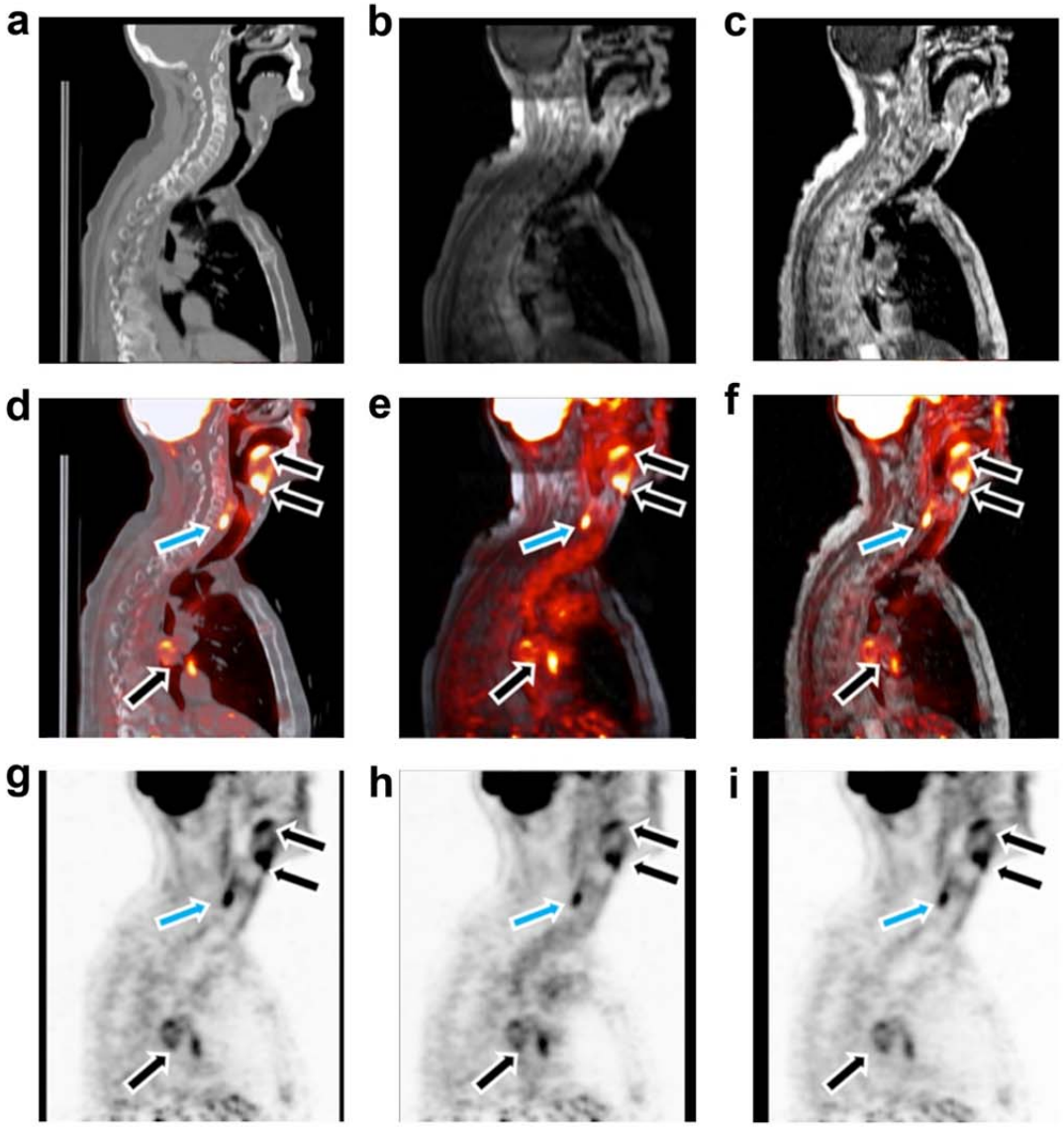

Figure 1S. Representative mid sagittal slice illustrating lesion conspicuity. (a) CT, (b) atMR, (c) in phase Dixon, (d) fusion of PET-CTAC and CT, (e) fusion of PET-MRAC3c and atMR, (f) fusion of PET-MRAC4c and in phase Dixon, (g) PET-CTAC, (h) PET-MRAC3c, and (i) PET-MRAC4c. Black arrows point at lesions with high tracer uptake (malignant lesions in the floor of the mouth and metastatic mediastinal lymph nodes). Blue arrows point at physiologic uptake in the cricopharyngeus muscle.

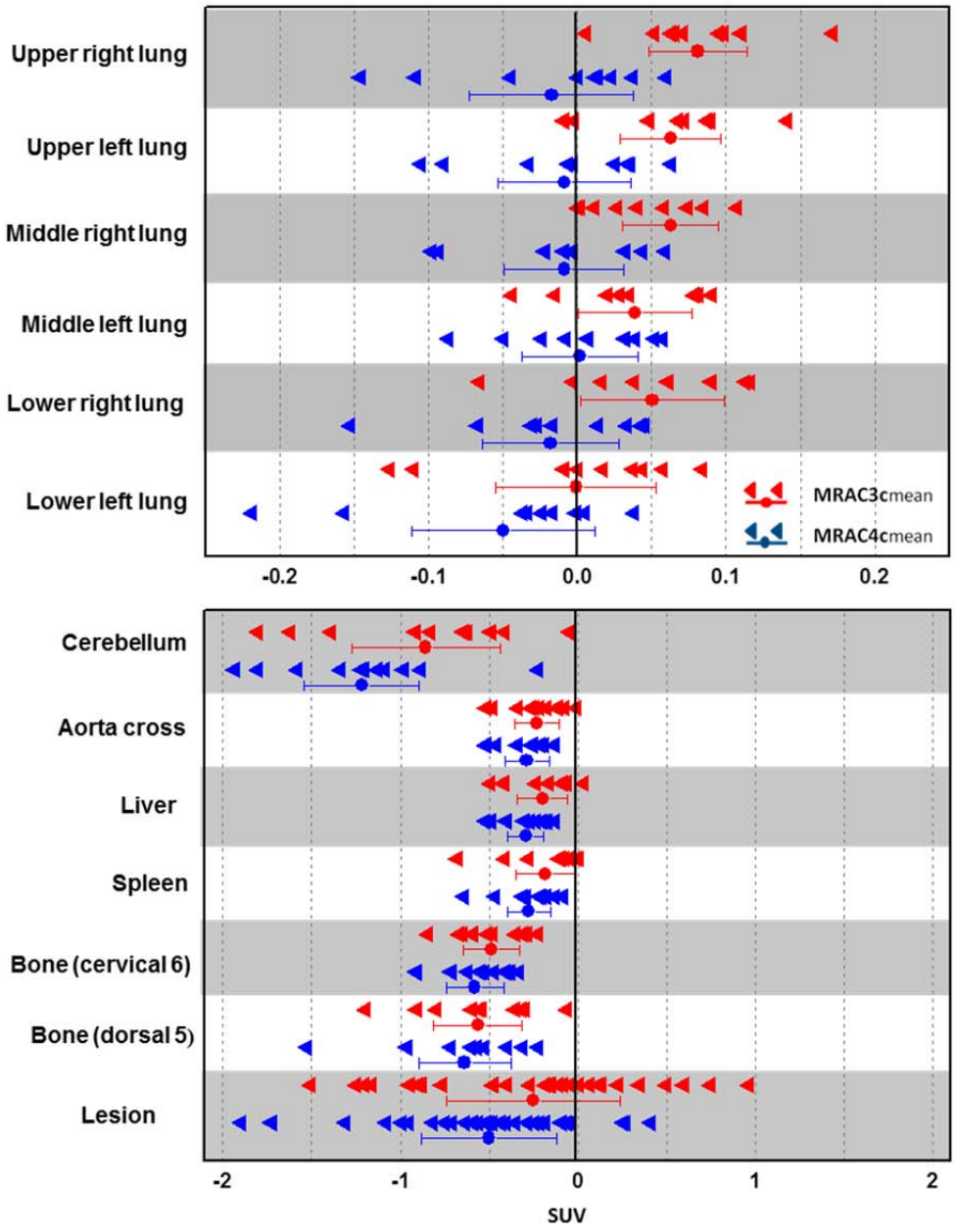

Figure 2S. Absolute errors between SUV_{mean} estimated using PET images corrected of attenuation using three- (PET-MRAC3c) and four-class (PET-MRAC4c) based MR-guided attenuation correction compared to CT-based attenuation correction (PET-CTAC) for different organs.

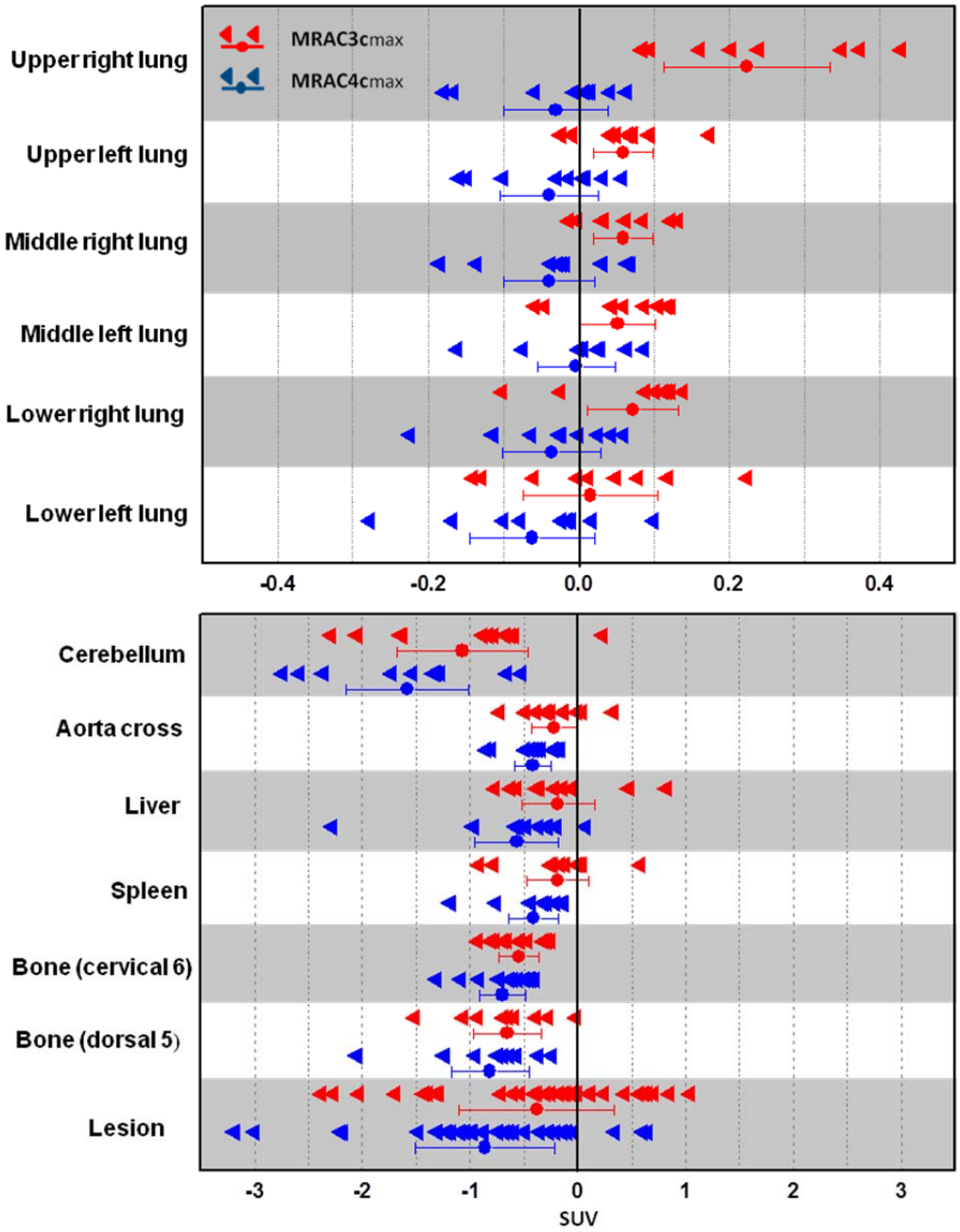

Figure 3S. Absolute errors between SUV_{max} estimated using PET images corrected of attenuation using three- (PET-MRAC3c) and four-class (PET-MRAC4c) based MR-guided attenuation correction compared to CT-based attenuation correction (PET-CTAC) for different organs.

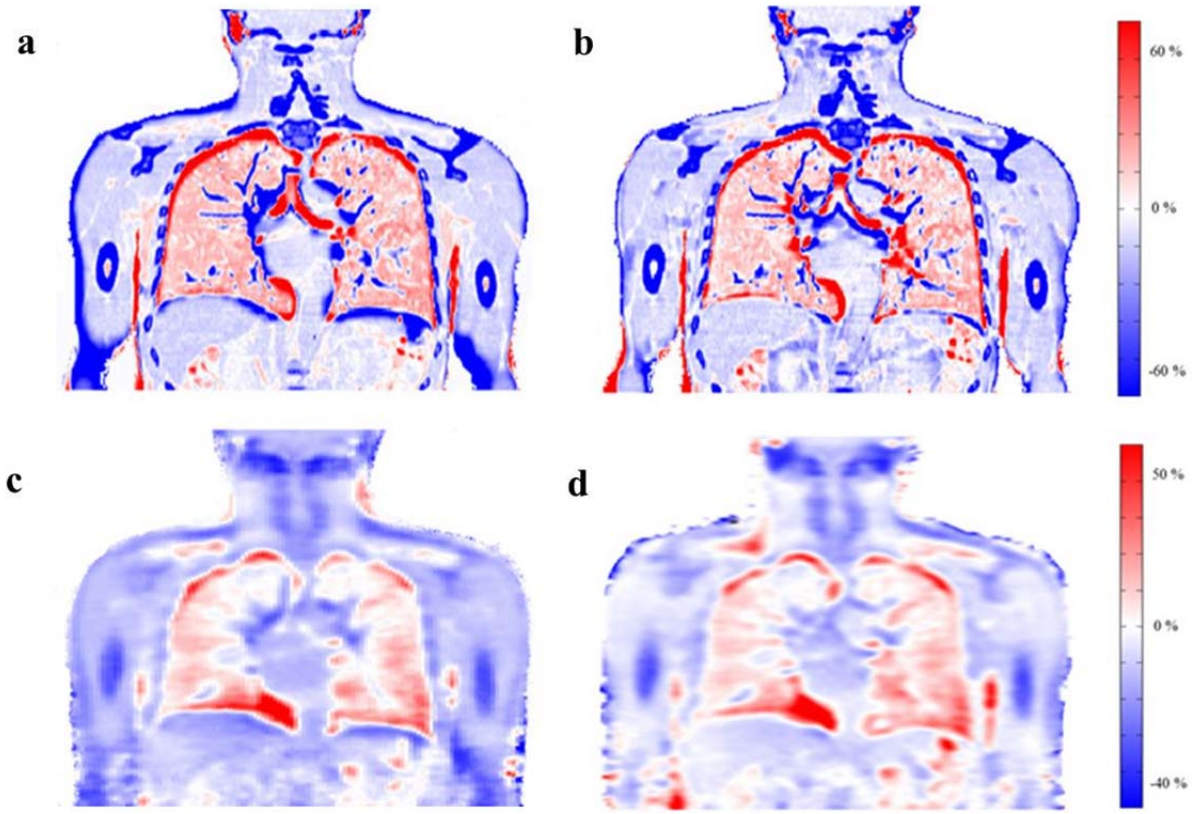

Figure S4. Difference images between CTAC and MRAC3c (a), and CTAC and MRAC4c (b) attenuation maps. Error maps (relative bias) between PET-CTAC and PET-MRAC3c (c), and PET-CTAC and PET-MRAC4c (d).

References

[1] M. S. Judenhofer, H. F. Wehrl, D. F. Newport, C. Catana, S. B. Siegel, M. Becker*, et al.*, "Simultaneous PET-MRI: a new approach for functional and morphological imaging.," *Nat Med,* vol. 14, pp. 459-465, Apr 2008.

[2] K. A. Zukotynski, F. H. Fahey, M. Kocak, A. Alavi, T. Z. Wong, S. T. Treves*, et al.*, "Evaluation of 18F-FDG PET and MRI associations in pediatric diffuse intrinsic brain stem glioma: a report from the Pediatric Brain Tumor Consortium.," *J Nucl Med,* vol. 52, pp. 188-195, Feb 2011.

[3] F. W. Hirsch, B. Sattler, I. Sorge, L. Kurch, A. Viehweger, L. Ritter*, et al.*, "PET/MR in children. Initial clinical experience in paediatric oncology using an integrated PET/MR scanner.," *Pediatr Radiol,* vol. 43, pp. 860-875, Jul 2013.

[4] H. Zaidi and A. Del Guerra, "An outlook on future design of hybrid PET/MRI systems.," *Med Phys,* vol. 38, pp. 5667-5689, 2011.

[5] A. Varoquaux, O. Rager, A. Poncet, B. M. Delattre, O. Ratib, C. D. Becker*, et al.*, "Detection and quantification of focal uptake in head and neck tumours: (18)F-FDG PET/MR versus PET/CT.," *Eur J Nucl Med Mol Imaging,* vol. 41, pp. 462-475, Mar 2014.

[6] M. Wiesmuller, H. H. Quick, B. Navalpakkam, M. M. Lell, M. Uder, P. Ritt*, et al.*, "Comparison of lesion detection and quantitation of tracer uptake between PET from a simultaneously acquiring whole-body PET/MR hybrid scanner and PET from PET/CT.," *Eur J Nucl Med Mol Imaging,* vol. 40, pp. 12-21, Jan 2013.

[7] M. Becker and H. Zaidi, "Imaging in head and neck squamous cell carcinoma: the potential role of PET/MRI.," *Br J Radiol,* p. 20130677, 2014.

[8] H. Zaidi, "Is MRI-guided attenuation correction a viable option for dual-modality PET/MR imaging?," *Radiology,* vol. 244, pp. 639-642, September 1, 2007 2007.

[9] I. Bezrukov, F. Mantlik, H. Schmidt, B. Scholkopf, and B. J. Pichler, "MR-based PET attenuation correction for PET/MR imaging.," *Semin Nucl Med,* vol. 43, pp. 45-59, Jan 2013.

[10] H. Zaidi, M.-L. Montandon, and D. O. Slosman, "Magnetic resonance imaging-guided attenuation and scatter corrections in three-dimensional brain positron emission tomography.," *Med Phys,* vol. 30, pp. 937-948, 2003.

[11] A. Martinez-Moller, M. Souvatzoglou, G. Delso, R. A. Bundschuh, C. Chefd'hotel, S. I. Ziegler*, et al.*, "Tissue classification as a potential approach for attenuation correction in whole-body PET/MRI: Evaluation with PET/CT data.," *J Nucl Med,* vol. 50, pp. 520-526, Apr 2009.

[12] V. Schulz, I. Torres-Espallardo, S. Renisch, Z. Hu, N. Ojha, P. Börnert*, et al.*, "Automatic, three-segment, MR-based attenuation correction for whole-body PET/MR data.," *Eur J Nucl Med Mol Imaging,* vol. 38, pp. 138-152, 2011.

[13] M.-L. Montandon and H. Zaidi, "Atlas-guided non-uniform attenuation correction in cerebral 3D PET imaging.," *Neuroimage,* vol. 25, pp. 278-286, 2005.

[14] M. Hofmann, I. Bezrukov, F. Mantlik, P. Aschoff, F. Steinke, T. Beyer*, et al.*, "MRI-based attenuation correction for whole-body PET/MRI: Quantitative evaluation of segmentation- and Atlas-based methods.," *J Nucl Med,* vol. 52, pp. 1392-1399, Sep 2011.

[15] C. Catana, A. van der Kouwe, T. Benner, C. J. Michel, M. Hamm, M. Fenchel*, et al.*, "Toward implementing an MRI-based PET attenuation-correction method for neurologic studies on the MR-PET brain prototype.," *J Nucl Med,* vol. 51, pp. 1431-1438, Sep 2010.

[16] V. Keereman, Y. Fierens, T. Broux, Y. De Deene, M. Lonneux, and S. Vandenberghe, "MRI-based attenuation correction for PET/MRI using ultrashort echo time sequences.," *J Nucl Med,* vol. 51, pp. 812-818, May 2010.

[17] Y. Berker, J. Franke, A. Salomon, M. Palmowski, H. C. Donker, Y. Temur*, et al.*, "MRI-based attenuation correction for hybrid PET/MRI systems: A 4-class tissue segmentation technique using a combined Ultrashort-Echo-Time/Dixon MRI sequence.," *J Nucl Med,* vol. 53, pp. 796-804, May 2012.

[18] A. Salomon, A. Goedicke, B. Schweizer, T. Aach, and V. Schulz, "Simultaneous reconstruction of activity and attenuation for PET/MR.," *IEEE Trans Med Imaging,* vol. 30, pp. 804-813, 2011.

[19] M. Defrise, A. Rezaei, and J. Nuyts, "Time-of-flight PET data determine the attenuation sinogram up to a constant.," *Phys Med Biol,* vol. 57, pp. 885-899, Feb 21 2012.

[20] A. Rezaei, M. Defrise, G. Bal, C. Michel, M. Conti, C. Watson*, et al.*, "Simultaneous reconstruction of activity and attenuation in time-of-flight PET.," *IEEE Trans Med Imaging,* p. *in press*, 2012.

[21] G. Schramm, J. Langner, F. Hofheinz, J. Petr, B. Beuthien-Baumann, I. Platzek*, et al.*, "Quantitative accuracy of attenuation correction in the Philips Ingenuity TF whole-body PET/MR system: a direct comparison with transmission-based attenuation correction.," *Magn Reson Mat Phys Biol Med,* vol. 26, pp. 115-126, 2013.

[22] J. Ouyang, S. Y. Chun, Y. Petibon, A. A. Bonab, N. Alpert, and G. El Fakhri, "Bias atlases for segmentation-based PET attenuation correction using PET-CT and MR.," *IEEE Trans Nucl Sci,* vol. 60, pp. 3373-3382, 2013.
[23] A. Samarin, C. Burger, S. D. Wollenweber, D. W. Crook, I. A. Burger, D. T. Schmid*, et al.*, "PET/MR imaging of bone lesions - implications for PET quantification from imperfect attenuation correction," *Eur J Nucl Med Mol Imaging,* vol. 39, pp. 1154-1160, Jul 2012.
[24] V. Keereman, R. V. Holen, P. Mollet, and S. Vandenberghe, "The effect of errors in segmented attenuation maps on PET quantification.," *Med Phys,* vol. 38, pp. 6010-6019, 2011.
[25] A. Akbarzadeh, M. R. Ay, A. Ahmadian, N. Riahi Alam, and H. Zaidi, "MRI-guided attenuation correction in whole-body PET/MR: assessment of the effect of bone attenuation.," *Ann Nucl Med,* vol. 27, pp. 152-162, Feb 2013.
[26] N. Burgos, M. J. Cardoso, M. Modat, S. Pedemonte, J. Dickson, A. Barnes*, et al.*, "Attenuation correction synthesis for hybrid PET-MR scanners.," *Med Image Comput Comput Assist Interv,* vol. 16, pp. 147-154, 2013.
[27] H. Zaidi, N. Ojha, M. Morich, J. Griesmer, Z. Hu, P. Maniawski*, et al.*, "Design and performance evaluation of a whole-body Ingenuity TF PET-MRI system.," *Phys Med Biol,* vol. 56, pp. 3091-3106, Apr 20 2011.
[28] W. T. Dixon, "Simple proton spectroscopic imaging.," *Radiology,* vol. 153, pp. 189-194, Oct 1984.
[29] G. Delso, S. Furst, B. Jakoby, R. Ladebeck, C. Ganter, S. G. Nekolla*, et al.*, "Performance measurements of the Siemens mMR integrated whole-body PET/MR scanner.," *J Nucl Med,* vol. 52, pp. 1914-1922, Dec 2011.
[30] M. Eiber, A. Martinez-Moller, M. Souvatzoglou, E. Rummeny, M. Schwaiger, A. Beer*, et al.*, "Value of a Dixon based MR-PET attenuation correction sequence for the localization and evaluation of PET positive lesions.," *J Nucl Med,* vol. 52, p. 105, May 1, 2011 2011.
[31] S. Klein, M. Staring, K. Murphy, M. A. Viergever, and J. P. W. Pluim, "elastix: A toolbox for intensity-based medical image registration.," *IEEE Trans Med Imaging,* vol. 29, pp. 196-205, 2010.
[32] A. Akbarzadeh, D. Gutierrez, A. Baskin, M. R. Ay, A. Ahmadian, N. Riahi Alam*, et al.*, "Evaluation of whole-body MR to CT deformable image registration.," *J Appl Clin Med Phys,* vol. 14, pp. 238-253, 2013.
[33] Z. Hu, N. Ojha, S. Renisch, V. Schulz, I. Torres, D. Pal*, et al.*, "MR-based attenuation correction for a whole-body sequential PET/MR system," in *IEEE Nuclear Science Symposium & Medical Imaging Conference*, 25-31 October 2009, Orlando (FL), USA, 2009, pp. 3508-3512.
[34] M. Kass, A. Witkin, and D. Terzopoulos, "Snakes: active contour models.," *Int J Comput Vision,* vol. 1, pp. 321-331, 1988.
[35] P. A. Yushkevich, J. Piven, H. C. Hazlett, R. G. Smith, S. Ho, J. C. Gee*, et al.*, "User-guided 3D active contour segmentation of anatomical structures: significantly improved efficiency and reliability.," *Neuroimage,* vol. 31, pp. 1116-1128, Jul 1 2006.
[36] N. Otsu, "A threshold selection method from gray-level histograms.," *IEEE Trans Sys Man Cyber,* vol. 9, pp. 62-66, 1979.
[37] S. C. Huang, "Anatomy of SUV. Standardized uptake value," *Nucl Med Biol,* vol. 27, pp. 643-646, Oct 2000.
[38] J. M. Bland and D. G. Altman, "Statistical methods for assessing agreement between two methods of clinical measurement.," *Lancet,* vol. 1, pp. 307-310, Feb 8 1986.
[39] M. Gönen, K. S. Panageas, and S. M. Larson, "Statistical Issues in Analysis of Diagnostic Imaging Experiments with Multiple Observations per Patient1," *Radiology,* vol. 221, pp. 763-767, December 1, 2001 2001.
[40] S. Galbraith, J. A. Daniel, and B. Vissel, "A Study of Clustered Data and Approaches to Its Analysis," *The Journal of Neuroscience,* vol. 30, pp. 10601-10608, August 11, 2010 2010.
[41] C. N. Ladefoged, F. L. Andersen, S. H. Keller, J. Lofgren, A. E. Hansen, S. Holm*, et al.*, "PET/MR imaging of the pelvis in the presence of endoprostheses: reducing image artifacts and increasing accuracy through inpainting.," *Eur J Nucl Med Mol Imaging,* vol. 40, pp. 594-601, Jan 8 2013.
[42] J. H. Kim, J. S. Lee, I. C. Song, and D. S. Lee, "Comparison of segmentation-based attenuation correction methods for PET/MRI: Evaluation of bone and liver standardized uptake value with oncologic PET/CT data.," *J Nucl Med,* vol. 53, pp. 1878-1882, Dec 2012.
[43] J. Bini, D. Izquierdo-Garcia, J. Mateo, J. Machac, J. Narula, V. Fuster*, et al.*, "Preclinical evaluation of MR attenuation correction versus CT attenuation correction on a sequential whole-body MR/PET scanner.," *Invest Radiol,* vol. 48, pp. 313-322, May 2013.
[44] K. Soejima, K. Yamaguchi, E. Kohda, K. Takeshita, Y. Ito, H. Mastubara*, et al.*, "Longitudinal follow-up study of smoking-induced lung density changes by high-resolution computed tomography.," *Am J Respir Crit Care Med,* vol. 161, pp. 1264-1273, Apr 2000.

Chapter 4

Magnetic resonance imaging-guided attenuation correction in whole-body PET/MRI using a sorted atlas approach

Hossein Arabi and Habib Zaidi

Medical Image Analysis, Vol. 31, No. July, pp 1-15 (2016)

Abstract

Purpose: Quantitative whole-body PET/MR imaging is challenged by the lack of accurate and robust strategies for attenuation correction. In this work, a new pseudo-CT generation approach, referred to as sorted atlas pseudo-CT (SAP), is proposed for accurate extraction of bones and estimation of lung attenuation properties.

Methods: This approach improves the Gaussian process regression (GPR) kernel proposed by Hofmann *et al.* which relies on the information provided by a co-registered atlas (CT and MRI) using a GPR kernel to predict the distribution of attenuation coefficients. Our approach uses two separate GPR kernels for lung and non-lung tissues. For non-lung tissues, the co-registered atlas dataset was sorted on the basis of local normalized cross-correlation similarity to the target MR image to select the most similar image in the atlas for each voxel. For lung tissue, the lung volume was incorporated in the GPR kernel taking advantage of the correlation between lung volume and corresponding attenuation properties to predict the attenuation coefficients of the lung. In the presence of pathological tissues in the lungs, the lesions are segmented on PET images corrected for attenuation using MRI-derived 3-class attenuation map followed by assignment of soft-tissue attenuation coefficient. The proposed algorithm was compared to other techniques reported in the literature including Hofmann's approach and the 3-class attenuation correction technique implemented on the Philips Ingenuity TF PET/MR where CT-based attenuation correction served as reference. Fourteen patients with head and neck cancer undergoing PET/CT and PET/MR examinations were used for quantitative analysis. SUV measurements were performed on 12 normal uptake regions as well as high uptake malignant regions. Moreover, a number of similarity measures were used to evaluate the accuracy of extracted bones.

Results: The Dice similarity metric revealed that the extracted bone improved from 0.58±0.09 to 0.65±0.07 when using the SAP technique compared to Hofmann's approach. This enabled to reduce the SUV_{mean} bias in bony structures for the SAP approach to -1.7±4.8% as compared to -7.3±6.0% and -27.4±10.1% when using Hofmann's approach and the 3-class attenuation map, respectively. Likewise, the 3-class attenuation map produces a relative absolute error of 21.7±11.8% in the lungs. This was reduced on average to 15.8±8.6% and 8.0±3.8% when using Hofmann's and SAP techniques, respectively.

Conclusion: The SAP technique resulted in better overall PET quantification accuracy than both Hofmann's and the 3-class approaches owing to the more accurate extraction of bones and better prediction of lung attenuation coefficients. Further improvement of the technique and reduction of the computational time are still required.

I. Introduction

There is growing research and clinical interest in hybrid PET/MRI technology owing to its potential to provide a major breakthrough in diagnostic imaging and clinical practice [1]. The rationale behind the combination of PET and MRI is the higher soft-tissue contrast of MR images compared to CT, the possibility of using various MRI sequences enabling multiparametric imaging and above all the absence of radiation exposure, a critical issue particularly in serial follow-up studies and paediatric imaging [2, 3].

Accurate quantification of tracer uptake requires correction for attenuation of annihilation photons, which is not straightforward on current PET/MRI systems that are not equipped with x-ray CT or transmission sources [4, 5]. Owing to the lack of a direct correspondence between MRI intensities and electron densities, alternative methods are sought for MRI-guided attenuation correction in PET/MRI. The strategies proposed for attenuation correction in PET/MRI can be classified into three major categories: tissue segmentation [6-8], template or atlas-based machine learning approaches [9-13], and joint estimation of emission and attenuation [14, 15]. Early attempts to estimate the attenuation map from non-time of flight (TOF) emission data [16] achieved limited success. The advent of TOF PET technology introduced new opportunities for accurate derivation of attenuation information from emission data. TOF enables to measure the detection time differences of the coincident annihilation photons with a temporal uncertainty governed by the timing resolution of the PET detectors, which narrows the solution space of PET reconstruction. Tissue segmentation methods rely on segmenting an MR image into a number of tissue classes followed by assignment of uniform linear attenuation coefficients. Atlas-based methods utilize target specific deformed datasets or an anatomical model to consider bones and produce a continuous attenuation map. In addition, machine learning approaches take advantage of the machine learning task of inferring a function from labelled training data consisting of a set of training examples containing voxel-by-voxel correspondence between MR and CT images to predict a continuous attenuation map.

Owing to the difficulties associated with bone segmentation, MRI segmentation into 3-classes on the Philips Ingenuity TF PET/MR (background air, lung and soft-tissue) [6, 17] or 4/5-classes on the Siemens mMR PET/MR (background air, lung, fat, mixture of fat and water, and water) [8, 18] are the most widely used strategies on commercial PET/MR systems. Although segmentation-based attenuation correction is deemed to provide satisfactory results in whole-body PET/MR, ignoring bone has noticeable impact on the quantification of tracer uptake in the vicinity of bony structures [10, 18-20]. Recently, a template-based attenuation correction technique which accounts for the presence of the skull in PET brain imaging was introduced on the SIGNA PET/MRI scanner (GE Healthcare, Waukesha, WI) [21]. The use of ultrashort echo time (UTE) [22] or zero time echo (ZTE) [23] sequences to distinguish between bony structures and air proved to be capable of addressing this challenge; however, its applications are currently limited to brain imaging owing to the long acquisition time. Alternatively, it was suggested that the use of a deformed atlas along with patient-specific MR images can overcome this limitation [9, 10, 12], particularly for whole-body imaging where long MR sequences are not feasible yet.

Hofmann et al. proposed a novel approach to merge the information obtained from patient-specific MR images and prior knowledge provided by an existing co-registered atlas dataset for the purpose of pseudo-CT generation [10]. In this approach, a Gaussian process regression (GPR) [24] is utilized to predict the pseudo-CT value for each voxel using intensity information of small patches defined on MR images and the corresponding CT numbers on the aligned atlas dataset. The performance of Hofmann's approach in terms of deriving bony structures depends highly on the accuracy of the registration with the atlas dataset. To increase the robustness of atlas-based methods to miss-registration errors, Burgos et al. developed synthetic CTs through a multi-atlas information propagation scheme where the MRI-derived patient's morphology is locally matched to the aligned MRI-CT pairs using a robust local image similarity measure based on local normalized cross-correlation (LNCC) criterion (Burgos et al., 2014). The local matching through morphological similarity enables the algorithm to find local matches and similar anatomy across the atlas dataset. Therefore, poorly matched atlases are discarded or at least given lower weights, which leads to a more patient-specific pseudo-CT. This method was mainly developed for brain PET/MR imaging and was therefore evaluated for this particular application. One of our objectives in this work is to modify Hofmann's pseudo-CT generation approach in order to improve the accuracy of bone extraction and reduce potential errors due to the miss-registration typical in whole-body imaging situations.

The bottleneck of atlas-based segmentation and attenuation correction in whole-body PET/MRI is the level of accuracy achieved by the registration procedure for inter-subject image alignment. Regardless of the type of algorithm, the validation of image registration algorithms depends on the geometry of both target and source images. Introducing a thorough concept that guarantees the accuracy of the registration procedure in non-rigid organs proved to be a difficult task [25]. In this work, we relied on a registration procedure validated in a previous work by our group [26] using the elastix software [27]. The alignment was performed by combining rigid and non-rigid registration based on normalized mutual information criterion using B-spline interpolator with an adaptive stochastic gradient descent optimizer.

Another challenging issue in whole-body PET/MR attenuation correction is the prediction of patient-specific attenuation coefficients for the lung. The density of the lungs might vary between patients owing to respiratory motion [28], smoking habits, age or disease state [29]. As a consequence, large SUV bias and substantial patient to patient activity recovery variations were reported in the literature [10]. Izquierdo-Garcia et al. reported more than 20% underestimation of SUV in the lung region and noticeable lung density variation from patient to patient (even from left to right lung in the same patient) [13]. To address this issue, Marshall et al. used linear regression to correlate the intensity of the lungs in specific MR sequences (T2 weighted and extrapolated proton density images) and corresponding CT values [30]. Berker et al. used maximum likelihood reconstruction of attenuation and activity for the estimation of lung attenuation coefficients from time-of-flight (TOF) PET emission data [31]. A more stable solution was achieved by exploiting a regularized MLAA algorithm for estimation of lung linear attenuation coefficients using prior knowledge on the Gaussian distribution of lung attenuation coefficients [32].

The second major objective of this work is to propose an improved machine learning approach based on GPR for patient-specific prediction of lung attenuation coefficients. The technique incorporates the correlation between lung volume and corresponding density and advantages of morphological similarity between target MRI and atlas datasets.

The quantitative assessment of the proposed algorithm was performed using pairs of clinical whole-body PET/MR and PET/CT studies where CT-based attenuation corrected PET images are used as reference. Comparison was also made with Hofmann's approach as a baseline for evaluation of our method and the 3-class attenuation map technique implemented on the Philips Ingenuity TF PET/MR scanner since segmentation-based methods are commonly used in clinical PET/MR.

II. Materials and Methods

II.A. PET/CT and PET/MRI data acquisition

The study population comprised 14 patients, who underwent whole body 18F-FDG PET/MR and whole-body 18F-FDG PET/CT for staging of head and neck malignancies. A single injection of 18F-FDG (371±23 MBq) was used to perform whole-body 18F-FDG PET/CT studies at free shallow breathing on a Biograph 64 True Point scanner (Siemens Healthcare, Erlangen, Germany). After a localization scout scan, an unenhanced low dose CT scan (120 kVp, 60 mAs, 24×1.5 collimation) was performed for attenuation correction. The typical acquisition time for whole-body CT scans was less than 10 seconds (axial FOV of 16.2 cm, pitch of 1.2 and 1 s per rotation). PET data acquisition started 146.2±20 min post-injection with 3 min per bed position for a total of 5-6 beds, resulting in a total acquisition time of 15-18 min.

PET/MRI examinations were performed on the Ingenuity TF PET/MR (Philips Healthcare, Cleveland, USA) [17]. The patients were almost in the same position during both examinations with arms down. The so-called atMR whole-body MRI sequence was used for fast (<3 min) derivation of the 3-class attenuation map. It consists of a 3D multi-stack spoiled T1-weighted gradient echo sequence with the following parameters: flip angle 10°, TE 2.3 ms, TR 4.1 ms, smallest water–fat shift, 600 mm transverse FOV with a slab thickness of 120 mm, voxel size 1.9×1.9×6 mm3, 12 mm overlap between adjacent stacks [6]. The Philips Ingenuity TF PET/MR utilizes this 3-class attenuation map (air: 0 cm-1, lung: 0.022 cm-1, soft-tissue: 0.098 cm-1) for the purpose of PET attenuation correction [6, 17].

The proposed MRI-derived pseudo-CT generation approach uses a whole body MRI Dixon volumetric interpolated T1-weighted sequence [33] with the following parameters: flip angle 10°, TE1 1.1 ms, TE2 2.0 ms, TR 3.2 ms, 450×354 mm2 transverse FOV, 0.85×0.85×3 mm3 voxel size, and a total acquisition time of 2 min 17 s. The study protocol was approved by the institutional ethics committee and all patients gave informed consent.

II.B. MR data pre-processing

The acquired MR images contain a relatively high level of noise, corruption due to the low frequency bias field and inter-patient intensity inhomogeneity [34-36]. As such, the presence of any aforementioned source of intensity uncertainty in MR images might bias the pseudo-CT generation result. To overcome these prospective sources of error, in-phase images of all patients underwent the following pre-processing steps to minimize statistical noise in MR images (gradient anisotropic diffusion filtering), cancel out intra-subject intensity inhomogeneity (N4 bias field correction) and correct inter-subject intensity non-uniformity (histogram matching). Other techniques reported in the literature [37] can also be employed for this purpose.

- Gradient anisotropic diffusion filtering [38] using the following parameters: conductance = 4, number of iterations = 10 and time step = 0.01. This is an edge preserving smoothing algorithm that adjusts the conductance term to produce large diffusion inside regions where the gradient magnitude is relatively small (homogenous regions) and lesser diffusion in regions where the gradient magnitude is large (i.e. edges).
- N4 bias field correction [39]: B-spline grid resolution = 400, number of iterations = 200 (at each grid resolution), convergence threshold = 0.001, B-spline order = 3, spline distance = 400, number of histogram bins = 256 and shrink factor = 3.
- Histogram matching [40]: Histogram level = 512 and match points = 64. In order to get the best result from histogram matching, we excluded background air voxels of both reference and target images before processing. The mean absolute inter-patient MRI intensity variability decreased from 29% to 10% after application of the aforementioned corrections [41].

The proposed pseudo-CT generation procedure entails segmentation of the external body contour as well as lung identification. To this end, the external body contour was determined by applying a 3D snake active contour algorithm on the in-phase MR images [42]. Identification and segmentation of the lungs was performed through connected-component analysis of the lower intensity in the inner part of the body using the ITK-SNAP image processing software [43]. The segmentation was performed semi-automatically following initialization by user-specified seeds.

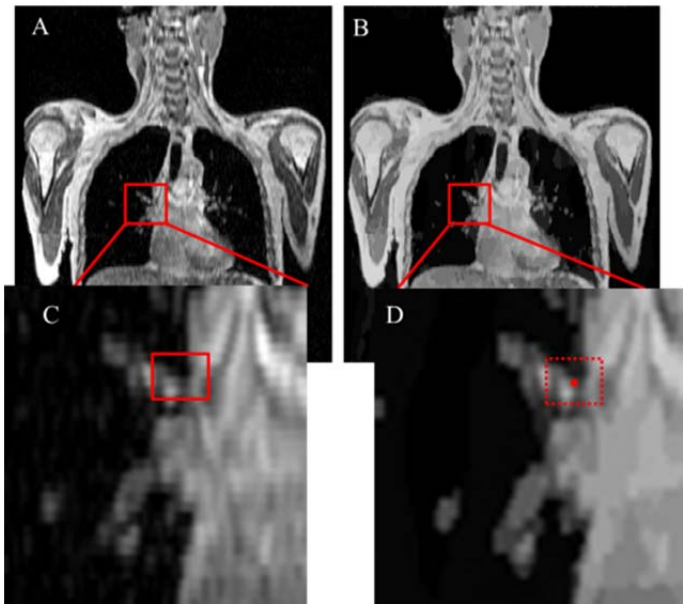

Figure 1. (A) Representative slice of in-phase MR Dixon image. (B) Intensity clustered version of the image shown in (A) using K-means Markov random field algorithm in which neighbouring voxels with similar intensity are assigned the same cluster level (1 to 512). (C) In Hofmann's method, the information extraction from MR images is performed by calculating the weighted average of voxel intensities confined by rectangular sub-volumes (patch). (D) In our SAP approach, the voxel value within the clustered image (dot point) is directly used in the GPR kernel to facilitate the training process and maintain the edge information.

In Hofmann's approach, local information extraction from MRI is performed by calculating the weighted average of intensities confined to rectangular sub-volumes (patches) [10]. These weighted average values are used to assess the local similarity of MRI intensity across subjects as is indicated in figure 1. To alleviate the

computational burden involved by computing weighted averages for each patch and more importantly avoid information loss due to the averaging process (particularly at the boundary of organs or in regions with abrupt intensity variations), intensity clustered MR images are utilized in our approach. The clustering process assigns the same cluster label to voxels with similar intensity considering Markov random field regularisation for noise and intensity non-homogeneity reduction. The clustering is carried out using the K-means Markov random field algorithm implemented in the ITK software package [44]. A 512 bins clustering with 50 iterations and a tolerance of 0.001 was performed to produce the MRc image (figure 1). Therefore, our approach uses the proximity cluster values (the cluster value to which voxels under study belong to) instead of comparing local information across subjects on the basis of weighed intensity averaging of surrounding voxels (figure 1). This enables to further reduce the noise and intensity non-uniformity across the subjects.

II.C. Pseudo-CT generation approach

1) Hofmann's approach

Since the proposed pseudo-CT generation approach builds on the technique proposed by Hofmann et al. [10], a brief description of this method is provided here. A Gaussian process regression is utilized to merge the atlas registration and local patch information in order to predict more accurately the pseudo-CT values for each voxel of interest [9]. To this end, a number of CT/MRI pairs served as atlas after undergoing pairwise non-rigid registration to the target MR image (Eq. 1). In addition to the local information in the co-registered atlas database and intensity similarity of patches, the 5-class segmentation (background air, lung, fat, fat and non-fat mixture and non-fat tissue) of in-phase MR images [8] and corresponding patch information is used in equation (1).

$$k(d_i, d_j) = \exp\left(\frac{-\|W(P_{MR,i}) - W(P_{MR,j})\|^2}{2\sigma^2_{MR,patch}}\right) \times \exp\left(\frac{-\|X_i - X_j\|^2}{2\sigma^2_{pos}}\right) \times \exp\left(\frac{-\|W(P_{Seg,i}) - W(P_{Seg,j})\|^2}{2\sigma^2_{Seg,patch}}\right) \quad (1)$$

Where $d=(P_{MR}, P_{Seg}, X)$ and P_{MR} and P_{Seg} are sub-volume patches from the in-phase MR image and 5-class segmented MR image, respectively. W is a weighting vector assigning a higher weight to central voxels than peripheral ones in the patch, X is the training center position. Equation (1) represents the kernel of GPR which yields a covariance matrix. The indices i and j refer to the different patches defined on training MR images. In effect, the three terms in the GPR kernel measure the intensity, position and tissue type distance of different patches on training datasets. The parameters σ_{pos}, $\sigma_{MR,patch}$ and $\sigma_{Seg,patch}$ determine how the overall kernel value is influenced by similarity in position, patch intensity value in MR and 5-class segmented image. The training is performed on samples of d_i and $d_j=(P_{MR,j}, P_{Seg,j}, X_j)$, $i/j=1,2,\ldots,n$, drawn from random locations in the MRI atlas database on the basis of known CT values for the corresponding patches. Once the Gaussian regression is trained and the free parameters of σ_{pos}, $\sigma_{MR,patch}$ and $\sigma_{Seg,patch}$ determined, equation (2) is used to calculate the pseudo-CT value for each voxel of interest.

$$c_l = k_l{}^T C^{-1} y \quad (2)$$

Where c_l denotes the calculated pseudo-CT value of a voxel of interest l. $k_l=k(d_i,d_l)$ is an $(n\times1)$ matrix where $d_i=(P_{MR,i}, P_{Seg,i}, X_i)$ is the information extracted from the patches defined on the MRI atlas dataset and $d_l=(P_{MR,l}, P_{Seg,l}, X_l)$ represents the patch defined on the target MRI. $C=k(d_i,d_j)$ is the $(n \times n)$ covariance matrix obtained from equation (1) using d_i and d_j patches defined on MR atlas data set. y stands for a $(n\times1)$ vector of CT values corresponding to the central voxel of training patches d_i.

2) Proposed sorted atlas pseudo-CT (SAP) approach

The proposed pseudo-CT generation approach, referred to as SAP, employs the morphological similarity between the target in-phase MRI and the co-registered atlas database MRIs, which is computed locally using the local normalized cross-correlation (LNCC) metric proposed by Yushkevich *et al.* [45]. The LNCC process provides a measure based on which the well-matched atlas images can be selected. The LNCC process is employed to identify the best match or most similar atlas image for each target voxel. Let the MR of the target subject be denoted by I_{ref} and the warped MR images in the atlas database by Im. The LNCC between I_{ref} and Im at voxel v is calculated by:

$$LNCC_v = \frac{\langle Im, Iref \rangle_v}{\sigma(Im)_v \,.\, \sigma(Iref)_v} \tag{3}$$

According to [46], the mean and standard deviation at each voxel *v* are computed using a Gaussian kernel K_G, with a standard deviation of N_{std} = 0.9 cm, through the convolution process:

$$\begin{aligned} \overline{Im}_v &= K_G * Im \\ \sigma(Im)_v &= \sqrt{\overline{Im_v^2} - \overline{Im_v}^2} = \sqrt{(K_G * Im^2) - (K_G * Im)^2} \\ \langle Im, Iref \rangle_v &= \overline{Im.Iref}_v - \overline{Im}_v.\overline{Iref}_v = (K_G * Im.Iref) - ((K_G * Im).(K_G * Iref)) \end{aligned} \tag{4}$$

The range of LNCC values varies considerably among the subjects and locations within a patient. Moreover, since the LNCC is calculated voxelwise, the output is prone to noise and local uncertainty arising from the lack of sufficient local information in the images [12, 45]. To overcome these shortcomings of LNCC similarity measure, k-nearest neighbour kernel was employed to pool the information in the near vicinity in order to choose the most similar image to the target image from the atlas database [47]. To this end, in the first step, the LNCC is calculated for each voxel of the target in-phase image across all the co-registered atlas images using equations (4) and (5). Then, for each voxel, the most similar atlas to the target image is selected on the basis of its k-nearest neighbour LNCC values. To minimize the impact of noise, a fixed size window is defined around the target voxel and the atlas with the highest score within the window is selected as the most similar atlas for that voxel. It should be noted that negative LNCC scores were converted to zeros before the k-nearest filtering. The information about selected atlases is stored in the *ASM(x)*, the atlas selection matrix, whose voxels indicate IDs of the most similar atlas images to the target. Optimization of the k-nearest neighbour (as described in section 2.4) led to a window size of 5 cm × 5 cm (defined in 2D on each slice). A large window size guarantees robust similar atlas selection carried out by the LNCC process. Although using a wide Gaussian kernel for the LNCC step may lead to similar outcome as the k-nearest filter, exploiting the k-nearest filter resulted in more robust similarity measure between large image patches. Figure 2 depicts a representative sample of the ASM with its corresponding in-phase image where each colour stands for one individual image in the atlas dataset that is locally most similar to the target image. The LNCC metric enables to detect and eliminate the causes of error due to misalignment and anatomical dissimilarity across the aligned atlas dataset. In the presence of morphological discrepancy (owing to registration errors or anatomical dissimilarity) between the target and atlas images, the LNCC analysis yields relatively low scores thus triggering the elimination of the corresponding atlas (or sub-volume) from further processing (supplemental figure 1). After constructing the ASM, the GPR algorithm for non-lung region is run on the most similar atlas images on a voxel by voxel basis using the ASM data.

This method employs the above described Gaussian process regression but splits the main kernel in equation (1) into two separate Gaussian processing kernels for non-lung and lung tissues. Figure 3 depicts a schematic diagram of the SAP approach summarizing the different steps required to generate a pseudo-CT image. In fact, two distinct Gaussian process regressions are trained and utilized separately for lung and non-lung body regions. For non-lung region, the Gaussian kernel is modified as follows:

$$K_{non-lung}(b_i, b_j) = \exp\left(\frac{-\|MR_{c,i} - MR_{c,j}\|^2}{2\sigma^2_{MR,cluster}}\right) \times \exp\left(\frac{-\|X_i - X_j\|^2}{2\sigma^2_{pos}}\right) \tag{5}$$

where, b_i and b_j=($MR_{c,j}$, X_j) represent the vector of information extracted from MRI training dataset for voxels *i*/*j*=1,2,…,*n* and MR_c and *X* represent the voxel value (cluster level between 1 to 512) and position in the clustered atlas MR images, respectively. As mentioned earlier, the voxel value in the clustered MR images is used in our approach instead of weighted averages of voxels within patches of the image used by Hofmann *et al.* [10]. In this way, the 9mm × 9mm patches of voxels (defined in 2D on each slice) in Hofmann's method are replaced by the cluster number of the target voxel. As such, the parameter $\sigma_{MR,patch}$ in Eq. (1) is replaced by $\sigma_{MR,cluster}$. Comparing equations (1) and (3), the term dealing with similarity in the 5-class segmented MR image has been omitted in the modified version of the algorithm since it was found to have negligible influence on the output.

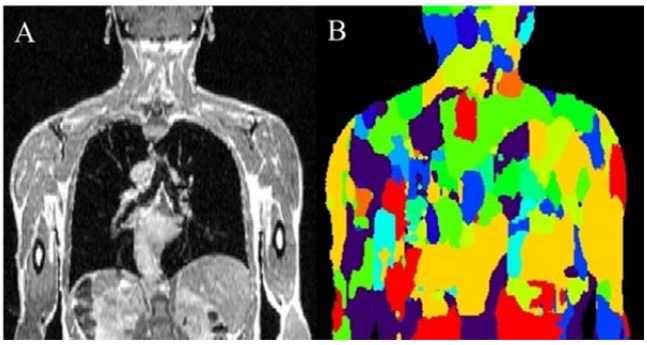

Figure 2. A) In-phase Dixon image of the target patient and B) Target patient atlas selection matrix where each colour stands for one particular image in the atlas dataset.

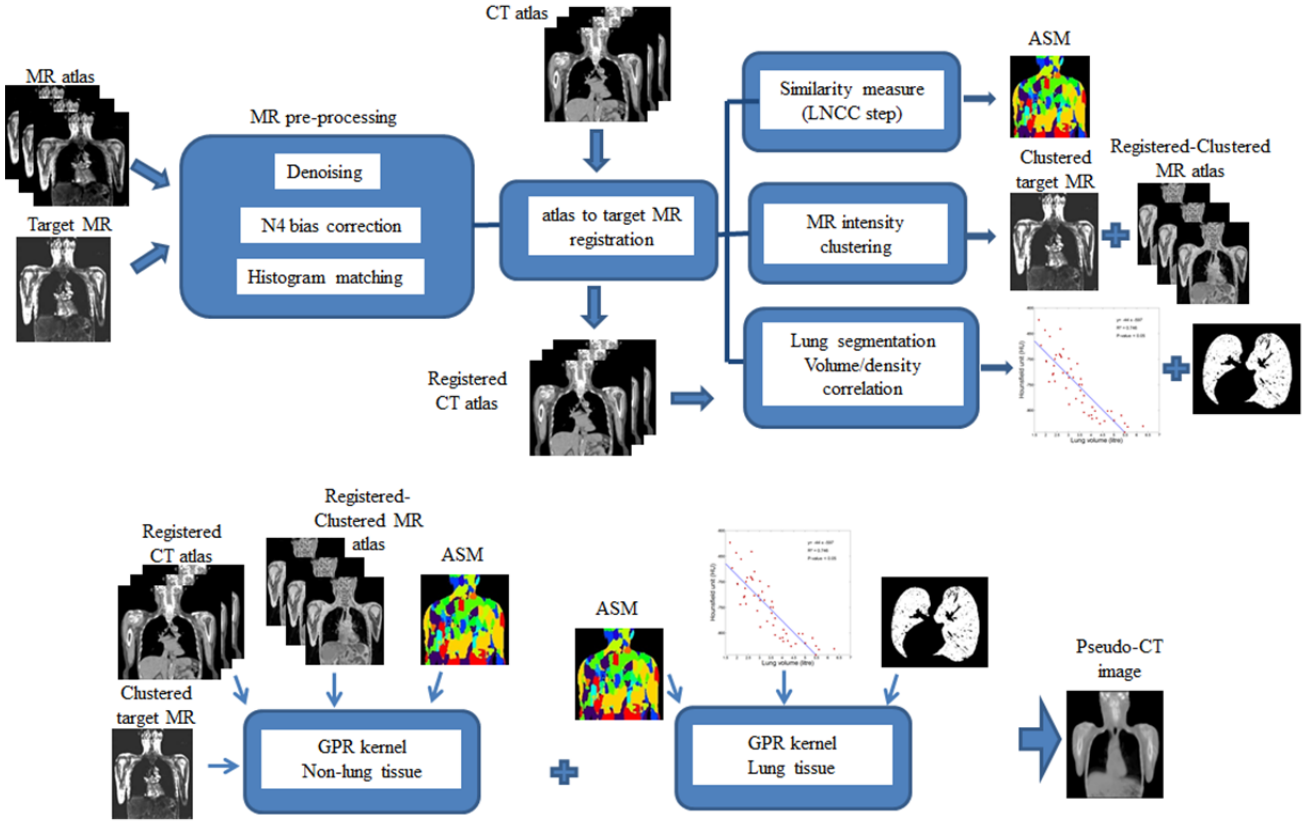

Figure 3. Schematic diagram of the SAP method's workflow.

In fact, in the SAP method, the atlas registration is carried out on denoised MR images as described in section 2.2 (before clustering) and the aligned images are further processed using the LNCC algorithm. After determining the most similar atlas for each voxel in the target image, the selected atlases in the ASM undergo a clustering process before being fed to the GPR kernel. The training and pseudo-CT generation are performed using the GPR kernel running over the most similar atlas for each voxel according to the information provided by the ASM. The information for each voxel from MR atlas images is extracted in the form of clusters rather than patches of voxels as opposed to what is done in the original method. In other words, the LNCC step is run over the original MR images and after determining the most similar atlas for each region, an MR "composite" image is constructed using the corresponding regions from the clustered image. Thereafter, the GPR is run over the MR composite image (with clustered intensity) and the clustered target image. Thus, the clustering is performed one step before constructing the MR composite image. Alternatively, the LNCC could be run over the

clustered MR images provided a large number of cluster bins is used. Otherwise, it may skew the similarity measurement.

In contrast, in Hofmann's method, the GPR kernel is built based on patches of voxels (not clustered images) and run non-selectively over the entire registered images.

3) Lung attenuation coefficients estimation

We propose a separate Gaussian kernel for estimation of lung attenuation coefficients. To this end, the kernel in equation (3) is modified but the term regarding the intensity similarity between target and atlas MR images remained unchanged in equation (6) on the ground that there is potentially a correlation between MR intensity and CT attenuation coefficients [48]. On the other hand, the position similarity term was replaced with lung volume proximity (V_{aj} and V_{ai}) where the *ai* and *aj* denote the atlas index of the corresponding *i* and *j* clusters, respectively (the V_{aj} and V_{ai} refer to the lung volumes of atlases, which the clusters $MR_{c,i}$ and $MR_{c,j}$ are taken from).

$$K_{lung}(l_i, l_j) = \exp\left(\frac{-\|MR_{c,i} - MR_{c,j}\|^2}{2\sigma^2_{MR,cluster}}\right) \times exp\left(\frac{-\|V_{ai} - V_{aj}\|^2}{2\sigma^2_{lung\ volume}}\right) \quad (6)$$

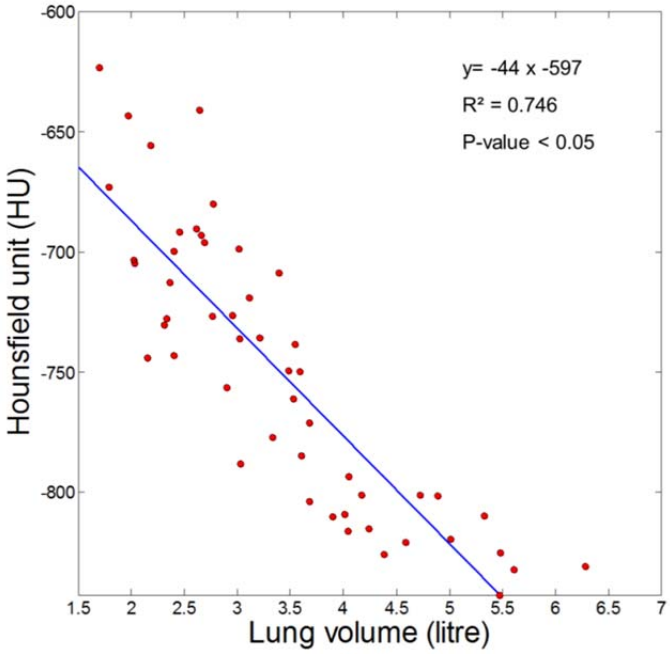

Figure 4. Correlation plots between lung attenuation coefficients (HU) vs. lung volume obtained from CT image segmentation of 50 patients.

It is hypothesized that the lung intensity is correlated with the lung volume [49]. In order to evaluate the degree to which lung attenuation coefficients are correlated with the lung volume, CT images of 50 patients (31 male and 19 female; age ranging from 35 to 96 years) chosen randomly from the clinical database without any preference acquired in free shallow breathing were examined. All the 50 patients were administered whole-body ^{18}F-FDG PET/CT acquired on a Biograph 64 True Point scanner (Siemens Healthcare, Erlangen, Germany) using the protocol described in section 2.1. The technique described in section 2.2 was employed to segment the lungs from CT images. Thereafter, the average lung attenuation coefficient vs. volume was plotted (Figure 4). Taking advantage of the established correlation between lung volume and density, the additional information regarding the lung volume was incorporated in the lung GPR kernel (K_{lung}) using the weight $\sigma_{lung\ volume}$. Splitting up the original kernel gives us the possibility to include lung tissue characteristics into lung-specific kernel. The lung volume term added to the kernel (Eq. 6) tends to predict lung attenuation coefficients considering the close relationship of lung volume between the target and atlas images.

In addition, a simple technique was devised to estimate the attenuation coefficients of prospective malignant lesions in the lungs which might have a different density. PET images corrected for attenuation using the 3-class μ-map (PET-MRAC3c) were analyzed to detect lung tumours. To this end, a lung mask obtained from segmentation of in-phase MR images was overlaid (after resolution matching) on PET-MRAC3c images and a threshold of 2.5 SUV was applied on voxels located within the lung mask [50]. Voxels with an SUV higher than 2.5 were considered as belonging to the lesion and were assigned soft-tissue attenuation coefficient in the pseudo-CT attenuation map. Since noisy voxels in the lungs with spurious SUV over 2.5 might be mapped to soft-tissue, 3D median filtering with a kernel dimension of 3×3×3 was applied to PET-MRAC3c images before thresholding followed by connectivity analysis [51] to exclude regions having a maximum diameter below 4 mm based on recommendations in [52].

In the final step, an automatic post-processing rule is applied on the generated pseudo-CT images to account for gas pockets in the abdomen area. First, the bone tissue is segmented using an intensity threshold of 140 HU. Then a distance map [53] is computed on the obtained binary bone map. The voxels that have a low MRI intensity in the target in-phase image and reside at least 10 mm far from nearest bony structures are assumed to belong to massive and mobile air cavities with a pseudo-CT value of -1,000 HU. This procedure enables to detect air cavities (particularly in the abdomen) even when there is no similar structure in the atlas database.

II.D. Parameter optimization

We employed a leave-one-out cross-validation (LOOCV) scheme to find the optimum value for all free parameters and settings. In the first step, MR images are non-rigidly aligned to the corresponding CT images ensuring appropriate MRI-CT matching. The coregistered images are carefully checked visually and in case of misalignment, the registration parameters, such as final grid space and optimisation parameters are tuned to achieve the best possible alignment between MR and CT images. The aligned atlas dataset is created using 13 out of the 14 available clinical studies. As such, for each individual patient, all the remaining 13 in-phase MR images were deformably registered to the target image.

The k-nearest window in the LNCC step plays a key role in the implementation of our SAP method. Voxelwise searching for the most similar atlas through the window of k-nearest neighbour was optimized via varying the window size from 1 to 10 cm with a step of 1 cm and the resulting pseudo-CT images were evaluated in terms of bone extraction accuracy at each step. To this end, the Dice similarity measure was employed to evaluate the accuracy of extracted bone from the resulting pseudo-CT images considering the bone map extracted from CT images as reference. This procedure was repeated for the whole dataset and the highest Dice metric was achieved at a window size of 5 cm × 5 cm.

The parameters $\sigma_{pos,}$ $\sigma_{MR,patch}$ and $\sigma_{Seg,patch}$ are the most influential factors in the original kernel. Firstly, the associated parameters were roughly determined for each test patient through examination of the variance of patch intensity, position and segmentation terms in Eq. (1). The exact parameter setting was empirically achieved through pseudo-CT generation for each of the 14 atlas images. The parameters that maximized the similarity between pseudo-CT and actual CT images were selected. The similarity between the resulting pseudo-CT and actual CT images was assessed based on the Dice metric for bone volume as described earlier. A patch size of 9×9 voxels was used to feed the GPR kernel and for each target voxel, 80 patches of voxels were chosen to train the kernel. A higher sampling density (120 samples) was used near bone regions as they are of special interest. The same procedure was followed to train the non-lung SAP kernel and setting of the parameters $\sigma_{MR,cluster}$ and σ_{pos}. Since a separate kernel was employed for the lung tissue in the SAP method, all the patches were sampled outside the lung volume (inside the body contour) with the same sampling density to train the kernel in Eq. (3).

The training of Eq. (6) was performed in a similar way, except that all the patches were chosen inside the lung volume using 80 patches for each target voxel. The associated parameters for lung-kernel ($\sigma_{lung\ volume}$ and $\sigma_{MR,cluster}$) were optimized through the same scheme described above but instead of the Dice metric, the absolute lung attenuation difference between pseudo-CT and actual CT images was used for parameter tuning.

II.E. Quantitative evaluation

Pseudo-CT images were generated for the 14 clinical studies and the obtained attenuation maps used for attenuation correction of corresponding PET data. Calculations were performed on a PC equipped with Intel

Xeon CPU (2.3 GHz) running Matlab. It took approximately 1100 min on average to create one pseudo-CT image (almost 70% for the atlas registration and 25% for the GPR training). PET images were reconstructed by means of the e7 tool (Siemens Healthcare, Knoxville, TN) using ordinary Poisson ordered subset-expectation maximization (OP-OSEM) iterative reconstruction algorithm. Default parameters (4 iterations, 8 subsets, and a post-processing Gaussian kernel with a FWHM of 5 mm) adopted in clinical protocols were applied. Image reconstruction was performed four times for each clinical study: PET images corrected for attenuation using CT (PET-CTAC) used as reference, using the 3-class attenuation map (PET-MRAC3c) obtained from the Ingenuity TF PET/MR scanner [6], using the pseudo-CT generated by Hofmann's approach (PET-HofmannAC) [10] and our proposed SAP approach (PET-SAPAC). A nuclear medicine physician drew manually the VOIs on regions of normal physiologic uptake, six regions in the lungs (on the upper, middle and lower parts of the right and left lung), liver, spleen, cerebellum, 2 bony structures (cervical vertebrae 6 and dorsal vertebrae 5), aorta, and malignant lesions [54]. The VOIs were carefully drawn at the centre of each organ far away from organ boundaries. The differences between the attenuation correction techniques were quantified in terms of change in the standard uptake value (SUV). The SUVs were calculated by dividing the activity concentration in each VOI by the injected activity divided by body weight. The accuracy of attenuation correction was assessed through the relative mean error (Eq. 7) and relative mean absolute error (Eq. 8) between SUV measured on PET attenuation corrected using MR-derived attenuation maps (MRAC) and PET attenuation corrected using reference CT image averaged over all patients. In addition to the ROI-based analysis, anatomical regions corresponding to the liver, cerebellum, cervical vertebrae 6, dorsal vertebrae 5 and spleen were segmented on CT images using the ITK-SNAP software and the same PET quantitative evaluation was carried out.

$$Relative\ error\ (\%) = \frac{MRAC\ (SUV) - Reference\ (SUV)}{Reference\ (SUV)} \times 100\% \tag{7}$$

$$Relative\ absolute\ error\ (\%) = \frac{ABS[MRAC\ (SUV) - Reference\ (SUV)]}{Reference\ (SUV)} \times 100\% \tag{8}$$

In addition to ROI-based analysis, voxel-based comparison was carried out between PET images corrected for attenuation using the two pseudo-CT images and PET-CTAC used as reference. The voxel-based relative mean bias (RMB) and relative mean absolute bias (RMAB) were computed for bone, lung, fat and soft-tissue class using equations (7) and (8), respectively. The segmentation of tissue classes was performed based on CT Hounsfield units (HU) using the following thresholds; bone if HU $\geq$ 140, soft-tissue if -20 < HU $\leq$ 140, and fat if -350 < HU $\leq$ -20. The lung mask was obtained as described in the data processing section.

The assessment of the accuracy and robustness of the extracted bones using the proposed (SAP) and Hofmann's approaches was performed through comparison with the bone segmented from the corresponding CT images. Bone segmentation was performed by applying a threshold of 140 HUs on the generated pseudo-CT and corresponding CT images. The validation of bone segmentation is reported using seven volume/distance-based metrics [55]: Dice similarity (DSC) [56], relative volume difference (RVD) [57], Jaccard similarity (JC) [58], sensitivity (S) [59], mean absolute surface distance (MASD) [60], Hausdorff distance (HD) [61] and distance error (DE) [27].

$$\begin{aligned}
DSC(A,M) &= \frac{2|A \cap M|}{|A|+|M|} \\
RVD(A,M) &= 100 \times \frac{|M|-|A|}{|A|} \\
JC(A,M) &= \frac{|A \cap M|}{|A \cup M|} \\
S(A,M) &= \frac{|A \cap M|}{|M|} \\
MASD(A,M) &= \frac{d_{ave}\ (S_A,A_M) + d_{ave}\ (A_M,S_A)}{2} \\
DE(A,M) &= \frac{1}{N}\sum_{p=1}^{N} mindist(A_p, M_p) \\
HD(A,M) &= \max_A\{\min_M\{d(A,M)\}\}
\end{aligned} \tag{9}$$

where A is the bone segmented from the reference CT image and M denotes the extracted bone from the pseudo-CT attenuation maps. $d_{ave}(S_A,S_M)$ is the average direct surface distance from all points on the CT bone surface S_A and to the pseudo-CT bone surface S_M. The distance error is equal to the minimum distance from each boundary

point of the source region (A_p) to the entire set of points of the target region (Mp) averaged across the N boundary points. The Hausdorff distance measures the maximum distance one would need to move the boundaries of the source region (A) to completely cover the target region (M).

Moreover, the generated pseudo-CTs were compared to the ground truth CT through metrics measuring the voxel-wise error (in HUs) between bone volumes using the mean error (ME) and mean absolute error (MAE) defined as:

$$ME = \frac{\sum_v (\mathrm{MCT}_v - \mathrm{CT}_v)}{V} \tag{10}$$

$$MAE = \frac{\sum_v |\mathrm{MCT}_v - \mathrm{CT}_v|}{V} \tag{11}$$

where V is the number of voxels in the bone volume, MCT_v and CT_v denote voxel values in the pseudo-CT and ground truth CT images, respectively.

Furthermore, we expanded our evaluation by separating cortical bone (>300 HUs) from spongy bone (140-300 HU) by thresholding reference CT images and generated pseudo-CT images. Then, all the above mentioned segmentation accuracy measures were applied separately on the segmented spongy and cortical bones to precisely quantify the performance of the proposed method.

The accuracy of the predicted lung attenuation coefficient was evaluated by calculating the average lung attenuation coefficient on the obtained pseudo-CT images using a lung mask and comparing it with the corresponding CT images for each individual patient. Paired t-test analysis was used to assess if the differences between the obtained results are statistically significant. A threshold of 0.05 was used for statistical significance.

III. Results

Figure 5 depicts a representative sagittal slice of the generated pseudo-CT attenuation map along with corresponding in-phase MR and CT images. The visual inspection of images revealed sharper bone edges when using our SAP approach.

According to Table 1, considerable bone detection enhancement was achieved using the SAP attenuation map based on the average of 14 patients. However, the differences were not statistically different for all metrics. Figure 6 illustrates the segmented bone of the clinical study shown in figure 5 using Hofmann's and SAP approaches. Figures 5D and 5E depict the corresponding distance error maps calculated by comparing segmented bones using Hofmann's and SAP attenuation maps with the CT-based attenuation map. A relatively smaller average distance error is achieved by SAP (7 mm max) compared to Hofmann's method (12 mm max).

Fgure 5. A) Target patient CT image, B) corresponding in-phase MR image, and attenuation maps generated using C) Hofmann' technique and D) our proposed SAP approach.

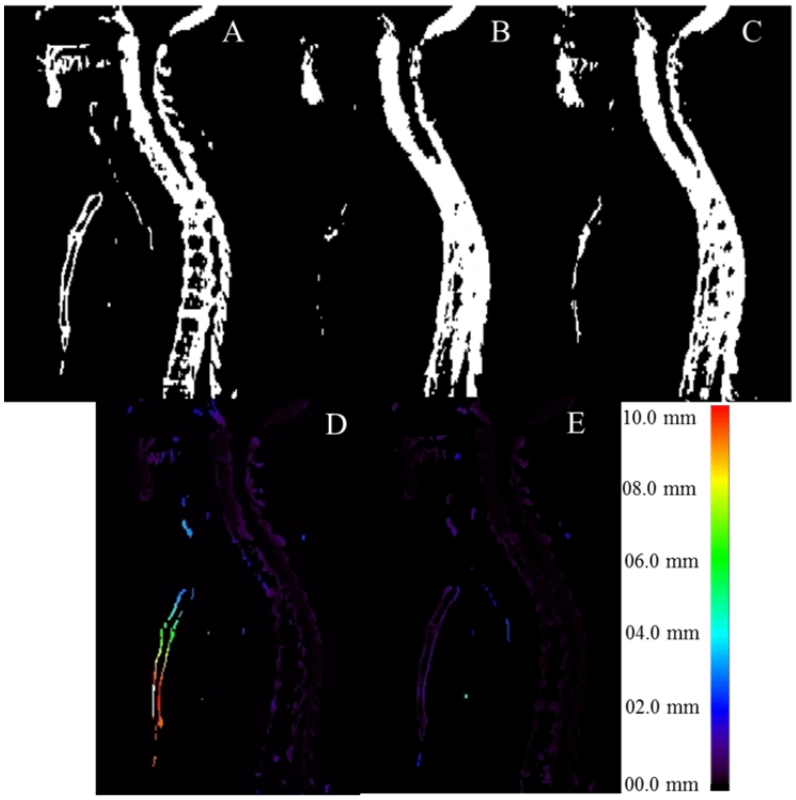

Figure 6. Representative slice of bone segmentation from MR images showing: A) Binary image of segmented bone from CT images, segmented bone using B) Hofmann' technique and C) our proposed SAP approach. Distance error map calculated by comparing Hofmann' technique D) and our SAP approach E) with the reference bone segmented on CT images.

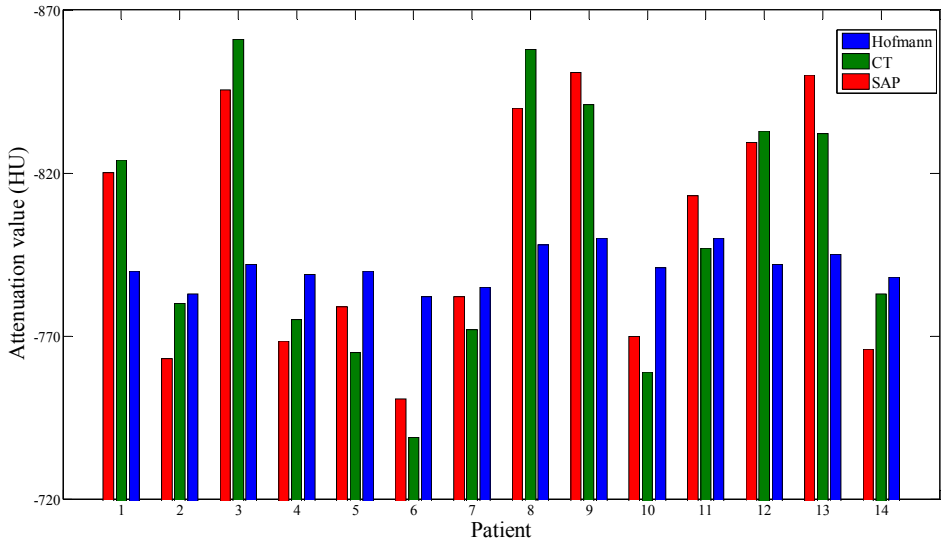

Figure 7. Predicted average lung attenuation coefficients using Hofmann's and the proposed SAP approaches compared to actual value obtained from CT images of each individual patient averaged over the whole lung volume.

Figure 7 compares the average lung attenuation coefficient obtained using both MRI-derived pseudo-CT approaches compared with the actual coefficient obtained from CT images for each individual patient. The lung attenuation coefficient predicted by Hofmann's approach is very close to the average attenuation coefficient of the atlas database resulting in an average lung attenuation estimation error of 7.92±20% (average±SD) over all patients using CT as reference, whereas the SAP approach yielded an error of -0.25±8% (in terms of linear attenuation coefficients at 511 keV). The errors in HUs were 8.14±35 and -1.71±14, respectively, indicating a lower SD for the SAP method.

Table 1. Comparison of cortical bone (>300 HU) and spongy bone (140-300 HUs) segmentation accuracy (mean±SD) between Hofmann's and SAP approaches using various evaluation metrics including Dice similarity (DSC), relative volume distance (RVD), Jaccard similarity (JC), sensitivity (S), mean absolute surface distance (MASD), Hausdorff distance (HD), distance error (DE), mean absolute error (MAE) and mean error (ME).

	Hofmann (All bones cortical spongy)	P-value	SAP (All bones cortical spongy)	P-value
DSC	0.58±0.09	0.10	0.65±0.07	<0.05
	0.53±0.09	0.10	0.60±0.06	<0.05
	0.57±0.08	0.09	0.64±0.07	<0.05
RVD (%)	-36.6±10.0	0.23	-30.7±9.10	0.17
	-41.2±11.0	0.25	-34.2±8.90	0.18
	-38.9±10.0	024	-32.8±9.20	0.17
JC	0.35±0.06	0.15	0.41±0.05	0.10
	0.31±0.05	0.16	0.38±0.04	0.10
	0.33±0.06	0.15	0.40±0.05	0.10
S	0.40±0.15	0.11	0.48±0.12	0.08
	0.37±0.14	0.12	0.43±0.12	0.08
	0.39±0.15	0.11	0.47±0.11	0.08
MASD (mm)	6.92±3.10	0.08	4.81±2.60	<0.05
	7.32±3.40	0.08	4.92±2.53	<0.05
	7.12±3.00	0.08	4.99±2.61	<0.05
HD (mm)	15.9±4.70	0.09	10.9±3.80	<0.05
	16.3±4.80	0.09	11.4±3.79	<0.05
	16.1±4.70	0.09	11.2±3.83	<0.05
DE (mm)	2.6±1.70	<0.05	1.1±0.90	<0.05
	2.8±1.65	<0.05	1.2±0.92	<0.05
	2.7±1.72	<0.05	1.1±0.89	<0.05
MAE (HU)	127±26.0	<0.05	89±12.5	<0.05
	135±27.4	<0.05	93±12.9	<0.05
	132±26.8	<0.05	91±12.4	<0.05
ME (HU)	-29±32.0	0.06	-11±20.0	<0.05
	-31±32.8	0.06	-12±23.2	<0.05
	-30±32.3	0.06	-11±22.8	<0.05

Figure 8 illustrates a clinical study presenting with non-small cell lung cancer. The lesion was overlooked by the 3-class segmentation procedure implemented on the Philips TF PET/MR system (Figure 8D) and consequently assigned the wrong attenuation coefficient of the lung (0.022 cm^{-1}). The SUV_{mean} of the lesion is 6.1 for PET-MRAC3c (figure 8H) significantly underestimates the SUV_{mean} for PET-CTAC (9.7) serving as reference owing to the assignment of the wrong attenuation coefficient to the lesion. Figure 8E shows the same 3-class attenuation map with correct identification of the lung lesion using the proposed PET segmentation technique and proper assignment of soft-tissue attenuation coefficient. The measured SUV_{mean} of the lesion after correction (PET-CorrectedMRAC3c) is 7.8 (figure 8I). Due to the low MR intensity of the lung lesion, Hofmann's approach fails to assign the correct attenuation coefficient to the lesion (figure 8F), thus leading to underestimation of SUV_{mean} of (8.2) (figure 8J). Yet, our SAP approach correctly identified the lung lesion (figure 8G), leading to an SUV_{mean} of 9.5 on PET-SAPAC (figure 8K).

Figure 9 shows the relative errors between SUV_{mean} estimated using PET images corrected for attenuation using SAP and Hofmann's approaches and PET-CTAC images taken as reference. Significant improvement in the accuracy of SUV estimates was achieved in bony structures (cervical 6 and dorsal 5) and structures located near cortical bone (cerebellum and some malignant lesions). Furthermore, the SAP approach decreased considerably the standard deviation of the estimated SUV_{mean} in the lungs. The SUV underestimation using the 3-class approach in or near bony structures such as the cerebellum and vertebrae is larger with errors of -13.0±6.2% and -27.4±10.1%, respectively. In contrast, Hofmann and SAP approaches yield relative errors of -8.8±3.8% and -7.3±6.0%, and -3.3±04.9% and -1.7±4.8%, respectively (Table 2).

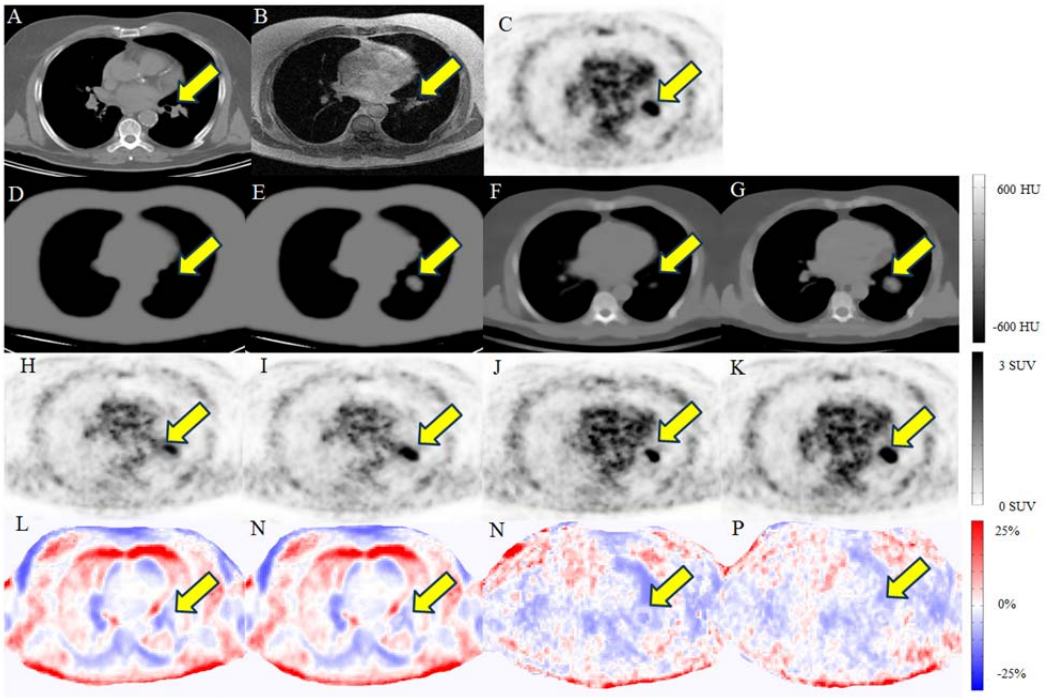

Figure 8. Representative slices showing a clinical study with non-small cell lung cancer with a lesion in the left lung. A) CT, B) in-phase MRI, C) PET-CTAC, D) 3-class attenuation map, E) corrected using the 3-class attenuation map where the attenuation coefficient of soft-tissue is assigned to the lung lesion, attenuation maps generated using F) Hofmann's and G) our SAP approaches, H) PET-MRAC3c, I) PET-correctedMRAC3c, J) PET-HofmannAC and K) PET-SAPAC. Voxelwise SUV bias maps obtained by comparing PET-CTAC and L) PET-MRAC3c, M) PET-correctedMRAC3c, N) PET-HofmannAC and O) PET-SAPAC, respectively. The estimated SUV_{mean} in the malignant lesion was 6.1 for PET-MRAC3c, 7.8 for PET-CorrectedMRAC3c, 8.2 for PET-HofmannAC, and 9.5 for PET-SAPAC. The latter is closer to SUV_{mean} of 9.7 obtained on PET-CTAC serving as reference. The patient bed derived from CT images was inserted in all attenuation maps; however, some bias, particularly at the back of the patient, might stem from slight bed mispositioning.

Table 2. Mean relative errors (bias) between SUV_{mean} estimated using PET images corrected for attenuation using MRI-guided three-class (MRAC3c), Hofmann's and SAP (SAPAC) attenuation correction techniques and CT-based attenuation correction used as reference.

Region	MRAC3c	P-value	Hofmann	P-value	SAPAC	P-value
Upper right lung	21.8±10.2	0.39	04.9±17.2	<0.02	02.4±7.3	<0.01
Upper left lung	18.7±10.4	0.27	07.0±15.4	<0.05	00.3±7.2	<0.01
Middle right lung	19.3±15.8	0.30	08.4±15.4	0.06	01.6±7.5	<0.01
Middle left lung	21.0±18.1	0.33	-06.5±11.3	<0.02	01.9±7.6	<0.01
Lower right lung	20.8±21.2	0.34	02.3±20.2	<0.01	-04.8±9.8	<0.05
Lower left lung	06.6±15.1	0.10	-07.3±12.0	<0.05	-03.0±7.2	0.05
Cerebellum	-13.0±6.2	0.07	-08.8±3.8	<0.05	-03.3±4.9	<0.01
Aorta cross	-15.8±8.6	0.06	-02.7±4.7	<0.01	-02.3±3.5	<0.01
Liver	-11.2±7.0	0.05	-05.8±3.8	<0.05	-04.1±4.7	<0.05
Spleen	-10.0±10.4	0.05	00.2±3.5	<0.01	-00.6±4.5	<0.01
Bone (cervical 6)	-29.9±10.0	0.43	-08.7±6.52	0.05	-02.8±5.5	<0.01
Bone (dorsal 5)	-25.0±10.2	0.40	-05.8±5.5	<0.01	-00.6±4.0	<0.02
Lesions	-03.7±9.1	0.03	-02.2±7.5	<0.01	-01.4±4.2	<0.01

Table 3. Mean relative absolute errors between SUV_{mean} estimated using PET images corrected for attenuation using MRI-guided three-class (MRAC3c), Hofmann's and SAP (SAPAC) attenuation correction techniques and CT-based attenuation correction used as reference.

Region	MRAC3c	[min, max]%	Hofmann	[min, max]%	SAPAC	[min, max]%
Upper right lung	24.3±9.5	[45.4, 1.0]	17.7±13.0	[-39.2, 43.3]	7.5±3.4	[-9.5, 16.7]
Upper left lung	20.3±9.4	[-1.6, 46.9]	15.1±8.8	[-16.5, 31.7]	7.3±4.2	[-17.4, 13.0]
Middle right lung	21.0±11.2	[0.0, 56.2]	16.7±7.1	[-15.5, 39.7]	7.1±3.4	[-8.9, 16.3]
Middle left lung	24.5±14.1	[-10.3, 50.6]	12.8±6.3	[-29.4, 15.6]	8.2±3.3	[-11.8, 15.0]
Lower right lung	25.1±17.2	[-12.3, 55.6]	20.2±8.2	[-43.3, 28.9]	10.5±4.3	[-21.6, 11.1]
Lower left lung	15.0±9.8	[-26.8, 32.0]	12.6±8.4	[-31.3, 15.4]	7.6±3.9	[-19.1, 8.5]
Cerebellum	15.4±5.3	[-29.5, -01.1]	9.2±3.3	[-17.1, 3.0]	5.6±2.9	[-14.5, 6.8]
Aorta cross	17.9±7.6	[-38.6, -01.0]	5.1±2.7	[-10.8, 7.6]	4.2±2.5	[-7.7, 8.6]
Liver	14.2±8.1	[-21.0, 1.4]	6.2±3.5	[-12.7, 1.7]	6.5±2.4	[-12.7, 7.7]
Spleen	16.0±9.4	[-19.1, 1.0]	3.4±2.5	[-07.6, 10.0]	4.6±3.3	[-10.8, 11.1]
Bone (cervical 6)	33.6±11.3	[-51.5, -13.0]	10.5±5.0	[-18.7, 3.2]	5.8±2.9	[-8.6, 6.5]
Bone (dorsal 5)	27.2±10.2	[-41.0, -1.1]	6.7±4.8	[-20.3, 7.0]	4.2±2.4	[-14.3, 7.4]
Lesions	09.8±4.5	[-31.0, 21.4]	8.3±6.1	[-14.4, 21.4]	6.1±3.4	[-17.5, 15.9]

Table 4. Average and standard deviation of the voxelwise RMB and RMAB results between PET-MRAC3c, PET-SAPAC and PET-HofmannAC and the ground truth PET-CTAC computed for lung, fat, soft-tissue and bone classes [RMB mean±SD (RMAB mean±SD)].

Method	Lung	Fat	Soft-tissue	Bone	
MRAC3c	15.8±10.1 (18.6±7.4)		1.8±8.3 (5.1±5.8)	-9.6±8.2 (11.7±6.1)	-19.9±11.5 (20.7±9.8)
SAPAC	-1.0±6.8 (7.8±4.9)		1.2±5.9 (6.6±4.4)	-3.4±5.2 (5.7±4.1)	-0.7±7.8 (6.8±5.9)
Hofmann	3.9±11.7 (10.9±7.6)		6.5±7.1 (9.8±6.2)	-4.9±6.7 (7.2±5.3)	-6.0±7.9 (9.7±6.1)

The relative mean absolute errors together with min-max intervals are summarized in Table 3 to examine the precision of MRI-guided attenuation correction techniques. The 3-class attenuation map assigning a uniform attenuation coefficient of 0.022 cm^{-1} (-770 HU) to the lungs produces a relative absolute error of 21.7±11.8%. This was reduced on average to 15.8±8.6% and 8.0±3.8% when using Hofmann and SAP techniques, respectively. Average and standard deviations of voxelwise RMB and RMAB between the ground truth PET-CTAC and PET-MRAC3c, PET-SAPAC and PET-HofmannAC computed for lung, fat, soft-tissue and bone regions are summarized in Table 4.

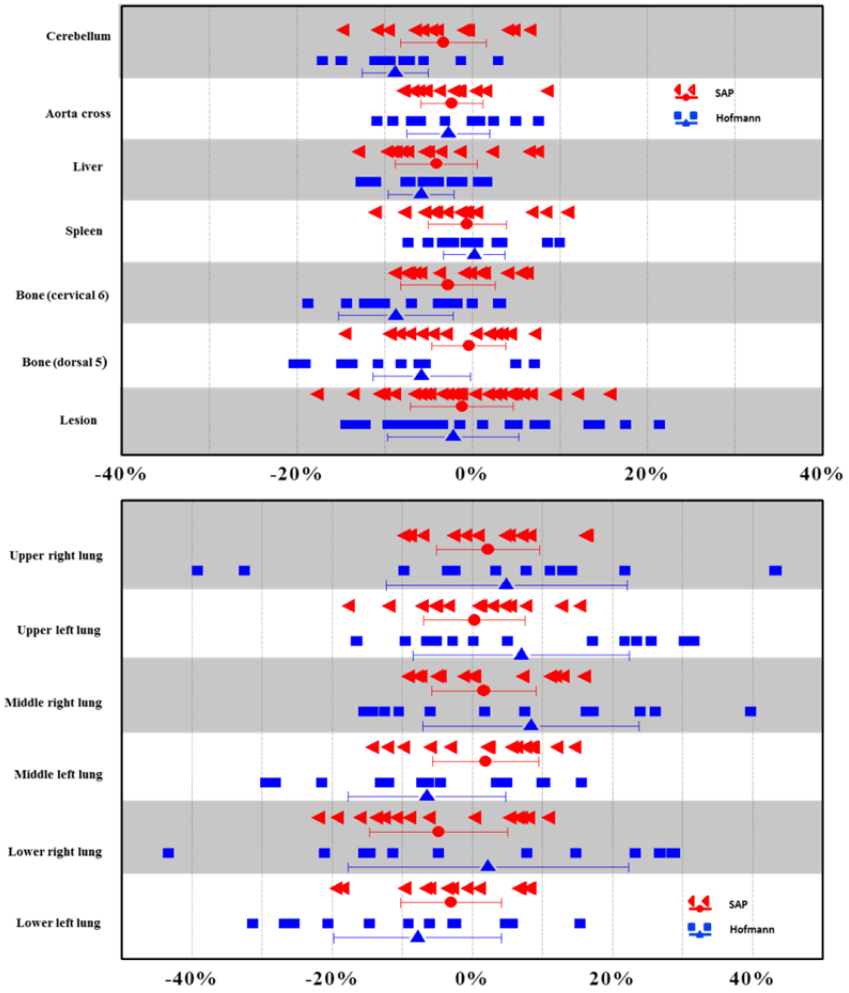

Figure 9. Mean relative errors (bias) of SUV_{mean} for PET images reconstructed using Hofmann's and SAP attenuation correction techniques for VOIs corresponding to 12 normal uptake regions and 36 malignant lesions.

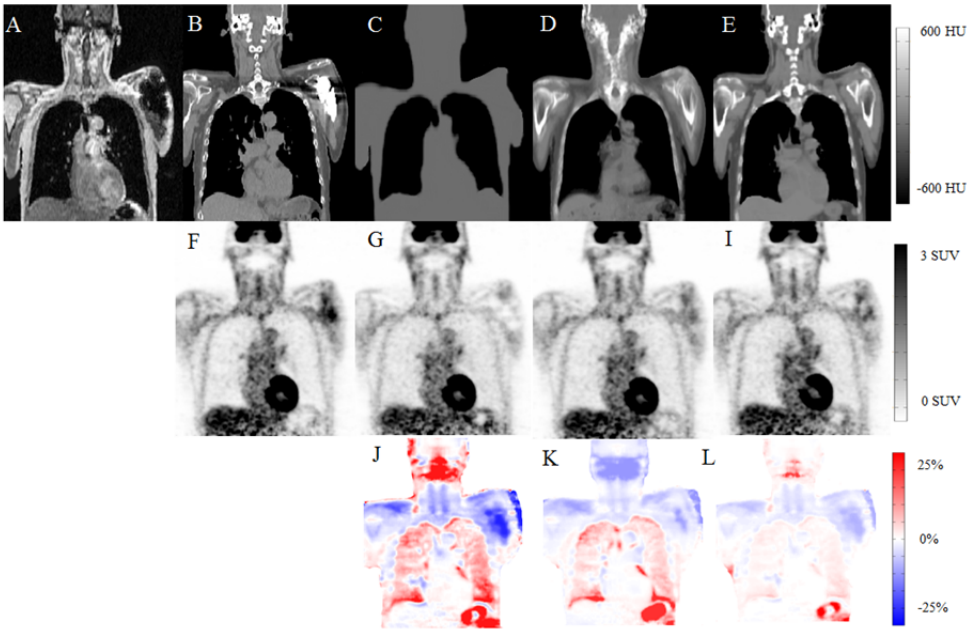

Figure 10. Impact of metallic artefacts. A) In-phase MRI, B) CT, attenuation map generated using C) 3-class attenuation map, D) Hofmann's technique, and E) our SAP approach. Corresponding attenuation corrected PET images: F) PET-CT, G) PET-MRAC3c, H) PET-HofmannAC and I) PET-SAPAC. Voxelwise SUV bias maps obtained by comparing PET-CTAC and J) PET-MRAC3c, K) PET-HofmannAC and L) PET-SAPAC. The estimated SUV_{mean} were 1.8 for PET-CT, 0.7 for PET-MRAC3c, 1.0 for PET-HofmannAC, and 1.2 PET-SAPAC.

Figure 10 depicts an example of metal artefacts portrayed on the MR image and its impact on the attenuation maps produced by the various strategies as well as the resulting PET images. The 3-class attenuation map generated by the Ingenuity TF PET/MR scanner (figure 10C) gave rise to body truncation reflected by the presence of a gap correlated with the void signal produced by MR in the presence of metallic objects. Given that metal implants usually replace bony structures, most atlas images predict bones for these regions. As such, both Hofmann and SAP approaches assigned close to bone attenuation coefficients to metallic objects, albeit the SAP attenuation map exhibited a higher contrast (figure 10D and E). The SUV_{mean} measured at the site of the metallic object (a large ROI was defined to cover the surrounding tissue) is 1.9, 0.7, 1.2 and 1.1 for PET-CTAC (figure 10F), PET-3CAC (figure 10G), PET-HofmannAC (figure 10H) and PET-SAPAC (figure 10I), respectively. It should be emphasized that it is likely that the SUV for the PET-CTAC doesn't reflect the actual value owing to the corruption of the CT images by metallic artefacts.

IV. Discussion

In this work, we focused on the accuracy of bone extraction as the most challenging issue in MRI-guided attenuation correction in PET/MRI. The visual inspection of figure 5 and the results presented in Table 1 revealed that superior bone extraction accuracy was achieved using our SAP approach (figure 5D). Since Hofmann's approach relies only on local similarity measure provided by the GPR kernel, thus lacking a semi-global scheme (such as the LNCC step) to discard misaligned atlases, the corresponding attenuation map (figure 5C) suffers from the lack of consensus in the warped atlas dataset.

Owing to the superior performance of our approach for bone extraction, the mean relative error (relative mean absolute error) decreased from -8.7±6.5% (10.5±5.0%) to -2.8±5.5% (5.8±2.9%) for cervical 6 and from -5.8±5.5 (6.7±4.8%) to -0.6±4.0% (4.2±2.4)% for dorsal 5 when using SAP compared to Hofmann's approach. The mean relative error of SUV_{mean} estimation in soft-tissue regions, such as the aorta cross, liver and spleen, didn't show significant differences between SAP and Hofmann's techniques according to the ROI-based analysis (Tables 2 and 3 and figure 9), since in both attenuation maps, these areas are filled with an average soft-tissue attenuation coefficient and are far from cortical bone [62, 63]. This is in agreement with observations made by Bezrukov et al. [18] who reported that filling areas far from bony structures with soft-tissue and fat attenuation coefficients had no significant impact on PET quantification. The atlas selection strategy primarily brings improvement to bone identification while fat and/or soft-tissue regions (particularly those far from bony structures) are less affected. In this regard, voxelwise SUV bias analysis (Table 4) and anatomical regions analysis (Supplemental Table 1) demonstrate slight improvement in soft-tissue class while more pronounced bias reduction is observed in bony regions.

The high negative bias for bony structures observed when using PET-MRAC3c (due to ignoring bone) is consistent with results reported in the literature, namely, -15% [63], -18% [64], -29% and -16% [10], -35% and -25% [62]. Likewise, similar SUV bias reduction was observed after including bones in the attenuation map [10, 62]. Although the mean SUV bias in lesions when using the 3-class technique is only 3.9% (with a relative mean absolute error of 9.8±4.5%), the absolute SUV difference between PET-MRAC3c and PET-CTAC is larger compared to other regions with a maximum SUV value of 2 for one lesion, causing a bias of -31.0%.

The average of mean relative absolute errors obtained in six lung regions decreased from 15.8±8.6% to 8.0±3.8% when using Hofmann and SAP approaches, respectively (Table 3). Apart from the overall SUV bias reduction, the standard deviation also decreased significantly for the VOIs defined in the lungs when using the SAP approach. The differences between SUV estimates were statistically significant in most regions except for the lungs where there was no proof of statistical difference for some VOIs (particularly the lower left lung). It is worth to mention that the maximum absolute SUV error observed in the lung region was 0.2. Attenuation correction using the 3-class technique exhibited an average positive bias (mean relative absolute error) in the lungs of 18.0% (21.7%) compared to -0.27% (8.0%) when using our SAP approach. The uniform lung attenuation coefficient of 0.022 cm^{-1} (770 HU) utilized on the Ingenuity TF PET/MRI seems to overcorrect the activity uptake. Ouyang *et al.* [63] also observed a positive uptake bias in the lungs for the 3-class attenuation map (5.8±14.6%).

The clinical study used to evaluate the correlation between lung volume and corresponding attenuation coefficients (figure 4) demonstrated a wide range of volume and density changes among subjects. Since patients were chosen randomly and CT scans likely acquired at slightly different respiratory phases, the wide range of

lung volumes can be attributed to either natural lung volume discrepancy among patients or different phase of the breathing cycle. Human lung volume and weight vary drastically across subjects depending on body height, altitude where they live and degree of obesity (actually ranging from 370 to 1.852 g and 1 to 8 litres, respectively) [65-67]. The results shown in figure 4 were not used in the learning process since the lung volumes were calculated by segmenting CT images (not MR Dixon images). Conversely, the lung mask used in the learning process was obtained by segmenting in-phase MR images with the same settings and parameters. Segmentation-based lung volume estimation is sensitive to the MR sequence used and the produced contrast and quality as well as the segmentation technique used. In particular cases where the MR image contrast and segmentation technique allow including the vascular tree and the boundary of peripheric structures, such as the heart (because of partial volume effect), the measured lung volume is expected to be larger. Therefore, the pre-processing utilities and segmentation protocol must be kept constant to avoid erroneous prediction. The correlation between segmented lung volumes using CT and MR images was carefully checked during the adjustment of segmentation parameters. The mean relative difference between lung volumes obtained from segmenting MR and CT images is -1.17±3.8% whereas the absolute mean relative difference is 3.39±1.7% over the 14 patients.

In figure 8, an attenuation coefficient of 0.022 cm^{-1} (770 HU) was assigned to the lesion in the 3-class attenuation map, whereas its average attenuation coefficient as estimated on the corresponding CT image is 0.0976 cm^{-1} (34 HU). The factors hampering the identification of these lesions include their low intensity on the MR image, limitations of segmentation techniques used, and size and position of lesions. The consequence is a significant underestimation of the tracer uptake in PET-MRAC3c (SUV_{mean} of 6.1) compared to 7.8 estimated after correcting the 3-class attenuation map and 9.7 obtained from PET-CTAC.

This method was used because of its simplicity but other sophisticated PET segmentation approaches which might have better performance can be used in this context [68]. The application of this approach was restricted to the lung region where the corresponding density is assumed to be known a priori and equivalent to soft-tissue. The same methodology could be extended to lesions located in different regions provided they can be accurately delineated.

In the case of existing connectivity between void areas inside the body caused by metallic artefacts and surrounding background air, it is very likely that the segmentation procedure fails to differentiate the inner body area from background air which leads to large misclassifications. Bezrukov *et al.* proposed an automated technique for susceptibility artefact correction enabling to assign proper attenuation coefficients to metal induced void regions [18]. Time-of-flight (TOF) PET image reconstruction has also been shown to substantially reduce the impact of metallic artefacts [69]. Figure 10C shows a representative clinical study presenting with metallic artefact where soft-tissue and the metallic implant in the patient shoulder have been misclassified as background air in the 3-class attenuation map. Since both SAP and Hofmann's approaches rely on information provided by the co-registered atlas dataset, they are less affected by metallic artefacts since void regions corresponding to the implant are usually filled with matching bony structures in the co-registered atlas. Moreover, using the k-nearest neighbour method in the SAP technique helps to pool the information from nearby textures to void areas to determine the most similar patient in the atlas dataset.

The method proposed in this work differs from that of (Burgos et al., 2014) in the sense that two different similarity measures are used and exploited for different purposes. The LNCC process exhibits local fluctuation and susceptibility to noise when it comes to local similarity measure. However, it shows suitable performance to detect misalignment at a relatively larger scale (large patch of images). Therefore, in contrast to Burgos' approach, the LNCC is not used to generate weighting factors for atlas fusion; instead it is used to exclude atlas images exhibiting misalignment errors within large patches of the image. For this reason, a relatively large window was used for the LNCC processing, ensuring a robust similarity measure. In essence, the LNCC is used for coarse atlas refinement and sieving while the GPR kernel is used for local matching.

The GPR kernel inherently contains a similarity measure based on intensity difference between patches of voxels within the image. The GPR kernel (Eqs. 1 or 3) acts very locally, in contrast to LNCC similarity measure, as there is a position-dependent term which decays exponentially as a function of the patch position. As such, this similarity measure is computed very locally (considering a patch size of 9×9 voxels with a voxel size of 1 mm). As such, the GPR kernel alone may be unable to identify similar anatomy between target and atlas images due to insufficient local information. The major improvement achieved by the proposed method can be attributed to the semi-local atlas sorting step achieved by the LNCC step (supplemental figure 2). Conversely, clustering

the MR images turned out to have a minor contribution compared to the atlas sorting step (supplemental figure 3), while rendering the algorithm more robust to inter-patient intensity non-uniformity.

Registration errors and anatomical differences across patients are the major challenges in atlas-based methods. Despite the improvement brought by the proposed method, slight imperfections can still be seen in some cases (figure 10E), particularly in the shoulders and head and neck areas. Further investigation is underway to minimize such errors by improving the accuracy of the registration algorithm and exploiting advanced pattern recognition techniques. Future work will focus on further improvement of bone extraction accuracy through optimization of atlas fusion and reduction of the computational time needed for atlas registration through alignment of multiple atlas images using a single registration to make the technique practical for clinical use.

V. Conclusion

We proposed a new whole-body pseudo-CT generation approach exploiting the concept of co-registered atlas and pattern recognition. The SAP technique improved bone extraction leading to more accurate SUV estimation, particularly in bony structures and lung regions even in the presence of malignant abnormalities.

Acknowledgments

This work was supported by the Swiss National Science Foundation under grant SNFN 31003A-149957.

Supplementary Material

Table 1S. Mean relative errors (mean relative absolute error) (mean±SD) between SUV_{mean} estimated using PET images corrected for attenuation using MRI-guided three-class (MRAC3c), Hofmann's and SAP (SAPAC) attenuation correction techniques and CT-based attenuation correction used as reference for the anatomical regions segmented on CT images.

Region	MRAC3c	Hofmann	SAPAC
Cerebellum	-14.6±6.5 (16.1±5.9)	-07.5±3.7 (8.6±3.1)	-02.5±4.5 (4.7±3.8)
Liver	-11.0±6.7 (14.0±7.9)	-06.0±4.0 (07.1 ±3.8)	-04.0±4.9 (6.5±2.5)
Spleen	-08.8±10.0 (14.9±8.5)	-01.0±4.0 (3.6±2.6)	-00.8±4.3 (5.0±3.5)
Bone (cervical 6)	-28.2±09.9 (31.5±10.5)	-10.3±6.6 (12.4±6.0)	-03.0±6.0 (6.1±3.0)
Bone (dorsal 5)	-23.9±10.4 (-24.1±10.0)	-06.5±5.6 (7.6±5.1)	-01.0±4.3 (5.0±2.9)

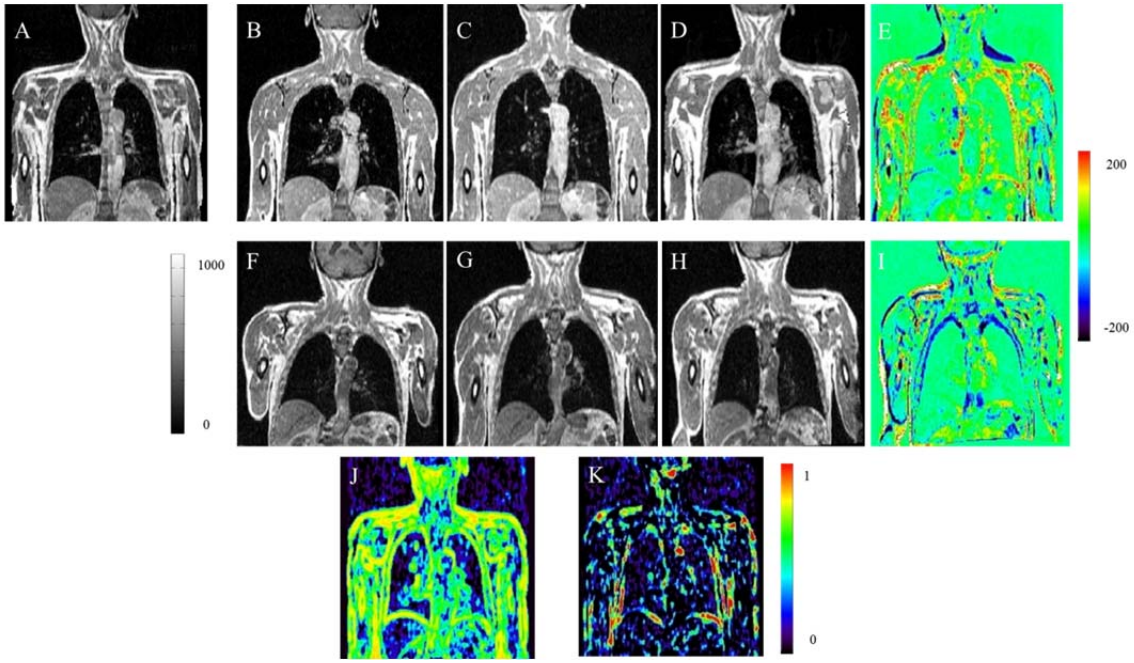

Figure 1S. Representative slices showing rigid and non-rigid registration of two clinical studies from the atlas dataset to the target image. (**A**) A representative slice of the target MRI. (**B**) MRI of a patient from the atlas dataset before registration. (**C**) Rigid registration of patient (**B**) to target (**A**). (**D**) Non-rigid registration of patient (**B**) to target (**A**). (**E**) The difference between (**D**) and (**C**) images. (**F**) Another patient from the atlas dataset before registration. (**G**) Rigid registration between patient (**F**) and target (**A**). (**H**) Non-rigid registration between patient (**F**) and target (**A**). (**I**) The difference between (H) and (G) images. (J) The LNCC score image computed between non-rigid registration result (**D**) and target subject (**A**) demonstrates a relatively good match. (K) The LNCC score image computed between non-rigid registration result (**H**) and target subject (**A**) demonstrates a poor match. The LNCC process is utilized to score atlas images on the basis of how well they are aligned to the target image in such a way that good matched images get a high score (**J**) and poor matched images tend to get a low score within the sub-image (**K**). It should be noted that negative LNCC scores in these images were folded to zeros.

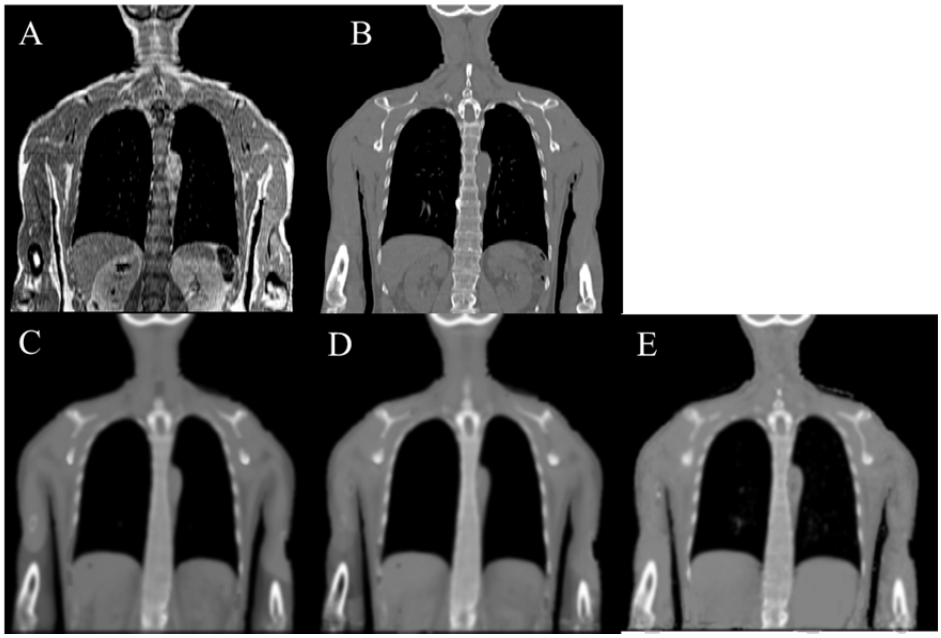

Figure 2S. Representative slices demonstrating the impact of LNCC step on the quality of the resulting pseudo CT. (**A**) A representative slice of the target MRI. (**B**) The corresponding CT image. (C) The resulting pseudo CT obtained from using Hofmann's method which exhibited DSC value of 0.645 for bone identification. (D) The resulting pseudo CT obtained from proposed method without LNCC step which exhibited DSC value of 0.652 for bone identification and (E) with LNCC step which exhibited DSC=0.727. The major portion of improvement brought by the proposed method was due to the impact of semi-local atlas sorting done by LNCC step.

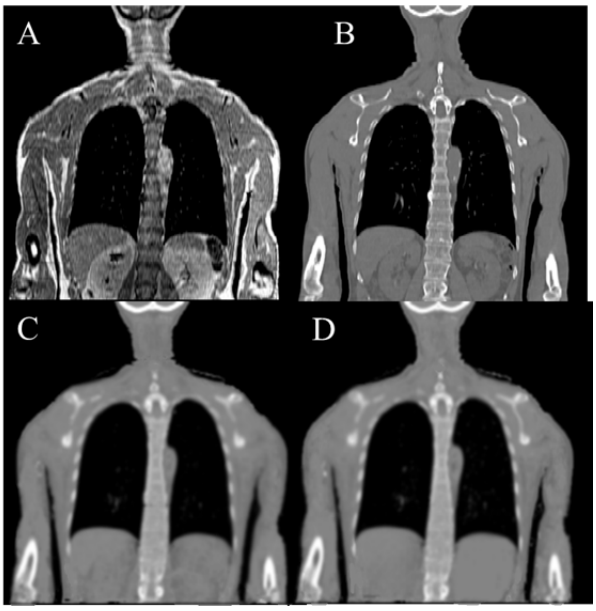

Figure 3S. Representative slices demonstrating the impact of clusterizing MR images on the quality of the resulting pseudo CT. (**A**) A representative slice of the target MRI. (**B**) The corresponding CT image. (C) The resulting pseudo CT obtained from using the proposed method without clusterization of MR image which exhibited DSC value of 0.718 for bone identification and (D) with clusterization step that exhibited DSC=0.727. The clusterization step has minor impact on the quality of resulting pseudo CT (as compared to atlas sorting step) while making the pseudo CT generation algorithm more robust to the inter-patient intensity variation.

References

[1] J. A. Disselhorst, I. Bezrukov, A. Kolb, C. Parl, and B. J. Pichler, "Principles of PET/MR Imaging.," *J Nucl Med,* vol. 55, pp. 2S-10S, May 12 2014.

[2] D. A. Torigian, H. Zaidi, T. C. Kwee, B. Saboury, J. K. Udupa, Z.-H. Cho*, et al.*, "PET/MR Imaging: Technical aspects and potential clinical applications," *Radiology,* vol. 267, pp. 26-44, 2013.

[3] H. Zaidi and A. Del Guerra, "An outlook on future design of hybrid PET/MRI systems.," *Med Phys,* vol. 38, pp. 5667-5689, 2011.

[4] I. Bezrukov, F. Mantlik, H. Schmidt, B. Scholkopf, and B. J. Pichler, "MR-based PET attenuation correction for PET/MR imaging.," *Semin Nucl Med,* vol. 43, pp. 45-59, Jan 2013.

[5] H. Zaidi and B. H. Hasegawa, "Determination of the attenuation map in emission tomography.," *J Nucl Med,* vol. 44, pp. 291-315, 2003.

[6] V. Schulz, I. Torres-Espallardo, S. Renisch, Z. Hu, N. Ojha, P. Börnert*, et al.*, "Automatic, three-segment, MR-based attenuation correction for whole-body PET/MR data.," *Eur J Nucl Med Mol Imaging,* vol. 38, pp. 138-152, 2011.

[7] H. Zaidi, M.-L. Montandon, and D. O. Slosman, "Magnetic resonance imaging-guided attenuation and scatter corrections in three-dimensional brain positron emission tomography.," *Med Phys,* vol. 30, pp. 937-948, 2003.

[8] A. Martinez-Moller, M. Souvatzoglou, G. Delso, R. A. Bundschuh, C. Chefd'hotel, S. I. Ziegler*, et al.*, "Tissue classification as a potential approach for attenuation correction in whole-body PET/MRI: Evaluation with PET/CT data.," *J Nucl Med,* vol. 50, pp. 520-526, Apr 2009.

[9] M. Hofmann, F. Steinke, V. Scheel, G. Charpiat, J. Farquhar, P. Aschoff*, et al.*, "MRI-based attenuation correction for PET/MRI: A novel approach combining pattern recognition and Atlas registration.," *J Nucl Med,* vol. 49, pp. 1875-1883, Oct 16 2008.

[10] M. Hofmann, I. Bezrukov, F. Mantlik, P. Aschoff, F. Steinke, T. Beyer*, et al.*, "MRI-based attenuation correction for whole-body PET/MRI: Quantitative evaluation of segmentation- and Atlas-based methods.," *J Nucl Med,* vol. 52, pp. 1392-1399, Sep 2011.

[11] A. Johansson, M. Karlsson, and T. Nyholm, "CT substitute derived from MRI sequences with ultrashort echo time.," *Med Phys,* vol. 38, pp. 2708-2714, May 2011.

[12] N. Burgos, M. Cardoso, K. Thielemans, M. Modat, J. Schott, J. Duncan*, et al.*, "Attenuation correction synthesis for hybrid PET-MR scanners: Application to brain studies.," *IEEE Trans Med Imaging,* vol. 33, pp. 2332-2341, Jul 17 2014.

[13] D. Izquierdo-Garcia, S. J. Sawiak, K. Knesaurek, J. Narula, V. Fuster, J. Machac*, et al.*, "Comparison of MR-based attenuation correction and CT-based attenuation correction of whole-body PET/MR imaging.," *Eur J Nucl Med Mol Imaging,* p. *in press*, Mar 21 2014.

[14] M. Defrise, A. Rezaei, and J. Nuyts, "Time-of-flight PET data determine the attenuation sinogram up to a constant.," *Phys Med Biol,* vol. 57, pp. 885-899, Feb 21 2012.

[15] A. Mehranian and H. Zaidi, "Joint estimation of activity and attenuation in whole-body TOF PET/MRI using constrained Gaussian mixture models.," *IEEE Trans Med Imaging,* p. *in press*, 2015.

[16] V. Y. Panin, F. Kehren, J. J. Hamill, and C. Michel, "Application of discrete data consistency conditions for selecting regularization parameters in PET attenuation map reconstruction," *Physics in medicine and biology,* vol. 49, p. 2425, 2004.

[17] H. Zaidi, N. Ojha, M. Morich, J. Griesmer, Z. Hu, P. Maniawski*, et al.*, "Design and performance evaluation of a whole-body Ingenuity TF PET-MRI system.," *Phys Med Biol,* vol. 56, pp. 3091-3106, Apr 20 2011.

[18] I. Bezrukov, H. Schmidt, F. Mantlik, N. Schwenzer, C. Brendle, B. Schölkopf*, et al.*, "MR-Based Attenuation Correction Methods for Improved PET Quantification in Lesions Within Bone and Susceptibility Artifact Regions," *Journal of Nuclear Medicine,* vol. 54, pp. 1768-1774, October 1, 2013 2013.

[19] G. Schramm, J. Langner, F. Hofheinz, J. Petr, B. Beuthien-Baumann, I. Platzek*, et al.*, "Quantitative accuracy of attenuation correction in the Philips Ingenuity TF whole-body PET/MR system: a direct comparison with transmission-based attenuation correction.," *Magn Reson Mat Phys Biol Med,* vol. 26, pp. 115-126, 2013.

[20] A. Varoquaux, O. Rager, A. Poncet, B. M. Delattre, O. Ratib, C. D. Becker*, et al.*, "Detection and quantification of focal uptake in head and neck tumours: (18)F-FDG PET/MR versus PET/CT.," *Eur J Nucl Med Mol Imaging,* vol. 41, pp. 462-475, Mar 2014.

[21] S. D. Wollenweber, S. Ambwani, G. Delso, A. H. R. Lonn, R. Mullick, F. Wiesinger*, et al.*, "Evaluation of an atlas-based PET head attenuation correction using PET/CT & MR patient data.," *IEEE Trans Nucl Sci,* vol. 60, pp. 3383-3390, 2013.

[22] V. Keereman, Y. Fierens, T. Broux, Y. De Deene, M. Lonneux, and S. Vandenberghe, "MRI-based attenuation correction for PET/MRI using ultrashort echo time sequences.," *J Nucl Med,* vol. 51, pp. 812-818, May 2010.

[23] G. Delso, F. Wiesinger, L. Sacolick, S. Kaushik, D. Shanbhag, M. Hullner*, et al.*, "Clinical evaluation of zero echo time MRI for the segmentation of the skull.," *J Nucl Med,* vol. 56, pp. 417-422, Feb 12 2015.

[24] M. Ebden, "Gaussian processes for regression: A quick introduction," *The Website of Robotics Research Group in Department on Engineering Science, University of Oxford,* 2008.

[25] K. Murphy, B. Van Ginneken, J. M. Reinhardt, S. Kabus, K. Ding, X. Deng*, et al.*, "Evaluation of registration methods on thoracic CT: the EMPIRE10 challenge," *Medical Imaging, IEEE Transactions on,* vol. 30, pp. 1901-1920, 2011.

[26] A. Akbarzadeh, D. Gutierrez, A. Baskin, M. R. Ay, A. Ahmadian, N. Riahi Alam*, et al.*, "Evaluation of whole-body MR to CT deformable image registration.," *J Appl Clin Med Phys,* vol. 14, pp. 238-253, 2013.

[27] A. Klein, J. Andersson, B. A. Ardekani, J. Ashburner, B. Avants, M.-C. Chiang*, et al.*, "Evaluation of 14 nonlinear deformation algorithms applied to human brain MRI registration," *Neuroimage,* vol. 46, pp. 786-802, 2009.

[28] L. J. Rosenblum, R. A. Mauceri, D. E. Wellenstein, F. D. Thomas, D. A. Bassano, B. N. Raasch*, et al.*, "Density patterns in the normal lung as determined by computed tomography.," *Radiology,* vol. 137, pp. 409-416, Nov 1980.

[29] K. Soejima, K. Yamaguchi, E. Kohda, K. Takeshita, Y. Ito, H. Mastubara*, et al.*, "Longitudinal follow-up study of smoking-induced lung density changes by high-resolution computed tomography.," *Am J Respir Crit Care Med,* vol. 161, pp. 1264-1273, Apr 2000.

[30] H. R. Marshall, F. S. Prato, L. Deans, J. Theberge, R. T. Thompson, and R. Z. Stodilka, "Variable lung density consideration in attenuation correction of whole-body PET/MRI.," *J Nucl Med,* vol. 53, pp. 977-984, Jun 2012.

[31] Y. Berker, A. Salomon, F. Kiessling, and V. Schulz, "Lung attenuation coefficient estimation using Maximum Likelihood reconstruction of attenuation and activity for PET/MR attenuation correction," in *IEEE Nuclear Science Symposium and Medical Imaging Conference (NSS/MIC)*, 2012, pp. 2282-2284.

[32] A. Mehranian and H. Zaidi, "Emission-based estimation of lung attenuation coefficients for attenuation correction in time-of-flight PET/MR.," *Phys Med Biol,* p. *under revision*, 2015.

[33] W. T. Dixon, "Simple proton spectroscopic imaging.," *Radiology,* vol. 153, pp. 189-194, Oct 1984.

[34] J. M. Lotjonen, R. Wolz, J. R. Koikkalainen, L. Thurfjell, G. Waldemar, H. Soininen*, et al.*, "Fast and robust multi-atlas segmentation of brain magnetic resonance images.," *Neuroimage,* vol. 49, pp. 2352-2365, Feb 1 2010.

[35] Y. Zhuge, J. K. Udupa, J. Liu, and P. K. Saha, "Image background inhomogeneity correction in MRI via intensity standardization," *Computerized Medical Imaging and Graphics,* vol. 33, pp. 7-16, 2009.

[36] L. G. Nyúl, J. K. Udupa, and X. Zhang, "New variants of a method of MRI scale standardization," *Medical Imaging, IEEE Transactions on,* vol. 19, pp. 143-150, 2000.

[37] Y. Tong, J. K. Udupa, D. Odhner, S. Sharma, and D. A. Torigian, "Interactive non-uniformity correction and intensity standardization of MR images," in *SPIE Medical Imaging*, 2015, pp. 94151N-94151N-6.

[38] J. Weickert, *Anisotropic diffusion in image processing* vol. 1: Teubner Stuttgart, 1998.

[39] N. J. Tustison, B. B. Avants, P. A. Cook, Y. Zheng, A. Egan, P. A. Yushkevich*, et al.*, "N4ITK: improved N3 bias correction.," *IEEE Trans Med Imaging,* vol. 29, pp. 1310-1320, Jun 2010.

[40] M. J. McAuliffe, F. M. Lalonde, D. McGarry, W. Gandler, K. Csaky, and B. L. Trus, "Medical Image Processing, Analysis and Visualization in clinical research," in *14th IEEE Symposium on Computer-Based Medical Systems, 2001. CBMS 2001. Proceedings*, 2001, pp. 381-386.

[41] N. Robitaille, A. Mouiha, B. Crépeault, F. Valdivia, and S. Duchesne, "Tissue-based MRI intensity standardization: application to multicentric datasets," *Journal of Biomedical Imaging,* vol. 2012, p. 4, 2012.

[42] M. Kass, A. Witkin, and D. Terzopoulos, "Snakes: active contour models.," *Int J Comput Vision,* vol. 1, pp. 321-331, 1988.

[43] P. A. Yushkevich, J. Piven, H. C. Hazlett, R. G. Smith, S. Ho, J. C. Gee*, et al.*, "User-guided 3D active contour segmentation of anatomical structures: significantly improved efficiency and reliability.," *Neuroimage,* vol. 31, pp. 1116-1128, Jul 1 2006.

[44] T. S. Yoo, M. J. Ackerman, W. E. Lorensen, W. Schroeder, V. Chalana, S. Aylward*, et al.*, "Engineering and algorithm design for an image processing Api: a technical report on ITK-the Insight Toolkit.," *Stud Health Technol Inform,* vol. 85, pp. 586-592, 2002.

[45] P. A. Yushkevich, H. Wang, J. Pluta, S. R. Das, C. Craige, B. B. Avants*, et al.*, "Nearly automatic segmentation of hippocampal subfields in in vivo focal T2-weighted MRI.," *Neuroimage,* vol. 53, pp. 1208-1224, Dec 2010.

[46] P. Cachier, E. Bardinet, D. Dormont, X. Pennec, and N. Ayache, "Iconic feature based nonrigid registration: the PASHA algorithm.," *Comp Vis Image Underst,* vol. 89, pp. 272-298, 2// 2003.

[47] N. S. Altman, "An Introduction to Kernel and Nearest-Neighbor Nonparametric Regression," *The American Statistician,* vol. 46, pp. 175-185, 1992/08/01 1992.

[48] M. Kapanen and M. Tenhunen, "T1/T2*-weighted MRI provides clinically relevant pseudo-CT density data for the pelvic bones in MRI-only based radiotherapy treatment planning," *Acta Oncologica,* vol. 52, pp. 612-618, 2013.

[49] A. R. Lonn and S. D. Wollenweber, "Estimation of mean lung attenuation for use in generating PET attenuation maps," in *IEEE Nuclear Science Symposium and Medical Imaging Conference (NSS/MIC)*, 2012, pp. 3017-3018.

[50] G. H. Chen, Z. F. Yao, X. W. Fan, Y. J. Zhang, H. Q. Gao, W. Qian*, et al.*, "Variation in background intensity affects PET-based gross tumor volume delineation in non-small-cell lung cancer: the need for individualized information.," *Radiother Oncol,* vol. 109, pp. 71-76, Oct 2013.

[51] A. Rosenfeld and A. C. Kak, *Digital Picture Processing: Vol.: 1*: Academic Press, Incorporated, 1982.

[52] R. L. Wahl, H. Jacene, Y. Kasamon, and M. A. Lodge, "From RECIST to PERCIST: Evolving considerations for PET response criteria in solid tumors.," *J Nucl Med,* vol. 50, pp. 122S-150, May 1, 2009 2009.

[53] P.-E. Danielsson, "Euclidean distance mapping," *Computer Graphics and image processing,* vol. 14, pp. 227-248, 1980.

[54] H. Arabi, O. Rager, A. Alem, A. Varoquaux, M. Becker, and H. Zaidi, "Clinical assessment of MR-guided 3-class and 4-class attenuation correction in PET/MR.," *Mol Imaging Biol,* vol. 17, pp. 264-276, 2015.

[55] M. R. Ay, A. Akbarzadeh, A. Ahmadian, and H. Zaidi, "Classification of bones from MR images in torso PET-MR imaging using a statistical shape model.," *Nucl Instrum Meth A,* vol. 734, Part B, pp. 196-200, 1/11/ 2014.

[56] L. R. Dice, "Measures of the amount of ecologic association between species.," *Ecology,* vol. 26, pp. 297-302, 1945.

[57] T. Heimann, B. van Ginneken, M. A. Styner, Y. Arzhaeva, V. Aurich, C. Bauer*, et al.*, "Comparison and evaluation of methods for liver segmentation from CT datasets.," *IEEE Trans Med Imaging,* vol. 28, pp. 1251-1265, Aug 2009.

[58] D. L. Collins and J. C. Pruessner, "Towards accurate, automatic segmentation of the hippocampus and amygdala from MRI by augmenting ANIMAL with a template library and label fusion.," *Neuroimage,* vol. 52, pp. 1355-1366, Oct 1 2010.

[59] Y. Xia, J. Fripp, S. S. Chandra, R. Schwarz, C. Engstrom, and S. Crozier, "Automated bone segmentation from large field of view 3D MR images of the hip joint.," *Phys Med Biol,* vol. 58, pp. 7375-7390, 2013.

[60] G. Gerig, M. Jomier, and M. Chakos, "Valmet: A New Validation Tool for Assessing and Improving 3D Object Segmentation," presented at the Proceedings of the 4th International Conference on Medical Image Computing and Computer-Assisted Intervention, 2001.

[61] W. R. Crum, O. Camara, and D. L. Hill, "Generalized overlap measures for evaluation and validation in medical image analysis," *Medical Imaging, IEEE Transactions on,* vol. 25, pp. 1451-1461, 2006.

[62] H. R. Marshall, J. Patrick, D. Laidley, F. S. Prato, J. Butler, J. Theberge*, et al.*, "Description and assessment of a registration-based approach to include bones for attenuation correction of whole-body PET/MRI.," *Med Phys,* vol. 40, p. 082509, Aug 2013.

[63] J. Ouyang, S. Y. Chun, Y. Petibon, A. A. Bonab, N. Alpert, and G. El Fakhri, "Bias atlases for segmentation-based PET attenuation correction using PET-CT and MR.," *IEEE Trans Nuc Sci,* vol. 60, pp. 3373-3382, 2013.

[64] J. H. Kim, J. S. Lee, I. C. Song, and D. S. Lee, "Comparison of segmentation-based attenuation correction methods for PET/MRI: Evaluation of bone and liver standardized uptake value with oncologic PET/CT data.," *J Nucl Med,* vol. 53, pp. 1878-1882, Dec 2012.

[65] D. K. Molina and V. J. M. DiMaio, "Normal Organ Weights in Men: Part II—The Brain, Lungs, Liver, Spleen, and Kidneys," *The American Journal of Forensic Medicine and Pathology,* vol. 33, pp. 368-372, 2012.

[66] R. L. Jones and M.-M. U. Nzekwu, "The effects of body mass index on lung volumes," *Chest journal,* vol. 130, pp. 827-833, 2006.

[67] E. N. Marieb and K. Hoehn, *Human anatomy & physiology*: Pearson Education, 2007.

[68] M. Abdoli, R. A. J. O. Dierckx, and H. Zaidi, "Contourlet-based active contour model for PET image segmentation.," *Med Phys,* vol. 40, pp. 082507-12, 2013.

[69] A. Mehranian and H. Zaidi, "Impact of time-of-flight PET on quantification errors in MR imaging-based attenuation correction," *J Nucl Med,* vol. 56, pp. 635-41, Apr 2015.

Chapter 5

Comparison of atlas-based techniques for whole-body bone segmentation

Hossein Arabi and Habib Zaidi

Medical Image Analysis Vol. 36, pp 98–112 (2017)

Abstract

Purpose: We evaluate the accuracy of whole-body bone extraction from whole-body MR images using a number of atlas-based segmentation methods. The motivation behind this work is to find the most promising approach for the purpose of MRI-guided derivation of PET attenuation maps in whole-body PET/MRI. To this end, a variety of atlas-based segmentation strategies commonly used in medical image segmentation and pseudo-CT generation were implemented and evaluated in terms of whole-body bone segmentation accuracy.

Methods: Bone segmentation was performed on 23 whole-body CT/MR image pairs via leave-one-out cross validation procedure. The evaluated segmentation techniques include: (i) intensity averaging (IA), (ii) majority voting (MV), (iii) global and (iv) local (voxel-wise) weighting atlas fusion frameworks implemented utilizing normalized mutual information (NMI), normalized cross-correlation (NCC) and mean square distance (MSD) as image similarity measures for calculating the weighting factors, along with other atlas-dependent algorithms, such as (v) shape-based averaging (SBA) and (vi) Hofmann's pseudo-CT generation method. The performance evaluation of the different segmentation techniques was carried out in terms of estimating bone extraction accuracy from whole-body MRI using standard metrics, such as Dice similarity (DSC) and relative volume difference (RVD) considering bony structures obtained from intensity thresholding of the reference CT images as the ground truth.

Results: Considering the Dice criterion, global weighting atlas fusion methods provided moderate improvement of whole-body bone segmentation (DSC=0.65±0.05) compared to non-weighted IA (DSC=0.60±0.02). The local weighed atlas fusion approach using the MSD similarity measure outperformed the other strategies by achieving a DSC of 0.81±0.03 while using the NCC and NMI measures resulted in a DSC of 0.78±0.05 and 0.75±0.04, respectively. Despite very long computation time, the extracted bone obtained from both SBA (DSC=0.56±0.05) and Hofmann's methods (DSC=0.60±0.02) exhibited no improvement compared to non-weighted IA. Finding the optimum parameters for implementation of the atlas fusion approach, such as weighting factors and image similarity patch size, have great impact on the performance of atlas-based segmentation approaches.

Conclusions: The voxel-wise atlas fusion approach exhibited excellent performance in terms of cancelling out the non-systematic registration errors leading to accurate and reliable segmentation results. Denoising and normalization of MR images together with optimization of the involved parameters play a key role in improving bone extraction accuracy.

I. Introduction

The emergence of hybrid imaging techniques, such as PET/CT and PET/MRI in clinical practice engendered a number of new clinical and research opportunities and improved the quantitative accuracy and diagnostic confidence of PET findings [1]. A number of active research groups are focusing their efforts on addressing the challenges of combined PET/MRI, encompassing instrumentation developments, optimization of workflow and data acquisition protocols and the improvement of the quantitative performance of both imaging modalities [2]. Beside the precious anatomical information provided by CT or MRI, additional information that can be extracted from these images, such as attenuation properties of body tissues and motion information can be exploited for correction of emission data and quantitative PET image reconstruction. However, MRI-guided attenuation correction in whole-body PET/MRI proved to be a challenging issue and has therefore remained an active and open research question during the last decade [3]. Commercially available PET/MR scanners employ tissue classification methods, which rely on segmentation of MR images into tissue classes and assigning uniform linear attenuation coefficients to each tissue class [4, 5]. The major drawback of such methods, particularly in the context of whole-body imaging, lies in ignoring bones as a separate tissue class. Since bone tissue generates a void signal when using common MR sequences, it is indistinguishable from air. As such, bony structures are commonly replaced by soft-tissue in current methods, thus leading to significant underestimation of tracer uptake in the vicinity of bony structures [6, 7].

A number of techniques have been proposed to consider bone tissue during attenuation correction (AC) in whole-body PET/MRI. Basically two categories have emerged: atlas-guided attenuation map generation approaches [6-10] and emission-based approaches [11, 12]. Atlas-guided methods primarily rely on prior information provided by registration of an atlas into target image coordinates to allow classification of bone tissues. Direct segmentation of bones from MR images, particularly in whole-body imaging, is a difficult task owing to anatomical complexity, low quality and high noise level of dedicated MR sequences used for the purpose of AC [13]. Atlas-guided segmentation has been successfully applied in various image segmentation tasks using a wide variety of imaging modalities [14]. In principle, each individual atlas image transformed to the coordinates of the target image is regarded as potential candidate. It has, however, been proven that using the information from multiple atlas images leads to more accurate results [15]. The information obtained from several atlas images can be pooled into an average atlas or into a so called probabilistic atlas [15, 16]. However, there is a trend to take full advantage of multiple atlas images at hand by exploiting pattern recognition techniques to identify morphologically similar cases in the atlas dataset during the multi-atlas fusion process. This dramatically reduces non-systematic registration errors and improves the accuracy of the segmentation [17].

Various strategies were proposed to incorporate bone tissue in PET/MRI attenuation maps in whole-body imaging [6-9, 18-20]. In whole-body imaging, almost all proposed methods, except joint attenuation-activity reconstruction techniques, rely on prior knowledge present in atlas images to predict bone from MRI. Moreover, owing to long acquisition time, application of ultra-short echo time (UTE) [21] or zero time echo (ZTE) [22] sequences are still limited to brain imaging (single bed position). Atlas-guided segmentation has been successfully applied in various image segmentation tasks using different imaging modalities, particularly for cases with very low contrast to the surrounding tissues [14]. Atlas-based methods are of special interest since they have so far exhibited superior performance in terms of bone identification [23] particularly in whole-body imaging [7]. Burgos et al. [23] demonstrated superior performance of atlas-based methods in CT synthesis and PET quantitative accuracy compared to a segmentation method using an UTE MRI sequence in brain imaging. Likewise, Mehranian et al, [24] demonstrated that atlas-based methods provide the most accurate attenuation maps compared to simultaneous activity-attenuation estimation and state-of-the-art 3-class segmentation method. In whole-body imaging, Hofmann et al. [7] proposed an atlas-based method combined with a pattern recognition technique, which resulted in less than 10% uptake error on average, thus outperforming standard segmentation methods in whole-body imaging. Marshall et al. [9] evaluated a method enabling to incorporate bony structures into attenuation maps based on a fast atlas-based approach. By including bone, the magnitude of the relative error was reduced to a range acceptable in clinical setting.

Various atlas-based methods were independently developed and evaluated using different MRI sequences, different atlas datasets in terms of sample size, patient variability, field of view and body region, different MRI quality (noise level or acquisition time) and evaluation procedures and metrics. Although there is substantial literature reporting promising results achieved by atlas-based methods, the performance of these techniques still

requires further investigation based on a common ground. Therefore, a comparison of various atlas-based strategies provides a valuable insight into their application to attenuation correction in PET/MRI.

Since the delineation of bones is the most challenging task in whole-body MRI-guided attenuation map generation, we focused our comparison of the various pseudo-CT generation approaches and atlas-based segmentation methods on the accuracy of extracted whole-body bone. To this end, we selected and implemented a number of conventional atlas-based segmentation methods, such as majority voting, intensity averaging, global and local weighting atlas fusion strategies together with Hofmann's algorithm (proposed for whole-body PET/MR attenuation map generation) and shape-based averaging (SBA) technique. In addition to the comparison of the different segmentation techniques, our goal is to select the most promising algorithm for attenuation correction in whole-body PET/MRI. The very preliminary results of this work have been previously published [25]. The present article presents a substantial extension of the previous work through the implementation and comparison of a higher number of algorithms using a larger database of clinical studies and reporting more detailed quantitative analysis of the data.

II. Materials and Methods

II.A. Atlas-based segmentation

The objective of atlas-based segmentation is to provide labeling of unknown tissue classes on the target image. Consider the segmentation of an image with potentially L different classes belonging to a label set $Label = \{1,2, \dots, L\}$. In the case of bone segmentation, the number of classes is confined to L=2 where label 1 stands for background and label 2 represents bony structures. Here, a set of 3-D MR images Amr_n along with their corresponding aligned CT images Act_n are considered as atlas images. An atlas-based classifier is defined by a set of atlas images Amr_n $n=1, \dots, N$ and transformation matrices (M_n) which map coordinates from the target image T to the atlas images n: M_n: $\mathbb{R}^3 \rightarrow \mathbb{R}^3$. Since bone segmentation can be simply carried out by intensity thresholding of CT images, Act_n images act as candidates for tissue labeling of the target MR image of T. Applying a given transformation matrix M_n to an atlas image Act_n yields an estimated segmentation of the target subject T_{An} where a set of segmentation candidates T_{An} $n=1, \dots, N$ must be combined to form the final estimated bone segmentation T_s. Atlas-based segmentation can be regarded as the classification of X unordered samples where the candidate n assigns x to class $l \in Label$. The output of N independent classifiers can be combined to generate a single response of the combination strategy, $E(x)$. The aim of building an ensemble classifier is to achieve a higher probability of correctly classifying the voxels of the image than that obtained by using an individual classifier maximizing the probability given all classifier decisions T_{An} and a classifier performance model C (Eq. 1) [26].

$$E(x) = arg\,max_l\, P(x = l\,|T_{A1}, \dots, T_{AN}, C) \quad (1)$$

II.B. PET/CT and PET/MR data acquisition

The study population comprised N=23 consecutive patients, 15 men and 8 women (mean age ± SD = 60 ± 8 y), refereed to our department for MRI of the head and neck, whole-body ^{18}F-FDG PET/MRI and whole-body ^{18}F-FDG PET/CT for staging of head and neck malignancies. The study protocol was approved by the institutional ethics committee and all patients gave their informed consent to participate in the study. ^{18}F-FDG PET/CT scans were performed on a Biograph 64 True Point scanner (Siemens Healthcare, Erlangen, Germany). The CT subsystem consists of a 40-row ceramic detector with 1344 channels per row using adaptive collimation and the z-sharp technique to acquire 64 slices per rotation. After a localization scout scan, an unenhanced CT scan (120 kVp, 180 mAs, 24×1.5 collimation, a pitch of 1.2, and 1 s per rotation) was performed for attenuation correction and localization. The typical acquisition time for whole-body CT was less than 10 s. PET/MRI examinations were performed on the Ingenuity TF PET/MR, a sequential system consisting of a whole-body time-of flight (TOF) GEMINI TF PET and a 3T Achieva TX MRI separated by a distance of 3 m sharing a common rotating table platform [27]. The gradient system value and the slew rate are 40mT/m and 100mT/m/s, respectively. The coils used for MR imaging include a SENSE neurovascular 16-channel coil for head and neck and a quadrature body coil for total body scanning. Whole-body Dixon examinations were performed on the 3T Achieva TX MRI of the Ingenuity TF PET/MR scanner. The whole body Dixon 3D volumetric interpolated T1-weighted sequence [28] was acquired using the following parameters: flip angle 10°, TE_1 1.1 ms, TE_2 2.0 ms, TR 3.2 ms, 450×354

mm^2 transverse FOV, 0.85×0.85×3 mm^3 voxel size, and a total acquisition time of 2 min 17 s. Both MRI and CT acquisitions were performed in free shallow breathing. This sequence produced in-phase and opposed-phase images that are then added together to obtain water only images, and subtracted to get fat-only images. In-phase images were used for the assessment of whole-body bone segmentation.

Due to temporal separation between MRI and CT acquisitions, in-phase MRI were deformably registered to the corresponding CT images using the Elastix framework based on the ITK library [29] using a combination of rigid registration based on maximum mutual information and non-rigid registration as described previously [30]. MRI and CT acquisitions were performed with the same patient positioning to minimize non-rigid deformation. However, in case of alignment errors owing for instance to breathing motion, the registration parameters were adjusted to achieve acceptable results. In case of gross registration errors, the studies were excluded.

II.C. Data preprocessing

Clinical whole-body MR images contain a relatively high level of noise and are commonly corrupted by low frequency bias field and inter-patient intensity inhomogeneity [31]. As will be described in the following section, bone segmentation procedures entail direct handling of MR image intensity. As such, the presence of aforementioned sources of intensity variation in MR images might skew bone segmentation accuracy. To overcome these prospective sources of error, in-phase MR images of all patients underwent some pre-processing procedures in the following order:

- Gradient anisotropic diffusion filtering to suppress noise using the following parameters: conductance= 4, iterations=10 and time step=0.01. This algorithm smoothes regions of an image where the gradient magnitude is relatively small (homogenous regions) but diffuses little over areas of the image where the gradient magnitude is large (i.e., edges). Therefore, the central regions of objects are smoothed but their edges are blurred to a lower extent.
- N4 bias field correction [32] to remove magnetic field inhomogeneity effect: Bspline grid resolution=400, number of iteration = 200 (at each grid resolution), convergence threshold = 0.001, Bspline order = 3, Spline distance = 400, number of histograms = 256 and shrink factor = 3.
- Histogram matching [33]: Histogram level = 1024 and match points = 128. In order to get the best result from histogram matching, it is recommended to exclude background air voxels of both reference and target images before processing.

The bone segmentation procedure requires the binary mask of segmented background air to save processing time. To this end, the external body contour was determined by applying a 3D active snake contour algorithm on in-phase MR images [34]. The segmentation process begins by manual selection of the initial seeds in the background using the ITK-SNAP image processing software [35].

II.D. Label fusion strategies

This study contains 23 pairs of co-registered in-phase MRI Dixon and CT images. All MR images were processed according to the procedure described in section 2.3. Using the leave-one-out cross-validation (LOOCV) method, for each subject, images of the remaining *N-1* (i.e. 22) patients are non-rigidly warped to the coordinates of the target image. Image registration was carried out using the Elastix package (based on the ITK library) [29] through a combination of affine and non-rigid alignment based on the advanced Mattes mutual information as described in previous work [30]. The following parameters were adopted: interpolate: Bspline, optimizer: standard gradient descent, image pyramid schedule: (16 8 4 2 2), grid spacing schedule (32.0 16.0 8.0 4.0 2.0), maximum number of iterations (4096 4096 2048 1024 512), number of histogram bins: 32. The obtained transformation matrices from the registration between atlas and target MR images were applied to the corresponding atlas CT images. For each target image, 22 candidate CT images are available from which bone can be segmented by intensity thresholding using a threshold of 180 HU. This work focuses on how well the label fusion strategies can pool the information from 22 segmentation candidates to maximize the final bone extraction accuracy. In the following sections, we describe in detail label fusion strategies commonly used in atlas-based segmentation.

1) General averaging

A commonly used approach for pseudo-CT generation and segmentation of anatomical structures is to simply calculate the arithmetic average of the aligned atlas images [16, 36]. In our case, general arithmetic averaging is performed by computing the intensity average of *N=22* aligned atlas CT images (Eq. 2). There is no selective or weighting strategy in this approach and all atlas images (regardless of their morphological similarity to the target subject) contribute equally to bone extraction process.

$$T_{av} = \frac{1}{N}\sum_{n=1}^{N} T_{An} \qquad Bn(x) = \begin{cases} 1, & \text{if } T_{av}(x) > 180 \\ 0, & \text{otherwise} \end{cases} \tag{2}$$

Here T_{An} is the n^{th} aligned atlas CT image to the target image *T*. As mentioned earlier, bone segmentation (B_n) can be performed by applying intensity thresholding to the average image, T_{av}. Hereafter, we call this approach intensity averaging (IA), meaning bone segmentation is performed after the averaging process.

The same task can be achieved by the well-known majority voting framework where instead of taking the average intensity of aligned atlas CT images, each CT image is converted to a binary bone mask (T_{Sn}) followed by the averaging process. The voxel the majority of classifiers agree on is labeled as bone (Eq. 3) [17, 37-39].

$$T_{Sav} = \frac{1}{N}\sum_{n=1}^{N} T_{Sn} \qquad B(x) = \begin{cases} 1, & \text{if } T_{Sav}(x) > 0.5 \\ 0, & \text{otherwise} \end{cases} \tag{3}$$

T_{Sav} is also called bone probability map where values of 1 and 0 indicate that all the atlases unanimously predict bony and non-bony tissues for that voxel, respectively.

It is hypothesized that the number of atlas images *N* has a major impact on the accuracy of extracted bone [37]. To evaluate this feature, bone segmentation was carried out for various numbers of atlases selected randomly among the 22 patient datasets.

Conventional multi-atlas segmentation approaches entails *N* online registrations between target and atlas images. A number of studies utilized only one single atlas image or template (obtained from taking the average of population) is utilized to delineate the anatomical structures in the target image after warping the atlas image to the target coordinates to reduce the computation time [36, 37]. Consequently, this approach requires only one online registration, which makes it computationally efficient. The performance evaluation of the single atlas approach is of special interest since it introduces a tradeoff between computational time and the quality of the outcome compared to conventional multi-atlas approach. The single atlas approach, referred as "single atlas image" in Table 4, was compared to various multi-atlas approaches. To evaluate the accuracy of this approach, an iterative atlas generation framework was utilized via the LOOCV scheme [16]. In summary, an MR image belonging to the patient with the median body mass index of the population was selected as the initial atlas for atlas space alignment. The initial iteration contains the registration of other MR images to the selected atlas using the sequential affine and non-rigid registration procedure described in section 2.4. At the end of each iteration, the new average atlas is generated and used in the subsequent iteration. Since the template obtained from the previous iteration serves better as common/reference spatial coordinate, after each iteration, the obtained template would be more representative for the target subject. In the present work, we used five iterations and the final transformation field was applied on the corresponding CTs to yield the average CT atlas. In the last step, the average MRI atlas is non-rigidly aligned to the target MRI and bone segmentation is carried out on the warped average CT image. As mentioned earlier, this approach requires only one online registration and the atlas creation is performed offline.

2) Global weighting

The methods described in section 2.4.1 do not involve any strategy to detect and consequently discard miss-registration errors. Registration errors occur due to local minima, inter-patient anatomy variability and presence of noise, which might incur gross mismatch on the resulting images [15]. One strategy to overcome the misalignment error consists in assigning weights to the atlas images globally (as opposed to local or voxel-wise approach) on the basis of morphological similarity between target and atlas images. By this approach, aligned atlas images presenting the higher degree of anatomy and pose similarities contribute more effectively to the resulting segmentation [17, 39-41]. The first step toward weighted atlas-based segmentation consists in developing a similarity criterion between the target image and aligned atlas images. Normalized mutual information (NMI), normalized cross correlation (NCC) and mean square distance (MSD) are the most common

similarity measures used for implementation of weighted atlas-based segmentation [38, 39]. These similarity measures are briefly described below. Normalized mutual information is defined as:

$$NMI = \frac{H(T)+H(M(Amr_n))}{H(T,M(Amr_n))} \tag{4}$$

where $H(T)$ is the entropy of image T and $H(T,M(Amr_n))$ indicates the joint entropy of both images. The entropy of an image can be computed from its histogram $h(x)$ as:

$$H(T) = -\sum_{i=1}^{F} h(c_i) log_2 h(c_i)$$

where F is the number of histogram bins and c_i corresponds to the centroid of the i^{th} histogram bin [42].

The normalized cross-correlation between the two images is defined as:

$$NCC = \frac{Cov(T,M(Amr_n))}{\sqrt{Var(T)}.\sqrt{Var(M(Amr_n))}} \tag{5}$$

where $Cov(T, M(Amr_n))$ is the covariance of the images and $Var(T)$ indicates the variance of the image T.

The mean square distance is simply the intensity difference between two images. Here, we used the following formulation to measure the intensity similarity between the target MR image (T) and the co-registered atlas MR images ($M(Amr_n)$). X denotes the total number of image voxels.

$$MSD = \frac{X}{\sum_{x=0}^{X} |T(x) - M(Amr_n(x))|^2} \tag{6}$$

Previously published works in the realm of multi-atlas based segmentation employed various ways of incorporating weighting factors in either majority voting (MV) or intensity averaging (IA) label fusion schemes. In this work, we examined three most commonly used schemes for whole-body bone segmentation through global weighting. Each of these schemes can be performed using either of three above introduced similarity criteria. Ying *et al.* [41] exploited NMI similarity measure to identify similar atlas images via the following equation for the purpose of bone elements segmentation of hip and femur from MR images.

$$w_n = \frac{SM(T,M(Amr_n)) - min_m[SM(T,M(Amr_m))]}{max_m[SM(T,M(Amr_m))] - min_m[SM(T,M(Amr_m))]} \quad \text{subject to } w_n \geq \Phi \tag{7}$$

Here SM can be any similarity measure criterion (NMI, NCC and MSD) between the target MR image and transformed atlas images Amr_n. The *min* and *max* of the SM are calculated among all atlases to normalize the weighing factor w. After obtaining the weighting factor w, the next step is to select the atlases which satisfy the condition $w \geq \Phi$ ($0 \leq \Phi \leq 1$), where Φ is the threshold used to discard poorly performing atlases. Therefore, the weighted average of atlases T_{av} can be calculated using the following formulation:

$$T_{av} = \frac{1}{Nr} \sum_{n=1}^{N} w_n . T_{An} \qquad Bn(x) = \begin{cases} 1, & \text{if } T_{av}(x) > 180 \\ 0, & \text{otherwise} \end{cases} \tag{8}$$

Nr is the normalization factor obtained by $Nr = \sum_{n=1}^{N} w_n$. The majority voting scheme [17] can be adapted for this purpose as:

$$T_{Sav} = \frac{1}{Nr} \sum_{n=1}^{N} w_n . T_{Sn} \qquad Bn(x) = \begin{cases} 1, & \text{if } T_{Sav}(x) > 0.5 \\ 0, & \text{otherwise} \end{cases} \tag{9}$$

Ying *et al.* [41] utilized only NMI similarity measure along with a fixed threshold $\Phi = 0.9$ while in our work all three similarity criteria and a variable threshold were examined for the both MV and IA schemes in order to determine the optimal threshold value and the most efficient similarity measure.

The second approach to incorporate the similarity weights in the atlas fusion process is through gain exponent. In this case, the weighting factor is defined as $w=SM(T,M(Amr_n))^P$, where the gain exponent P might be increased if the similarity measure is not sensitive enough to provide appropriate differences between weights [17]. The weighting factor w can be incorporated either in equations (8) or (9). Presently, our aim is to find the optimum value of the gain exponent P for the three similarity criteria via IA and MV schemes.

The third atlas weighting scheme is based on Yushkevich *et al.* [38] work which assumed that the range of similarity measures can vary quite dramatically between subjects and locations. The same scheme was used by Burgos *et al*. [43] for pseudo-CT generation in the head region. As such, a ranking scheme is proposed whereby

the similarity measure value for each transformed atlas is ranked across all atlases. Let's suppose that ranked atlases are denoted as R_n. The conversion to the weight is performed by applying an exponential decay function.

$$w_n = e^{-aR_n}\ 10 \tag{10}$$

Where R_n denotes the ranked atlas indices (e.g. 1, 2, 3, …) and a is a weighting parameter to be optimized. By adopting the ranking scheme, the training subject that best matches the target subject is given a weight of 1. The training subject with the second best match is assigned a weight e^{-a} and so on. Thus, the segmentation can be performed by applying the weighting factor w_n to equations (8) and (9). Here, the ranking process was repeated three times using the NMI, NCC and MSD similarity measures and for each one the optimum parameter a, which maximized the accuracy of segmented bone was determined.

In some studies, the most similar subject is selected for either MRI segmentation or attenuation map generation in PET/MRI to reduce the computation time [9, 36]. The most similar atlas can be determined before the registration process on the basis of meta-data and image processing features [9]. In our work, the most similar subject to the target image was determined after the registration process using the three aforementioned similarity measures and the extracted bone was validated for each one.

3) STAPLE

A well-established approach aiming at maximizing multi-atlas based segmentation accuracy is Simultaneous Truth and Performance Level Estimation (STAPLE) [44]. A number of studies using multi-atlas based segmentation employed STAPLE algorithm to find the optimal combination of segmentations suggested by the different classifiers [17, 39]. STAPLE is an expectation-maximization algorithm for simultaneous truth and performance level estimation that considers a collection of segmentations and computes a probabilistic estimate of the true segmentation and a measure of the performance level represented by each segmentation. The source of each segmentation in the collection may be an appropriately trained human rater (or raters), or an automated segmentation algorithm, such as registered atlas classifiers. The probabilistic estimate of the true segmentation is formed by estimating an optimal combination of the segmentations, weighting each segmentation depending upon the estimated performance level, and incorporating a prior model of the spatial distribution of structures being segmented as well as spatial homogeneity constraints [44]. The STAPLE algorithm estimates a ground truth bone map from given bone atlas binary maps (T_{Sn}). Let θ_n be a matrix where each element describes the probability that atlas n labels a voxel as bone (b) when the true label is s ($\theta_n(b,s)$). The perfect atlas will have a probability matrix (θ_n) equal to the identity matrix. Let $\theta=[\ \theta_1 \ldots\ \theta_N]$ be the unknown set of all probability matrices characterizing all atlas images (N) and $B=[B_1 \ldots B_N]$ be a vector representing the unknown ground truth bone label map and D be an $V \times N$ matrix (V is the number of image voxels) whose columns indicate the N unknown segmentations. STAPLE estimates the ground truth bone segmentation (B) as well as the parameter matrix (θ) by maximizing the log likelihood $f = (D, B|\theta)$ using the expectation maximization algorithm [44].

Since the implementation of STAPLE algorithm is not very straightforward and is computationally demanding, Martin-Fernandez et al. [45] proposed Williams' index whereby the classifiers are assigned weights based on mutual similarity with other classifiers and the general consensus agreed on by all classifiers. Williams' index is defined as:

$$I_n = \frac{(N-2)\sum_{i\neq n}^{N} a(T_{An},T_{Ai})}{2\sum_{i\neq n}^{N}\sum_{k\neq n}^{i} a(T_{Ai},T_{Ak})} \tag{11}$$

where N is the number of classifiers or atlases, T_{An} denotes the segmented bone provided by the n^{th} atlas and $a(T_{An},T_{Ai})$ is the agreement between the classifier T_{An} and T_{Ai} over all image voxels. Various agreement measures can be used; a few of them will be defined in section 2.5. We used the Dice similarity coefficient [46] for this purpose. In case the atlas n generates an index (I_n) greater than one, it can be concluded that the performance of this atlas coincides with the majority of the other atlases. Therefore, this index can be used to select effective atlases [47]. The evaluation performed in [45] demonstrates that the output of STAPLE analysis and Williams' index are similar. In this work, we implemented both algorithms to compare their performance in terms of segmentation accuracy.

4) Local weighting

The voxel-wise weighting procedure is carried out similarly to the global weighting scheme, except that the similarity measure between the target image and transformed atlas is obtained independently for each voxel within its surrounding image patch (*D*). The same image similarity criteria (NMI, NNC and MSD) used in global weighting are utilized here, except that the searching window parameter *D* (patch size) introduced above needs to be optimized. As such, the NMI similarity measure between the target MR image *T* and the n^{th} transferred atlas image $M(Amr_n)$ for voxel *x* considering its *D* neighborhood is defined as:

$$NMI_D(x) = \frac{H_D(T)+H_D(M(Amr_n))}{H_D(T,M(Amr_n))} \tag{12}$$

The fast convolution-based approach proposed by Cachier *et al.* [48] is used to compute the local normalized cross-correlation (LNCC).

$$LNCC_D(x) = \sum_D \frac{\langle T,M(Amr_n)\rangle_x}{\sigma(T)_x \,.\, \sigma(M(Amr_n))_x} \tag{13}$$

$$\text{where } \sigma(T)_x = \sqrt{\overline{T_x^2} - \overline{T}_x^{\,2}} \qquad \overline{T}_x = K_G * T_x$$

$$\langle T, M(Amr_n)\rangle_x = \overline{T.M(Amr_n)}_x - \overline{T}_x.\overline{M(Amr_n)}_x$$

where K_G and * denote the Gaussian kernel and convolution operator, respectively. A Gaussian kernel with standard deviation equal to 3 voxels (4 mm) was adopted in this study. The MSD image similarity over the image patch *D* is defined as:

$$MSD_D(x) = \frac{D}{\sum_{x\in D}|T(x)-M(Amr_n(x))|^2} \tag{14}$$

Voxel-wise weighting atlas fusion using the gain exponent was used in [17] for brain MR image segmentation. The gain exponent is used to boost the sensitivity of the similarity measure across the atlas dataset. The weighing factor would have the form $w_n(x)_D=SM_D(T,M(Amr_n))_x^P$. SM_D could be any of the image similarity criteria (NMI, LNCC and MSD) calculated over the block *D* centered at voxel *x*. The obtained weighting factor could be incorporated in IA or MV schemes as:

$$T_{av}(x)_D = \frac{1}{Nr}\sum_{n=1}^{N} w_n(x)_D.T_{An}(x) \qquad Bn(x) = \begin{cases}1, & \text{if } T_{av}(x)_D > 180\\ 0, & \text{otherwise}\end{cases} \tag{15}$$

$$T_{Sav}(x)_D = \frac{1}{Nr}\sum_{n=1}^{N} w_n(x)_D.T_{Sn}(x) \qquad Bn(x) = \begin{cases}1, & \text{if } T_{Sav}(x)_D > 0.5\\ 0, & \text{otherwise}\end{cases} \tag{16}$$

$$Nr = \sum_{n=1}^{N} w_n(x)_D$$

The second approach for calculating the weighting factors is similar to that described in section 2.4.2 as ranking scheme. The only difference is that the ranking step must be performed for each image voxel (considering the surrounding voxels in the window *D*) rather than the entire atlas image across the whole dataset. After calculating the voxel-wise ranking vector $R(x)_D$ on the basis of image similarity criteria, the weighting factor is obtained via:

$$w_n(x)_D = e^{-aR(x)_D} \tag{17}$$

Again, this weighting factor can be replaced either in equation (15) or (16) to perform the final segmentation step. The same local weighting atlas fusion strategy was exploited by Burgos *et al.* for attenuation map synthesis in brain PET/MRI [23, 43].

Another strategy for utilizing voxel-wise similarity considers only the information of the most similar voxel. To this end, after computing the voxel-wise ranking vector $R(x)_D$, only the intensity information (or segmentation label) of the foremost voxel is assigned to the final segmented image. From now on, this is referred to as the most similar voxel (MSV).

In this section, three voxel-wise atlas fusion schemes were introduced with the aim to seek the optimal value of their free parameters, namely *P, a* and *D.* To fulfill this endeavor, we first calculated the image similarity

measure between the target and any of the atlas images using NMI, LNCC and MSD formula for a searching window D = 10 mm (in each direction x, y and z). Then, at a fixed value of D, the optimal values of the parameters P and a were determined. In the next step, the obtained optimal values of the parameters P and a were kept fixed to find the optimal value of D.

5) Hofmann's approach

Hofmann *et al.* [7] proposed an approach of generating whole-body pseudo-CT images from MRI. This method relies on a combination of atlas registration and pattern recognition via Gaussian process regression (GPR) [13]. Atlas registration process might fail to match the target patient perfectly because of local minima of non-rigid deformation energy function. To alleviate the adverse effect of the local signal mismatch, the nearby texture information of a given voxel was fed into a GPR via the patch of surrounding voxels to predict more accurate pseudo-CT values. To this end, a set of MRI/CT pairs are non-rigidly aligned to the target MR image and then the GPR kernel is formed using the local image patches on target and atlas images. In addition, 5-class segmentation (background air, lung, fat, fat & non-fat mixture and non-fat tissue) is performed on in-phase MR images [6, 7] and the corresponding patch information is used into the GPR kernel through equation (18).

$$k(d_i, d_j) = \exp\left(\frac{-\|W(P_{MR,i}) - W(P_{MR,j})\|^2}{2\sigma^2_{MR,patch}}\right) \times \exp\left(\frac{-\|X_i - X_j\|^2}{2\sigma^2_{pos}}\right) \times \exp\left(\frac{-\|W(P_{Seg,i}) - W(P_{Seg,j})\|^2}{2\sigma^2_{Seg,patch}}\right) \quad (18)$$

Where $d=(P_{MR}, P_{Seg}, X)$ while P_{MR} and P_{Seg} are sub-volume patches from the in-phase MR image and 5-class segmented MR image, respectively. W is a weighting vector with higher value for central voxels in the patch relative to surrounding voxels, X is the training and test patch center position. The parameters σ_{pos}, $\sigma_{MR,patch}$ and $\sigma_{Seg,patch}$ determine how the overall kernel value is influenced by similarity in position and patch intensity value in MRI and 5-class segmentation image. The training is performed on the samples d drawn from random locations in the atlas database. Finally, equation (19) is used to calculate the pseudo-CT value of a given voxel.

$$c_l = k^T C^{-1} y \quad (19)$$

Where c_l denotes the calculated pseudo-CT value of the voxel of interest l. $k_l=k(d_i,d_l)$ stands for a $(n\times 1)$ vector where $d_i=(P_{MR,i}, P_{Seg,i}, X_i)$ is the information extracted from the patches of the MRI atlases and $d_l=(P_{MR,l}, P_{Seg,l}, X_l)$ indicates the information obtained from the patches of the target MRI. $C=k(d_i,d_j)$ represents the covariance matrix $(n\times n)$ obtained from equation (18) using d_i and d_j patches on the MRI atlases. y is an $(n\times 1)$ vector containing CT values corresponding to the central voxel of training patches d_i.

6) Shape-based averaging

Shape-based averaging (SBA), categorized as an atlas-based segmentation technique, is a voting scheme where each vote is weighted by the signed Euclidean distance computed for each input label. SBA voting is the only method incorporating spatial information in the label fusion process [49]. Let $d_n(x)$ denote the signed Euclidean distance of voxel x from the nearest surface voxel with bone label in the n^{th} atlas segmentation. A negative value of $d_n(x)$ corresponds to the inside bony structure of the n^{th} atlas while a positive value implies that x is located outside. A value equal to zero is obtained if and only if voxel x is on the surface of bony structure. In effect, the signed Euclidean distance provides a probability map for the presence of bone based on every single atlas segmentation. By computing the distance maps of bony structures in all aligned atlas images, the average distance of a given voxel x from the bone surface is obtained from:

$$AD(x) = \frac{1}{N}\sum_{n=1}^{N} d_n(x) \quad (20)$$

Interested readers are referred to [50] for more details on implementation of the SBA algorithm.

In addition to the spatial weight that is assigned to each voxel using the SBA algorithm on the basis of the Euclidean distance, the local weight corresponding to the image similarity measure can also be incorporated in equation (20). Sabuncu *et al.* [51] included voxel-wise similarity weighting factors in the SBA algorithm to enhance its performance in the context of brain image segmentation. As an extension to this work, we used identical weighting factors defined in section 2.4.4 and included them in equation (20):

$$AD(x) = \frac{1}{N}\sum_{n=1}^{N} w_n(x)_D d_n(x) \quad (21)$$

Applying image similarity measure weighting factor to the SBA method introduces the same optimization parameters, namely *P, a* and *D*, for each image similarity criteria (NMI, LNCC and MSD). Since the SBA technique is computationally intensive and time-consuming [50], the optimal value of *D* obtained from experiments described in section 2.4.4 was used to optimize the rest of contributing parameters.

II.E. Evaluation metrics

The evaluation of the accuracy of extracted bone using the various atlas-based segmentation strategies described in 2.4 section was carried out by comparing the segmentation output to the bone segmented on the corresponding reference CT images using five volume/distance-based measures: Dice similarity (DSC) [46], relative volume difference (RVD) [52], Jaccard similarity (JC) [52], sensitivity (S) [41] and mean absolute surface distance (MASD) [37].

$$DSC(A,M) = \frac{2|A\cap M|}{|A|+|M|},\ RVD(A,M) = 100 \times \frac{|A|-|M|}{|M|},\ JC(A,M) = \frac{|A\cap M|}{|A\cup M|},\ S(A,M) = \frac{|A\cap M|}{|M|},$$

$$MASD(A,M) = \frac{d_{ave}(S_A,S_M) + d_{ave}(S_M,S_A)}{2}$$

where *A* is the segmented bone from the reference CT image and *M* denotes the extracted bone by the atlas-based segmentation technique. $d_{ave}(S_A,S_M)$ is the average direct surface distance from all points on the reference bone surface S_A to the segmented bone surface S_M.

The Shapiro-Wilk test was used to examine the null hypothesis that the calculated evaluation metrics follow a normally distributed population and the calculated *P*-values were reported for each individual segmentation scheme. The differences were considered statistically significant if the *P*-value was less than 0.05.

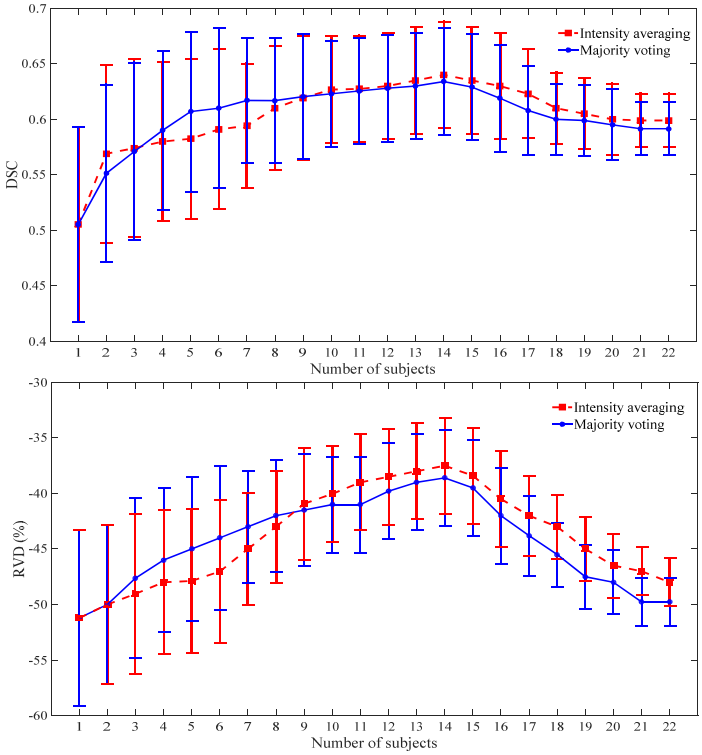

Figure 1. DSC (top) and RVD (bottom) similarity measures vs. the number of subjects using the intensity averaging and majority voting frameworks.

III. Results

Whole-body bone segmentation through non-weighting averaging was performed for varying number of atlases selected randomly from the entire dataset. Figure 1 illustrates the accuracy of extracted bone in terms of DSC

and RVD validation measures using both IA and MV. The bars show the standard deviation at each measured point.

Figure 2 depicts the accuracy of extracted bone using the weights defined in equation (7) for varying threshold levels. The top and bottom rows depict the results obtained using IA and MV frameworks, respectively, for NMI, NCC and MSD image similarity measures. A similar analysis was repeated to obtain the optimal value of parameters P and a (Table 1). The comparison was made using the five validation measures described in section 2.5.

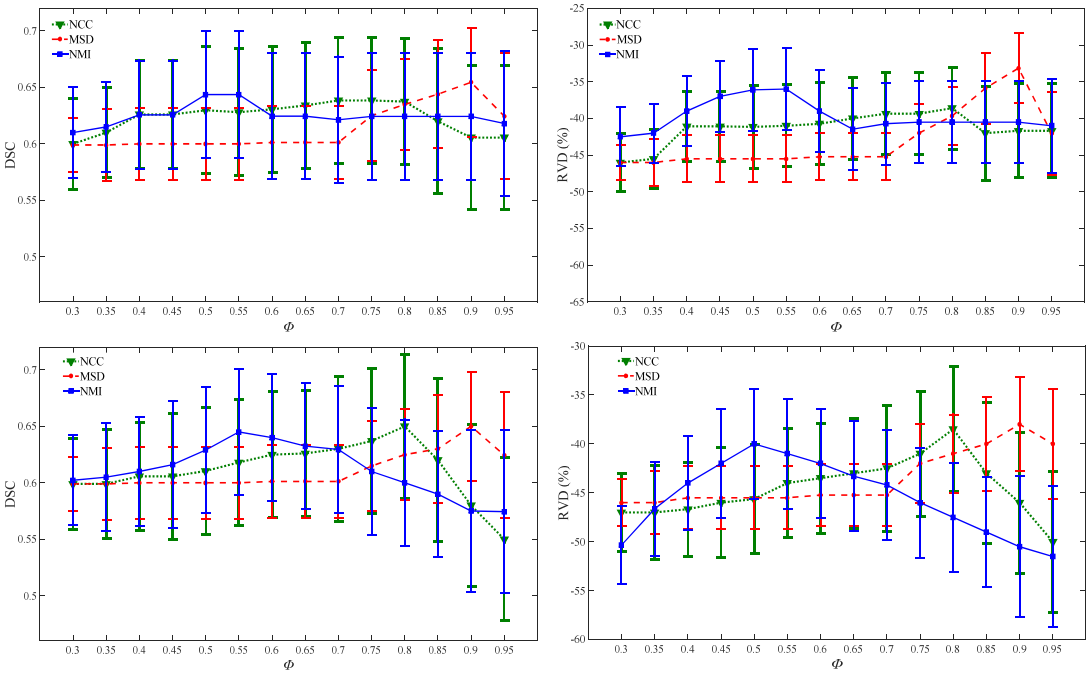

Figure 2. Plots of DSC and RVD vs. global atlas weighting parameter Φ measured using NCC, MSD and NMI similarity criteria for intensity averaging (top row) and majority voting (bottom row) frameworks.

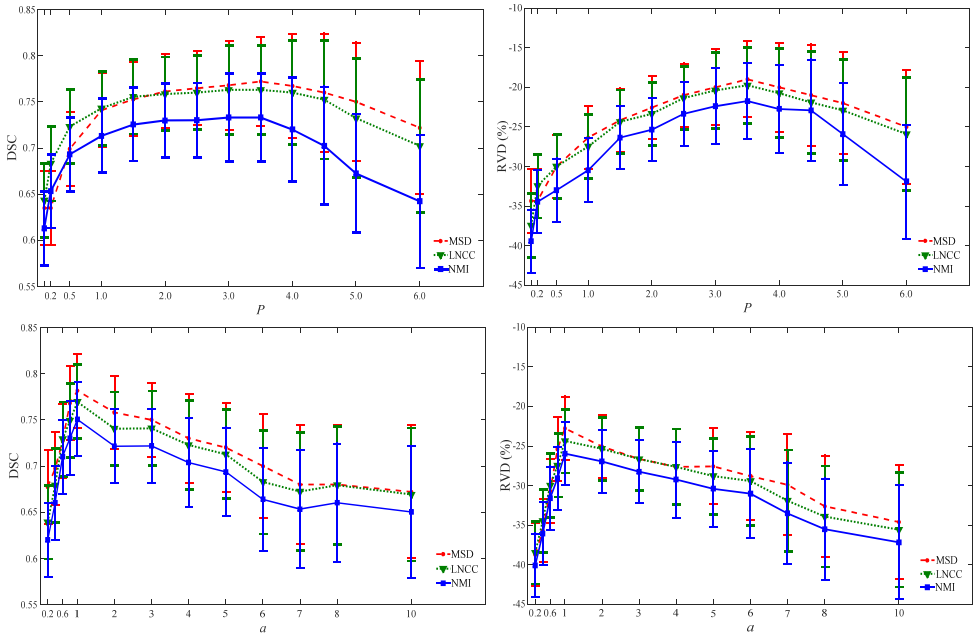

Figure 3. The effect of varying voxel-wise label weighting parameters (P and a) on DSC and RVD validation measures obtained from IA segmentation framework using LNCC, MSD and NMI similarity criteria for D=10 mm.

Table 3. Comparison of validation measures (mean±SD), including Dice similarity (DSC), relative volume distance (RVD), Jaccard similarity (JC), sensitivity (S) and mean absolute surface distance (MASD) between the bone extracted from different methods of global weighting atlas fusion using intensity averaging (IA) and majority voting (MV) approaches together with the optimum weighting parameters Φ, P and a for MI, NCC and MSD image similarity measures. (*) indicates P-value < 0.05 according to the paired t-test analysis.

Similarity measure	Weighting parameter	DSC	RVD(%)	JC	S	MASD(mm)
NMI						
IA	Φ=0.50	0.64±0.06	-36.5±05.6	0.47±0.05	0.53±0.06	06.4±01.5
MV	Φ=0.55	0.64±0.05	-40.1±04.8	0.47±0.06	0.51±0.07	06.8±01.7
IA	P=5	0.63±0.06	-41.5±05.8	0.46±0.05	0.50±0.05	06.9±01.5
MV	P=4	0.63±0.07	-43.1±06.0	0.46±0.06	0.49±0.06	06.9±01.8
IA	a=1	0.63±0.05	-41.6±05.7	0.46±0.05	0.50±0.04	07.1±01.6
MV	a=1	0.63±0.06	-41.7±05.9	0.45±0.06	0.49±0.05	07.2±01.7
NCC						
IA	Φ=0.75	0.64±0.06	-39.9±05.6	0.47±0.06	0.51±0.06	06.7±01.5
MV	Φ=0.8	0.64±0.06	-39.2±05.9	0.47±0.07	0.51±0.07	06.9±01.7
IA	P=6	0.63±0.05	-42.0±6.0	0.46±0.05	0.50±0.05	06.9±01.6
MV	P=5	0.63±0.06	-43.9±6.0	0.45±0.06	0.49±0.06	07.0±01.7
IA	a=1	0.62±0.05	-43.0±6.1	0.45±0.05	0.49±0.06	07.1±01.6
MV	a=2	0.62±0.05	-43.0±6.3	0.45±0.06	0.49±0.07	07.1±01.7
MSD						
IA	Φ=0.9	0.65±0.05	-34.0±04.8	0.49±0.04	0.55±0.04	05.7±01.2
MV	Φ=0.9	0.64±0.05	-36.9±05.2	0.47±0.06	0.53±0.06	05.9±01.2
IA	P=10	0.64±0.05	-37.5±04.0	0.47±0.05	0.52±0.04	05.9±01.3
MV	P=10	0.64±0.06	-39.5±04.9	0.47±0.06	0.52±0.05	06.1±01.4
IA	a=2	0.63±0.05	-41.0±06.1	0.46±0.06	0.50±0.06	06.9±01.6
MV	a=2	0.63±0.06	-41.3±06.2	0.46±0.06	0.50±0.07	07.0±01.7

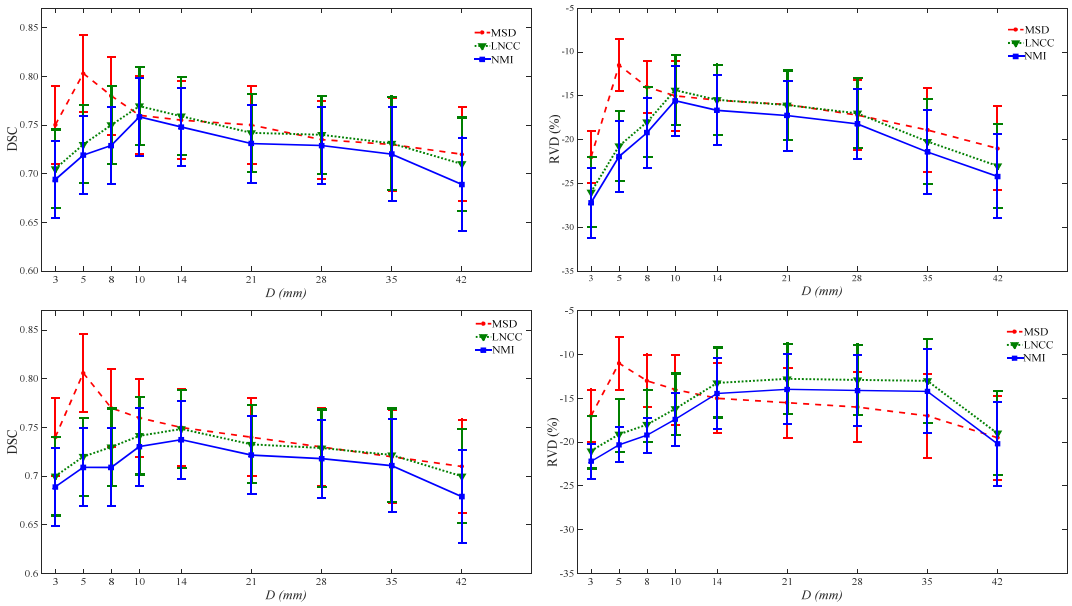

Figure 4. Plots of DSC and RVD similarity measures vs. neighborhood window D using local ranking voxel-wise weighting (top row) and most similar voxel (bottom row) label fusion approaches through the IA framework for LNCC, MSD and NMI similarity criteria.

Table 2. Comparison of validation measures (mean±SD), including Dice similarity (DSC), relative volume distance (RVD), Jaccard similarity (JC), sensitivity (S) and mean absolute surface distance (MASD) between the bone extracted from different methods of voxel-wise weighting calculated using intensity averaging (IA) and majority voting (MV) approaches at the optimum neighborhood window D and weighting parameters. (*) indicates P-value <0.05 according to the paired t-test analysis.

NMI	Weighting parameter	D (mm)	DSC	RVD(%)	JC	S	MASD(mm)
IA	*P=3.5*	14	0.75±0.04	-18.1±05.2	0.61±0.05	0.68±0.05	07.3±01.9
MV	*P=3.5*	14	0.75±0.05	-18.6±05.1	0.61±0.04*	0.69±0.05*	07.4±01.8
IA	*a=1*	10	0.75±0.04	-15.3±04.6	0.60±0.05	0.68±0.04	07.3±01.6
MV	*a=1*	10	0.74±0.04	-15.2±04.9	0.59±0.06	0.68±0.05	07.9±01.7
	MSV	14	0.74±0.05	-14.1±03.7	0.59±0.05	0.67±0.05	08.0±01.8
LNCC							
IA	*P=3.5*	14	0.77±0.04	-15.6±04.8	0.63±0.04	0.70±0.04	05.2±01.5
MV	*P=3.0*	14	0.76±0.05	-16.9±04.7	0.62±0.04	0.69±0.04	05.5±01.7
IA	*a=1*	10	0.78±0.05	-14.0±04.9	0.62±0.05	0.69±0.04	05.0±01.9
MV	*a=1*	10	0.77±0.05	-14.5±06.3	0.61±0.06	0.68±0.05	04.8±01.7
	MSV	14	0.75±0.04	-13.7±06.3	0.60±0.05	0.70±0.06	05.5±01.9
MSD							
IA	*P=3.5*	5	0.80±0.03	-12.4±04.3	0.74±0.05	0.77±0.05	03.3±01.3
MV	*P=3.0*	5	0.80±0.04	-12.0±04.4	0.74±0.05	0.77±0.05	03.4±01.4
IA	*a=1*	5	0.81±0.03	-11.7±4.1	0.75±0.04	0.77±0.04	03.0±01.1
MV	*a=1*	5	0.80±0.03	-11.9±5.2	0.74±0.04	0.77±0.05	03.3±01.2
	MSV	5	0.81±0.04	-10.9±4.7	0.74±0.03	0.77±0.04	04.9±01.0

Figure 3 depicts the accuracy of extracted bone based on DSC and RVD validation measures calculated at different values of P and a for NMI, LNCC and MSD similarity criteria using a searching window of D = 10 mm. The results illustrated in figure 3 are obtained using the IA framework.

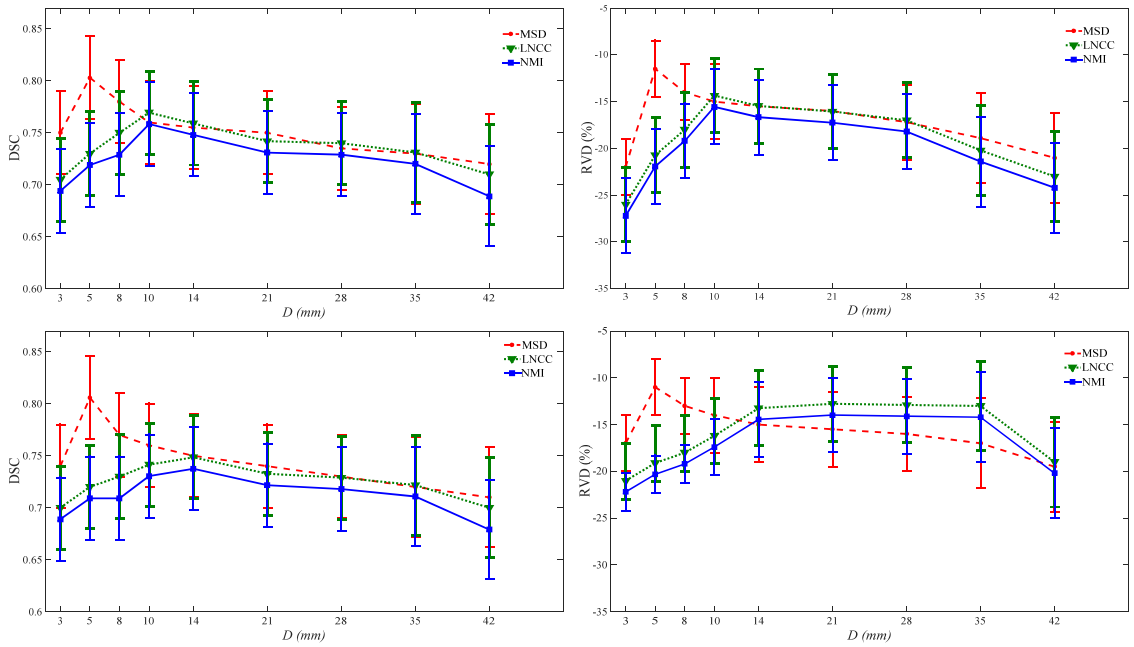

Figure 4. Plots of DSC and RVD similarity measures vs. neighborhood window *D* using local ranking voxel-wise weighting (top row) and most similar voxel (bottom row) label fusion approaches through the IA framework for LNCC, MSD and NMI similarity criteria.

Table 3. Comparison of validation measures (mean±SD), including Dice similarity (DSC), relative volume distance (RVD), Jaccard similarity (JC), sensitivity (S) and mean absolute surface distance (MASD) for SBA method with ranking voxel-wise weighting approach set at optimum parameter of *a*. (*) indicates P-value < 0.05 according to the paired t-test analysis.

	a	**DSC**	**RVD(%)**	**JC**	**S**	**MASD(mm)**
SBA (without weighting)	-	0.56±0.05	-15.3±04.7	0.39±0.05	0.52±0.06	11.1±04.1
SBA local weighting (NMI) for *D*=10 mm	5	0.74±0.05	-26.2±06.7	0.57±0.05	0.62±0.06	08.5±03.6
SBA local weighting (LNCC) for *D*=10 mm	5	0.75±0.06	-24.8±06.4	0.58±0.06	0.64±0.07	09.7±03.9
SBA local weighting (MSD) for *D*= 5 mm	2	0.76±0.05	-24.4±03.2	0.76±0.07	0.79±0.06	07.6±03.3

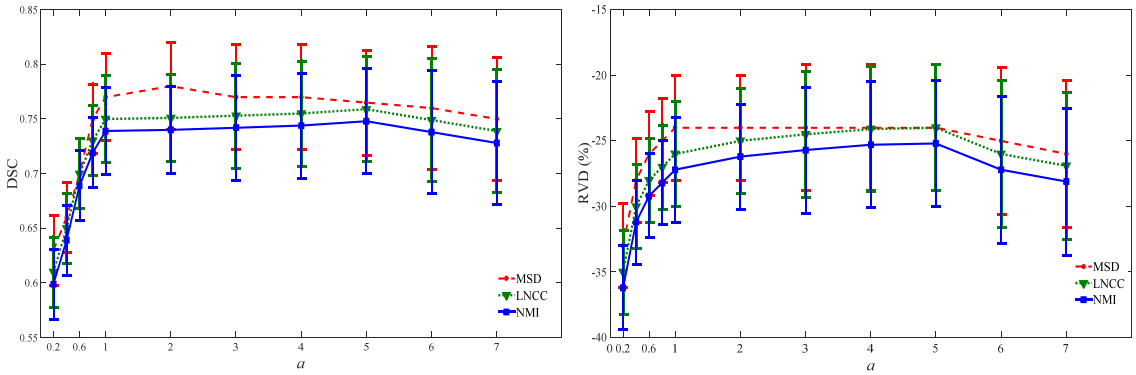

Figure 5. Impact of varying the voxel-wise weighting parameter (*a*) on DSC and RVD validation measures obtained from the SBA segmentation techniques using an optimum neighborhood window (*D*) of 5 mm for MSD and 10 mm for LNCC and NMI.

The best result at D = 10 mm is achieved by the MSD similarity measure with P=3.5 using the IA framework, yielding a DSC of 0.75, thus demonstrating significant improvement compared to the global weighting strategy (DSC = 0.65). After determining the optimal value of P and a, these parameters were kept fixed and the optimum size of the searching window D was calculated. Figure 4 depicts the impact of varying size of the searching window D on the accuracy of extracted bone for different image similarity criteria. The top row corresponds to the ranking scheme obtained from equation (17) at a = 1 whereas the bottom row corresponds to the MSV approach using the IA framework. Table 2 summarizes voxel-wise atlas fusion results together with optimal parameter values. The best results were achieved when applying voxel-wise weighting ranking scheme (using a = 1) and the MSV approach (using D = 5 and MSD similarity measure) with a DSC=0.81 (Table 2).

Although the SBA method was the most time consuming approach among those studied in this work, this technique exhibited poor performance without local weighting (Table 3). However, incorporating voxel-wise weighting improved the DSC from 0.56 to 0.76. Figure 5 illustrates the performance of SBA at varying values of *a* obtained using different image similarity criteria.

A comparison of the performance of the various segmentation techniques is provided in Table 4. The techniques incorporating optimization parameters are reported at their optimal values. Figures 6 to 8 illustrate a representative slice of segmented bone from a whole-body MR image together with corresponding error distance map using a combination of methods presented in Table 4.

IV. Discussion

Bone segmentation from whole-body MR images proved to be a challenging task. We investigated the accuracy of a number of atlas-guided segmentation approaches. Our primary motivation for conducting this work is to identify the most promising algorithms for atlas-guided attenuation correction in PET/MRI. Since the identification and segmentation of bony structures for MRI-guided attenuation map generation, particularly in whole-body imaging, we focused our evaluation on metrics reflecting the accuracy of bone extraction among the various approaches.

Table 4. Comparison of validation measures (mean±SD), including Dice similarity (DSC), relative volume distance (RVD), Jaccard similarity (JC), Sensitivity (S) and mean absolute surface distance (MASD) for all combinations of atlas-based segmentation methods at optimum weighting parameters and neighborhood windows. (*) indicates P-value < 0.05 according to the paired t-test analysis.

Methods	DSC	RVD(%)	JC	S	MASD(mm)
Average of all atlas images	0.60±0.02	-46.0±02.4	0.43±0.02	0.46±0.02	10.7±03.9
Single atlas image (template)	0.60±0.02	-46.4±02.5	0.44±0.02	0.47±0.02	11.1±03.9
General Majority voting	0.59±0.02	-49.8±02.4	0.42±0.02	0.44±0.02	09.8±03.6
Williams' index	0.61±0.05	-46.2±06.3	0.43±0.06	0.45±0.04	10.4±04.1
STAPLE	0.62±0.05	-4.7±05.8	0.44±0.05	0.49±0.03	08.6±03.8
Hofmann	0.61±0.02	-45.5±02.4	0.42±0.02	0.45±0.02	10.1±03.3
SBA (without weighting)	0.56±0.05	-55.3±04.7	0.39±0.05	0.52±0.06	11.1±04.1
Global weighting (NMI)	0.64±0.06	-39.9±05.6	0.47±0.05	0.53±0.06	06.4±01.5
Global weighting (NCC)	0.64±0.06	-41.5±05.6	0.47±0.06	0.51±0.06	06.7±01.5
Global weighting (MSD)	0.65±0.05	-34.0±04.8	0.49±0.04	0.55±0.04	05.7±01.2
Most similar subject	0.58±0.09	-39.2±08.1	0.41±0.10	0.52±0.11	06.2±02.0
Local weighting (NMI)	0.75±0.04	-15.3±04.6	0.60±0.05	0.68±0.04	07.3±01.6
Local weighting (LNCC)	0.78±0.05	-14.0±04.9	0.62±0.05	0.69±0.04	05.0±01.9
Local weighting (MSD)	0.81±0.03	-11.7±04.1	0.75±0.04	0.77±0.04	03.0±01.1
MSV (MSD)	0.81±0.04	-10.9±04.7	0.74±0.03	0.77±0.04	04.9±01.0

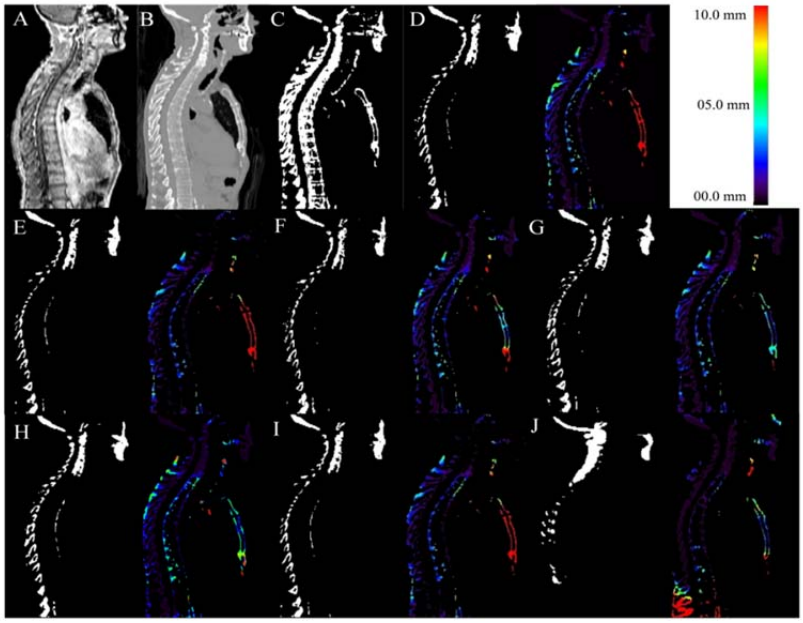

Figure 6. Representative slice illustrating the performance of the different MRI bone segmentation techniques (left) along with the corresponding error distance map (right) showing: (A) In-phase MRI, (B) corresponding CT image, (C) binary image of reference bone extracted from CT, (D) general intensity averaging, (E) single atlas image, (F) general majority voting, (G) Williams' index, (H) STAPLE, (I) Hofmann's method and (J) SBA.

A commonly used approach to combine the information provided by deformed atlas images is through IA or MV label fusion schemes [53]. In theory, in multiple atlas segmentation, increasing the number of input atlases would improve the outcome. As such, the quality of segmentation is expected to improve monotonically by adding more atlases. However, in practice at a certain number of input atlases, the improvement reaches a peak (at a number of 14 in figure 1). The rising part of the DSC plot (from 1 to 14 subjects) can be justified by the nonsystematic misalignment cancelation due to uncorrelated error between atlases (Artaechevarria et al., 2009; Heckemann et al., 2006). By increasing the number of atlases beyond the peak, the resulting segmentations tend to approach the population mean and the segmentation accuracy will reach an asymptotic value. An overly increased number of atlases would degrade the segmentation accuracy because of the high level of smoothness

and the lack of patient-specific details. Assuming that input atlases are of similar quality and are selected randomly, adding more atlases after reaching the peak (here more than 15 in figure 1) would average out fine details leading to non-patient-specific and biased segmentation. Moreover, the quality of added atlases is not the same (even though they are chosen randomly), and as such, some fluctuations may be observed with added new atlases. Similar results have been reported in [54] in the context of brain imaging. However, the optimal number of input atlases may vary from one experiment to another since it strongly depends on the shape of the target organ/tissue and quality of atlases. This trend do not seem to be a standard behavior of atlas-based methods since in many studies monotonically increasing or a plateau curve reaching an asymptotic value was reported [37, 55, 56]. It should be noted that this trend holds for non-selective atlas fusion schemes since an increased number of atlases would increase the likelihood of finding more similar cases to the target image, for instance in local weighting atlas fusion schemes which leads to a asymptotically rising curve. In some studies, only one atlas image is used to carry out the segmentation procedure, which involves a single online registration procedure [20, 57]. Marshall *et al.* [9] proposed to select the most similar subject for PET/MRI attenuation correction on the basis of available metadata, such as sex and age and some image-derived features, such as body volume, lung volume, etc. The rationale behind using a single atlas or template is to avoid the computational burden of multiple atlas registration. In this work, rather than using metadata, the most similar subject was selected after pair-wise atlas registration using the aforementioned image similarity criteria. Since the most similar atlas is selected after registration, the outcome would be comparable to the original scheme even though it employs a larger database of atlases. The results shown in Table 4 indicate that single patient registration results in large error bias owing to the variability of patients' anatomy while using a single average atlas (template) led to slightly better bone extraction accuracy. Basically, the templates are close to the mean of patient population (compared to single atlas), which reduces non-rigid registration errors and consequently improve the outcome.

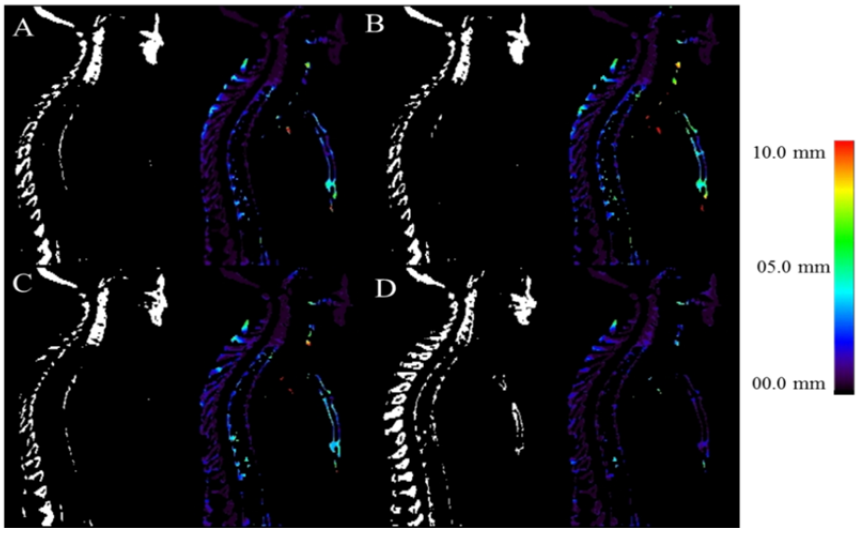

Figure 7. Representative slice illustrating the performance of the different MRI bone segmentation techniques (left) along with the corresponding error distance map (right) showing: (A) global weighting using NMI, (B) global weighting using NCC and (C) global weighting using MSD, and (D) most similar subject.

The global atlas weighting strategy exhibited moderate improvement compared to the general averaging method as transformed atlases with large misalignment errors are excluded or are at least given relatively low weights during the atlas fusion process. Due to the large axial field-of-view in whole-body imaging, local miss-match between the target and atlases might occur in some cases. Global strategies are not capable of evaluating the registration performance locally and only atlases with gross miss-matches are discarded as demonstrated by [17]. Therefore, global atlas weighting is much less effective when applied for large axial field-of-view. The similar approach was exploited by Ying *et al.* [41] for automated bone segmentation from MR images of the hip joint using the NMI similarity criterion, which resulted in a DSC of 0.95. The marked difference between these results and those reported in our study stems from the different MRI sequence and image quality, registration algorithm and on top of all the smaller field-of-view, which led to better registration outcome and less local miss-matches. According to Table 1, the best performance was achieved by the IA segmentation framework

using the MSD image similarity measure with $\Phi = 0.9$, which led to bone segmentation accuracy with a DSC of 0.65.

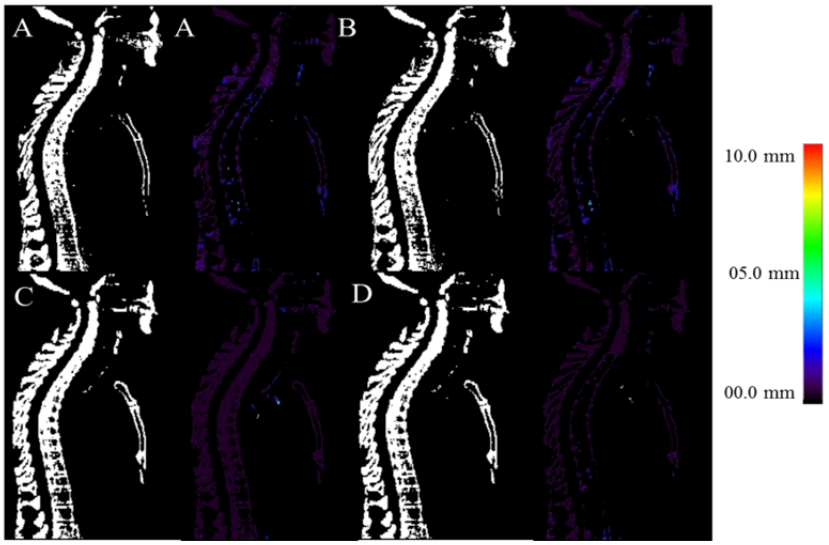

Figure 8. Representative slice illustrating the performance of the different MRI bone segmentation techniques (left) along with the corresponding error distance map (right) showing: (A) local weighting using NMI, (B) local weighting using LNCC, (C) local weighting using MSD, and (D) most similar voxel using MSD.

There is still a remarkable difference between voxel-wise and global weighting strategies resulting in DSCs of 0.81 and 0.65, respectively. This is mainly due to locally discarded miss-matches between target and atlas images. The transformed atlas image might be aligned almost perfectly in one region whereas other regions bear massive misalignment errors, for instance because of anatomical variability that can properly dealt with it using local weighting strategies. The optimization of free parameters in local strategies (such as the neighborhood window in figure 4) plays a key role in local miss-match cancellation. Too large neighborhood windows would result in similar outcome to that of global weighting whereas too small windows would be severely affected by noise and factitious local intensity/pattern similarities. The optimization of the searching window D seems to be essential since it had significant impact on the accuracy of extracted bone (figure 4) [58].

MSD achieves the best performance among other image similarity criteria presumably owing to proper intensity normalization of MR images as described in section 2.3. Implementing the MSD similarity measure adds inconsequential extra computation time to the segmentation procedure, as opposed to NMI which is prohibitively time-consuming when it comes to the voxel level processing [31]. NMI exhibited the poorest performance as image similarity measure in this particular study. However, in other experiments such as in [23], the LNCC similarity measure outperformed other techniques. This issue largely depends on the employed MR sequence, level of noise, inter-subject intensity normalization and registration algorithm. In case the registration between target and atlas images is performed for instance using MI image similarity measure, image alignment is already optimized on the basis of MI. Thus, employing MI after registration did not improve the outcome. On the other hand, the other image similarity measures, particularly MSD, provided more useful information about the similarity between target and atlas images.

The STAPLE framework, regarded as a state-of-the-art atlas fusion method, barely improved bone segmentation accuracy. The competing William's index method performed even slightly worse, nevertheless, it converges up to 4 times faster. The plausible reason of the sub-optimal performance is that both methods solely rely on the correlation between different atlases to determine fusion weights rather than using a similarity measure between target and atlas images. Moreover, the fusion weights are defined in global fashion (similar to global weighting strategies). Therefore, local miss-matches degrade the quality of the outcome. Similar observations were reported elsewhere in the context of prostate and brain segmentation [17, 39].

Overall, voxel-wise weighting label fusion provided dramatic improvements to the accuracy of segmentation owing to local cancelation of misalignment errors. It is strongly recommended to employ a similarity measure different from the one used for the registration process. Apart from that, the performance of the image similarity

criterion largely depends on the type and quality of images under study. In this light, for each study, the optimization step to determine the most effective image similarity criteria and associated optimal parameters, such as image similarity patch size (*D),* is indispensable to reach the best performance [17].

In essence, MRI sequences commonly used to generate PET attenuation maps suffer from high noise level and partial volume effect owing to short acquisition time. Using high quality MR images may possibly improve the registration outcome and consequently the segmentation accuracy; however, fast sequences should be used on PET/MRI systems in the clinic. Using MRI sequences other than the Dixon sequence used in this study would not significantly affect the quality of registration as far as they have similar signal to noise and provide similar anatomical details.

In this work, we focused on conventional atlas-based methods. Patch-based methods rely on a database of atlas images to find similar patches to predict segmentation labels or attenuation values for the target image. However, the characteristic difference between patch-based methods and the methods evaluated in this work is that atlas registration is not performed in patch-based methods while this process is the heart of multiple atlas segmentation.

The major drawback of atlas-based segmentation techniques is the relatively long computation time taken mostly by the image registration process. Future work will focus on reducing the overall computation time and on evaluating the performance of the obtained synthetic pseudo-CT images in the context of attenuation correction in whole-body PET/MRI.

V. Conclusion

We evaluated the accuracy of whole-body bone extraction from MR images using a number of atlas-based segmentation techniques. In particular, global and local weighted atlas fusion strategies as well as some commonly used atlas-based pseudo-CT generation methods were implemented and optimized for the task of whole-body bone segmentation. The voxel-wise weighted atlas fusion approach based on the MSD morphological similarity measure outperformed other segmentation approaches (provided proper MR image denoising and normalization are performed) by achieving a DSC of 0.81. This is in contrast to the non-weighted atlas fusion framework, which yielded a DSC of 0.60. Overall, the voxel-wise weighted atlas fusion approach is capable of canceling out the non-systematic registration errors. Optimization of contributing factors is crucial to reach optimal performance since they are largely determined by the type and quality of images under study.

Acknowledgment

This work was supported by the Swiss National Science Foundation under grant SNFN 31003A-149957 and the Swiss Cancer Research Foundation under Grant KFS-3855-02-2016.

References

[1] M. S. Judenhofer, H. F. Wehrl, D. F. Newport, C. Catana, S. B. Siegel, M. Becker*, et al.*, "Simultaneous PET-MRI: a new approach for functional and morphological imaging.," *Nat Med,* vol. 14, pp. 459-465, Apr 2008.

[2] H. Zaidi and A. Del Guerra, "An outlook on future design of hybrid PET/MRI systems.," *Med Phys,* vol. 38, pp. 5667-5689, 2011.

[3] A. Mehranian, H. Arabi, and H. Zaidi, "Vision 20/20: Magnetic resonance imaging-guided attenuation correction in PET/MRI: Challenges, solutions, and opportunities.," *Med Phys,* vol. 43, pp. 1130-1155, 2016.

[4] A. Martinez-Moller, M. Souvatzoglou, G. Delso, R. A. Bundschuh, C. Chefd'hotel, S. I. Ziegler*, et al.*, "Tissue classification as a potential approach for attenuation correction in whole-body PET/MRI: Evaluation with PET/CT data.," *J Nucl Med,* vol. 50, pp. 520-526, Apr 2009.

[5] H. Arabi, O. Rager, A. Alem, A. Varoquaux, M. Becker, and H. Zaidi, "Clinical assessment of MR-guided 3-class and 4-class attenuation correction in PET/MR.," *Mol Imaging Biol,* vol. 17, pp. 264-276, 2015.

[6] I. Bezrukov, H. Schmidt, F. Mantlik, N. Schwenzer, C. Brendle, B. Schölkopf*, et al.*, "MR-Based Attenuation Correction Methods for Improved PET Quantification in Lesions Within Bone and Susceptibility Artifact Regions," *Journal of Nuclear Medicine,* vol. 54, pp. 1768-1774, October 1, 2013 2013.

[7] M. Hofmann, I. Bezrukov, F. Mantlik, P. Aschoff, F. Steinke, T. Beyer*, et al.*, "MRI-based attenuation correction for whole-body PET/MRI: Quantitative evaluation of segmentation- and Atlas-based methods.," *J Nucl Med,* vol. 52, pp. 1392-1399, Sep 2011.

[8] H. Arabi and H. Zaidi, "Magnetic resonance imaging-guided attenuation correction in whole-body PET/MRI using a sorted atlas approach.," *Med Image Anal,* vol. 31, pp. 1-15, 7, 2016.

[9] H. R. Marshall, J. Patrick, D. Laidley, F. S. Prato, J. Butler, J. Théberge*, et al.*, "Description and assessment of a registration-based approach to include bones for attenuation correction of whole-body PET/MRI," *Medical physics,* vol. 40, p. 082509, 2013.

[10] H. Arabi and H. Zaidi, "One registration multi-atlas-based pseudo-CT generation for attenuation correction in PET/MRI," *Eur J Nucl Med Mol Imaging* Vol. 43, No. 11, pp 2021-2035 (2016).

[11] A. Rezaei, M. Defrise, G. Bal, C. Michel, M. Conti, C. Watson*, et al.*, "Simultaneous reconstruction of activity and attenuation in time-of-flight PET.," *IEEE Trans Med Imaging,* p. *in press*, 2012.

[12] A. Mehranian and H. Zaidi, "Joint estimation of activity and attenuation in whole-body TOF PET/MRI using constrained Gaussian mixture models.," *IEEE Trans Med Imaging,* vol. 34, pp. 1808-1821, 2015.

[13] M. Hofmann, F. Steinke, V. Scheel, G. Charpiat, J. Farquhar, P. Aschoff*, et al.*, "MRI-based attenuation correction for PET/MRI: A novel approach combining pattern recognition and Atlas registration.," *J Nucl Med,* vol. 49, pp. 1875-1883, Oct 16 2008.

[14] M. Lorenzo-Valdés, G. I. Sanchez-Ortiz, A. G. Elkington, R. H. Mohiaddin, and D. Rueckert, "Segmentation of 4D cardiac MR images using a probabilistic atlas and the EM algorithm," *Medical Image Analysis,* vol. 8, pp. 255-265, 2004.

[15] C. Svarer, K. Madsen, S. G. Hasselbalch, L. H. Pinborg, S. Haugbøl, V. G. Frøkjær*, et al.*, "MR-based automatic delineation of volumes of interest in human brain PET images using probability maps," *NeuroImage,* vol. 24, pp. 969-979, 2/15/ 2005.

[16] T. Rohlfing, R. Brandt, C. R. Maurer, Jr., and R. Menzel, "Bee brains, B-splines and computational democracy: generating an average shape atlas," in *Mathematical Methods in Biomedical Image Analysis, 2001. MMBIA 2001. IEEE Workshop on*, 2001, pp. 187-194.

[17] X. Artaechevarria, A. Munoz-Barrutia, and C. Ortiz-de-Solorzano, "Combination Strategies in Multi-Atlas Image Segmentation: Application to Brain MR Data," *Medical Imaging, IEEE Transactions on,* vol. 28, pp. 1266-1277, 2009.

[18] I. Bezrukov, H. Schmidt, S. Gatidis, F. Mantlik, J. F. Schafer, N. F. Schwenzer*, et al.*, "Quantitative evaluation of segmentation- and atlas-based attenuation correction for PET/MR on pediatric patients.," *J Nucl Med,* vol. 56, pp. 1067-1074, May 7 2015.

[19] M. R. Ay, A. Akbarzadeh, A. Ahmadian, and H. Zaidi, "Classification of bones from MR images in torso PET-MR imaging using a statistical shape model.," *Nucl Instrum Meth A,* vol. 734, Part B, pp. 196-200, 1/11/ 2014.

[20] D. H. Paulus, H. H. Quick, C. Geppert, M. Fenchel, Y. Zhan, G. Hermosillo*, et al.*, "Whole-Body PET/MR Imaging: Quantitative Evaluation of a Novel Model-Based MR Attenuation Correction Method Including Bone," *Journal of Nuclear Medicine,* p. jnumed. 115.156000, 2015.

[21] V. Keereman, Y. Fierens, T. Broux, Y. De Deene, M. Lonneux, and S. Vandenberghe, "MRI-based attenuation correction for PET/MRI using ultrashort echo time sequences.," *J Nucl Med,* vol. 51, pp. 812-818, May 2010.

[22] G. Delso, F. Wiesinger, L. Sacolick, S. Kaushik, D. Shanbhag, M. Hullner*, et al.*, "Clinical evaluation of zero echo time MRI for the segmentation of the skull.," *J Nucl Med,* vol. 56, pp. 417-422, Feb 12 2015.

[23] N. Burgos, M. J. Cardoso, K. Thielemans, M. Modat, S. Pedemonte, J. Dickson*, et al.*, "Attenuation Correction Synthesis for Hybrid PET-MR Scanners: Application to Brain Studies," *Medical Imaging, IEEE Transactions on,* vol. 33, pp. 2332-2341, 2014.

[24] A. Mehranian, H. Arabi, and H. Zaidi, "Quantitative analysis of MRI-guided attenuation correction techniques in time-of-flight brain PET/MRI," *NeuroImage,* vol. 130, pp. 123-133, 2016.

[25] H. Arabi and H. Zaidi, "Comparison of atlas-based bone segmentation methods in whole-body PET/MRI," *IEEE Nuclear Science Symposium & Medical Imaging Conference,* vol. Seattle, USA, 2014.

[26] T. Rohlfing, D. B. Russakoff, and C. R. Maurer, Jr., "Performance-based classifier combination in atlas-based image segmentation using expectation-maximization parameter estimation," *Medical Imaging, IEEE Transactions on,* vol. 23, pp. 983-994, 2004.

[27] H. Zaidi, N. Ojha, M. Morich, J. Griesmer, Z. Hu, P. Maniawski*, et al.*, "Design and performance evaluation of a whole-body Ingenuity TF PET-MRI system.," *Phys Med Biol,* vol. 56, pp. 3091-3106, Apr 20 2011.

[28] W. T. Dixon, "Simple proton spectroscopic imaging," *Radiology,* vol. 153, pp. 189-194, October 1, 1984 1984.

[29] S. Klein, M. Staring, K. Murphy, M. A. Viergever, and J. P. W. Pluim, "elastix: A toolbox for intensity-based medical image registration.," *IEEE Trans Med Imaging,* vol. 29, pp. 196-205, 2010.

[30] A. Akbarzadeh, D. Gutierrez, A. Baskin, M. R. Ay, A. Ahmadian, N. R. Alam*, et al.*, "Evaluation of whole-body MR to CT deformable image registration," *Journal of Applied Clinical Medical Physics,* vol. 14, 2013.

[31] J. M. P. Lötjönen, R. Wolz, J. R. Koikkalainen, L. Thurfjell, G. Waldemar, H. Soininen*, et al.*, "Fast and robust multi-atlas segmentation of brain magnetic resonance images," *NeuroImage,* vol. 49, pp. 2352-2365, 2/1/ 2010.

[32] N. J. Tustison, B. B. Avants, P. A. Cook, Z. Yuanjie, A. Egan, P. A. Yushkevich*, et al.*, "N4ITK: Improved N3 Bias Correction," *Medical Imaging, IEEE Transactions on,* vol. 29, pp. 1310-1320, 2010.

[33] M. J. McAuliffe, F. M. Lalonde, D. McGarry, W. Gandler, K. Csaky, and B. L. Trus, "Medical Image Processing, Analysis and Visualization in clinical research," in *Computer-Based Medical Systems, 2001. CBMS 2001. Proceedings. 14th IEEE Symposium on*, 2001, pp. 381-386.

[34] M. Kass, A. Witkin, and D. Terzopoulos, "Snakes: active contour models.," *Int J Comput Vision,* vol. 1, pp. 321-331, 1988.

[35] P. A. Yushkevich, J. Piven, H. C. Hazlett, R. G. Smith, S. Ho, J. C. Gee*, et al.*, "User-guided 3D active contour segmentation of anatomical structures: significantly improved efficiency and reliability.," *Neuroimage,* vol. 31, pp. 1116-1128, Jul 1 2006.

[36] T. Rohlfing, R. Brandt, R. Menzel, and C. R. Maurer Jr, "Evaluation of atlas selection strategies for atlas-based image segmentation with application to confocal microscopy images of bee brains," *NeuroImage,* vol. 21, pp. 1428-1442, 4// 2004.

[37] R. A. Heckemann, J. V. Hajnal, P. Aljabar, D. Rueckert, and A. Hammers, "Automatic anatomical brain MRI segmentation combining label propagation and decision fusion," *NeuroImage,* vol. 33, pp. 115-126, 10/15/ 2006.

[38] P. A. Yushkevich, H. Wang, J. Pluta, S. R. Das, C. Craige, B. B. Avants*, et al.*, "Nearly automatic segmentation of hippocampal subfields in in vivo focal T2-weighted MRI," *NeuroImage,* vol. 53, pp. 1208-1224, 12// 2010.

[39] X. Artaechevarria, A. Muñoz-Barrutia, and C. Ortiz-de-Solorzano, "Efficient classifier generation and weighted voting for atlas-based segmentation: Two small steps faster and closer to the combination oracle," in *Medical Imaging*, 2008, pp. 69141W-69141W-9.

[40] S. S. Chandra, J. A. Dowling, S. Kai-Kai, P. Raniga, J. P. W. Pluim, P. B. Greer*, et al.*, "Patient Specific Prostate Segmentation in 3-D Magnetic Resonance Images," *Medical Imaging, IEEE Transactions on,* vol. 31, pp. 1955-1964, 2012.

[41] X. Ying, F. Jurgen, S. C. Shekhar, S. Raphael, E. Craig, and C. Stuart, "Automated bone segmentation from large field of view 3D MR images of the hip joint," *Physics in Medicine and Biology,* vol. 58, p. 7375, 2013.

[42] W. M. Wells, P. Viola, H. Atsumi, S. Nakajima, and R. Kikinis, "Multi-modal volume registration by maximization of mutual information.," *Med Image Anal,* vol. 1, pp. 35-51, Mar 1996.

[43] N. Burgos, M. Cardoso, M. Modat, S. Pedemonte, J. Dickson, A. Barnes*, et al.*, "Attenuation Correction Synthesis for Hybrid PET-MR Scanners," in *Medical Image Computing and Computer-Assisted Intervention – MICCAI 2013*. vol. 8149, K. Mori, I. Sakuma, Y. Sato, C. Barillot, and N. Navab, Eds., ed: Springer Berlin Heidelberg, 2013, pp. 147-154.

[44] S. K. Warfield, K. H. Zou, and W. M. Wells, "Simultaneous truth and performance level estimation (STAPLE): an algorithm for the validation of image segmentation," *Medical Imaging, IEEE Transactions on,* vol. 23, pp. 903-921, 2004.

[45] M. Martin-Fernandez, S. Bouix, L. Ungar, R. W. McCarley, and M. E. Shenton, "Two methods for validating brain tissue classifiers," in *Medical Image Computing and Computer-Assisted Intervention–MICCAI 2005*, ed: Springer, 2005, pp. 515-522.

[46] L. R. Dice, "Measures of the amount of ecologic association between species.," *Ecology,* vol. 26, pp. 297-302, 1945.

[47] G. W. Williams, "Comparing the joint agreement of several raters with another rater," *Biometrics,* pp. 619-627, 1976.

[48] P. Cachier, E. Bardinet, D. Dormont, X. Pennec, and N. Ayache, "Iconic feature based nonrigid registration: the PASHA algorithm," *Computer Vision and Image Understanding,* vol. 89, pp. 272-298, 2// 2003.

[49] T. Rohlfing and C. R. Maurer, Jr., "Shape-Based Averaging," *Image Processing, IEEE Transactions on,* vol. 16, pp. 153-161, 2007.

[50] T. Rohlfing and C. R. Maurer Jr, "Shape-based averaging for combination of multiple segmentations," in *Medical Image Computing and Computer-Assisted Intervention–MICCAI 2005*, ed: Springer, 2005, pp. 838-845.

[51] M. R. Sabuncu, B. T. Yeo, K. Van Leemput, B. Fischl, and P. Golland, "A generative model for image segmentation based on label fusion," *Medical Imaging, IEEE Transactions on,* vol. 29, pp. 1714-1729, 2010.

[52] J. Uh, T. E. Merchant, Y. Li, X. Li, and C. Hua, "MRI-based treatment planning with pseudo CT generated through atlas registration.," *Med Phys,* vol. 41, pp. 051711-8, 2014.

[53] M. M. Chakravarty, P. Steadman, M. C. Eede, R. D. Calcott, V. Gu, P. Shaw*, et al.*, "Performing label-fusion-based segmentation using multiple automatically generated templates," *Human brain mapping,* vol. 34, pp. 2635-2654, 2013.

[54] P. Aljabar, R. Heckemann, A. Hammers, J. Hajnal, and D. Rueckert, "Classifier Selection Strategies for Label Fusion Using Large Atlas Databases," in *Medical Image Computing and Computer-Assisted Intervention – MICCAI 2007*. vol. 4791, N. Ayache, S. Ourselin, and A. Maeder, Eds., ed: Springer Berlin Heidelberg, 2007, pp. 523-531.

[55] D. L. Collins and J. C. Pruessner, "Towards accurate, automatic segmentation of the hippocampus and amygdala from MRI by augmenting ANIMAL with a template library and label fusion," *Neuroimage,* vol. 52, pp. 1355-1366, 2010.

[56] M. Wu, C. Rosano, P. Lopez-Garcia, C. S. Carter, and H. J. Aizenstein, "Optimum template selection for atlas-based segmentation," *NeuroImage,* vol. 34, pp. 1612-1618, 2/15/ 2007.

[57] P. B. Greer, J. A. Dowling, J. A. Lambert, J. Fripp, J. Parker, J. W. Denham*, et al.*, "A magnetic resonance imaging-based workflow for planning radiation therapy for prostate cancer.," *Med J Aust,* vol. 194, pp. S24-27, Feb 21 2011.

[58] Q. Xie and D. Ruan, "Low-complexity atlas-based prostate segmentation by combining global, regional, and local metrics," *Medical Physics,* vol. 41, pp. -, 2014.

Chapter 6

One Registration Multi Atlas-based Pseudo-CT Generation for Attenuation Correction in PET/MR

Hossein Arabi and Habib Zaidi

European Journal of Nuclear Medicine & Molecular Imaging, Vol. 43, No. 11, pp 2021-2035 (2016)

Abstract

Purpose: The outcome of a detailed assessment of various strategies for atlas-based whole-body bone segmentation from MRI was exploited to select the optimal parameters and setting with the aim to propose a novel one registration multi atlas (ORMA) pseudo-CT generation approach.

Methods: The proposed approach consists of only one online registration between the target and reference images, regardless of the number of atlas images (*N*), while for the remaining atlas images, the pre-computed transformation matrices to the reference image are used to align them to the target image. The performance characteristics of the proposed method was evaluated and compared with conventional atlas-based attenuation map generation strategies (direct registration of the entire atlas images followed by voxel-wise weighting (VWW) and arithmetic averaging atlas fusion). To this end, four different PET attenuation maps were generated via arithmetic averaging and VWW scheme using both direct registration and ORMA approaches as well as the 3-class attenuation map obtained from the Philips Ingenuity TF PET/MRI scanner commonly used in clinical setting. The evaluation was performed based on the accuracy of extracted whole-body bones by the different attenuation maps and quantitative analysis of resulting PET images compared to CT-based attenuation corrected PET images serving as reference.

Results: The comparison of validation metrics regarding the accuracy of extracted bone using the different techniques demonstrated the superiority of VWW atlas fusion algorithm achieving a Dice similarity measure of 0.82±0.04 compared to arithmetic averaging atlas fusion (0.60±0.02), which uses conventional direct registration. Application of the ORMA approach modestly compromised the accuracy yielding a Dice similarity measure of 0.76±0.05 for ORMA-VWW and 0.55±0.03 for ORMA-averaging. The results of quantitative PET analysis followed the same trend with less significant differences in terms of SUV bias,, whereas massive improvements were observed compared to PET images corrected for attenuation using the 3-class attenuation map. The maximum absolute bias achieved by VWW and VWW-ORMA methods was 06.4±5.5 in the lung and 07.9±4.8 in the bone, respectively.

Conclusions: The proposed algorithm is capable of generating decent attenuation maps. The quantitative analysis revealed a good correlation between PET images corrected for attenuation using the proposed pseudo-CT generation approach and the corresponding CT images. The computational time is reduced by a factor *1/N* at the expense of a modest decrease in quantitative accuracy, thus allowing to achieve a reasonable compromise between computing time and quantitative performance.

I. Introduction

Hybrid PET/MRI is establishing itself as a promising multi-modality imaging technology and is expected to provide a major breakthroughopen new insight in clinical diagnostic imaging [1]. In essence, the capability of MRI to provide higher soft-tissue contrast compared to CT, its ability of multiparametric imaging through the various sequences and, above all the absence of radiation exposure, has made it a promising candidate for combination with PET scannerscanning. The growing technical and clinical research interests are directed towards the development of compact concurrent PET/MRI systems with high temporal resolution time of flight capabilities and addressing the challenges of quantitative imaging [2]. Despite the promise of PET/MRI, defining a clear and unambiguous roadmap in terms of and clinical applications of this technology is still being debated [3-5]. In addition, correcting the PET emission data for attenuation is still a major challenge since there is no correlation between MR intensity and attenuation coefficients of biological tissues [6, 7]. Nonetheless, a number of attenuation map generation methods have been proposed, including MR image segmentation techniques implemented for brain [8] and whole-body imaging [9, 10], atlas and machine learning approaches evaluated on brain dataset [11] and developed for whole-body imaging [12, 13], the use of dedicated MRI sequences, such as ultra-short echo (UTE) [14, 15] or zero time echo (ZTE) [16] to extract bony structures, and the joint estimation of emission and transmission maps from the only the emission data [17, 18].

Tissue class segmentation type of techniques is are the most widely used on commercial PET/MRI scanners in clinical setting. Ignoring bones is the major limitation of commonly used segmentation approaches since segmenting bones from conventional MRI sequences is prohibitively difficult task, particularly in whole-body imaging [6, 7]. UTE/ZTE MRI sequences enable to identify a separate bone class owing to the distinct contrast between air and bone; however, the relatively long scanning time has limited its usage to single-bed acquisition protocols, such as such as brain imaging [14]. An alternative option to include bony structures in MRI-based attenuation maps is to use prior knowledge provided by atlas registration [12, 19]. Promising results have been reported using atlas registration techniques for attenuation correction in the head region [12, 19-26]. Most of the proposed attenuation map generation approaches considering bone in whole-body PET/MRI rely on prior information provided by atlas images to delineate bony structures [12, 27-29]. Hofmann et al. used a machine learning technique based on the registration of multiple MRI/CT pairs to the patient's MRI [12]. Bezrukov et al. modified the original technique by using bone probability maps to address signal loss arising from metal object artifacts in MR images and to reduce the processing time [27]. More recently, Arabi and Zaidi further improved the performance of this approach by introducing a dedicated regression kernel for lung attenuation estimation and enhancing bone identification through atlas sorting [13]. Still the computational time required for multiple atlas registration and training the algorithm is considered to be the main limitation of this category of techniques. Moreover, comparative studies demonstrated that there is still scope for improving further their accuracy [30, 31]. To reduce the processing time, Marshall et al. proposed a scheme enabling to find the most similar subject to the target image in terms of body geometry [29].

In previous work, we compared a number of atlas-based segmentation techniques for bone segmentation from whole-body MRI [31]. As a result, an optimized segmentation algorithm was devised which outperformed previous methods of whole-body attenuation map generation in terms of bone extraction accuracy. The aim of this work is to evaluate the accuracy of the proposed whole-body bone segmentation method using clinical PET/MRI studies and, more importantly, propose a novel one registration multiple atlas (ORMA) pseudo-CT generation approach that drastically enabling to reduces drastically the computation time. The proposed approach requires only one online registration for each target subject regardless of the number of used atlas images (N) and at the same time benefits from the information available from multiple atlas datasets.

The performance of the proposed method was compared with direct registration of the entire atlas images to the target followed by arithmetic averaging and voxel-wise weighting (VWW) atlas fusion schemes. The resulting pseudo-CT images were evaluated in terms of accuracy of extracted bone using standard segmentation validation measures and quantitative analysis of tracer uptake in corresponding attenuation corrected PET images.

II. Materials and methods

II.A. PET/MRI/CT data acquisition and reconstruction

The patient population in this study consists of 23 patients (15 men and 8 women); mean age ± SD = 60 ± 8 y), referred to our department for whole-body 18F-FDG PET/MRI examinations for staging of head and neck malignancies. The study protocol was approved by the institutional ethics committee and all patients gave their written informed consent. A single injection of 18F-FDG (371±23 MBq) was administrated and patients underwent MRI examinations on the Ingenuity TF PET/MRI system (Philips Healthcare, Cleveland, OH) [32]. The aforementioned PET/MR scanner utilizes a 3-class segmentation attenuation map derived from a 3D multi-stack spoiled T1-weighted MRI (flip angle 10°, TE 2.3 ms, TR 4.1 ms) comprising background air 0.0 cm-1 (-1,000 HU), lung 0.022 cm-1 (-770 HU), and soft-tissue 0.096 cm-1 (0 HU) for PET attenuation correction [10]. The 3-class attenuation map technique is also evaluated in this work as a common attenuation correction approach used in the clinic. Our MRI-guided pseudo-CT generation approach uses a whole-body Dixon 3D volumetric interpolated T1-weighted sequence acquired using the following parameters: flip angle 10°, TE 11.1 ms, TE 22.0 ms, TR 3.2 ms, 450×354 mm2 transverse FOV, 0.85×0.85×3 mm3 voxel size. The total acquisition time for each patient was 2 min and 17 s and fat-only, water-only, out-phase, and in-phase images were produced separately.

After PET/MRI scan completion, PET/CT scanning was performed on a Biograph 64 True Point scanner (Siemens Healthcare, Erlangen, Germany). After patient positioning and a localization scout scan, an unenhanced CT scan (120 kVp, 180 mAs, 24×1.5 collimation, a pitch of 1.2, and 1 s per rotation) was performed for the purpose of attenuation correction and anatomic localization. PET data acquisition started 146.2±20 min post-injection with 3 min per bed position for a total of 5–6 bed positions, resulting in a total acquisition time of 15–18 min. CT-based attenuation corrected PET data (PET/CTAC) of the PET/CT scans served as reference for quantitative evaluation of PET images corrected using the various attenuation maps. Both T1-weighted and Dixon MR images were non-rigidly aligned to the corresponding CT images using the elastix package [33] as described in a previous study [34]. PET images corrected for attenuation using the different techniques were reconstructed using the ordinary Poisson, ordered subset-expectation maximization (OP-OSEM) iterative reconstruction algorithm implemented in the e7 tools (Siemens) using default parameters (4 iterations, 8 subsets, and a post-processing Gaussian kernel with a FWHM of 5 mm).

II.B. Data preprocessing

The high level of noise, corruption from the low frequency bias field inhomogeneity, and inter-patient intensity non-uniformity are among the weaknesses of short acquisition time MR sequences developed chiefly for attenuation correction, which can affect the performance of the registration procedure and local image similarity measurement. These factors have even more profound influence on image similarity analysis since the artificial intensity variation between MR images can directly affect the final outcome. To alleviate the impact of these factors, the following processing was performed on MR in-phase images.

In the first step, noise suppression was achieved by gradient anisotropic diffusion filtering [35]. This filter blurs over regions where the gradient magnitude is relatively small (homogenous regions) but diffuses little over areas of the image where the gradient magnitude is large (i.e., edges). Therefore, anatomical regions are blurred but their edges are less blurred. The anisotropic filtering parameters are conductance= 4, iteration=10 and time step=0.01. N4 bias field correction algorithm [36] was employed to cancel out intra-patient intensity inhomogeneity using the following parameters: B-spline grid resolution=400, number of iteration=200 (at each grid resolution), convergence threshold = 0.001, B-spline order=3, spline distance=400, number of Histograms=256 and shrink factor=3. The presence of low-frequency intensity non-uniformity within a subject, known as bias field or illumination inhomogenuity, is considered as a potential confounder in various image analysis tasks. Bias field correction minimizes the intensity inhomogeneity within an MR image caused by the non-uniform magnetic field in MR imaging. Inter-patient intensity inhomogeneity was handled through histogram matching [37] using the following settings: histogram level = 1024 and match points = 128. To obtain the best result from histogram matching, it is recommended to exclude background air voxels of both reference and target images before processing.

II.C. Mean geometry patient

The first step required for implementation of the ORMA pseudo-CT generation algorithm is the determination of the mean geometry of the patient population. The common practice to create an atlas representing a population is

to pick a reference patient image to which other patient images will be aligned to, in such a way that the reference image coordinates act as common spatial frame. The major drawback of this approach is that the resulting atlas would be inherently biased towards the chosen reference image. For instance, when the reference image happens to be an extreme case of the population, the resulting common spatial frame does not adequately represent the common population geometry. In this case, warping a query image into the reference space may lead to flawed outcome since the geometric distance that the query image has to travel to reach the reference spatial frame is not optimal compared to the case of reaching an atlas residing at the mean geometry of the population. Therefore, determining the closest patient to the mean geometry of the population is thought to be an essential prerequisite step.

The first step needed to determine the mean geometry of the population includes pair-wise deformable alignment of the entire patient images to each other, which requires *N(N-1)/2* registrations (*N* is the number of atlases). Finding the patient with mean population geometry is performed offline and only once on CT images (figure 1). The *N(N-1)/2* non-rigid registrations were performed by combining affine and non-rigid alignment based on the advanced Mattes mutual information [38] implemented in the elastix package [33] by considering the following settings: interpolate: thin-plate spline, optimizer: standard gradient decent, image pyramid schedule: (32 16 8 4 2 2), grid spacing schedule (32.0 32.0 16.0 8.0 4.0 2.0), maximum number of iterations (8192 4096 4096 2048 1024 1024), number of histogram bins: 64. Given the *N(N-1)/2* geometric transform matrices between patient images, the geometric distance between each pair of images can be measured by the roughness of the geometric transform. Here, we define the geometric distance between two images on the basis of the bending energy, which is the sum of squared second partial derivatives of the geometric distance as described in [39]. The analytic formula used to calculate the bending energy for the thin-plate spline algorithm is given elsewhere [40].The patient image residing at the mean population geometry has the minimum sum of distances to other images. Determining the closest image to the mean geometry is possible if all the relative locations of the population are known. In this work, the geometric distances obtained from pair-wise registration of the atlas images were used as surrogate of image distances. Given the relative distance of the atlas images, multidimensional scaling (MDS) was exploited to determine the mean geometry subject. MDS defines a new coordinate system in which the absolute distance of each atlas image to the origin of the new coordinate system can be calculated. The subject residing at the minimum distance to the origin in the new coordinate system is defined as the reference image (figure 2). More details about the MDS procedure are provided in the Appendix.

Given a reference image, all the remaining subject images are non-rigidly warped (applying the aforementioned registration procedure) to the reference image spatial coordinates. All these procedures are performed offline as illustrated in figure 1. At the end of this step, *(N-1)* transformation matrices *Tr(A,R)* mapping the atlas images *(A)* to the selected reference image *(R),* are produced.

II.D. ORMA pseudo-CT generation procedure

The underlying idea behind ORMA pseudo-CT generation approach is the combination of the pre-computed transformation matrices, *Tr(A,R),* with the reference to target image transform matrix, *Tr(R,T),* to transform all images of the atlas dataset to the target image spatial coordinate (figure 1). *Tr(R,T)* obtained from online registration between the reference and target image is combined with the pre-computed transformation matrices *Tr(A,R)* to map the *N-1* MR images to the target image. The same transformation is applied to the corresponding CT images. This produces *N* pairs of MR/CT images aligned to the target MR image (*N-1* through the indirect and 1 through direct registration), thus allowing the generation of an atlas-based pseudo-CT attenuation map. The proposed method requires only one online registration and benefits from the anatomical variability provided by multiple atlas images.

The performance of ORMA pseudo-CT generation approach was assessed through comparison with direct registration of the entire atlas images to the target subject to evaluate the loss in accuracy. A leave-one out cross validation framework was employed for all patient datasets. Two commonly used atlas fusion schemes were adopted for attenuation map generation: arithmetic averaging and voxel-wise weighting (VWW). Arithmetic averaging consists of simple averaging of all the aligned atlas CT images:

$$Average = \frac{1}{N} \sum_{n=1}^{N} Tr(CT)_n \quad (1)$$

where $Tr(CT)_n$ indicates the n^{th} directly aligned atlas CT to the target image. Similarly, the average of atlas images using the ORMA framework is obtained by:

$$ORMA\ average = \frac{1}{N} \sum_{n=1}^{N} ORMA(CT)_n \quad (2)$$

The second approach incorporates VWW based on image similarity measurement within patches of voxels to mitigate the impact of non-systematic registration errors [42, 43]. In the VWW atlas fusion approach, the local similarity between the target and each of the atlas images is commonly measured using normalized mutual information (NMI), local normalized cross-correlation (LNCC) or mean square distance (MSD) similarity criteria. In our previous study [31], we addressed the optimization aspect of VWW atlas fusion based on the accuracy of bone extraction in whole-body MR imaging using the same datasets. The obtained optimal parameters and setting are employed here to generate pseudo-CT attenuation maps.

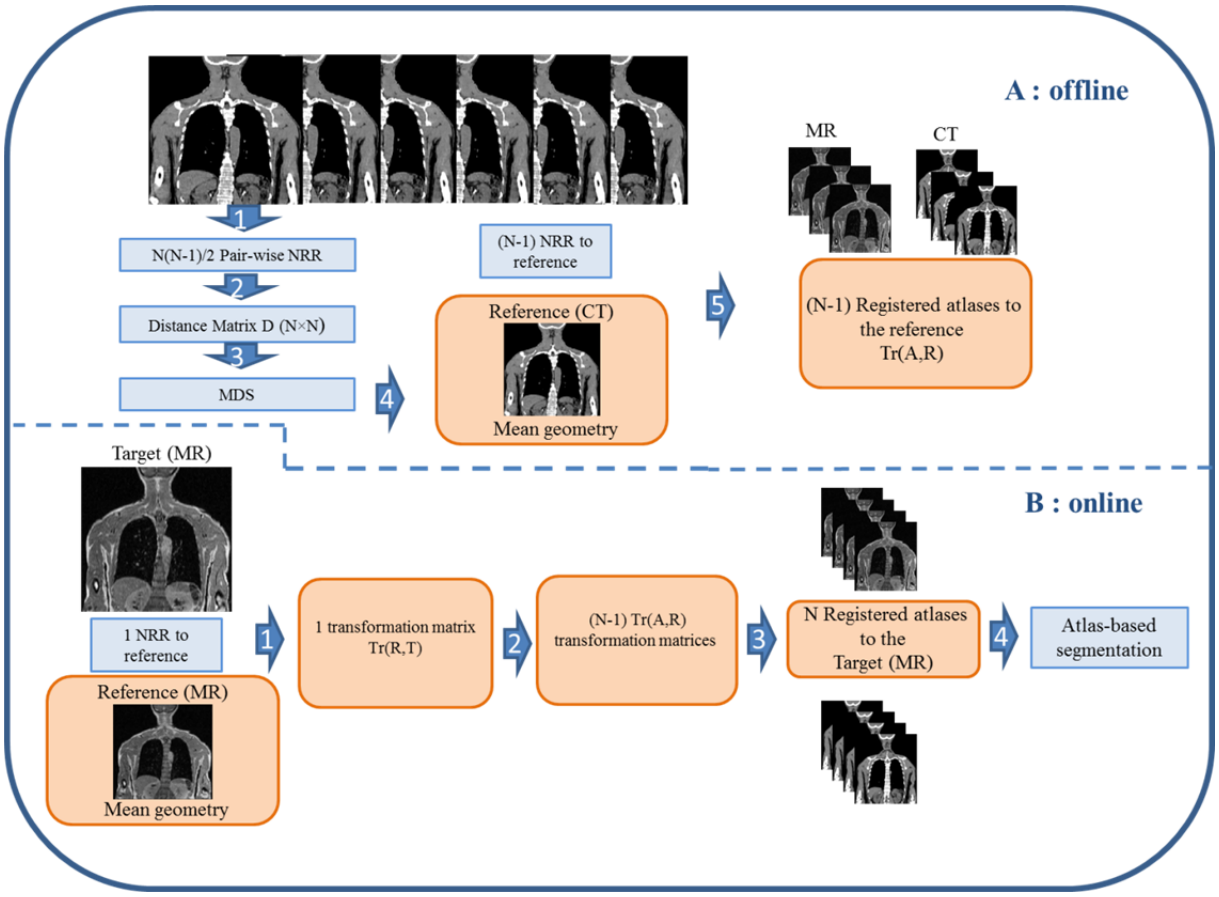

Figure 1. Flowchart describing the different steps involved in the implementation of the proposed one registration multiple atlas (ORMA) pseudo-CT generation approach.

The reference above concluded that the MSD image similarity measure outperformed the other aforementioned similarity criteria. The MSD between two patches of atlas and target images is calculated considering the following equation:

$$MSD_D(x) = \frac{|D|}{\sum_{x \in D} |T(x) - Tr(MR(x))_n|^2} \quad (3)$$

where, T is the MR image of the target subject, $Tr(.)$ indicates the transformation of the n^{th} MR atlas to the target image, D stands for the neighboring voxel in the vicinity of the central voxel x and $|D|$ represents the cardinality of D. The obtained optimal patch size (D) for calculation of the MSD similarity was 5 mm, corresponding to the edge of a cube centered at x. Since the range of calculated similarity measures can vary quite dramatically between subjects and locations, which may adversely affect the atlas fusion process, a ranking scheme was employed whereby the similarity measure value for each transformed atlas is ranked across all atlases [44]. Let's

suppose that ranked atlases based on similarity measurements on patch D are denoted $R(n,x)_D$, the conversion to appropriate weights is performed by applying an exponential decay function:

$$w(x)_n = e^{-aR(n,x)_D} \tag{4}$$

By adopting a ranking scheme, the training subject at voxel x that best matches the target subject is assigned a weight of 1 whereas the training subject presenting with the second best match is assigned a weight e^{-a} and so on. Thus, the pseudo-CT generation can be carried out by including the weighting factor w_n in the following equation:

$$VWW(x) = \frac{1}{Nr} \sum_{n=1}^{N} w(x)_n \times Tr(CT(x))_n \quad \text{subject to} \quad Nr = \sum_{n=1}^{N} w(x)_n \tag{5}$$

Tr(.) used to transform atlas images to the target spatial coordinates can be generated through either direct registration or using the ORMA approach. The resulting pseudo-CTs are referred to as VWW and ORMA-VWW, respectively. The voxel-wise atlas fusion introduces the free parameter (a), whose value after optimization was equal to 1 [31].

Tr(.) used to transform atlas images to the target spatial coordinates can be generated through either direct registration or using the ORMA approach. The resulting pseudo-CTs are referred to as VWW and ORMA-VWW, respectively. The voxel-wise atlas fusion introduces the free parameter (a), whose value after optimization was equal to 1 [31].

The performance of ORMA pseudo-CT generation approach was assessed through comparison with direct registration of the entire atlas images to the target subject to evaluate the loss in accuracy. A leave-one out cross validation framework was employed for all patient datasets. Two commonly used atlas fusion schemes were adopted for attenuation map generation: arithmetic averaging and voxel-wise weighting (VWW). Arithmetic averaging consists of simple averaging of all the aligned atlas CT images:

$$Average = \frac{1}{N} \sum_{n=1}^{N} Tr(CT)_n \tag{1}$$

where $Tr(CT)_n$ indicates the n^{th} directly aligned atlas CT to the target image. Similarly, the average of atlas images using the ORMA framework is obtained by:

$$ORMA\ average = \frac{1}{N} \sum_{n=1}^{N} ORMA(CT)_n \tag{2}$$

The second approach incorporates VWW based on image similarity measurement within patches of voxels to mitigate the impact of non-systematic registration errors [42, 43]. In the VWW atlas fusion approach, the local similarity between the target and each of the atlas images is commonly measured using normalized mutual information (NMI), local normalized cross-correlation (LNCC) or mean square distance (MSD) similarity criteria. In our previous study [31], we addressed the optimization aspect of VWW atlas fusion based on the accuracy of bone extraction in whole-body MR imaging using the same datasets. The obtained optimal parameters and setting are employed here to generate pseudo-CT attenuation maps.

The reference above concluded that the MSD image similarity measure outperformed the other aforementioned similarity criteria. The MSD between two patches of atlas and target images is calculated considering the following equation:

$$MSD_D(x) = \frac{|D|}{\sum_{x \in D} |T(x) - Tr(MR(x))_n|^2} \tag{3}$$

where, T is the MR image of the target subject, *Tr(.)* indicates the transformation of the n^{th} MR atlas to the target image, D stands for the neighboring voxel in the vicinity of the central voxel x and $|D|$ represents the cardinality of D. The obtained optimal patch size (D) for calculation of the MSD similarity was 5 mm, corresponding to the edge of a cube centered at x. Since the range of calculated similarity measures can vary quite dramatically between subjects and locations, which may adversely affect the atlas fusion process, a ranking scheme was employed whereby the similarity measure value for each transformed atlas is ranked across all atlases [44]. Let's suppose that ranked atlases based on similarity measurements on patch D are denoted $R(n,x)_D$, the conversion to appropriate weights is performed by applying an exponential decay function:

$$w(x)_n = e^{-aR(n,x)_D} \quad (4)$$

By adopting a ranking scheme, the training subject at voxel *x* that best matches the target subject is assigned a weight of 1 whereas the training subject presenting with the second best match is assigned a weight e^{-a} and so on. Thus, the pseudo-CT generation can be carried out by including the weighting factor w_n in the following equation:

$$VWW(x) = \frac{1}{Nr} \sum_{n=1}^{N} w(x)_n \times Tr(CT(x))_n \quad \text{subject to} \quad Nr = \sum_{n=1}^{N} w(x)_n \quad (5)$$

Tr(.) used to transform atlas images to the target spatial coordinates can be generated through either direct registration or using the ORMA approach. The resulting pseudo-CTs are referred to as VWW and ORMA-VWW, respectively. The voxel-wise atlas fusion introduces the free parameter (*a*), whose value after optimization was equal to 1 [31].

II.D. Data analysis

First, the attenuation maps obtained using the four different attenuation map generation strategies (arithmetic averaging and VWW using direct registration, ORMA-average and ORMA-VWW) are evaluated based on the accuracy of extracted whole-body bone (obtained by thresholding at 140 HU). Bone identification accuracy was assessed using five volume/distance-based measures, including the Dice similarity (DSC) [45], relative volume difference (RVD) [30], Jaccard similarity (JC) [30], sensitivity (S) [46] and mean absolute surface distance (MASD) [47].

$$DSC(C,P) = \frac{2|C \cap P|}{|C|+|P|}, RVD(C,P) = 100 \times \frac{|C|-|P|}{|P|}, JC(C,P) = \frac{|C \cap P|}{|C \cup P|}, S(C,P) = \frac{|C \cap P|}{|P|}, MASD(C,P) = \frac{d_{ave}(S_C,S_P) + d_{ave}(S_P,S_C)}{2} \quad (6)$$

where *C* and *P* denote segmented bone from the reference CT and generated pseudo-CT images, respectively. $d_{ave}(S_C,S_P)$ computes the average direct surface distance from all points on the reference bone surface S_C to the segmented bone surface S_P. Paired t-test analysis was used to determine if two datasets are different from each other and the obtained results were considered statistically significant if the p-value was less than 0.05.

In addition to bone extraction, the accuracy of the generated attenuation maps was assessed in terms of lung volume overlap and air cavities identification. To this end, the lungs and air cavities in the head region were segmented separately on each attenuation map followed by application of above described segmentation metrics to report the results. The ITK-SNAP image processing software [48] initialized by user-specified seeds was used to segment the lungs. Thereafter, the mean linear attenuation coefficient of the lungs produced by the different methods was calculated and compared to the reference value derived from CT images.

Quantitative analysis of tracer uptake was also performed on PET images corrected for attenuation using the various pseudo-CT attenuation maps. To this end, the raw PET data of the PET/CT scan were used to assess the performance of 5 different MRI-guided attenuation correction techniques including direct registration and arithmetic averaging (PET_Ave), ORMA plus arithmetic averaging (PET_ORMA-Ave), direct registration plus VWW atlas fusion (PET_VWW), ORMA plus VWW atlas fusion (PET_ORMA-VWW), and the 3-class attenuation map (PET_MR3C). CT-based attenuation correction of PET data using CT (PET_ACCT) was considered as reference for assessment of these techniques. SUV bias analysis was performed using VOIs defined on both normal uptake anatomical regions and malignant abnormalities split into soft-tissue and bone lesions. Soft-tissue lesions reside far from bony structures whereas bone lesions are located in or very close to bones. An experienced nuclear medicine physician manually drew the VOIs on regions of normal physiologic uptake (lungs, liver, cerebellum, bone tissue (cervical vertebrae 6), aorta cross) and on malignant lesions located near and distant from bony structures. The differences between the various attenuation correction techniques were quantified in terms of changes in the standardized uptake value (SUV). The mean SUV measured in each VOI (*PET_MRAC*) was used to calculate the relative SUV bias (Eq. 7) and relative absolute SUV bias (Eq. 8) considering ACCT PET images (*PET_ACCT*) as reference:

$$Relative\ error\ (\%) = \frac{PET\_MRAC\ (SUV) - PET\_ACCT\ (SUV)}{PET\_ACCT\ (SUV)} \times 100(\%) \quad (7)$$

$$Relative\ absolute\ error\ (\%) = \frac{|PET_{MRAC}(SUV) - PET_{ACCT}(SUV)|}{PET\_ACCT\ (SUV)} \times 100(\%) \quad (8)$$

In addition to the calculated relative SUV errors, linear regression analysis results and joint histograms of MRI-derived attenuation maps versus reference CT images and PET/MRI-derived AC versus PET/CT were plotted for each technique (over all patients).

III. Results

The obtained two-dimensional projection of the coordinates is illustrated in figure 2. The origin of figure 2 indicates the location of the mean geometry which is calculated by taking the arithmetic mean of 23 coordinates. The image residing at the closest location to the origin (atlas number 10) was chosen to be the best reference image.

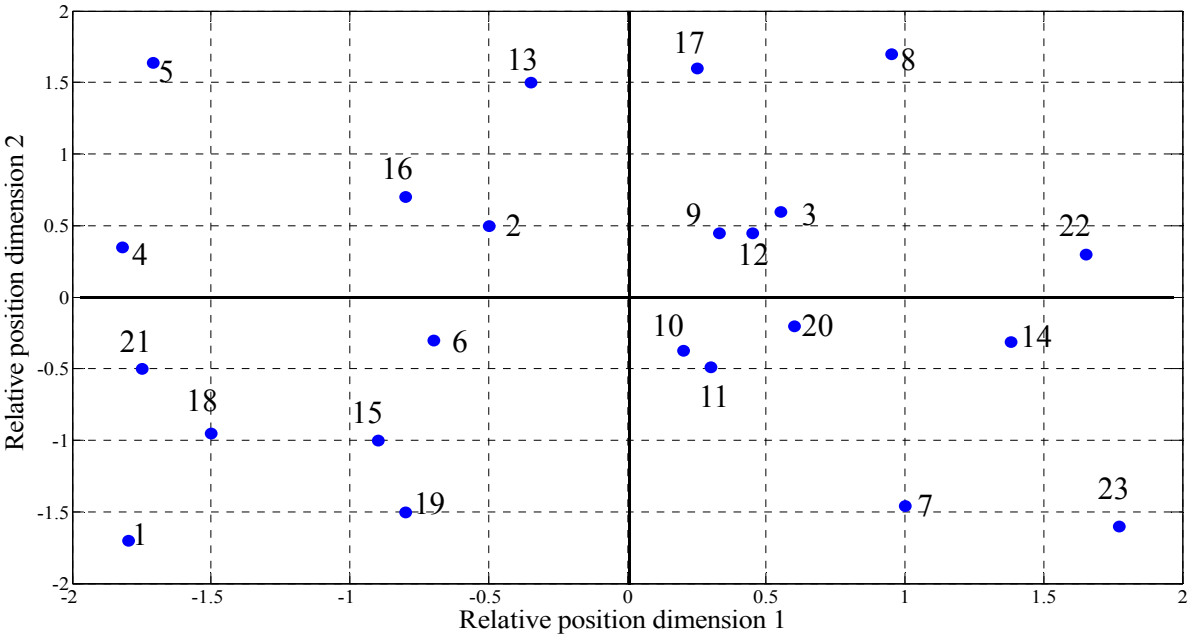

Figure 2. Relative locations of 23 subject images obtained by multi-dimensional scale (MDS) where the mean location is sited at coordinate (0,0) and the closest image to the mean is determined to be atlas number 10.

Representative sagittal slices of the generated MRI-derived pseudo-CT images are shown in figure 3. These slices were chosen for visual assessment of bone extraction accuracy as well as the sharpness of the lungs and windpipe boundaries. Visual inspection revealed that the averaging atlas fusion method using either direct registration (figure 3C) or ORMA (figure 3E) tends to induce significant blurring and un-sharpness compared to VWW (figures 3D and 3F, respectively). Table 1 summarizes bone extraction metrics between the different pseudo-CT generation methods. VWW atlas fusion approaches improve significantly all validation measures compared to averaging fusion (from 0.60 DSC to 0.82 DSC for direct registration). However, the accuracy is slightly compromised when employing ORMA (from 0.55 to 0.76 DSC).

Table 1. Comparison of extracted bone accuracy validation measures (mean±SD) between the different pseudo-CT generation techniques, including Dice similarity (DSC), relative volume distance (RVD), Jaccard (JC), Sensitivity (S) and mean absolute surface distance (MASD). (*) indicates P-value > 0.05 according to the paired t-test

	DSC	RVD(%)	JC	S	MASD(mm)
Average	0.60±0.02*	46.0±02.4*	0.43±0.02*	0.46±0.02*	10.7±03.9*
ORMA-average	0.55±0.03*	52.6±02.5*	0.38±0.02*	0.41±0.03*	11.3±03.6*
VWW	0.82±0.04	-09.0±04.1	0.75±0.04	0.77±0.04	02.0±01.1
ORMA-VWW	0.76±0.05	-16.8±05.4	0.66±0.05	0.69±0.06	03.9±01.8

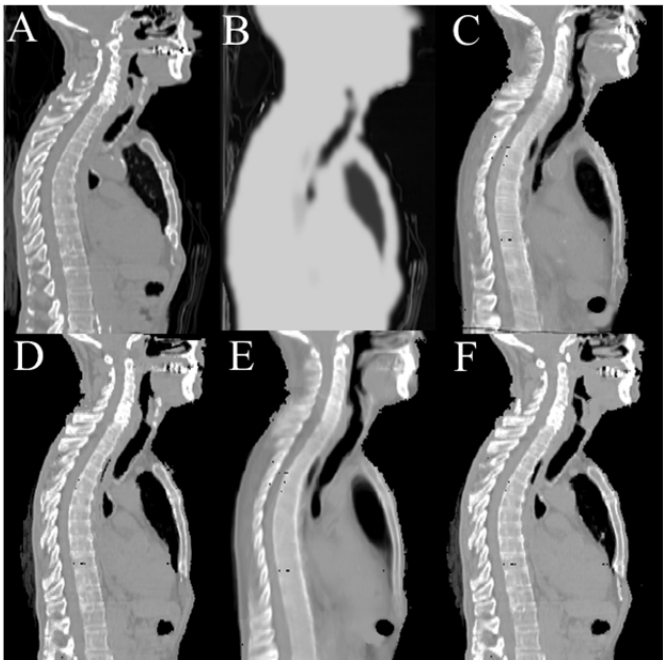

Figure 3. Representative slice showing (A) reference CT, and MRI-guided attenuation maps: (B) 3-class, (C) Average, (D) VWW, (E) ORMA-average and (G) ORMA-VWW.

Table 2. Comparison of the accuracy of extracted air cavities in the head region between the different pseudo-CT generation techniques using different metrics, including Dice similarity (DSC), relative volume distance (RVD), Jaccard (JC), Sensitivity (S) and mean absolute surface distance (MASD). (*) indicates P-value > 0.05 according to paired t-test analysis.

Methods	DSC	RVD(%)	JC	S	MASD(mm)
Average	0.65±0.03	42.5±02.9*	0.47±0.03*	0.51±0.03*	1.2±01.6
ORMA-average	0.61±0.03	48.3±03.0*	0.42±0.03*	0.46±0.03*	1.4±01.8
VWW	0.83±0.04	08.2±03.8	0.77±0.04	0.78±0.05	00.5±00.8
ORMA-VWW	0.78±0.05	13.9±04.9	0.69±0.05	0.72±0.05	00.9±01.0

Figure 4 depicts representative binary masks of extracted bone when using the four pseudo-CT generation techniques together with their corresponding error distance map calculated through comparison with CT-derived bone (figure 4C). In addition, the evaluation of lung and air cavity segmentations revealed the same trend observed on bone extraction accuracy. The accuracy of air cavities delineation in the head region obtained from the different methods is slightly improved compared to bone results (Table 2). The VWW method resulted in air volume identification accuracy of 0.83 DSC while the ORMA approach resulted in 0.78 DSC. Table 3 compares the accuracy of lung volume delineation whereas Table 4 compares the mean attenuation coefficient of the lung expressed in Hounsfield units (HU) estimated by the different methods. The VWW approach not only enhances lung delineation accuracy and estimation of mean attenuation coefficients but also reduces the variability of the estimates. However, ORMA introduces moderate degradation of the results.

Table 3. Comparison of lung delineation accuracy between the different pseudo-CT generation techniques using standard validation measures (mean±SD): Dice similarity (DSC), relative volume distance (RVD), Jaccard (JC), Sensitivity (S) and mean absolute surface distance (MASD). There are no statistically significant differences between the results ($p<0.05$) in all cases.

Methods	DSC	RVD(%)	JC	S	MASD (mm)
Average	0.87±0.05	07.1±02.9	0.78±0.03	0.81±0.02	9.7±06.6
ORMA-average	0.84±0.05	08.0±03.0	0.75±0.02	0.78±0.02	10.4±07.1
VWW	0.92±0.04	05.9±02.8	0.88±0.04	0.88±0.03	03.1±03.0
ORMA-VWW	0.90±0.04	06.6±02.9	0.85±0.04	0.85±0.03	03.9±03.4

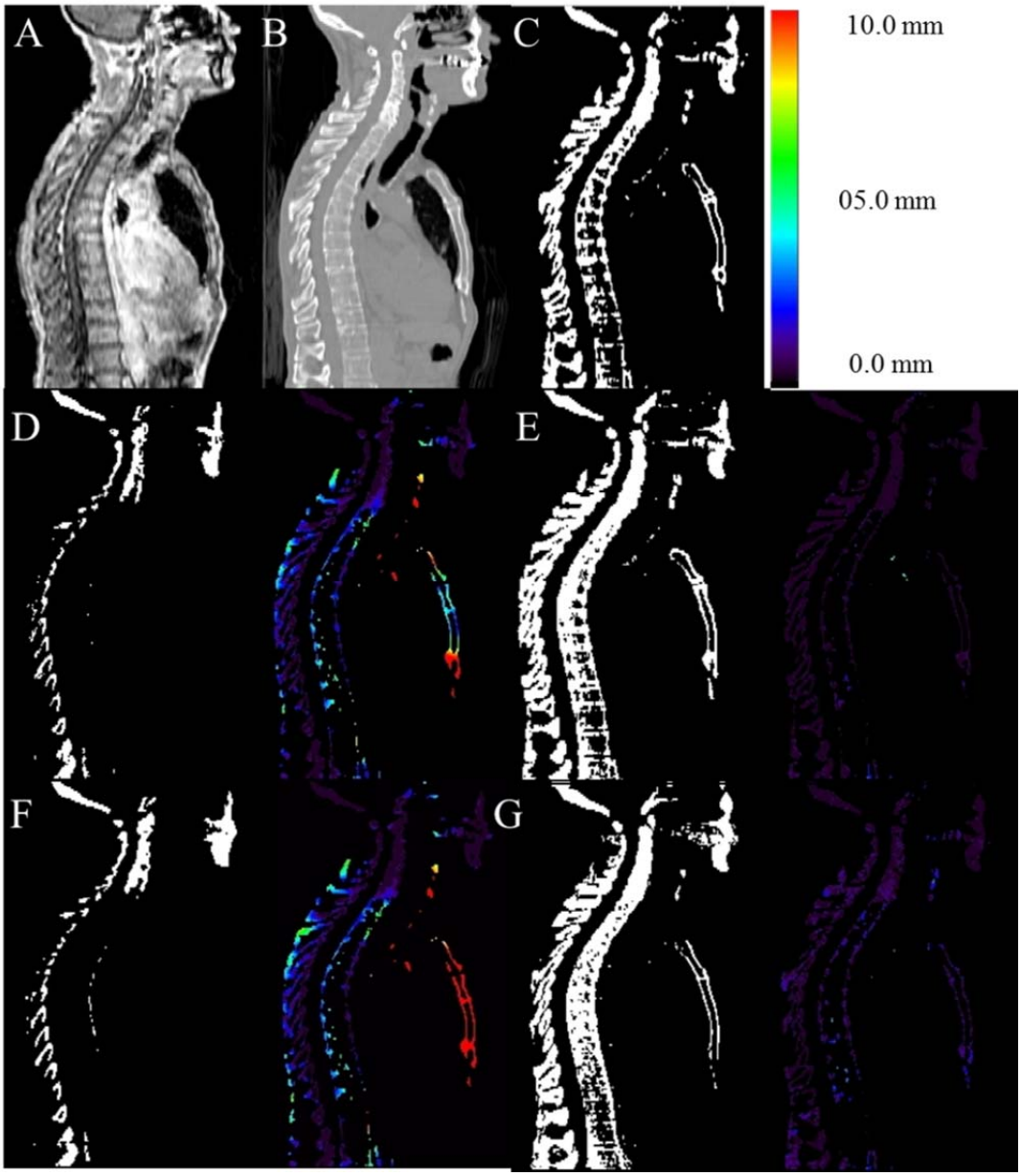

Figure 4. Representative slice of bone segmentation from MR images together with corresponding error distance map. (A) In-phase MR image, (B) corresponding CT image, (C) binary image of reference bone (extracted using a threshold of 140 HUs), (D) Average, (E) VWW, (F) ORMA-average, (G) ORMA-VWW.

Table 5 (top) summarizes the relative errors between SUVmean measured on PET images corrected for attenuation using four different atlas-based attenuation correction methods together with the 3-class and CT-based attenuation corrected PET images. The measured SUVs in bones (cervical 6) exhibit significant improvement from -29.3±9.4 (PET_MR3C) to 3.4±4.5 (PET_VWW) while a modest SUV recovery improvement is observed by exploiting direct atlas registration instead of ORMA approach in almost all regions. Similarly, the relative absolute errors shown in Table 5 (bottom) show only slight degradation when applying the ORMA approach even for bony lesions. The VWW-ORMA method resulted in an absolute error of 4.4±4.3 compared to 4.0±4.2 obtained using the VWW technique.

Table 4. Comparison of lung attenuation in Hounsfield units (HUs) obtained from different methods.

CT	MR3C	Average	ORMA-average	VWW	ORMA-VWW
-798±54	-770±00	-789±70	-784±79	-805±57	-794±62

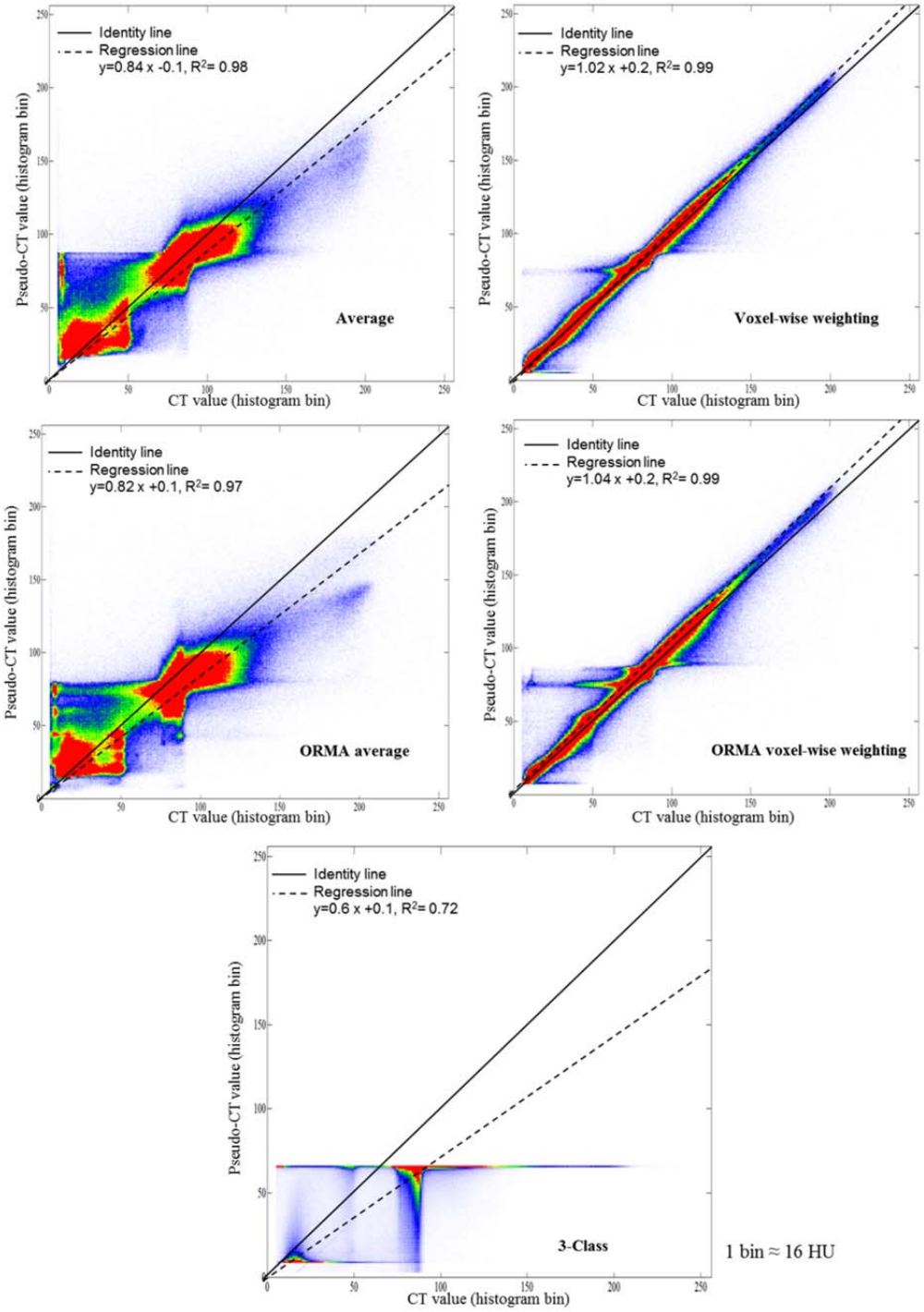

Figure 5. Joint histograms correlating Average, VWW, ORMA-average and ORMA-VWWpseudo-CTs with reference CT values. Each histogram bin corresponds almost to 16 HU.

Figure 5 depicts the joint histogram graphs obtained by plotting the correlation between different MRI-derived attenuation maps and the reference CT image. The VWW scheme yielded the best regression correlation ($y=1.02x +0.2$ and $R^2= 0.99$) while the 3-class attenuation map deviated substantially from the identity line ($y=0.6x +0.1$ and $R^2= 0.72$). Applying the ORMA approach to the pseudo-CT generation process slightly degraded the correlation compared to the direct atlas registration framework. The same trend is seen in figure 6 where the joint histograms are plotted for PET tracer uptake values. PET images corrected for attenuation using the 3-class attenuation map underestimates tracer uptake while atlas-based techniques improved significantly quantitative accuracy.

Applying the ORMA approach as an alternative to direct atlas registration engendered a trivial deviation from tracer uptake values measured on PET/CT images. Figure 7 shows the error maps (relative bias) between reference CT images and five different MRI-derived attenuation maps for one representative clinical study. The

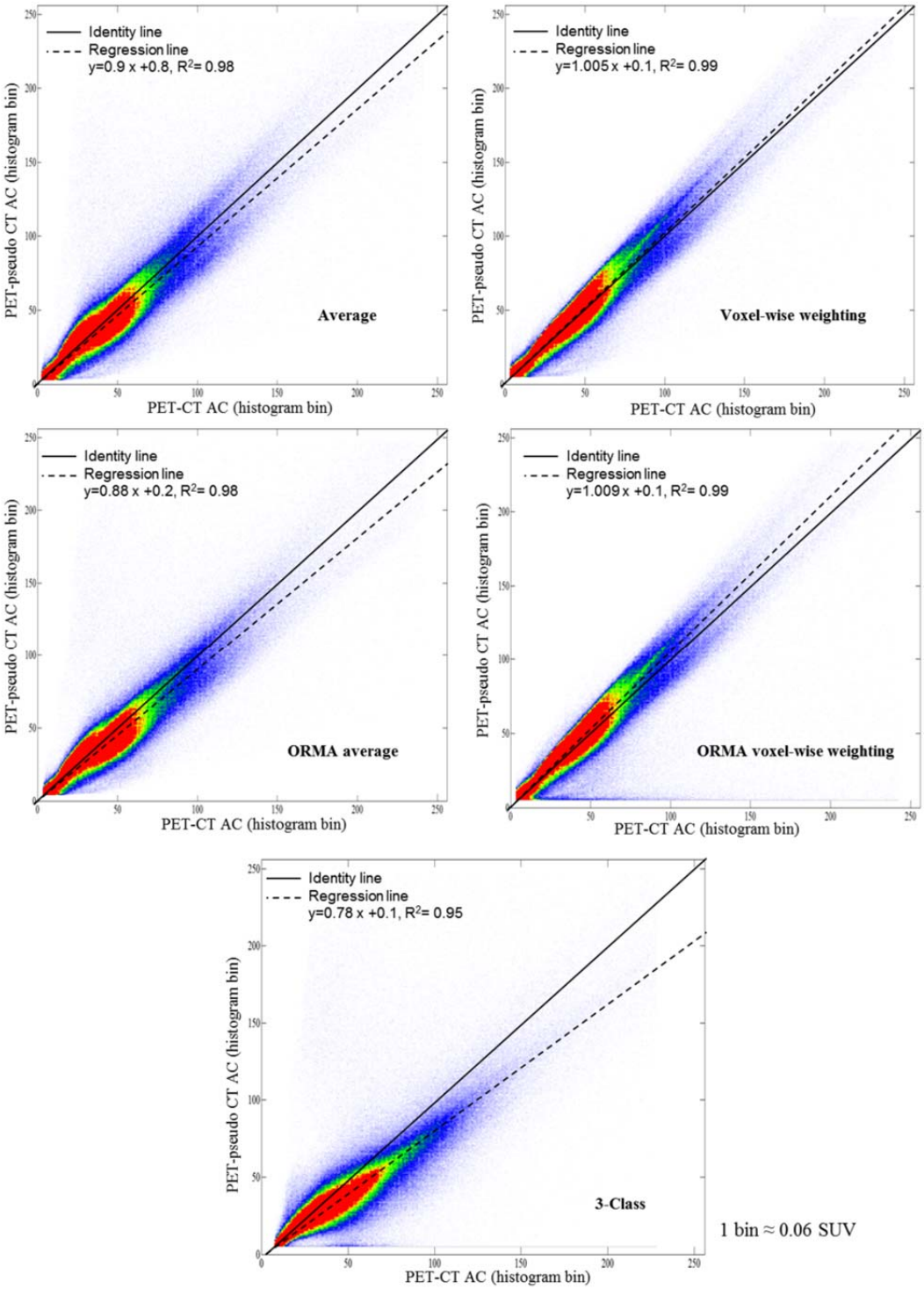

estimated activity bias maps between PET/CT and PET images corrected for attenuation using five different attenuation maps of the same patient are illustrated in Figure 8.

Figure 6. Joint histograms correlating tracer uptake values from PET images corrected for attenuation using Average, VWW, ORMA-average and ORMA-VWWpseudo-CT attenuation maps with CT-based PET attenuation corrected images. Each histogram bin corresponds almost to 0.06 SUV.

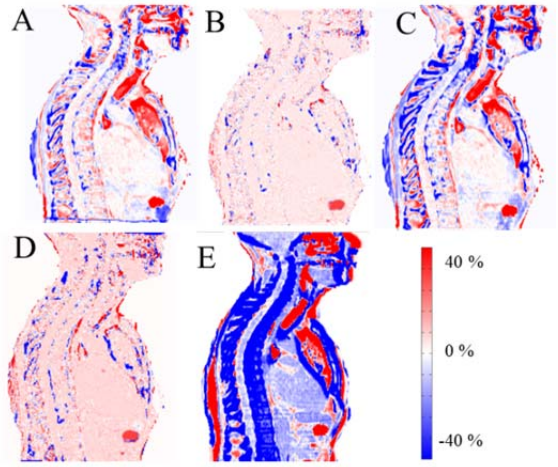

Figure 7. Error maps (relative bias) between refrence CT image and (A) Average (B) VWW (C) ORMA-average (D) ORMA-VWWand (E) MR-derived 3-class attenuation maps.

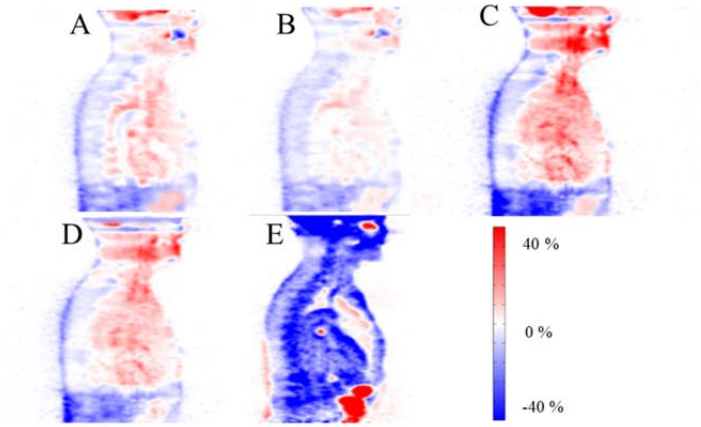

Figure 8. SUV error maps (relative bias) between PET_CTAC and (A) PET_Ave, (B) PET_VWW, (C) PET_ORMA-Ave (D) PET_ORMA-VWW and (E) PET_MR3C.

IV. Discussion

Employing the VWW scheme, whether applying or not the ORMA technique, had remarkable impact on the quality of resulting pseudo-CT images in terms of extracted bone accuracy considering the validation measures summarized in Table 1. The inspection of figure 3 shows the superior quality of the VWW approach where the lung boundaries are remarkably sharper compared to simple averaging, which suffers from considerable diffusion of nearby soft-tissue. This would result in overestimation of tracer uptake in lung regions particularly near the boundaries. The resolved bony structures also exhibit major improvement in terms of anatomical details and boundary sharpness as reflected by the improvement of the Dice similarity measure from 0.60±0.02 to 0.82±0.04 and from 0.55±0.03 to 0.76±0.05 using direct registration and ORMA approaches, respectively. A plausible explanation for this improvement is that the local registration misalignment and anatomical variability are effectively handled by similarity weights and decent local matched atlases contribute more to the resulting attenuation map. The same trend was observed in air cavities and lung delineation when applying the VWW and ORMA schemes. However, predominant rigid motion in the head region caused slight improvement in air cavities delineation (0.83±0.04 DSC) compared to bone (0.82±0.04 DSC). Moreover, the enhanced accuracy in the lung delineation (0.92±0.04 DSC) can partially be justified by the relatively large volume of the lung, which tends to reduce the impact of alignment errors.Similar improvement using local similarity weights were reported in atlas-based segmentation methods [31, 42] as well as pseudo-CT generation in the head region [24, 43]. The regression analysis performed on the joint histogram of CT and pseudo-CT images revealed excellent correlation

when using the VWW approach while the pseudo-CT obtained from arithmetic averaging led to significant deviation of the fitted regression line from the identity line. Since the 3-class attenuation map does not contain bone and the soft-tissue and lung classes are assigned uniform attenuation coefficients, the joint histogram shows two concentrated regions corresponding to lung and soft-tissue predefined attenuation coefficients. These regions induce a large deviation from the reference line (figure 5).

The ORMA approach slightly degrades the quality of resulting pseudo-CT images when using either arithmetic averaging or VWW atlas fusion. The Dice validation measure reflecting bone extraction accuracy is reduced from 0.60±0.02 to 0.55±0.03 and from 0.82±0.04 to 0.76±0.05, respectively. Yet, ORMA-VWW considerably outperforms arithmetic average of direct registration. It is worth noticing that computing and applying local weights adds negligible computational burden to the procedure, particularly when MSD is used as an image similarity measure which is very much faster than other criteria, such as NMI and LNNC [49]. The bulk of computation time in multi-atlas based segmentation or attenuation map generation methods is taken by the task of atlas to target registration consisting of N online image registrations. Depending on the registration algorithm, computer power, image size and resolution, each non-rigid atlas registration may take about 10 minutes to 2 hours (~1 hour in this work). Furthermore, if unweighted averaging is the method of choice, increasing the number of atlas images beyond a certain limit leads to over-smoothed outcome since there is no currently implemented mechanism to discard poorly matched or anatomically different atlases. On the other hand, the use of too few number of atlas images suffers from statistical uncertainty [31, 42, 47]. In contrast, when employing the VWW framework, increasing the number of atlas images tends to improve the outcome since it increases the probability of finding appropriate local matches at the cost of increased computational time. The ORMA-VWW approach combines the advantage of selecting locally matched atlases with short computation time. The time needed for performing ORMA is almost independent of the number of atlas images where only one online registration is carried out. This characteristic of ORMA makes it a promising option for potential combination with VWW atlas fusion. Although a slight degradation of quality is observed when using ORMA compared to direct registration, owing to imperfect serial image registration, the quality of the produced pseudo-CT images according to the joint histogram analysis and quantitative analysis of PET images is satisfactory for the purpose of PET attenuation correction.

In an attempt to reduce the computation time or number of required image registrations in atlas-based attenuation correction, Marshal et al. [29] proposed to select only the most similar atlas image based on meta-data, such as gender, weight, sex, and body mass index together with some image-derived features, such as fat to lean tissue ratio, body volume, lung volume, …etc. The proposed method benefits from requiring only one image registration; however, the major drawback is its inability to take advantage of multi-atlas consensus to diminish the unsystematic bias imposed by each individual atlas image and inherent anatomical variability among subjects [42, 50].

The quantitative evaluation of SUV bias demonstrated a similar trend to that of attenuation maps. However, PET images show less sensitivity to errors in attenuation maps owing to lower spatial resolution and higher level of noise. The use of VWW attenuation maps did not lead to significant reduction of SUV bias in ROIs defined on soft-tissue owing to the superiority of VWW over the averaging technique in terms of delineation of organ boundaries while the central parts of organs, where the ROIs were drawn, have almost similar attenuation coefficients. The same effect can also be observed for soft-tissue lesions located far away from bony structures. In this respect, the joint histogram plot and regression analysis are thought to be more descriptive since they offer a proper performance assessment of each technique. The MR3C technique resulted in significant SUV positive bias in the lung region (18.6±13.5% relative error and 22.7±12.2% absolute error) while the other approaches achieved relatively lower bias. The mean attenuation value of the lung determined by different methods (Table 4) explains the observed biases in the lung region. The MR3C method overestimated the average lung attenuation (-770 HU) while VWW schemes, with or without ORMA, produced values (-794 and -805 HU, respectively) close to reference CT (-798 HU).

According to Table 5 (top), PET-VWW achieved the best performance in terms of both mean bias and variability. The ORMA method slightly increases the mean bias and its variability. However, even when applying the ORMA method to VWW, the variability tends to be significantly lower than MR-3C, except in the cerebellum. The same trend is observed for PET-Ave and PET-ORMA-Ave where the mean and SD of the bias increases when applying the ORMA method. However, the SD of PET-ORMA-Ave is, in most of the regions (except the cerebellum), lower than PET-MR3C. Although, ORMA introduces a trade-off between computation

time and the achieved accuracy of the generated attenuation maps, the overall performance is improved compared to the 3-class attenuation map even when using the ORMA-Ave method. The VWW scheme resulted in relative absolute errors of less than 10% in all regions even when utilizing the accelerated ORMA approach.

The quantitative analysis of PET images did not reveal significant difference between VWW and ORMA-VWW pseudo-CT attenuation maps whereas the computation time for generation of ORMA-VWW pseudo-CT is almost 1/Nth (N is the number of used atlas images) that of direct registration VWW method. The attractive feature of the ORMA approach is that by increasing the number of atlas images, the computation time does not change significantly. The technique is time efficient and promising for use in clinical routine compared to that of the direct registration approach.

V. Conclusion

In this work, we proposed an atlas-based pseudo-CT generation techniques for whole-body imaging requiring only one online registration, regardless of number of atlas images, integrated within a voxel-wise atlas fusion framework. The proposed method generates acceptable PET attenuation maps with a Dice similarity of 0.76±0.05 for extracted bone compared to 0.82±0.04 achieved by the conventional atlas-based method, which entails lengthy N (number of used atlas images) image registrations. The quantitative analysis revealed good correlation between PET images corrected for attenuation using the proposed pseudo-CT algorithm and the corresponding reference CT images. Despite the modest loss of accuracy, the required computation time is reduced by factor *N*, thus enabling the clinical implementation of the technique.

Appendix

The geometric distances obtained from pair-wise registrations are used to form an $N \times N$ distance matrix (D) (whose elements d_{ij} stand for geometric distances between objects i and j) to be processed by multidimensional scaling (MDS). The purpose of the MDS technique is to provide relative spatial locations from a set of pair-wise distances [41]. Since the distance used in MDS does not necessarily need to be metric or based on a system of standard measurements (any set of arbitrary values can be used), the geometric distances calculated from pair-wise registration are valid for use by the MDS procedure. MDS produces a number of coordinates in a user defined dimension based on the Eigen structure of the distance matrix. Here, we transformed the distance matrix into two most meaningful coordinates computed by MDS where the closest subject to the origin represents the reference image, which is the closest to the mean geometry of the population of subjects using the following procedure:

1. The matrix B is computed considering $B = -\frac{1}{2} JD^2J$ using the matrix $= I - N^{-1}11'$, where N is the number of subjects, I is the identity matrix and $11'$ denotes a square matrix of ones.
2. The two largest Eigenvalues λ_1 and λ_2 of B and the corresponding two Eigenvectors are extracted,
3. A 2-dimensional spatial configuration of the N subjects is derived from the coordinate matrix $X = E_2 \, C_2^{1/2}$, where E_2 is the matrix of 2 Eigenvectors and C_2 is the diagonal matrix of 2 Eigenvalues of B, respectively.
4. The subject residing at the minimum distance to the origin in the new coordinate space is defined as the reference image (figure 2).

Acknowledgment

This work was supported by the Swiss National Science Foundation under grant SNFN 31003A-149957.

Compliance with ethical standards

1. Disclosure of potential conflicts of interest: none of the authors have affiliations that present financial or non-financial competing interests for this work.
2. Research involving human participants: All procedures performed in studies involving human participants were in accordance with the ethical standards of the institutional and/or national research committee and with the 1964 Helsinki declaration and its later amendments or comparable ethical standards.
3. Informed consent: informed consent was obtained from all individual participants included in the study.

References

[1] M. S. Judenhofer, H. F. Wehrl, D. F. Newport, C. Catana, S. B. Siegel, M. Becker*, et al.*, "Simultaneous PET-MRI: a new approach for functional and morphological imaging.," *Nat Med,* vol. 14, pp. 459-465, Apr 2008.

[2] H. Zaidi and A. Del Guerra, "An outlook on future design of hybrid PET/MRI systems.," *Med Phys,* vol. 38, pp. 5667-5689, 2011.

[3] M. Wiesmuller, H. H. Quick, B. Navalpakkam, M. M. Lell, M. Uder, P. Ritt*, et al.*, "Comparison of lesion detection and quantitation of tracer uptake between PET from a simultaneously acquiring whole-body PET/MR hybrid scanner and PET from PET/CT.," *Eur J Nucl Med Mol Imaging,* vol. 40, pp. 12-21, Jan 2013.

[4] M. Becker and H. Zaidi, "Imaging in head and neck squamous cell carcinoma: the potential role of PET/MRI," *Br J Radiol,* vol. 87, p. 20130677, Apr 2014.

[5] C. Spick, K. Herrmann, and J. Czernin, "18F-FDG PET/CT and PET/MRI perform equally well in cancer patients: Evidence from studies in more than 2300 patients.," *J Nucl Med,* vol. 57, pp. 420-430, Jan 7 2016.

[6] I. Bezrukov, F. Mantlik, H. Schmidt, B. Scholkopf, and B. J. Pichler, "MR-based PET attenuation correction for PET/MR imaging.," *Semin Nucl Med,* vol. 43, pp. 45-59, Jan 2013.

[7] A. Mehranian, H. Arabi, and H. Zaidi, "Vision 20/20: Magnetic resonance imaging-guided attenuation correction in PET/MRI: Challenges, solutions, and opportunities.," *Med Phys,* vol. 43, pp. 1130-1155, 2016.

[8] H. Zaidi, M.-L. Montandon, and D. O. Slosman, "Magnetic resonance imaging-guided attenuation and scatter corrections in three-dimensional brain positron emission tomography.," *Med Phys,* vol. 30, pp. 937-948, 2003.

[9] A. Martinez-Moller, M. Souvatzoglou, G. Delso, R. A. Bundschuh, C. Chefd'hotel, S. I. Ziegler*, et al.*, "Tissue classification as a potential approach for attenuation correction in whole-body PET/MRI: evaluation with PET/CT data," *J Nucl Med,* vol. 50, pp. 520-6, Apr 2009.

[10] V. Schulz, I. Torres-Espallardo, S. Renisch, Z. Hu, N. Ojha, P. Börnert*, et al.*, "Automatic, three-segment, MR-based attenuation correction for whole-body PET/MR data.," *Eur J Nucl Med Mol Imaging,* vol. 38, pp. 138-152, 2011.

[11] M.-L. Montandon and H. Zaidi, "Atlas-guided non-uniform attenuation correction in cerebral 3D PET imaging.," *Neuroimage,* vol. 25, pp. 278-286, 2005.

[12] M. Hofmann, I. Bezrukov, F. Mantlik, P. Aschoff, F. Steinke, T. Beyer*, et al.*, "MRI-based attenuation correction for whole-body PET/MRI: Quantitative evaluation of segmentation- and Atlas-based methods.," *J Nucl Med,* vol. 52, pp. 1392-1399, Sep 2011.

[13] H. Arabi and H. Zaidi, "Magnetic resonance imaging-guided attenuation correction in whole-body PET/MRI using a sorted atlas approach.," *Med Image Anal,* vol. 31, pp. 1-15, 7, 2016.

[14] V. Keereman, Y. Fierens, T. Broux, Y. De Deene, M. Lonneux, and S. Vandenberghe, "MRI-based attenuation correction for PET/MRI using ultrashort echo time sequences.," *J Nucl Med,* vol. 51, pp. 812-818, May 2010.

[15] Y. Berker, J. Franke, A. Salomon, M. Palmowski, H. C. Donker, Y. Temur*, et al.*, "MRI-based attenuation correction for hybrid PET/MRI systems: A 4-class tissue segmentation technique using a combined Ultrashort-Echo-Time/Dixon MRI sequence.," *J Nucl Med,* vol. 53, pp. 796-804, May 2012.

[16] G. Delso, F. Wiesinger, L. Sacolick, S. Kaushik, D. Shanbhag, M. Hullner*, et al.*, "Clinical evaluation of zero echo time MRI for the segmentation of the skull.," *J Nucl Med,* vol. 56, pp. 417-422, Feb 12 2015.

[17] A. Rezaei, M. Defrise, G. Bal, C. Michel, M. Conti, C. Watson*, et al.*, "Simultaneous reconstruction of activity and attenuation in time-of-flight PET.," *IEEE Trans Med Imaging,* p.31:2224–33, 2012.

[18] A. Mehranian and H. Zaidi, "Joint estimation of activity and attenuation in whole-body TOF PET/MRI using constrained Gaussian mixture models.," *IEEE Trans Med Imaging,* vol. 34, pp. 1808-1821, 2015.

[19] D. Izquierdo-Garcia, A. E. Hansen, S. Forster, D. Benoit, S. Schachoff, S. Furst*, et al.*, "An SPM8-based approach for attenuation correction combining segmentation and nonrigid template formation: Application to simultaneous PET/MR brain imaging.," *J Nucl Med,* vol. 55, pp. 1825-1830, Nov 2014.

[20] E. Schreibmann, J. A. Nye, D. M. Schuster, D. R. Martin, J. Votaw, and T. Fox, "MR-based attenuation correction for hybrid PET-MR brain imaging systems using deformable image registration.," *Med Phys,* vol. 37, pp. 2101-2109, 2010.

[21] B. Fei, X. Yang, J. A. Nye, J. N. Aarsvold, N. Raghunath, M. Cervo*, et al.*, "MRPET quantification tools: Registration, segmentation, classification, and MR-based attenuation correction.," *Med Phys,* vol. 39, pp. 6443-6454, Oct 2012.

[22] M. Hofmann, F. Steinke, V. Scheel, G. Charpiat, J. Farquhar, P. Aschoff*, et al.*, "MRI-based attenuation correction for PET/MRI: A novel approach combining pattern recognition and Atlas registration.," *J Nucl Med,* vol. 49, pp. 1875-1883, Oct 16 2008.
[23] I. B. Malone, R. E. Ansorge, G. B. Williams, P. J. Nestor, T. A. Carpenter, and T. D. Fryer, "Attenuation correction methods suitable for brain imaging with a PET/MRI scanner: a comparison of tissue atlas and template attenuation map approaches.," *J Nucl Med,* vol. 52, pp. 1142-1149, Jul 2011.
[24] N. Burgos, M. Cardoso, K. Thielemans, M. Modat, J. Schott, J. Duncan*, et al.*, "Attenuation correction synthesis for hybrid PET-MR scanners: Application to brain studies.," *IEEE Trans Med Imaging,* vol. 33, pp. 2332-2341, Jul 17 2014.
[25] J. Sjölund, D. Forsberg, M. Andersson, and H. Knutsson, "Generating patient specific pseudo-CT of the head from MR using atlas-based regression.," *Phys Med Biol,* vol. 60, pp. 825-839, 2015.
[26] A. Mehranian, H. Arabi, and H. Zaidi, "Quantitative analysis of MRI-guided attenuation correction techniques in time-of-flight brain PET/MRI," *Neuroimage,* vol. 130, pp. 123-133, Feb 4 2016.
[27] I. Bezrukov, H. Schmidt, F. Mantlik, N. Schwenzer, C. Brendle, B. Scholkopf*, et al.*, "MR-based attenuation correction methods for improved PET quantification in lesions within bone and susceptibility artifact regions.," *J Nucl Med,* vol. 54, pp. 1768-1774, Oct 2013.
[28] G. Hermosillo, V. Raykar, and X. Zhou, "Learning to locate cortical bone in MRI.," in *Machine Learning in Medical Imaging*. vol. 7588, F. Wang, D. Shen, P. Yan, and K. Suzuki, Eds., ed: Springer Berlin Heidelberg, 2012, pp. 168-175.
[29] H. R. Marshall, J. Patrick, D. Laidley, F. S. Prato, J. Butler, J. Theberge*, et al.*, "Description and assessment of a registration-based approach to include bones for attenuation correction of whole-body PET/MRI.," *Med Phys,* vol. 40, p. 082509, Aug 2013.
[30] J. Uh, T. E. Merchant, Y. Li, X. Li, and C. Hua, "MRI-based treatment planning with pseudo CT generated through atlas registration.," *Med Phys,* vol. 41, pp. 051711-8, 2014.
[31] H. Arabi and H. Zaidi, "Comparison of atlas-based bone segmentation methods in whole-body PET/MRI," in *IEEE Nuclear Science Symposium and Medical Imaging Conference (NSS/MIC)*, Seattle, WA, USA, 2014.
[32] H. Zaidi, N. Ojha, M. Morich, J. Griesmer, Z. Hu, P. Maniawski*, et al.*, "Design and performance evaluation of a whole-body Ingenuity TF PET-MRI system.," *Phys Med Biol,* vol. 56, pp. 3091-3106, Apr 20 2011.
[33] S. Klein, M. Staring, K. Murphy, M. A. Viergever, and J. P. W. Pluim, "elastix: A toolbox for intensity-based medical image registration.," *IEEE Trans Med Imaging,* vol. 29, pp. 196-205, 2010.
[34] H. Arabi, O. Rager, A. Alem, A. Varoquaux, M. Becker, and H. Zaidi, "Clinical assessment of MR-guided 3-class and 4-class attenuation correction in PET/MR.," *Mol Imaging Biol,* vol. 17, pp. 264-276, 2015.
[35] P. Perona and J. Malik, "Scale-space and edge detection using anisotropic diffusion," *Pattern Analysis and Machine Intelligence, IEEE Transactions on,* vol. 12, pp. 629-639, 1990.
[36] N. J. Tustison, B. B. Avants, P. A. Cook, Y. Zheng, A. Egan, P. A. Yushkevich*, et al.*, "N4ITK: improved N3 bias correction.," *IEEE Trans Med Imaging,* vol. 29, pp. 1310-1320, Jun 2010.
[37] M. J. McAuliffe, F. M. Lalonde, D. McGarry, W. Gandler, K. Csaky, and B. L. Trus, "Medical Image Processing, Analysis and Visualization in clinical research," in *14th IEEE Symposium on Computer-Based Medical Systems, 2001. CBMS 2001. Proceedings*, 2001, pp. 381-386.
[38] D. Mattes, D. R. Haynor, H. Vesselle, T. K. Lewellen, and W. Eubank, "PET-CT image registration in the chest using free-form deformations," *Medical Imaging, IEEE Transactions on,* vol. 22, pp. 120-128, 2003.
[39] H. Park, P. H. Bland, A. O. Hero, 3rd, and C. R. Meyer, "Least biased target selection in probabilistic atlas construction.," *Med Image Comput Comput Assist Interv,* vol. 8, pp. 419-426, 2005.
[40] F. L. Bookstein, "Principal warps: thin-plate splines and the decomposition of deformations," *IEEE Trans Pattern Analy Machine Intell,* vol. 11, pp. 567-585, 1989.
[41] X. Artaechevarria, A. Munoz-Barrutia, and C. Ortiz-de-Solorzano, "Combination strategies in multi-atlas image segmentation: application to brain MR data.," *IEEE Trans Med Imaging,* vol. 28, pp. 1266-1277, Aug 2009.
[42] N. Burgos, M. J. Cardoso, M. Modat, S. Pedemonte, J. Dickson, A. Barnes*, et al.*, "Attenuation correction synthesis for hybrid PET-MR scanners.," *Med Image Comput Comput Assist Interv,* vol. 16, pp. 147-154, 2013.
[43] P. A. Yushkevich, H. Wang, J. Pluta, S. R. Das, C. Craige, B. B. Avants*, et al.*, "Nearly automatic segmentation of hippocampal subfields in in vivo focal T2-weighted MRI," *NeuroImage,* vol. 53, pp. 1208-1224, 12// 2010.
[44] L. R. Dice, "Measures of the amount of ecologic association between species.," *Ecology,* vol. 26, pp. 297-302, 1945.

[45] Y. Xia, J. Fripp, S. S. Chandra, R. Schwarz, C. Engstrom, and S. Crozier, "Automated bone segmentation from large field of view 3D MR images of the hip joint.," *Phys Med Biol,* vol. 58, pp. 7375-7390, 2013.
[46] R. A. Heckemann, J. V. Hajnal, P. Aljabar, D. Rueckert, and A. Hammers, "Automatic anatomical brain MRI segmentation combining label propagation and decision fusion.," *Neuroimage,* vol. 33, pp. 115-126, Oct 15 2006.
[47] P. A. Yushkevich, J. Piven, H. C. Hazlett, R. G. Smith, S. Ho, J. C. Gee*, et al.*, "User-guided 3D active contour segmentation of anatomical structures: significantly improved efficiency and reliability.," *Neuroimage,* vol. 31, pp. 1116-1128, Jul 1 2006.
[48] J. M. P. Lötjönen, R. Wolz, J. R. Koikkalainen, L. Thurfjell, G. Waldemar, H. Soininen*, et al.*, "Fast and robust multi-atlas segmentation of brain magnetic resonance images," *NeuroImage,* vol. 49, pp. 2352-2365, 2/1/ 2010.
[49] T. Rohlfing, R. Brandt, R. Menzel, and C. R. Maurer, Jr., "Evaluation of atlas selection strategies for atlas-based image segmentation with application to confocal microscopy images of bee brains.," *Neuroimage,* vol. 21, pp. 1428-1442, Apr 2004.
[50] F. W. Young and R. M. Hamer, *Multidimensional scaling: History, theory, and applications.* New York: Taylor & Francis, 1987.

Chapter 7

Atlas-guided generation of pseudo-CT images for MRI-only and hybrid PET-MRI guided radiotherapy treatment planning

Arabi H, Koutsouvelis H, Rouzaud M, Miralbell M and Zaidi H

Physics in Medicine and Biology, Vol. 61, No. 17, pp 6531-6552 (2016).

Abstract

Purpose: Magnetic resonance imaging (MRI)-guided attenuation correction of positron emission tomography (PET) data and/or radiation therapy treatment planning is challenged by the lack of a direct link between MRI voxel intensities and electron density. Therefore, even if this is not a trivial task, a pseudo-CT image must be predicted from MRI alone. In this work, we propose a two-step (segmentation and fusion) atlas-based algorithm focusing on bone tissue identification to create a pseudo-CT image from conventional MRI sequences and evaluated its performance against conventional MRI segmentation technique and a recently proposed multi-atlas approach.

Methods: The clinical studies consisted of pelvic CT, PET and MRI scans of 12 patients with loco-regionally advanced rectal disease. In the first step, bone segmentation of the target image is optimized through local weighted atlas voting. The obtained bone map is then used to assess the quality of deformed atlases to perform voxelwise weighted atlas fusion. To evaluate the performance of the method, a leave-one-out-cross-validation scheme was devised to find optimal parameters for the model. Geometric evaluation of the produced pseudo-CT images and quantitative analysis of the accuracy of PET attenuation correction were performed. Moreover, a dosimetric evaluation of volumetric modulated arc therapy photon treatment plans calculated using the different Pseudo-CT images was carried out and compared to those produced using CT images serving as reference.

Results: The pseudo-CT images produced using the proposed method exhibits bone identification accuracy of 0.89 based on Dice similarity metric compared to 0.75 achieved by the other atlas-based method. The superior bone extraction resulted in a mean SUV bias of -1.5±5.0% (mean±SD) in bony structures compared to -19.9±11.8% and -8.1±8.2% achieved by MRI segmentation-based (water-only) and atlas-guided attenuation correction. Dosimetric evaluation using DVHs and average difference between min/max absorbed doses revealed a mean error of less than 1% for the both target volumes and organs at risk. Two-dimensional gamma analysis of the isocenter dose distributions at 1%/1 mm criterion revealed pass rates of 91.40±7.56%, 96.00±4.11% and 97.67±3.6% for MRI segmentation, atlas-guided and the proposed methods, respectively.

Conclusion: The proposed method generates accurate pseudo-CT images from conventional Dixon MRI sequences with improved bone extraction accuracy. The approach is promising for potential use in PET attenuation correction and MRI-only or hybrid PET/MRI-guided radiation therapy treatment planning.

I. Introduction

Magnetic resonance imaging (MRI) is increasingly being used and is becoming the modality of choice in radiation therapy (RT) treatment planning of a number of indications [1]. Likewise, positron emission tomography (PET) provides valuable complimentary information to the RT process, especially when combined with computed tomography (CT) using hybrid PET/CT scanners. In PET imaging, correcting for photon attenuation, which is commonly performed using CT, is essential for accurate quantification of tracer uptake and improved lesion detectability. The primary merit of MRI is its capability to provide superior soft tissue contrast, which leads to reliable identification of malignancies and precise delineation of target volumes and organs at risk (OARs) compared to CT [2-4]. The organs delineated on MRI should be copied on CT images and as such, the two images must be spatially aligned. Manual and/or automated rigid registration between the MRI and CT scans is commonly used in the clinic. However, a mean registration error of approximately 2 mm can be expected in this process for body sites such as the prostate, which results in a systematic shift in organ contours and may ultimately lead to target under- or over-dosage or excessive dose delivery to neighbouring organs [5-7]. RT treatment planning based solely on MRI provides a number of advantages [1, 8]; however, excluding CT from the RT chain is not trivial since MRI signal is correlated to proton density and magnetic relaxation properties, not to electron density and linear attenuation coefficient (LACs) of tissues [9]. In addition, conventional MRI sequences contain no or very weak signal from cortical bone which makes patient setup using digitally reconstructed radiographs (DRRs) practically unfeasible. Since both the patient and the treatment machine are virtual, the simulation film or DRR is a reconstructed image which resembles a standard 2D simulation radiograph but is in practice generated from CT images. The lack of a separate bone tissue class or inaccurate bone delineation in the attenuation map has been shown to result in a substantial PET quantification bias [10, 11] and dose calculation inaccuracy [12]. Therefore, generation of accurate pseudo-CT images or attenuation maps (μ-maps) from MR images for the purpose of PET attenuation correction (AC) and dose calculation and patient setup in RT planning is highly desired.

Two different approaches have been used for automatic density assignment or generation of pseudo-CT images in MRI-guided PET attenuation correction and RT treatment planning: tissue segmentation and atlas-based methods [13]. In the tissue segmentation approach, a μ-map is generated using tissue segmentation followed by subsequent assignment of predefined density [14, 15]. To include bony structures, a specialized dual ultra-short echo time (dUTE) sequence, able to capture transient signal from components with a short T2 relaxation time and consequently distinguish bone from air [16-18], was used. However, this sequence suffers from long acquisition time, low signal-to-noise ratio, partial volume artefacts and bone prediction errors [19]. On the other hand, atlas-based pseudo-CT generation can be implemented using conventional MR sequences where bone/air ambiguity in MR images is compensated through utilization of prior knowledge existing in one or multiple atlases of paired CT/MR images aligned to the target MRI spatial coordinates [12, 20-22]. In combination with atlas registration, machine learning techniques have been exploited to generate patient-specific attenuation maps [23-25]. In addition to the above described pseudo-CT generation methods, joint reconstruction of activity and attenuation exploiting time-of-flight capability of PET was proposed as an alternative [26]. In this method, the activity distribution and attenuation map are estimated iteratively in an alternate way where the prior knowledge present in MRI can be incorporated to constrain the final solution space [27].

It has been demonstrated that atlas-based methods are potentially able to generate reliable pseudo-CT images from conventional MR sequences outperforming conventional segmentation-based approaches that neglect bone, thus leading to more accurate PET quantitative accuracy [21, 24, 28, 29] and RT planning outcome [12, 30-32]. Several atlas-based methods have been proposed in brain imaging to take the skull into account. Burgos et al. [21] developed an approach to generate synthetic CT images using a multi-atlas information propagation scheme where the MRI-derived patient's morphology is locally matched to the aligned dataset of MRI-CT pairs using a robust voxelwise image similarity measure. Izquierdo-Garcia et al. presented an approach utilizing Statistical Parametric Mapping (SPM8) software taking advantage of both segmentation and atlas-derived features to generate a robust attenuation map for AC of brain PET data [33]. Similarly in the context of MRI-guided RT planning, Sjölund et al. [34] proposed an approach based on a deformable image registration algorithm to generate the electron density of the head from MR images using a novel atlas fusion scheme. An alternative technique enabling to generate electron density image without atlas registration is the patch-based pseudo-CT generation approach for RT planning based on a library of MR-CT image patch pairs [30]. Kapanen et al.

established a relationship between T1/T2 weighted MRI intensity and CT values for pelvic bone, thus allowing estimation of patient-specific bone electron density from MRI [35].

In this work, we propose a two-step scheme based on the principle of multi-atlas propagation to synthesize a pseudo-CT image from MRI. In the first step, bone segmentation is optimized on the target MRI. The obtained bone label is then utilized together with the morphological similarity between target and atlas images to define voxelwise weights for the atlas fusion task. The proposed method is developed to excel in bone identification for the purpose of attenuation map generation and MR-only and/or PET/MRI-guided RT treatment planning [36]. This method is evaluated through comparison with conventional segmentation- and atlas-based methods using as metrics the accuracy of bone extraction, quantitative analysis of tracer uptake and dose distribution errors in the pelvic region.

II. Materials and methods

II.A. Image acquisition and processing

The patient population consisted of 12 patients presenting with rectal cancer (loco-regionally advanced rectal disease, where the disease spreads only within the region in which it arose as opposed to the metastatic disease) who underwent whole body 18F-FDG PET/CT and PET/MRI examinations. The study protocol was approved by the institutional ethics committee and all patients gave informed consent. A single injection of 18F-FDG (171±30 MBq) was used to perform both studies sequentially. The PET/CT scans were performed on a Biograph 64 TruePoint scanner (Siemens Healthcare, Erlangen, Germany). After a localization scout scan, an unenhanced low dose CT scan (120 kVp, 60 mAs, 24×1.5 collimation, a pitch of 1.2, and 1 s per rotation) was performed for attenuation correction. PET data acquisition started 146.2±20 min post-injection with 3 min per bed position for a total of 5-6 beds, resulting in a total acquisition time of 15-18 min.

PET/MRI data acquisition was carried out on the Ingenuity TF PET/MRI scanner (Philips Healthcare, Cleveland, OH, USA) [37]. The proposed MRI-derived pseudo-CT generation approach uses an MRI Dixon volumetric interpolated T1-weighted sequence [38] for pelvis examination with the following parameters: flip angle 10°, TE1 1.1 ms, TE2 2.0 ms, TR 3.2 ms, 360×360 mm2 transverse FOV, 0.75×0.75×0.75 mm3 voxel size, and a total acquisition time of 4.5 min.

Due to temporal difference between PET/CT and MR examinations, a combination of rigid and non-rigid registrations based on normalized mutual information was employed to ensure appropriate inter-modal spatial image matching as described in previous work [39]. The PET/CT data were employed whereas only the in-phase MR images from the PET/MRI scan were used in this work. The accuracy of the alignment between co-registered MR and CT images was carefully checked visually.

MR images usually suffer from the presence of statistical noise and corruption due to low frequency bias field (intra-patient intensity non-uniformity) as well as inter-patient intensity inhomogeneity [40]. To minimize the adverse effect of the aforementioned factors, in-phase images of all patients underwent the following pre-processing corrections. Gradient anisotropic diffusion filtering was employed using a conductance of 4, 10 iterations and time step of 0.01 to suppress statistical noise while preserving prominent features and signals in MR images. Afterwards, N4 bias field correction [41] was employed to remove low frequency intensity non-uniformity present within subjects (considered as a potential confounder in various image analysis tasks) using a B-spline grid resolution = 400, number of iterations = 200, convergence threshold = 0.001, B-spline order = 3, spline distance = 400, histogram bins number = 256, and shrink factor = 3. Histogram matching [42] with a histogram level = 512 and match points = 64 was utilized to address inter-subject intensity inhomogeneity in MR images.

II.B. Pseudo-CT image generation

The atlas database is built based on pairs of spatially aligned (MRI to CT) in-phase Dixon MRI and CT pelvic images. In the first step, all atlas MR images are registered to the target MR image through a leave-one-out-cross-validation (LOOCV) scheme. Inter-subject coordinate mapping was obtained using a combination of rigid and non-rigid registration based on normalized mutual information and B-spline interpolator as described previously [39]. The registrations were performed using Elastix open source software [43]. Given the

transformation maps, all CT images in the atlas database are then mapped to the target MR image using the corresponding transformation maps.

Given these series of MR/CT pairs, a two-step atlas fusion framework was proposed to create MRI-guided pseudo-CT. In the first step, bone segmentation of the target MRI is optimized through voxel-by-voxel atlas voting scheme. The output of the first step is a binary bone map of the target subject, which can be assumed to represent the most likely bone delineation of the target image. The rationale behind this step is that bone identification is the major challenge and most important part of MRI-based attenuation map generation. This enables to achieve atlas fusion with special emphasis on bony structures. Given an initial estimation of the target bone, prior knowledge from atlas CT images can be utilized to establish a similarity assessment between them and the estimated target bone to define the weights accordingly for the atlas fusion task. In the second step, to generate continuous-valued attenuation map, an atlas fusion framework is locally optimized according to the resemblance to the obtained target bone map and the morphological similarity to the target MR image. To formulate this process, we use Mn to denote aligned training MRIs, which are continuous-valued intensity images with the corresponding bone label maps Ln. The binary bone label maps are obtained by applying an intensity threshold on the corresponding aligned CT images (atlas CT images after registration) using a Hounsfield unit (HU) value of 140. The primary goal of the first step is to estimate the most likely bone label map (L^) associated with the target MR image (T). We employed a joint probability of the label map and image intensity given the training data.

$$\hat{L} = arg\max_{L} p(L, T|\{M_n, L_n\}) \tag{1}$$

Here, n denotes the index of training subjects in the atlas dataset. We devised our model based on the assumption that the target MR image (T) can be a product or mixture distribution of either one or some of the training MR images (Mn) whose indices are unknown. In particular, the contribution of the training images is allowed to vary spatially (voxel-by-voxel). To formulate this relationship, a latent random variable (C(x)) is defined to specify the indices of the contributory training images at each voxel (x) in the target image (T). To simplify the optimization problem, we assume that the MR intensity values T(x) and the corresponding bone label L(x) are conditionally independent [44]. However, given the latent random variable (C(x)), a relationship is established between them in such a way that in this model T(x) and L(x) are bound together via (C(x)). At a later stage, we will determine relationships between training MR images (Mn) and the target MRI (T) as well as the target bone label (L) and training atlas bone label (Ln). Therefore, the initial conditional independence assumption, which might seem simplistic at first glance, is compensated by C(x) which establishes implicit dependency between bone label and MR intensity. Given the condition that each voxel in the target MR image is derived from a single training image specified by C(x), the generative model of the target MR image and its corresponding label map through the conditional probability would be

$$p\big((L, T|C, \{M_n, L_n\})\big) = \prod_{x}\big(p(L(x), T(x)|C(x), \{M_n, L_n\})\big)$$

As mentioned earlier, *L(x)* and *T(x)* are assumed to be conditionally independent. Therefore, the above conditional probability can be split into two multiplicative terms [44]:

$$\big(p(L(x), T(x)|C(x), \{M_n, L_n\})\big) = \big(p(L(x)|C(x), \{L_n\}) \times p(T(x)|C(x), \{M_n\})\big)$$

To simplify the problem, marginalization was calculated over the introduced latent variable *C(x)*, resulting in the following formulation:

$$p\big((L, T|\{M_n, L_n\})\big) = \sum_{C} p(C) \prod_{x}\big(p(L(x), T(x)|C(x), \{M_n, L_n\})\big)$$

Since there is no prior assumption about the degree of contribution of the atlas images to the final bone label map, *C(x)* takes a constant value (*P(C(x))=Const.*). Therefore, the bone segmentation would turn into the form:

$$\hat{L}(x) = arg\max_{L} \sum_{n=1}^{N} p_n\Big(\big(T(x)\big|M_n(x)\big)\Big)\ p_n\Big(\big(L(x)\big|L_n(x)\big)\Big) \tag{2}$$

where *N* is the number of training subjects in the atlas dataset. Considering equation (2), the estimated bone label at each voxel ($\hat{L}(x)$) depends on image morphology likelihood $p_n\big(T(x), M_n(x)\big)$ between the target and the atlas

MR images together with the second term $p_n\big(L(x), L_n(x)\big)$ which is called label prior ($L(x)$ is the bone label of the target image). The main objective in defining image morphology likelihood is to give greater weights to similar atlases. To achieve this goal, the similarity measure has to provide discriminative information about the underlying structures and at the same time be robust to intensity variation across patients. Phase congruency map (PCM) has been shown to be a robust image feature against the inter-subject intensity variation and provide valuable information about the prominent structures of the image [45]. In PCM, the local Fourier components of the image are all in phase (congruent) in locations where there are meaningful edges in the image. A PCM can be used to detect structural characteristics of an image, such that it is invariant to image intensity and adequately robust to noise [45]. Equation (3) calculates the phase congruency of an image at location x where $En_{loc}(x)$ represents the local energy of the image defined as $En_{loc}(x) = \sqrt{F^2(x) + H^2}$, where $F(x)$ is the image signal with its DC component removed and H is the Hilbert transform of $F(x)$, Tr is an offset to avert the effect of noise on the calculation of the local energy ($T_r = M_r + k\sigma_r$). The mean noise response (M_r) and variance σ_r^2 represent the Rayleigh distribution of the noise energy response. k usually takes a value of 2 or 3, F_m indicates the amplitude of the m^{th} Fourier component, and ϵ is a small value to avoid devision by 0 [45, 46]. Figure 1 depicts a representative example of PCM computation on the target and one of the MR images from the atlas dataset. The prominent signal in original images are nicely reflected on PCMs regarless intensity variation and noise.

$$PCM(x) = \frac{\lfloor En_{loc}(x) - Tr \rfloor}{\sum_m F_m(x) + \varepsilon} \tag{3}$$

Considering PCM as a proper image feature measure, we adopted a Gaussian distribution on PCM of target and MR atlas images with a stationary variance σ^2 as the image morphology likelihood term (Eq. 4). A representative example of Eq. (4) is depicted in figure 1.

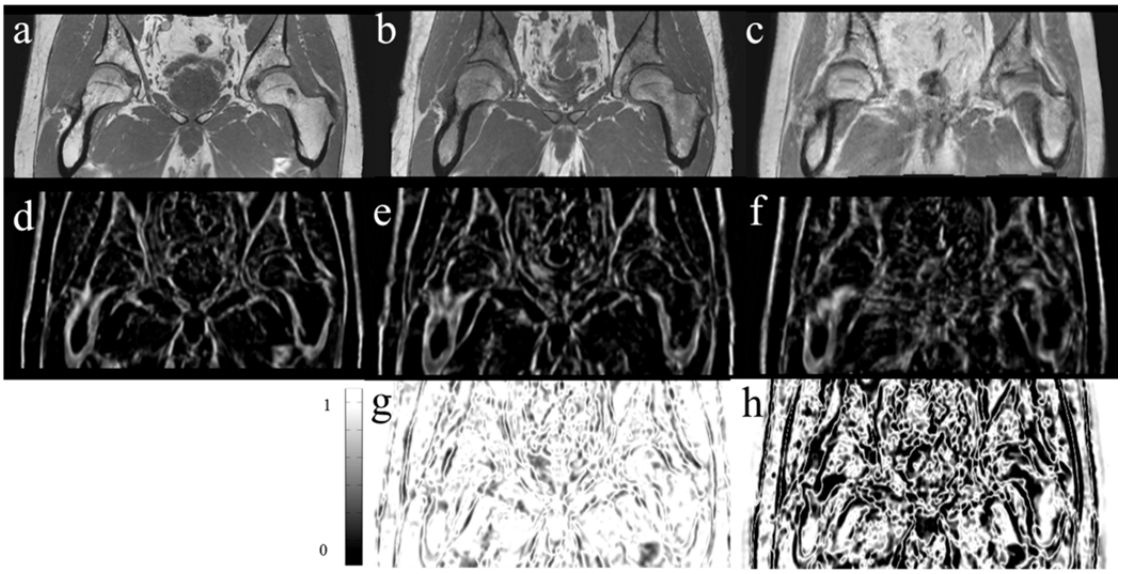

Figure 1. Representative slice of MR images and their corresponding phase congruency map (PCMs). (a) Target MR image; (b) atlas MR image (well aligned); (c) atlas MR image (poor aligned); (d) PCM of image (a); (e) PCM of image (b); (f) PCM of image (c); (g) morphology likelihood between (a) and (b) using Eq. 4; and (h) morphology likelihood between (a) and (c) using Eq. 4.

$$p_n\big((T(x)|M_n(x))\big) = \frac{1}{\sqrt{2\pi\sigma^2}} exp\left[-\frac{1}{2\sigma^2}\big(PCM\big(T(x)\big) - PCM(M_n(x))\big)^2\right] \tag{4}$$

On the other hand, to define the label prior term $p_n((L(x)|L_n(x)))$, a signed distance transform from the bone label map (L_n) of the atlas dataset was computed and based on which a label prior term was formed via

$$p_n\big((L(x)|L_n(x))\big) = \frac{1}{Nr(x)} exp(\rho D_n(x)) \tag{5}$$

where $D_n(x)$ denotes the signed distance transform of the bone label map on the training subject *n,* which is assumed to be positive inside bony structures and negative otherwise, $\rho > 0$ is the slope constant, and $Nr(x) = \sum_{t=1}^{2} exp(\rho D_n^t(x)$ is the partition function used for normalization, where the summation is over the number of labels (here equal to 2 – background and bone). A representative image of a binary bone mask and its corresponding bone probability map calculated using Eq. (5) is given in figure 2.

The output of this step ($\hat{L}$) is presumed to be the most likely bone segmentation of the target MR image. In the next step, this bone segmentation, which is a binary map, is used as a baseline to evaluate the registration accuracy and define weighting factors for each subject of the training dataset. To generate continuous valued pseudo-CT images, the atlas fussion task is achieved through Eq. (6) where $ACT_n(x)$ is the CT value of the n^{th} atlas image at voxel *x*.

$$LW(x) = \frac{\sum_{n=1}^{N} \omega_n(x) \times ACT_n(x)}{\sum_{n=1}^{N} \omega_n(x)} \tag{6}$$

where, $\omega_n(x)$ indicates the weighting factor determining the contribution of the n^{th} atlas at voxel *x* to generate the final locally weighted pseudo-CT (LW). It is defined as:

$$\omega_n(x) = \frac{1}{\sqrt{2\pi\alpha^2}} exp\left[-\frac{1}{2\alpha^2}(PCM(T(x)) - PCM(M_n(x)))^2\right] \times \frac{1}{\sqrt{2\pi\delta^2}} exp\left[-\frac{1}{2\delta^2}(D_n(x)) - D_B(x))^2\right]. \tag{7}$$

where DB indicates the signed distance transform of the obtained bone label of the target image (L^). The first term in Eq. (7) measures the morphological similarity between the target and nth atlas MR image (as described in Eq. (4)) while the second term estimates the ressemblance of the nth CT atlas image with respect to the presumably ground truth bone segmentation of the target MR image (L^). The two Gaussian distributions are adjusted using stationary variances α2 and δ2. The free parameters in the above equations, namely α, δ, ρ and σ, were optimized via LOOCV and a parameter sweeping scheme. To find the optimum value for each parameter, a range of reasonable values was assigned to the chosen parameter while the remaining parameters were kept fixed. Then, the value miximizing the accuracy of extracted bone in the final pseudo-CT image is selected. The free parameters α, δ, ρ and σ took values of 0.3, 0.25, 1.2, and 0.23, respectively.

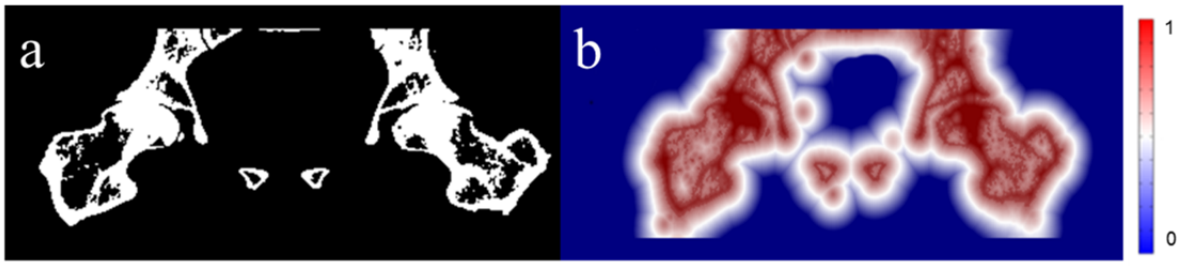

Figure 2. (a) Representative slice of a binary bone mask obtained by intensity thresholding at 140 HU and (b) its corresponding bone probability map calculated using Eq. (5).

II.C. Comparison of pseudo-CT images

The pseudo-CT images produced by the proposed method, referred to as local weighting (LW), was compared with reference CT images (in their original spatial coordinates) as well as two other commonly used methods to generate pseudo-CT images. A common approach adopted for attenuation correction on hybrid PET/MRI scanners is MR image segmentation of the body into a number of tissue classes followed by assignment of predefined LACs to each tissue class. The Philips Ingenuity TF PET/MR uses a 3-class attenuation map consisting of air, lung and soft-tissue to which the following attenuation coefficients are assigned: 0 cm−1 (−1,000 HU), 0.022 cm−1 (−770 HU), and 0.096 cm−1 (0 HU), respectively [47]. In-phase MR images underwent body contour segmentation through connected-component analysis of the low intensity surrounding air voxels initiated by manual seeds using the ITK-SNAP image processing software [48]. A LAC of 0 cm−1 (−1,000 HU) was assigned to surrounding air and 0.096 cm−1 (0 HU) to the body volume (figure 3-c) to produce a water-only attenuation map.

The second attenuation map evaluated in this work is also generated using a multi-atlas registration approach. Given a series of aligned CT images to the target MR image, the pseudo-CT image is generated by assigning the median value of the CT numbers across the entire atlas images for each voxel independently (Eq. 8).

$$MV(x) = median(ACT_1(x), \dots, ACT_n(x)) \quad (8)$$

This approach is equivalent to the well-known majority voting method described in [34]. The major advantage of the median compared to the mean is its robustness to outliers and the ability to better deal with multimodal distributions. Figure 3-d shows a representative example of median value (MV) attenuation map.

II.D. Image reconstruction and data analysis

The proposed pseudo-CT generation technique was evaluated using 3 different metrics, including accuracy of bone extraction, PET quantification bias and error in calculated dose distributions in radiation therapy treatment planning. A comparison with the aforementioned techniques was also performed using CT images as reference.

1) Bone extraction

The evaluation of bone volume extraction (3D) using the various pseudo-CT images was carried out by comparing the segmented bone from the reference CT images using two volume-based measures, including Dice similarity (DSC) [49] and relative volume difference (RVD) [20].

$$DSC(A,Z) = \frac{2|A \cap Z|}{|A|+|Z|} \ , \quad RVD(A,Z) = 100 \times \frac{|A|-|Z|}{|A|}$$

where, A is the segmented bone from the reference CT image and Z denotes the extracted bone obtained the pseudo-CT images. Paired t-test analysis was used to assess if the differences between the obtained results are statistically significant using a threshold of 0.05.

2) Quantitative PET analysis

The generated pseudo-CT images of 12 patients were used for AC of the corresponding PET data. PET images were reconstructed by means of the e7-tool (Siemens Healthcare, Knoxville, TN) using ordinary Poisson ordered subset-expectation maximization (OP-OSEM) iterative reconstruction algorithm. Default parameters (4 iterations, 8 subsets, and a post-processing Gaussian kernel with a FWHM of 5 mm) adopted in clinical protocols were applied. PET image reconstruction was performed four times for each clinical study using attenuation maps derived from CT (PET-CTAC) used as reference, water-only (PET-water), the pseudo-CT generated by the MV (PET-MV) and LW approaches (PET-LW). The differences between the attenuation correction techniques were quantified in terms of change in the standard uptake value (SUV). Voxel-based relative mean bias (RMB) and relative mean absolute bias (RMAB) were computed for bone, fat and soft-tissue classes using equations 9 and 10, respectively.

$$RMB = 100 \times \frac{\sum_v (\mathrm{P}_v - \mathrm{PCT}_v)}{\sum_v PCT_v} \quad (9)$$

$$RMAB = 100 \times \frac{\sum_v |\mathrm{P}_v - \mathrm{PCT}_v|}{\sum_v PCT_v} \quad (10)$$

where Pv denotes the SUV value of voxel v in PET images corrected for attenuation using the pseudo-CT images and PCT stands for the corresponding reference PET-CTAC. The segmentation of tissue classes was performed based on CT Hounsfield units (HU) using the following thresholds: bone if HU ≥ 140, soft-tissue if -20 < HU ≤ 140, and fat if -350 < HU ≤ -20.

3) Dose distribution analysis

Volumetric-modulated arc therapy (VMAT) technique was employed for treatment planning using the Eclipse™ treatment planning system (Varian Medical Systems Inc, Palo Alto, CA). RT treatments were performed by irradiating target volumes defined on the rectum and prostate. The dose differences were calculated on target volumes consisting of gross target volume (GTV), clinical target volume (CTV), planning target volume (PTV), rectum and prostate. The patients received radiation doses varying between 45 and 60 Gy with a mean dose of 1.5-2 Gy in 30 fractions targeting the PTV. In addition to target volumes, the dose calculation was also

performed for in field organs at risk (OARs) including left and right femur, bladder, bowel bag, anus, spinal cord, iliac crest, genitalia, vagina (2 patients), uterus (2 patients), penile bulb and bladder wall for each patient. The same structure set was associated with both reference CT and pseudo-CTs as they were generated in the same spatial coordinates. All volume and organ delineations were performed by a radiation oncologist on the target MRI and were then copied on the reference CT and pseudo-CT images. The dose calculation was carried out on each patient's pseudo-CT. The treatment plans were then transferred to the reference CT images and recalculated using same structure set and monitor units. The field-of-view and number of slices were kept identical on each image series ensuring matched organ contours. Dose volume histograms (DVHs) and dose distribution maps were exported for both the reference CT and pseudo-CTs. The DVH represents a histogram relating radiation dose to tissue volume in radiation therapy planning, summarizing 3D dose distributions in a 2D graphical format. The "volume" term in DVH analysis stands for a target of radiation treatment or a healthy organ at risk. Dose calculations were performed using the anisotropic analytical algorithm (AAA v. 10) for a 6 MV photon beam and a dose matrix of 2.5×2.5×2.5 mm3.

For dose comparisons, the absorbed Dose-max, Dose-min and Dose-mean to the target volumes and OARs were compared (Eq. 11) between plans optimized on the reference CT and pseudo-CT images considering DoseCT and DosepCT as measured dose in the plan calculated on CT and pseudo-CT images, respectively.

$$Difference = 100 \times \frac{Dose_{pCT} - Dose_{CT}}{Dose_{CT}} \tag{11}$$

Moreover, the DVHs of different organs were used to evaluate the dosimetric differences between dose distributions calculated using CT and pseudo-CT images. Given the DVH curves, each point on the curves representing a specific dose level was compared with the reference CT. The percentage point deviation was calculated and averaged for all points of DVHs corresponding to each organ absorbed dose using equations 12 and 13 for mean absolute errors (MAE) and mean errors (ME), respectively.

$$MAE = 100 \times \frac{1}{P}\sum_{i=1}^{P} \frac{|D_{pCT}(i) - D_{CT}(i)|}{D_{CT}(i)} \tag{12}$$

$$ME = 100 \times \frac{1}{P}\sum_{i=1}^{P} \frac{D_{pCT}(i) - D_{CT}(i)}{D_{CT}(i)} \tag{13}$$

where, P represents the total number of DVH points between Dose100% and Dose0% in dose increments of 0.1 Gy, whereas DpCT(i) and DCT(i) are the accumulated doses in Gy given to the volume i in the reference CT and pseudo-CT images, respectively.

The calculated dose distributions using the different pseudo-CTs images were compared with the corresponding reference CTs and the volume (cc) receiving a certain amount of different dosage was measured. To this end, the dose difference maps were computed through voxel-by-voxel subtraction of dose values calculated on pseudo-CTs from those of the reference CT. Then, at each dose difference level, the associated volume was computed. The measured volumes were plotted versus dose discrepancy ranging from -1 to 1 Gy. Moreover, two-dimensional gamma analysis [50] (evaluated at 2%/2 mm and 1%/1 mm dose difference/distance to agreement) was used to analyze axial dose distributions intersecting the isocenter. The Gamma test is a widely used metric for comparing dose distributions, which combines features of dose difference and distance-to-agreement [51].

Table 1. Accuracy of extracted bone (mean ± SD) from pseudo-CT images derived using local weighting (LW) and median value (MV) approaches.

	MV	P-value	LW	P-value
DSC	0.75±0.10	0.07	0.89±0.06	<0.05
RVD (%)	-18.9±03.8	0.05	-10.9±03.1	0.05

III. Results

Representative slices of the generated pseudo-CTs along with reference MR and CT images are shown in figure 3 where visual inspection reveals the considerable improvement brought by the proposed method in terms of anatomical structures sharpness. Table 1 summarizes the results of bone extraction accuracy for LW and MV

techniques. It can be observed that the LW approach outperforms the other techniques considering for all four metrics used (with statistical significance proven only for DSC and sensitivity). Figure 4 depicts SUV and attenuation bias maps for the different methods for the same slices shown in figure 3. Voxelwise SUV bias evaluation on PET images corrected for attenuation using different μ-maps considering PET-CTAC as the reference are provided in Table 2. Likewise, the LW technique leads to significant PET quantification bias reduction, particularly in bone tissue.

Table 2. Voxelwise relative mean ± SD (absolute mean ± SD) SUV bias for PET images corrected for attenuation using the different pseudo-CT images.

Method	Fat mean ± SD (absolute mean ± SD)	Soft-tissue mean ± SD (absolute mean ± SD)	Bone mean ± SD (absolute mean ± SD)
Water-only	7.5±8.3 (8.3±6.8)	-5.4±6.2 (9.8±6.8)	-19.9±11.8 (21.1±9.9)
LW	2.2±5.5 (5.6±4.5)	-2.0±4.1 (5.0±3.9)	-1.5±5.0 (4.1±2.2)
MV	4.9±6.1 (7.7±5.9)	-4.0±6.2 (7.1±5.2)	-8.1±8.2 (11.1±6.2)

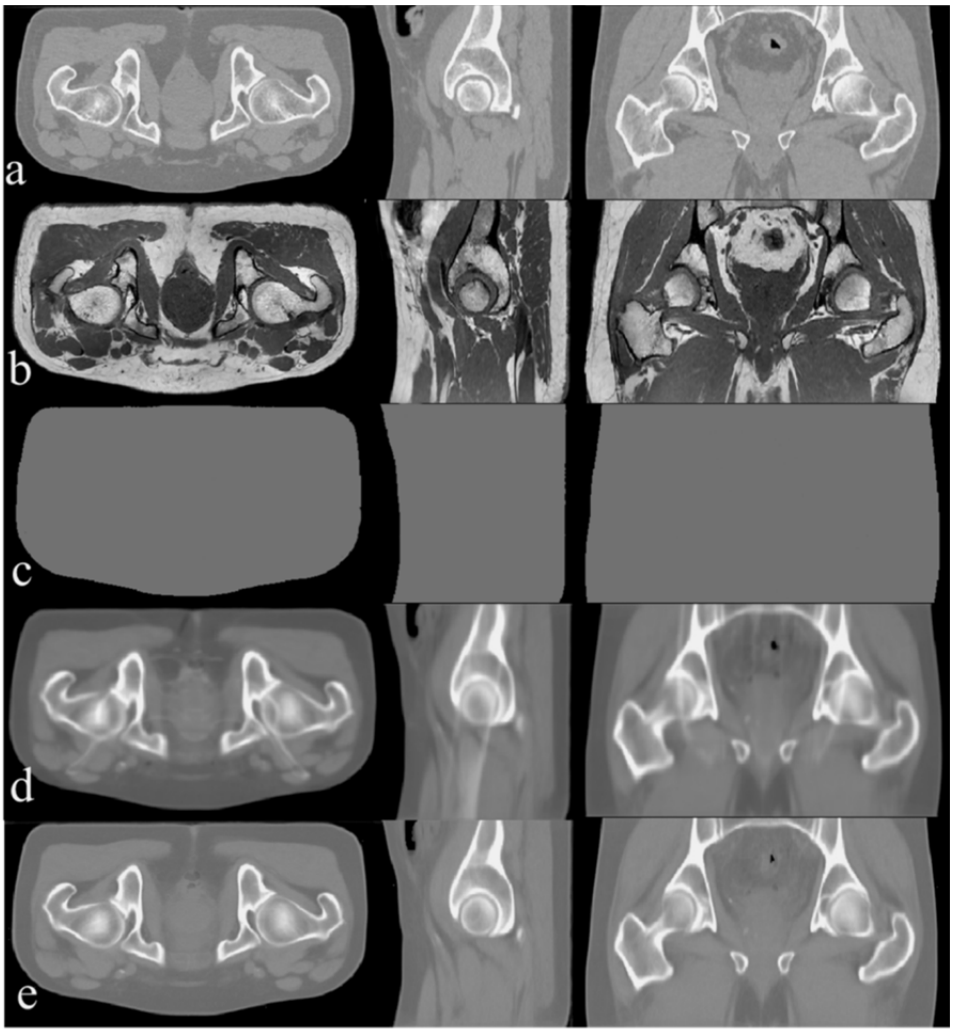

Figure 3. (a) Reference CT; (b) target MRI; (c) water-only attenuation map (d) pseudo-CT generated using median value technique (MV); (e) pseudo-CT generated using local weighting atlas fusion (LW) method.

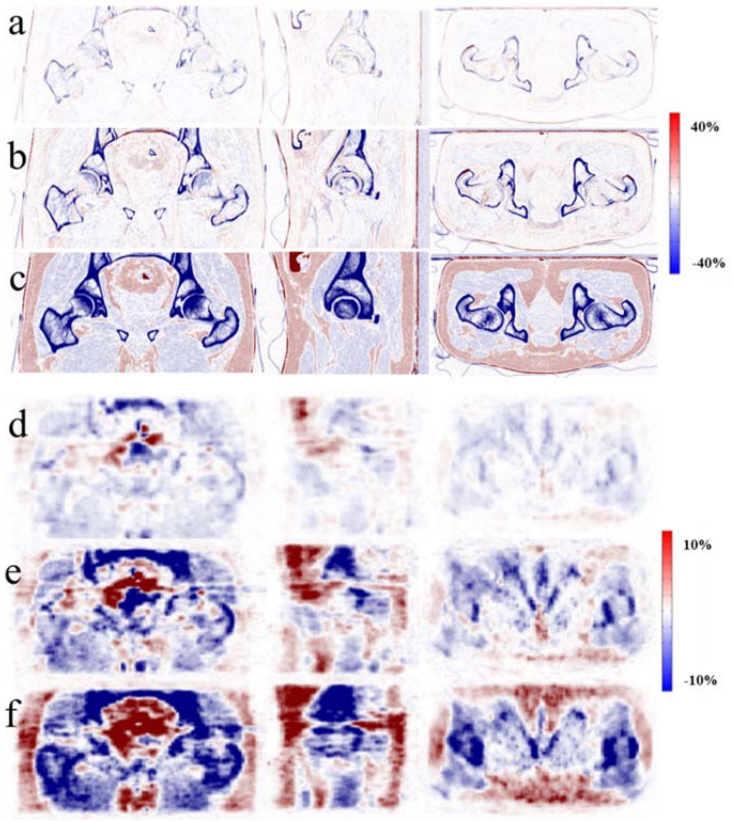

Figure 4. Representative slices of attenuation error maps for (a) LW; (b) MV; (c) water-only and SUV bias maps for (d) LW; (e) MV; (f) water-only methods.

Radiation therapy dose distribution calculations performed using the different pseudo-CT images were evaluated based on the resulting DVHs for a number of regions. The results of the analysis are presented separately for target volumes and OARs considering that 2 out of 12 patients were female. Therefore, 10 contours were defined on the prostate and 2 on the uterus and vagina. Tables 3 and 4 summarize the results of point-by-point analysis of DVHs between maximum and minimum absorbed dose in dose increment of 0.1 Gy. Dosimetric errors are reported in terms of relative mean and absolute mean averaged over 12 patients. Figure 5 shows a representative dose distribution map calculated using the various pseudo-CT images along with dose distribution error maps taking the one calculated using patient-specific CT as reference. Moreover, the volume associated with a certain magnitude of absolute dose difference is presented in figure 6. The measured volume and absorbed dose differences are averaged over the entire patient datasets.

Table 3. Dosimetric errors [relative mean ± SD (absolute mean ± SD)] for organs at risk (OARs) calculated using the total number of DVH points between $D_{100\%}$ and $D_{0\%}$ in dose increments of 0.1 Gy employing equations

Region (OAR)	**Water-only** ME±SD (MAE±SD)	**MV** ME±SD (MAE±SD)	**LW** ME±SD (MAE±SD)
Femur R	–4.0 ± 3.5 (5.3 ± 1.1)	–2.2 ± 1.6 (3.1 ± 1.0)	–0.3 ± 1.3 (1.2 ± 0.4)
Femur L	–3.9 ± 2.9 (4.8 ± 1.2)	–2.2 ± 1.9 (3.2 ± 0.9)	0.5 ± 1.0 (1.1 ± 0.5)
Bladder	2.5 ± 2.4 (3.2 ± 1.4)	1.4 ± 1.4 (3.3 ± 0.9)	0.4 ± 1.4 (1.0 ± 0.4)
Bowel bag	1.4 ± 1.9 (3.6 ± 1.2)	0.9 ± 1.9 (3.2 ± 1.1)	0.1 ± 1.6 (0.9 ± 0.5)
Anus	3.3 ± 2.5 (4.6 ± 1.5)	-0.6 ± 2.3 (3.1 ± 0.9)	-0.3 ± 1.2 (1.0 ± 0.4)
Spinal cord	3.7 ± 2.6 (4.4 ± 1.6)	1.5 ± 2.0 (3.3 ± 1.0)	0.8 ± 0.9 (1.2 ± 0.4)
Iliac crest	–3.2 ± 2.8 (4.3 ± 1.2)	2.1 ± 1.7 (3.0 ± 0.8)	-0.4 ± 1.1 (1.2 ± 0.5)
Genitalia	3.5 ± 2.7 (4.2 ± 1.1)	–2.8 ± 1.9 (3.1 ± 0.9)	0.7 ± 1.6 (1.1 ± 0.6)
Penile bulb	1.1 ± 2.5 (4.1 ± 1.2)	–1.4 ± 1.3 (2.8 ± 0.6)	-0.5 ± 1.1 (1.0 ± 0.4)
Bladder wall	3.7 ± 2.7 (4.2 ± 1.5)	0.6 ± 1.5 (2.6 ± 0.7)	0.5 ± 1.0 (1.2 ± 0.3)
Uterus (2 patients)	1.6 ± 2.8 (4.6 ± 1.6)	1.8 ± 1.9 (3.0 ± 0.8)	0.6± 0.9 (1.8 ± 0.5)
Vagina (2 patients)	3.5 ± 2.9 (4.8 ± 1.4)	2.7 ± 2.9 (4.4 ± 1.1)	0.8 ± 0.8 (1.3 ± 0.6)

Table 4. Dosimetric errors [relative mean ± SD (absolute mean ± SD)] for target regions calculated using the total number of DVH points between $D_{100\%}$ and $D_{0\%}$ in dose increments of 0.1 Gy employing Eqs. 12 and 13.

Region (target)	Water-only ME±SD (MAE±SD)	MV ME±SD (MAE±SD)	LW ME±SD (MAE±SD)
Prostate	2.1 ± 1.9 (3.2 ± 1.1)	1.2 ± 1.9 (2.8 ± 0.9)	0.4 ± 1.2 (1.2 ± 0.5)
Rectum	2.8 ± 2.6 (3.3 ± 1.2)	–1.3 ± 1.6 (2.9 ± 0.8)	0.3 ± 1.0 (1.0 ± 0.4)
PTV-45	2.4 ± 2.8 (3.0 ± 1.1)	1.3 ± 1.1 (2.5 ± 0.7)	0.4 ± 1.1 (0.9 ± 0.3)
PTV-50	3.5 ± 2.7 (4.0 ± 1.0)	2.6 ± 2.1 (3.2 ± 0.7)	0.1 ± 1.2 (0.8 ± 0.4)
CTV-45	3.2 ± 2.9 (4.2 ± 1.0)	2.0 ± 1.2 (2.9 ± 0.6)	-0.1 ± 1.3 (1.0 ± 0.3)
CTV-50	3.7 ± 2.8 (4.3 ± 0.9)	2.1 ± 2.3 (3.0 ± 0.8)	-0.6 ± 1.4 (1.1 ± 0.5)
GTV	1.3 ± 2.7 (4.0 ± 1.0)	1.0 ± 1.4 (2.9 ± 0.6)	-0.7 ± 1.2 (1.2 ± 0.4)

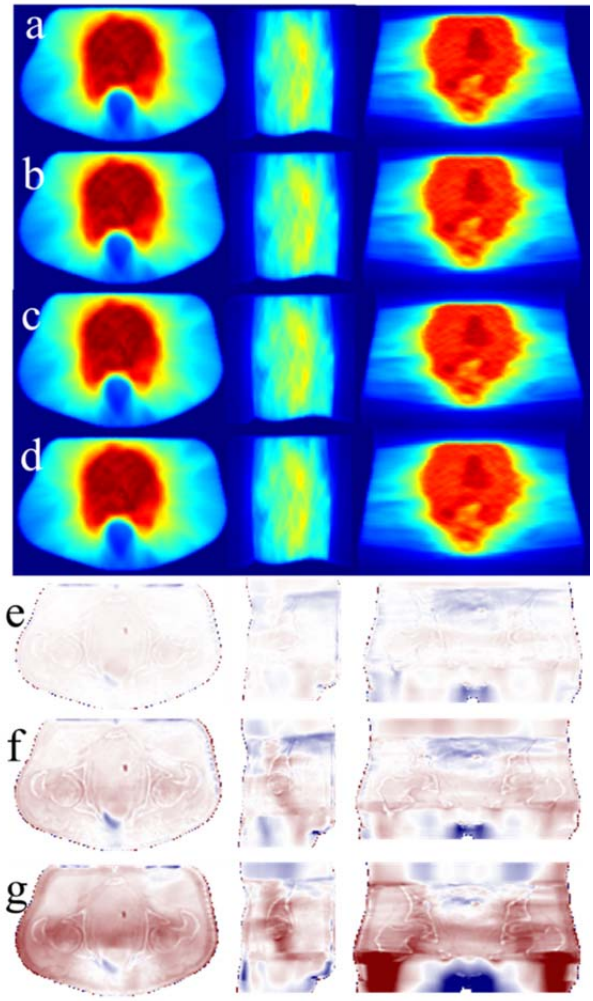

Figure 5. Representative slices of dose distributions calculated using (a) CT, (b) LW pseudo-CT, (c) MV pseudo-CT and (d) water-only. Dose distribution error maps are also shown: (e) LW, (f) MV and (g) water-only.

For each body organ and target volume, the minimum, mean, and maximum absorbed doses calculated using the different pseudo-CT image series were compared. Tables 5 and 6 present the average differences between the dose distributions calculated using the different pseudo-CT images for both OARs and target volumes, whereas figures 7 and 8 depict representative DVHs of OARs and target volumes. The two-dimensional gamma analysis of isocenter dose distributions evaluated at 2%/2 mm dose difference/distance to agreement revealed pass rates of 99.66±0.39%, 99.65±0.70% and 99.86±0.27% (mean±SD) for water-only, MV and LW, respectively. Reducing the evaluation criteria to 1%/1 mm lowered the pass rates to 91.40±7.56%, 96.00±4.11% and 97.67±3.60, respectively, which remains within clinically acceptable tolerance.

Table 5. Average differences (relative mean ± SD) between max, mean, and min absorbed doses calculated using different pseudo-CT images and reference CT for organs at risk (OARs).

Region (OAR)	Water-only [Diff. Dose-max (%) Diff. Dose-mean (%) Diff. Dose-min (%))]	MV [Diff. Dose-max (%) Diff. Dose-mean (%) Diff. Dose-min (%))]	LW [Diff. Dose-max (%) Diff. Dose-mean (%) Diff. Dose-min (%))]
Femur R	–7.1 ± 4.1	–3.2 ± 1.7	–0.5 ± 1.1
	–3.0 ± 3.2	–2.2 ± 1.5	–0.4 ± 1.0
	–6.2 ± 3.7	–3.0 ± 1.6	–0.5 ± 1.2
Femur L	–5.9 ± 3.9	–2.4 ± 1.7	0.8 ± 1.0
	–4.0 ± 3.2	–2.1 ± 1.4	0.6 ± 0.8
	–4.9 ± 2.7	–2.1 ± 1.5	0.9 ± 1.1
Bladder	3.0 ± 2.5	2.6 ± 1.2	0.7 ± 1.0
	2.8 ± 2.2	2.2 ± 1.3	0.6 ± 0.8
	2.7 ± 2.4	2.3 ± 1.2	0.8 ± 1.1
Bowel bag	2.9 ± 2.0	2.1 ± 2.1	0.9 ± 1.7
	2.8 ± 1.9	2.0 ± 1.8	0.5 ± 1.6
	2.8 ± 2.0	2.3 ± 2.0	0.8 ± 1.5
Anus	3.9 ± 2.5	–1.9 ± 2.3	-0.8 ± 1.4
	3.7 ± 2.6	–1.4 ± 2.0	-0.6 ± 1.3
	3.9 ± 2.6	–1.9 ± 2.1	-0.9 ± 1.5
Spinal cord	4.3 ± 2.6	–2.6 ± 2.1	1.1 ± 1.0
	3.9 ± 2.4	–2.5 ± 1.9	0.8 ± 0.9
	4.0± 2.5	–2.4 ± 2.1	1.0 ± 1.0
Iliac crest	–3.9 ± 3.0	-2.6 ± 2.0	-1.0 ± 1.1
	–3.2 ± 2.7	-2.2 ± 1.8	-0.9 ± 1.0
	–4.0 ± 2.9	-2.9 ± 2.2	-1.1 ± 1.1
Genitalia	3.9 ± 2.8	–3.0 ± 2.1	0.9 ± 1.5
	3.6 ± 2.3	–2.8 ± 1.9	0.7 ± 1.4
	4.6 ± 2.8	–2.9 ± 1.9	0.9 ± 1.4
Penile bulb	3.5 ± 2.3	–1.9 ± 1.8	-1.2 ± 1.1
	3.3 ± 2.5	–1.3 ± 1.5	-0.9 ± 1.1
	3.6 ± 2.6	–2.0 ± 1.8	-1.2 ± 1.0
Bladder wall	4.1 ± 2.6	2.7 ± 1.5	0.7 ± 1.1
	3.9 ± 2.5	2.2 ± 1.7	0.5 ± 1.0
	4.5 ± 2.6	2.9 ± 1.6	0.9 ± 1.1
Uterus (2 patients)	3.4 ± 2.7	2.0 ± 1.7	-0.8 ± 1.0
	3.2 ± 2.4	1.5 ± 1.5	-0.6 ± 0.9
	3.5 ± 2.8	2.1 ± 1.9	-0.9 ± 1.1
Vagina (2 patients)	3.6 ± 2.4	2.1 ± 1.9	0.6 ± 1.0
	3.5 ± 2.5	1.6 ± 1.6	0.5 ± 0.9
	3.7 ± 2.7	2.3 ± 2.0	0.7 ± 1.1

IV. Discussion

We proposed a surrogate CT generation approach using a two-step optimization paradigm to improve the accuracy of bone identification and provide a continuous-valued pseudo-CT image at the same time. In the first step, the segmentation is optimized for bone extraction from the target MRI, whereby the prior knowledge from the atlas CT images is utilized to assess resemblance of bony structures to the target image. Without the initial target bone estimation, the prior knowledge from CT cannot be used in the atlas fusion scheme owing to the lack of supposedly ground truth to compare CT images with. It is worth mentioning that the initial bone estimation does not represent the bone identification in the final pseudo-CT image and only contribute to determine the weights (according to Eq. 7) for the atlas fusion scheme. The initial step enhances the accuracy of bone extraction by roughly 10% due to additional emphasis on bony structures. The improvement observed in bone identification (DSC of 0.89 instead of 0.75) stems from effective pattern recognition and local mis-alignment detection provided by the two-step segmentation and fusion optimization scheme. Similar studies were performed using an atlas-based method developed for dose calculation and DRR generation using a conjugate

electron density database generated from co-registered CT-MRI scans [12]. Comparisons made using 26 whole-pelvic scans revealed an agreement (based on the DSC metric) of 0.79±0.12 and 0.64±0.16 for pelvic bone and the bladder, respectively. In a more recent study conducted by Andreasen et al. [30], a patch-based pseudo-CT generation method was proposed and compared with a Gaussian mixture regression model using dUTE scans [52] and a multi-atlas information propagation approach [21]. The patch-based method yielded a DSC of 0.84 for bone volume while the multi-atlas and the Gaussian mixture regression approaches resulted in DSC of 0.83 and 0.67, respectively. It should be noted that this comparison was performed using cranial MRI/CT scans of five patients.

Table 6. Average differences (relative mean ± SD) between max, mean, and min absorbed doses calculated using different pseudo-CT images and reference CT for target regions.

Region (target)	**Water-only [Diff. Dose-max (%) Diff. Dose-mean (%) Diff. Dose-min (%))]**	**MV [Diff. Dose-max (%) Diff. Dose-mean (%) Diff. Dose-min (%))]**	**LW [Diff. Dose-max (%) Diff. Dose-mean (%) Diff. Dose-min (%))]**
Prostate	2.9 ± 1.6 2.2 ± 1.6 2.7 ± 1.5	1.6 ± 2.0 1.4 ± 1.9 1.9 ± 2.1	1.1 ± 1.1 0.8 ± 10 1.1 ± 1.0
Rectum	3.7 ± 2.2 3.1 ± 2.1 3.8 ± 2.4	–1.7 ± 1.6 –1.2 ± 1.5 –1.9 ± 1.6	0.6 ± 1.0 0.3 ± 0.9 0.8 ± 1.1
PTV-45	2.8 ± 2.3 2.5 ± 2.0 3.0 ± 2.1	1.8 ± 1.0 1.6 ± 1.0 1.9 ± 1.1	0.6 ± 1.1 0.4 ± 1.0 0.5 ± 1.0
PTV-50	4.1 ± 2.1 3.9 ± 1.9 4.0 ± 2.0	2.8 ± 2.1 2.4 ± 1.7 2.6 ± 2.0	0.6 ± 1.2 0.4 ± 1.0 1.0 ± 1.1
CTV-45	3.6 ± 2.3 3.2 ± 2.0 3.9 ± 2.4	2.6 ± 1.5 2.1 ± 1.2 2.7 ± 1.4	-0.7 ± 1.4 -0.3 ± 1.0 -0.8 ± 1.2
CTV-50	4.2 ± 2.5 4.1 ± 2.2 4.6 ± 2.5	3.1 ± 2.6 2.5 ± 2.2 3.2 ± 2.7	-1.3 ± 1.2 -0.6 ± 1.0 -1.5 ± 1.3
GTV	3.8 ± 2.5 3.3 ± 2.4 4.0 ± 2.6	1.9 ± 1.4 1.4 ± 1.3 2.0 ± 1.6	-1.0 ± 1.2 -0.8 ± 1.1 -1.1 ± 1.2

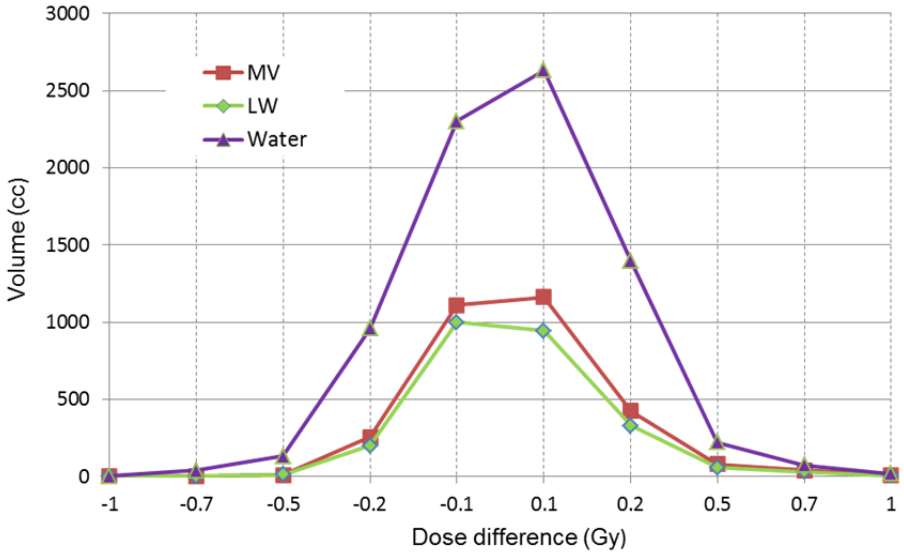

Figure 6. Volumes (cc) associated with a certain magnitude of dose difference (Gy) between dose distributions calculated using reference CT and different pseudo-CT images

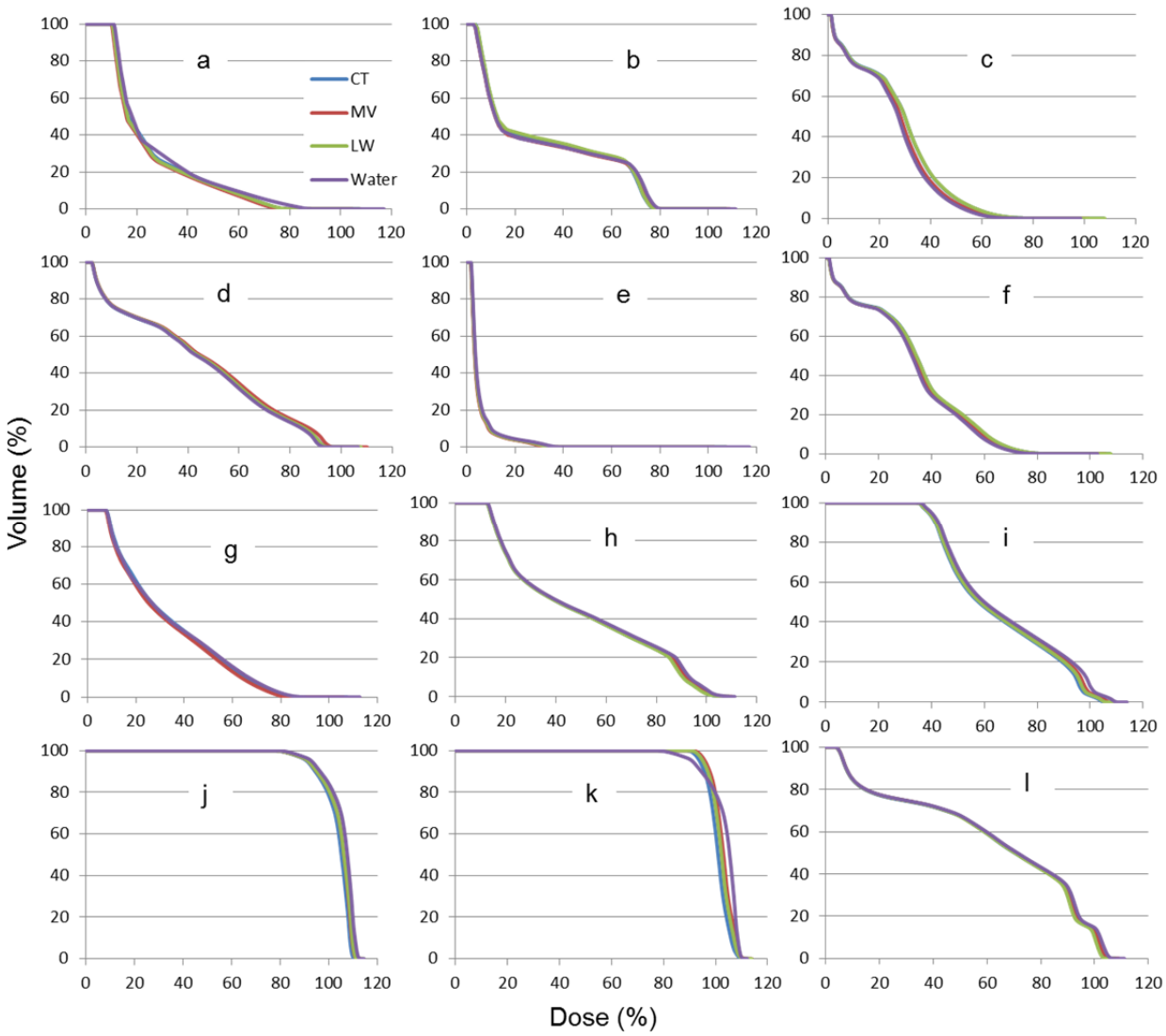

Figure 7. Representative dose volume histograms of dose distributions calculated using different pseudo-CT images for organs at risk, namely (a) anus, (b) spinal cord, (c) left femur, (d) iliac crest, (e) genitalia, (f) right femur, (g) penile bulb, (h) bladder wall, (i) bladder, (j) uterus, (k) vagina, and (l) bowel bag.

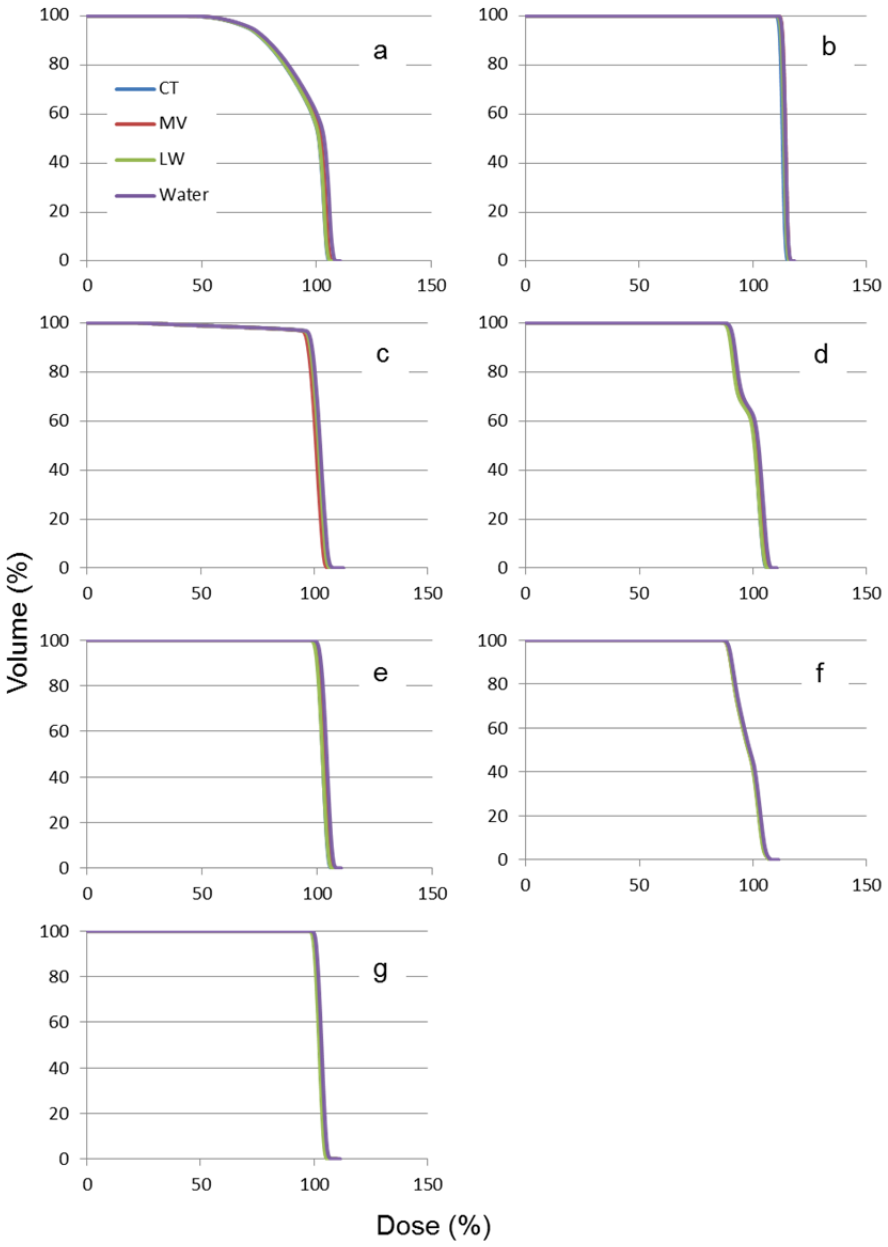

Figure 8. Representative dose volume histograms of dose distributions calculated using different pseudo-CT images for target regions, namely (a) the prostate, (b) GTV, (c) PTV_50, (d) CTV_45, (e) Rectum, (f) PTV_45, and (g) CTV_50.

IV. Discussion

We proposed a surrogate CT generation approach using a two-step optimization paradigm to improve the accuracy of bone identification and provide a continuous-valued pseudo-CT image at the same time. In the first step, the segmentation is optimized for bone extraction from the target MRI, whereby the prior knowledge from the atlas CT images is utilized to assess resemblance of bony structures to the target image. Without the initial target bone estimation, the prior knowledge from CT cannot be used in the atlas fusion scheme owing to the lack of supposedly ground truth to compare CT images with. It is worth mentioning that the initial bone estimation does not represent the bone identification in the final pseudo-CT image and only contribute to determine the weights (according to Eq. 7) for the atlas fusion scheme. The initial step enhances the accuracy of bone extraction by roughly 10% due to additional emphasis on bony structures. The improvement observed in bone identification (DSC of 0.89 instead of 0.75) stems from effective pattern recognition and local mis-alignment detection provided by the two-step segmentation and fusion optimization scheme. Similar studies were performed using an atlas-based method developed for dose calculation and DRR generation using a conjugate electron density database generated from co-registered CT-MRI scans [12]. Comparisons made using 26 whole-pelvic scans revealed an agreement (based on the DSC metric) of 0.79±0.12 and 0.64±0.16 for pelvic bone and the bladder, respectively. In a more recent study conducted by Andreasen et al. [30], a patch-based pseudo-CT generation method was proposed and compared with a Gaussian mixture regression model using dUTE scans

[52] and a multi-atlas information propagation approach [21]. The patch-based method yielded a DSC of 0.84 for bone volume while the multi-atlas and the Gaussian mixture regression approaches resulted in DSC of 0.83 and 0.67, respectively. It should be noted that this comparison was performed using cranial MRI/CT scans of five patients.

Voxelwise evaluation of PET quantification bias indicated superior performance of the proposed method over water-only (or 3-class MRI segmentation-based attenuation map) mostly due to the considerable improvement of bone extraction accuracy. Ignoring bony structures (water-only attenuation map) resulted in a mean SUV bias of -19.9±11.8% while the MV method yielded a mean bias of -8.1±8.2%. This is in agreement with results reported by Paulus et al. [53] where a mean SUV bias of -25.5±7.9% was obtained in bone regions using a 4-class attenuation map ignoring bone, which was reduced to -4.9±6.7% using a strategy enabling to incorporate bony tissue in the attenuation map for whole-body PET/MR imaging. Due to the higher photon energy employed in RT (here 6 MV beam) compared to the energy of annihilation photons (511 KeV), dose calculation using different pseudo-CT image series is less sensitive to tissue LACs in comparison with PET quantification bias. As such, the dosimetric errors summarized in Tables 3 and 4 based on DVH analysis exhibit a smaller range of errors among the different pseudo-CT generation techniques. However, a similar trend to PET SUV bias is observed where water-only map yielded the largest errors while the LV technique resulted in less than 1% errors for all target volumes and OARs. Similarly, Kapanen and Tenhunen [35] compared their pseudo-CT generation method against water-only pseudo-CT and reference CT considering a treatment plan for the pelvic region optimized for 15 MeV photons. Maximal dose differences between water-only and their proposed pseudo-CT with respect to reference CT for all points contained within the PTV were 3.7% and 1.2%, respectively. Therefore, our results (Tables 3 and 4) are in agreement with the range of dosimetric errors reported in the literature.

Dose comparison results between maximum, mean and minimum absorbed dose in different target volumes and OARs indicated a larger range compared to DVH analysis with a maximum error in large bony structures, such as the left and right femurs. Jonsson et al. [32] reported a maximum dose difference of -5.9±7.9% using an UTE-based pseudo-CT approach in the head region. For the prostate, Kim et al. [54] evaluated two pseudo-CT generation methods and reported mean dose errors of 1.22% and 0.54% for both techniques. Apart from the relatively low dosimetric errors achieved using the LW technique, the standard deviation of measured errors, for either the DVH analysis or min-max dose comparison, exhibited significant reduction compared to those obtained using water-only and MV techniques. Moreover, gamma analysis demonstrated the efficiency of the proposed method where 97.67±3.60% of voxels passed the evaluation criteria of 1%/1 mm compared to 95.85% reported in another study focusing on the brain region [32].

The outcome of this algorithm does not depend on the MRI sequence used as long as the target and training atlas images originate from the same MRI sequence. However, if the used MR sequence provides better image quality in terms of signal to noise ratio, this enhances the performance of the registration algorithm and feature extraction capability, which in turn will improve the outcome.

V. Conclusion

A novel atlas-based pseudo-CT generation approach was proposed using a clinically available conventional Dixon MRI sequence for the pelvic region. The superior performance of the proposed method was demonstrated using clinical studies in terms of bone identification, reduction in PET quantification bias, and reduction in dose distribution calculation errors for radiation therapy treatment planning compared to conventional methods. The proposed method can be easily applied to other body regions, such as the brain, and even to whole-body imaging. The proposed method is promising potential applications in either MRI-only or PET/MRI guided RT treatment planning or MRI-guided attenuation correction in hybrid PET/MR imaging.

Acknowledgments

This work was supported in part by the Swiss National Science Foundation under Grant SNSF 31003A-149957 and the Swiss Cancer Research Foundation under Grant KFS-3855-02-2016.

References

[1] M. A. Schmidt and G. S. Payne, "Radiotherapy planning using MRI.," *Phys Med Biol,* vol. 60, pp. R323-361, Nov 21 2015.

[2] R. Prabhakar, K. P. Haresh, T. Ganesh, R. C. Joshi, P. K. Julka, and G. K. Rath, "Comparison of computed tomography and magnetic resonance based target volume in brain tumors.," *J Cancer Res Ther,* vol. 3, pp. 121-123, Apr-Jun 2007.

[3] M. Ahmed, M. Schmidt, A. Sohaib, C. Kong, K. Burke, C. Richardson*, et al.*, "The value of magnetic resonance imaging in target volume delineation of base of tongue tumours--a study using flexible surface coils.," *Radiother Oncol,* vol. 94, pp. 161-167, Feb 2010.

[4] C. Rasch, R. Steenbakkers, and M. van Herk, "Target definition in prostate, head, and neck.," *Semin Radiat Oncol,* vol. 15, pp. 136-145, Jul 2005.

[5] G. M. Cattaneo, M. Reni, G. Rizzo, P. Castellone, G. L. Ceresoli, C. Cozzarini*, et al.*, "Target delineation in post-operative radiotherapy of brain gliomas: interobserver variability and impact of image registration of MR(pre-operative) images on treatment planning CT scans.," *Radiother Oncol,* vol. 75, pp. 217-223, May 2005.

[6] K. Ulin, M. M. Urie, and J. M. Cherlow, "Results of a multi-institutional benchmark test for cranial CT/MR image registration.," *Int J Radiat Oncol Biol Phys,* vol. 77, pp. 1584-1589, Aug 1 2010.

[7] T. Nyholm, M. Nyberg, M. G. Karlsson, and M. Karlsson, "Systematisation of spatial uncertainties for comparison between a MR and a CT-based radiotherapy workflow for prostate treatments.," *Radiat Oncol,* vol. 4, p. 54, 2009.

[8] J. N. Brunt, "Computed tomography-magnetic resonance image registration in radiotherapy treatment planning.," *Clin Oncol (R Coll Radiol),* vol. 22, pp. 688-697, Oct 2010.

[9] A. Mehranian, H. Arabi, and H. Zaidi, "Vision 20/20: Magnetic resonance imaging-guided attenuation correction in PET/MRI: Challenges, solutions, and opportunities.," *Med Phys,* vol. 43, pp. 1130-1155, 2016.

[10] J. C. Dickson, C. O'Meara, and A. Barnes, "A comparison of CT-and MR-based attenuation correction in neurological PET," *European journal of nuclear medicine and molecular imaging,* vol. 41, pp. 1176-1189, 2014.

[11] F. L. Andersen, C. N. Ladefoged, T. Beyer, S. H. Keller, A. E. Hansen, L. Hojgaard*, et al.*, "Combined PET/MR imaging in neurology: MR-based attenuation correction implies a strong spatial bias when ignoring bone.," *Neuroimage,* vol. 84, pp. 206-216, Aug 29 2014.

[12] J. A. Dowling, J. Lambert, J. Parker, O. Salvado, J. Fripp, A. Capp*, et al.*, "An atlas-based electron density mapping method for magnetic resonance imaging (MRI)-alone treatment planning and adaptive MRI-based prostate radiation therapy.," *Int J Radiat Oncol Biol Phys,* vol. 83, pp. e5-11, May 1 2012.

[13] B. Fei, X. Yang, J. A. Nye, J. N. Aarsvold, N. Raghunath, M. Cervo*, et al.*, "MRPET quantification tools: Registration, segmentation, classification, and MR-based attenuation correction.," *Med Phys,* vol. 39, pp. 6443-6454, Oct 2012.

[14] A. Martinez-Moller, M. Souvatzoglou, G. Delso, R. A. Bundschuh, C. Chefd'hotel, S. I. Ziegler*, et al.*, "Tissue classification as a potential approach for attenuation correction in whole-body PET/MRI: Evaluation with PET/CT data.," *J Nucl Med,* vol. 50, pp. 520-526, Apr 2009.

[15] I. Bezrukov, F. Mantlik, H. Schmidt, B. Schölkopf, and B. J. Pichler, "MR-Based PET Attenuation Correction for PET/MR Imaging," *Seminars in nuclear medicine,* vol. 43, pp. 45-59, 2013.

[16] V. Keereman, Y. Fierens, T. Broux, Y. De Deene, M. Lonneux, and S. Vandenberghe, "MRI-based attenuation correction for PET/MRI using ultrashort echo time sequences.," *J Nucl Med,* vol. 51, pp. 812-818, May 2010.

[17] Y. Berker, J. Franke, A. Salomon, M. Palmowski, H. C. Donker, Y. Temur*, et al.*, "MRI-based attenuation correction for hybrid PET/MRI systems: A 4-class tissue segmentation technique using a combined Ultrashort-Echo-Time/Dixon MRI sequence.," *J Nucl Med,* vol. 53, pp. 796-804, May 2012.

[18] J. M. Edmund, H. M. Kjer, K. Van Leemput, R. H. Hansen, J. A. Andersen, and D. Andreasen, "A voxel-based investigation for MRI-only radiotherapy of the brain using ultra short echo times," *Physics in medicine and biology,* vol. 59, p. 7501, 2014.

[19] C. M. Rank, C. Tremmel, N. Hunemohr, A. M. Nagel, O. Jakel, and S. Greilich, "MRI-based treatment plan simulation and adaptation for ion radiotherapy using a classification-based approach.," *Radiat Oncol,* vol. 8, p. 51, 2013.

[20] J. Uh, T. E. Merchant, Y. Li, X. Li, and C. Hua, "MRI-based treatment planning with pseudo CT generated through atlas registration.," *Med Phys,* vol. 41, pp. 051711-8, 2014.

[21] N. Burgos, M. Cardoso, K. Thielemans, M. Modat, J. Schott, J. Duncan*, et al.*, "Attenuation correction synthesis for hybrid PET-MR scanners: Application to brain studies.," *IEEE Trans Med Imaging,* vol. 33, pp. 2332-2341, Jul 17 2014.

[22] H. Arabi and H. Zaidi, "Comparison of atlas-based bone segmentation methods in whole-body PET/MRI," *IEEE Nuclear Science Symposium & Medical Imaging Conference,* vol. Seattle, USA, 2014.

[23] M. Hofmann, F. Steinke, V. Scheel, G. Charpiat, J. Farquhar, P. Aschoff*, et al.*, "MRI-based attenuation correction for PET/MRI: A novel approach combining pattern recognition and Atlas registration.," *J Nucl Med,* vol. 49, pp. 1875-1883, Oct 16 2008.

[24] M. Hofmann, I. Bezrukov, F. Mantlik, P. Aschoff, F. Steinke, T. Beyer*, et al.*, "MRI-based attenuation correction for whole-body PET/MRI: Quantitative evaluation of segmentation- and Atlas-based methods.," *J Nucl Med,* vol. 52, pp. 1392-1399, Sep 2011.

[25] Y. Chen, M. Juttukonda, Y. Z. Lee, Y. Su, F. Espinoza, W. Lin*, et al.*, "MRI based attenuation correction for PET/MRI via MRF segmentation and sparse regression estimated CT," in *Biomedical Imaging (ISBI), 2014 IEEE 11th International Symposium on*, 2014, pp. 1364-1367.

[26] A. Rezaei, M. Defrise, G. Bal, C. Michel, M. Conti, C. Watson*, et al.*, "Simultaneous reconstruction of activity and attenuation in time-of-flight PET.," *IEEE Trans Med Imaging,* p. *in press*, 2012.

[27] A. Mehranian and H. Zaidi, "Joint estimation of activity and attenuation in whole-body TOF PET/MRI using constrained Gaussian mixture models.," *IEEE Trans Med Imaging,* vol. 34, pp. 1808-1821, 2015.

[28] H. Arabi and H. Zaidi, "Magnetic resonance imaging-guided attenuation correction in whole-body PET/MRI using a sorted atlas approach.," *Med Image Anal,* vol. 31, pp. 1-15, 7, 2016.

[29] H. R. Marshall, J. Patrick, D. Laidley, F. S. Prato, J. Butler, J. Theberge*, et al.*, "Description and assessment of a registration-based approach to include bones for attenuation correction of whole-body PET/MRI.," *Med Phys,* vol. 40, p. 082509, Aug 2013.

[30] D. Andreasen, K. Van Leemput, R. H. Hansen, J. A. Andersen, and J. M. Edmund, "Patch-based generation of a pseudo CT from conventional MRI sequences for MRI-only radiotherapy of the brain.," *Med Phys,* vol. 42, pp. 1596-1605, Apr 2015.

[31] Y. H. Noorda, L. W. Bartels, M. Huisman, R. J. Nijenhuis, M. A. van den Bosch, and J. P. Pluim, "Registration of CT to pre-treatment MRI for planning of MR-HIFU ablation treatment of painful bone metastases.," *Phys Med Biol,* vol. 59, pp. 4167-4179, Aug 7 2014.

[32] J. H. Jonsson, M. M. Akhtari, M. G. Karlsson, A. Johansson, T. Asklund, and T. Nyholm, "Accuracy of inverse treatment planning on substitute CT images derived from MR data for brain. lesions," *Radiat Oncol,* vol. 10, p. 13, 2015.

[33] D. Izquierdo-Garcia, A. E. Hansen, S. Forster, D. Benoit, S. Schachoff, S. Furst*, et al.*, "An SPM8-based approach for attenuation correction combining segmentation and nonrigid template formation: Application to simultaneous PET/MR brain imaging.," *J Nucl Med,* vol. 55, pp. 1825-1830, Nov 2014.

[34] J. Sjölund, D. Forsberg, M. Andersson, and H. Knutsson, "Generating patient specific pseudo-CT of the head from MR using atlas-based regression.," *Phys Med Biol,* vol. 60, pp. 825-839, 2015.

[35] M. Kapanen and M. Tenhunen, "T1/T2*-weighted MRI provides clinically relevant pseudo-CT density data for the pelvic bones in MRI-only based radiotherapy treatment planning.," *Acta Oncol,* vol. 52, pp. 612-618, Apr 2013.

[36] D. H. Paulus, M. Oehmigen, J. Gruneisen, L. Umutlu, and H. H. Quick, "Whole-body hybrid imaging concept for the integration of PET/MR into radiation therapy treatment planning.," *Phys Med Biol,* vol. 61, pp. 3504-3520, May 7 2016.

[37] H. Zaidi, N. Ojha, M. Morich, J. Griesmer, Z. Hu, P. Maniawski*, et al.*, "Design and performance evaluation of a whole-body Ingenuity TF PET-MRI system.," *Phys Med Biol,* vol. 56, pp. 3091-3106, Apr 20 2011.

[38] W. T. Dixon, "Simple proton spectroscopic imaging.," *Radiology,* vol. 153, pp. 189-194, Oct 1984.

[39] A. Akbarzadeh, D. Gutierrez, A. Baskin, M. R. Ay, A. Ahmadian, N. Riahi Alam, *et al.*, "Evaluation of whole-body MR to CT deformable image registration.," *J Appl Clin Med Phys,* vol. 14, pp. 238-253, 2013.

[40] J. M. Lotjonen, R. Wolz, J. R. Koikkalainen, L. Thurfjell, G. Waldemar, H. Soininen, *et al.*, "Fast and robust multi-atlas segmentation of brain magnetic resonance images.," *Neuroimage,* vol. 49, pp. 2352-2365, Feb 1 2010.

[41] N. J. Tustison, B. B. Avants, P. A. Cook, Y. Zheng, A. Egan, P. A. Yushkevich, *et al.*, "N4ITK: improved N3 bias correction.," *IEEE Trans Med Imaging,* vol. 29, pp. 1310-1320, Jun 2010.

[42] M. J. McAuliffe, F. M. Lalonde, D. McGarry, W. Gandler, K. Csaky, and B. L. Trus, "Medical Image Processing, Analysis and Visualization in clinical research," in *14th IEEE Symposium on Computer-Based Medical Systems, 2001. CBMS 2001. Proceedings*, 2001, pp. 381-386.

[43] S. Klein, M. Staring, K. Murphy, M. A. Viergever, and J. P. W. Pluim, "elastix: A toolbox for intensity-based medical image registration.," *IEEE Trans Med Imaging,* vol. 29, pp. 196-205, 2010.

[44] X. Zhuang and J. Shen, "Multi-scale patch and multi-modality atlases for whole heart segmentation of MRI," *Medical Image Analysis,* vol. 31, pp. 77-87, 2016.

[45] P. Kovesi, "Phase congruency: a low-level image invariant.," *Psychol Res,* vol. 64, pp. 136-148, 2000.

[46] C. G. Ortiz and A. L. Martel, "Automatic atlas-based segmentation of the breast in MRI for 3D breast volume computation.," *Med Phys,* vol. 39, pp. 5835-5848, Oct 2012.

[47] Z. Hu, N. Ojha, S. Renisch, V. Schulz, I. Torres, D. Pal, *et al.*, "MR-based attenuation correction for a whole-body sequential PET/MR system," in *IEEE Nuclear Science Symposium & Medical Imaging Conference*, 25-31 October 2009, Orlando (FL), USA, 2009, pp. 3508-3512.

[48] P. A. Yushkevich, J. Piven, H. C. Hazlett, R. G. Smith, S. Ho, J. C. Gee, *et al.*, "User-guided 3D active contour segmentation of anatomical structures: significantly improved efficiency and reliability.," *Neuroimage,* vol. 31, pp. 1116-1128, Jul 1 2006.

[49] L. R. Dice, "Measures of the amount of ecologic association between species.," *Ecology,* vol. 26, pp. 297-302, 1945.

[50] J. H. Jonsson, A. Johansson, K. Soderstrom, T. Asklund, and T. Nyholm, "Treatment planning of intracranial targets on MRI derived substitute CT data.," *Radiother Oncol,* vol. 108, pp. 118-122, Jul 2013.

[51] D. A. Low, W. B. Harms, S. Mutic, and J. A. Purdy, "A technique for the quantitative evaluation of dose distributions," *Medical physics,* vol. 25, pp. 656-661, 1998.

[52] A. Johansson, M. Karlsson, and T. Nyholm, "CT substitute derived from MRI sequences with ultrashort echo time.," *Med Phys,* vol. 38, pp. 2708-2714, May 2011.

[53] D. H. Paulus, H. H. Quick, C. Geppert, M. Fenchel, Y. Zhan, G. Hermosillo, *et al.*, "Whole-body PET/MR imaging: Quantitative evaluation of a novel model-based MR attenuation correction method including bone.," *J Nucl Med,* vol. 57, pp. 1061-1066, May 29 2015.

[54] J. Kim, C. Glide-Hurst, A. Doemer, N. Wen, B. Movsas, and I. J. Chetty, "Implementation of a novel algorithm for generating synthetic CT images from magnetic resonance imaging data sets for prostate cancer radiation therapy.," *Int J Radiat Oncol Biol Phys,* vol. 91, pp. 39-47, Jan 1 2015.

Chapter 8

Quantitative analysis of MRI-guided attenuation correction techniques in time-of-flight brain PET/MRI

Abolfazl Mehranian, Hossein Arabi and Habib Zaidi

NeuroImage, Vol. 130, pp 123–133 (2016)

Abstract

Purpose: In quantitative PET/MR imaging, attenuation correction (AC) of PET data is markedly challenged by the need of deriving accurate attenuation maps from MR images. A number of strategies have been developed for MRI-guided attenuation correction with different degrees of success. In this work, we compare the quantitative performance of three generic AC methods, including standard 3-class MR segmentation-based, advanced atlas-registration-based and emission-based approaches in the context of brain time-of-flight (TOF) PET/MRI.

Methods: Fourteen patients referred for diagnostic MRI and ^{18}F-FDG PET/CT brain scans were included in this comparative study. For each study, PET images were reconstructed using four different attenuation maps derived from CT-based AC (CTAC) serving as reference, standard 3-class MR-segmentation, atlas-registration and emission-based AC methods. To generate 3-class attenuation maps, T1-weighted MRI images were segmented into background air, fat and soft-tissue classes followed by assignment of constant linear attenuation coefficients of 0, 0.0864 and 0.0975 cm^{-1} to each class, respectively. A robust atlas-registration based AC method was developed for pseudo-CT generation using local weighted fusion of atlases based on their morphological similarity to target MR images. Our recently proposed MRI-guided maximum likelihood reconstruction of activity and attenuation (MLAA) algorithm was employed to estimate the attenuation map from TOF emission data. The performance of the different AC algorithms in terms of prediction of bones and quantification of PET tracer uptake was objectively evaluated with respect to reference CTAC maps and CTAC-PET images.

Results: Fourteen patients referred for diagnostic MRI and ^{18}F-FDG PET/CT brain scans were included in this comparative study. For each study, PET images were reconstructed using four different attenuation maps derived from CT-based AC (CTAC) serving as reference, standard 3-class MR-segmentation, atlas-registration and emission-based AC methods. To generate 3-class attenuation maps, T1-weighted MRI images were segmented into background air, fat and soft-tissue classes followed by assignment of constant linear attenuation coefficients of 0, 0.0864 and 0.0975 cm^{-1} to each class, respectively. A robust atlas-registration based AC method was developed for pseudo-CT generation using local weighted fusion of atlases based on their morphological similarity to target MR images. Our recently proposed MRI-guided maximum likelihood reconstruction of activity and attenuation (MLAA) algorithm was employed to estimate the attenuation map from TOF emission data. The performance of the different AC algorithms in terms of prediction of bones and quantification of PET tracer uptake was objectively evaluated with respect to reference CTAC maps and CTAC-PET images.

Conclusion: The standard 3-class MRAC method significantly underestimated cerebral PET tracer uptake. While current state-of-the-art MLAA-AC methods look promising, they were unable to noticeably reduce quantification errors in the context of brain imaging. Conversely, the proposed atlas-AC method provided the most accurate attenuation maps, and thus the lowest quantification bias.

I. Introduction

Positron emission tomography (PET) and magnetic resonance imaging (MRI) provide complementary information about the physiology, function and morphology of different organs/tissues in normal and pathological states. This hybrid imaging technology proved to be valuable in a number of clinical indications, particularly in the assessment of brain disorders and in neuroscience research. Recent developments in integrated hybrid PET/MRI systems have streamlined the simultaneous acquisition of PET and MRI data and therefore the spatiotemporal correlation of the information provided by each modality alone. The availability of numerous PET radiotracers and advanced contrast-enhanced MR imaging techniques makes simultaneous PET/MRI especially attractive for multiparametric monitoring of physiopathological variations associated with brain disorders *in vivo* [1], staging and characterization of tumours [2] and quantitative measurement of neural activity and brain hemodynamics [3].

Despite of these advantages and still unexplored potential avenues for PET/MRI technology, the quantification of PET and MRI tracer and contrast concentrations in PET/MRI studies is currently one of the most involved and challenging tasks encountered by these modalities. For instance, the concentration of MR contrast agents in dynamic contract-enhanced MRI studies is affected by the underlying native T1 relaxation time of tissues and, as such, it is not linearly related to signal intensities. It is therefore necessary to design and perform additional MR sequences to calculate quantitative T1 maps of tissues and thereby to quantify the tracer concentration. Similarly, the quantification of PET radiotracer uptake in PET/MRI is challenged by the need of deriving underlying photon linear attenuation coefficients (LACs) of tissues from MR images. In contrast to x-ray computed tomography (CT) used on PET/CT scanners, MR image intensities are not directly related to the photon attenuating properties of tissues (i.e. atomic number, electron density) but rather to their magnetic properties (i.e. T1 and T2 relaxation times, proton density) as well as MR pulse timing parameters (i.e. flip angle, repetition time (TR), echo time (TE), inversion time (TI) ... etc. [4]. Hence, the direct conversion of MRI intensities to 511 KeV attenuation maps using experimentally derived mapping functions is not feasible.

Since the introduction of PET/MRI in clinical practice, segmentation-based AC methods were adopted to derive attenuation maps where MR images are segmented into a number of tissue classes and predefined LACs are assigned to each tissue class [5]. To achieve reliable PET quantification, MR images should ideally be segmented into 6 tissue classes, namely, soft-tissue, fat, lung, air, cortical and spongeous bones [6, 7]. However, a major challenge is the differentiation between bones and air cavities in the skull and surrounding soft-tissue in the vertebra, since bones do not exhibit detectable signals when using conventional MRI sequences mainly due to their short T2 relaxation time. In commercial PET/MRI scanners, bones are thus currently replaced by soft-tissues. However, neglecting bone in the resulting attenuation maps can give rise to substantial errors in quantification of brain PET images (5-10% [8], 10-29% [9]) and lesions seated close to bones (2-31% [10, 11]). In brain PET/MRI imaging, ultrashort echo-time (UTE) [12, 13] and more recently zero echo-time (ZTE) [14, 15] MR sequences have been developed to specifically delineate bones and include them in the attenuation maps. Initial UTE-based AC studies have reported quantification errors of less than 5% [16]; however, the inhomogeneous and imprecise classification of bones, particularly in the presence of diamagnetic susceptibility effects at air/bone or air/soft-tissue interfaces [17] can give rise to errors in the range 4-17% in different regions of the brain [9]. Recently, Delso *et al.* demonstrated that ZTE-based bone segmentation outperforms its UTE-based counterpart with reduced segmentation errors [15]. However, these two MRI sequences are time consuming (between 3-6 min for low and high resolution U/ZTE acquisitions [15]), which currently limits their adoption in clinical practice. The assignment of constant LACs to each tissue class is another source of error in segmentation-based AC techniques, since inter/intra-patient variability of attenuation coefficients is not accounted for.

Alternative AC approaches have therefore been explored in the context of brain imaging including registration-based and emission-based AC methods [18]. In registration-based methods, MRI of an atlas and co-registered CT (or transmission) are registered to the patient's MR image and then the CT or transmission maps are transformed using the same transformation fields to produce patient-specific attenuation map [19, 20]. Hofmann *et al.* proposed to combine atlas-based registration and Gaussian regression processing based on local similarities to increase the robustness to local miss-registration and derive more accurate patient-specific brain attenuation maps [21]. Quantitative analysis demonstrated that their proposed approach reduces the errors to less than 3% on average.

Burgos *et al.* proposed a pseudo-CT synthesization method using multi-atlas registration and local weighting of aligned CT-MRI atlases using a local image similarity measure, such as local normalized cross-correlation (LNCC) [22]. Comparison with UTE segmentation-based AC using 42 brain datasets showed that this method results in a mean relative error of <1%, while the UTE-based approach resulted in a mean error of 12%. The authors recently improved and validated their method using two different PET radiotracers for brain imaging reporting a mean error of <2%. Recently, Izquierdo-Garcia *et al.* improved atlas registration through segmentation of the target MR images into 6 distinct regions (using statistical parametric mapping software) followed by its registration to a CT/MRI atlas space [23]. For the atlas dataset, a CT template is calculated by averaging the co-registered CT images. A pseudo-CT is then generated by inverse transformation of the template CT images into the patient's space. Quantitative evaluation using 15 patients revealed that this method results in a mean error of <4%.

Emission-based AC methods have also been recently revisited exploiting time-of-flight (TOF) PET/MRI and PET/CT imaging [24]. In this so-called maximum likelihood reconstruction of activity and attenuation (MLAA) approach [25], the attenuation and PET activity maps are simultaneously estimated from TOF emission data. These AC methods are particularly promising for deriving patient-specific attenuation maps. Salomon *et al.* proposed to constrain the estimation of attenuation coefficients over many anatomical regions obtained from MR images, thereby improving the robustness of the MLAA algorithm. However, theoretical and experimental studies showed that the attenuation maps can be estimated from emission data up to a scaling factor [26, 27]. Mehranian and Zaidi improved the estimation of attenuation maps using a Gaussian mixture model (GMM) constrained by spatial MR and statistical CT information [28]. The quantitative analysis using clinical whole-body studies showed that the proposed MLAA-AC method resulted in –10.2% quantification error in bony structures compared to –18.4% induced by the 4-class MRAC method. For a more detailed survey of the strategies devised to address the challenges of AC in PET/MRI, interested readers are referred to recent reviews on the topic [29, 30].

There is growing evidence emphasizing the need to develop advanced AC methods enabling to include or predict bones in MR-guided derivation of attenuation maps, particularly for neurological studies. In this work, we compare the performance of segmentation-, atlas-registration- and emission-based attenuation correction methods using clinical brain PET/MRI studies to shed the light on the limitations and potential of the latter two methods in the prediction of bones. To the best of our knowledge, this is the first clinical study in which atlas registration-based and emission-based AC methods are juxtaposed and compared with each other. UTE-based AC methods were not included, since their performance has been compared with atlas-based AC methods elsewhere [22]. We emphasize on the PET quantitative performance of various AC methods with respect to the reference CT-based AC (CTAC)-PET using region and voxel-wise analyses.

II. Material and methods

II.A. PET/CT and MRI data acquisition

PET/CT and MRI brain datasets of 14 patients (64.6 ± 11.7 yrs) from Geneva University Hospital were retrospectively employed for the quantitative evaluation of the three generic MRI-guided attenuation correction methods, namely, the 3-class-AC, atlas-AC and MLAA-AC. The clinical indication of the studies was dementia (70%), epilepsy (25%) and grading of brain tumours (5%). As a first-line diagnostic step, the patients underwent an MRI scan on a 3T Siemens MAGNETOM Skyra scanner (Siemens Healthcare, Erlangen, Germany) with a 64 channel head coil. The MRI scans included a 3D T1-weighted magnetization-prepared rapid gradient-echo, MP-RAGE (TE/TR/TI, 2.3 ms/1900 ms/970 ms, flip angle 8º; NEX = 1, voxel size 0.8 × 0.8 × 0.8 mm^3) and a 2D T2-weighted turbo spin-echo, TSE (TE/TR, 100 ms/6200 ms, NEX = 2; voxel size 0.4 × 0.4 × 4 mm^3). In the next step, the patients underwent an ^{18}F-FDG PET/CT scan on the Biograph mCT scanner (Siemens Healthcare, Erlangen, Germany). The data were acquired for 20 minutes after injection of 210.2 ± 13.9 MBq ^{18}F-FDG. A brain CTAC scan was performed for PET attenuation correction using the following parameters: 120 kVp, 20 mAs, 0.3 sec. rotation speed, voxel size 0.9 × 0.9 × 2.5 mm^3.

II.B. Attenuation map generation

To generate the MRI-guided attenuation maps, T1- and T2-weighted MR images of each patient were non-rigidly registered to corresponding CTAC-PET images using the Hermes multimodality brain registration

software (Hermes medical solutions AB, Sweden). The field-of-view (FOV) and voxel size of the resulting MR images were then matched with CT images using the Elastix registration tool [31]. As described in the following sub-sections, the registered MR images were used for generation of segmentation-based MRAC map and to guide atlas-based and emission-based attenuation prediction.

1) CT-based and segmentation-based 3-class MRAC maps

For quantitative comparison of the MRI-guided AC methods against a reference AC method, CT-based attenuation maps were generated for each patient using Siemens e7 tools. CT Hounsfield units were converted to 511-keV attenuation coefficients using a kVp-dependent bilinear mapping approach [32]. The 512 × 512 attenuation maps are then matched with the FOV of PET and downsized to a resolution of 400 × 400. Finally, they were smoothed to the resolution of PET images using an isotropic Gaussian filter (4 mm full-width at half-maximum).

In neurological PET/MRI studies, brain MR images are typically segmented into 3 tissue classes: soft-tissue, fat and background, and if possible internal, air tissue classes. In this retrospective study, MR images have not been acquired for attenuation correction using the conventional Dixon fat and water sequence but rather for diagnostic purpose using high-resolution T1 MP-RAGE and T2 TSE sequence. Since adipose tissues have short T1 relaxation times, the fat tissue class existing in the scalp and neck area was segmented from T1-weighted images using a heuristically defined threshold. The outside air background was obtained from the reference CTAC images in order to minimize the errors induced by mis-registration between MRI and PET/CT datasets. The soft-tissue class was then defined as the complement of fat and outside air tissue classes. By this procedure, all bones and internal air cavities and metal-induced susceptibility artefacts were ignored and classified as soft-tissue. Mean linear attenuation coefficients of 0, 0.864 and 0.0975 cm^{-1} were assigned to the background, fat and soft-tissue classes, respectively. The resulting attenuation maps were downsized to the resolution of CTAC maps and the corresponding CT bed attenuation map added.

2) Atlas-based AC

The atlas database was constructed using pairs of T1-weighted MR and CT brain images. In the first step, MR images were denoised using gradient anisotropic diffusion filtering following intra-patient intensity inhomogeneity correction utilizing N4 bias correction [33]. Then, inter-patient intensity non-uniformity was addressed using histogram matching. As shown in Figure 1, all MRIs in the atlas database are then registered to the target MR image. This inter-subject coordinate mapping was obtained using a combination of rigid registration based on normalized mutual information and non-rigid registration as described previously [34]. All the CT images in the atlas database were then mapped to the target MR image using the same transformation that maps the subject's corresponding MR image to the target subject. By these registration and mapping processes, a series of MRI/CT pairs aligned to the MRI of the target subject is obtained.

Given a series of MRI/CT pairs, each aligned CT can be considered as a pseudo-CT candidate of the target subject. In order to improve the quality of resulting pseudo-CTs, the proposed atlas fusion framework consists of two consecutive steps. In the first step, the atlas fusion is locally optimized based on the accuracy of bone identification and then the atlases are locally weighted and fused based on their morphological similarity to the target MR image and accuracy of bone estimation. To do so, we use M_n to denote aligned training MR images with the corresponding bone label maps L_n obtained from simple thresholding of aligned CT images using a value of 140 Hounsfield units (HUs). We assume the label maps take a discrete value of 1 for bony regions and 0 elsewhere. The goal of the first step is to estimate the bone label map ($\hat{B}$) associated with the target MR image (T). This can be achieved via maximum-a-posteriori (MAP) estimation:

$$\begin{aligned} \hat{B} &= arg\max_L p(L|T;\{M_n, L_n\}) \\ &= arg\max_L p(L, T;\{M_n, L_n\}) \end{aligned} \quad (1)$$

The second term denotes the joint probability of the label map and image intensity given the training data, where n is the index of training subjects in the atlas dataset. In the following, we make the assumption that the image intensity values $M_n(x)$ and labels $L_n(x)$ at each voxel (x) are conditionally independent, which leads to the following formulation:

$$\hat{B}(x) = arg\max_L \sum_{n=1}^{N} p_n\big(T(x); M_n(x)\big)\, p_n\big(B(x); L_n(x)\big) \quad (2)$$

where N is the number of subjects in the atlas dataset. Here we call the first term in equation (2) $p_n\big(T(x); M_n(x)\big)$ image morphology likelihood and the second term $p_n\big(B(x); L_n(x)\big)$ label prior. The main objective in defining image morphology likelihood is to assign higher weights to similar atlases in such a way that the similarity measurement is robust to intensity variation across patients and features must represent information about the structures in the image. Phase congruency map (PCM) has been shown to be a robust image feature [35]. In PCM, the local Fourier components of the image are all in phase (congruent) in locations where there are meaningful edges in the image. A PCM can be used to detect structural characteristics of an image in a way that is invariant to image intensity and robust to noise [35]. Equation (3) calculates the phase congruency of an image at location x where $En_{loc}(x)$ represents the local energy of the image, Tr is an offset to avert the effect of noise on the calculation of the local energy, F_m indicates the amplitude of the m^{th} Fourier component, and ϵ is a small value used as a trick to avoid division by zero [35, 36].

$$PCM(x) = \frac{\lfloor En_{loc}(x) - Tr \rfloor}{\sum_m F_m(x) + \varepsilon} \tag{3}$$

We adopt a Gaussian distribution with a stationary variance σ^2 as the image morphology likelihood term based on phase congruency of target and atlas MR images as:

$$p_n(T(x); M_n(x)) = \frac{1}{\sqrt{2\pi\sigma^2}} exp\left[-\frac{1}{2\sigma^2}\big(PCM\big(T(x)\big) - PCM(M_n(x))\big)^2\right] \tag{4}$$

Moreover, we define the label prior term $p_n(B(x); L_n(x))$ based on the signed distance transform from the bone label map (L_n) in the atlas data set which is assumed to be positive inside the bony structures.

$$p_n(B(x); L_n(x)) = \frac{1}{Nr(x)} exp(\rho D_n(x)) \tag{5}$$

where $D_n(x)$ denotes the signed distance transform of the bone label map in training subject n, $\rho > 0$ is the slope constant, and $Nr(x)$ is the partition function.

By inserting the image morphology likelihood (Eq. 4) and label prior (Eq. 5) terms in Eq. (2), the optimization problem can be solved for each voxel independently. The fused label of each voxel is computed via a local weighted voting strategy. The local image morphology likelihood terms serve as weights and the label prior values serve as votes. Therefore, at each voxel, training images that are more similar to the target image at this voxel after registration are given higher weighted. The output of this step ($\hat{B}$) is the most likely bone segmentaion of the target MR image. In the next step, this bone segmentation is used to assess the performance and define weighting factors for each of the aligned atlas images. The atlas fusion is achieved using equation (6) where $ACT_n(x)$ is the CT value of the n^{th} atlas image at voxel x (Figure 1).

$$PCT(x) = \frac{\sum_{n=1}^{N} \omega_n(x) \times ACT_n(x)}{\sum_{n=1}^{N} \omega_n(x)} \tag{6}$$

Where $\omega_n(x)$ is the weighting factor determining the contribution of the n^{th} atlas at voxel x to generate the final pseudo-CT (PCT) which is defined as:

$$\begin{aligned} \omega_n(x) = \frac{1}{\sqrt{2\pi\alpha^2}} exp\left[-\frac{1}{2\alpha^2}\big(PCM\big(T(x)\big) - PCM(I_n(x))\big)^2\right] \\ \times \frac{1}{\sqrt{2\pi\delta^2}} exp\left[-\frac{1}{2\delta^2}(D_n(x)) - D_B(x))^2\right] \end{aligned} \tag{7}$$

Here D_B indicates the signed distance transform of the obtained bone label map of the target image ($\hat{B}$). The first term in Eq. (7) measures the morphological similarity between the n^{th} MRI atlas and target MR image while the second term assesses the performance of the n^{th} CT atlas image with respect to the estimated bone segmentation of the target MR image ($\hat{B}$). The two Gaussian distributions are adjusted using stationary variances α^2 and δ^2. The free parameters in the above equation were optimized via leave-one-out cross-validation (LOOCV) and parameter sweeping.

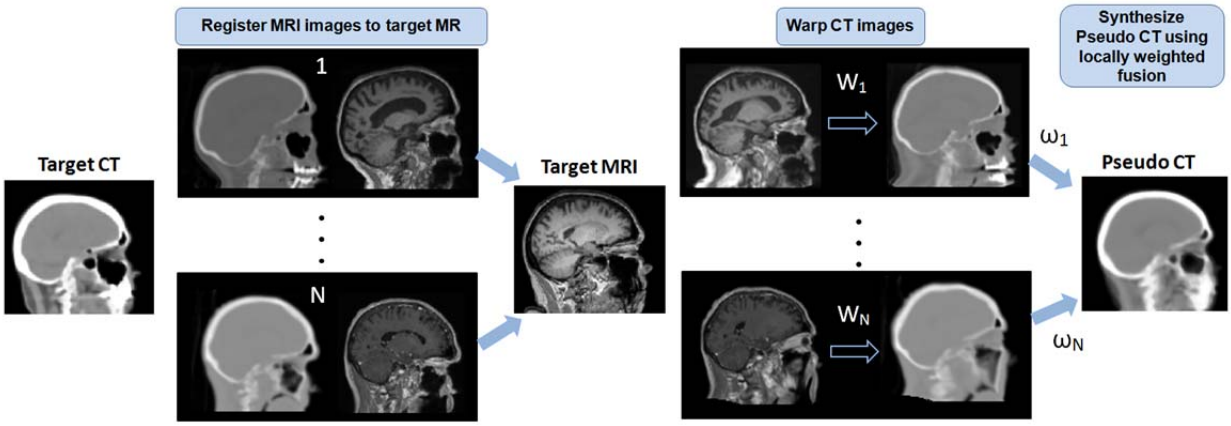

Figure 1. Flowchart of the multi-atlas registration AC method employed in this work. First, all MR images of the atlas dataset are non-rigidly registered one-by-one to the target MR image. Then, their corresponding CT images are wrapped with the same transformation to the target MRI space. Finally, the pseudo-CT is synthesized by local weighting of the wrapped CT images.

3) Emission-based AC

In this work, we employed our recently developed MLAA algorithm to estimate the attenuation map from TOF PET data of the mCT scanner [37]. Figure 2 shows the flowchart of the proposed MLAA-GMM algorithm where the activity and attenuation maps are alternatively reconstructed from emission data using a TOF ordinary Poisson ordered subset expectation maximization (OSEM) algorithm and a non-TOF ordered subset maximum likelihood for transmission tomography (OS-MLTR) algorithm. In the OS-MLTR step, two types of priors are imposed on the estimation of attenuation in order to regularize the solution space and therefore address some of the challenges associated with the original MLAA algorithm. To reduce noise in the attenuation estimates, a Markov random field smoothness prior with a quadratic potential function is employed. This prior favours attenuation maps that are smooth based on the weighted local differences between voxels in a neighbourhood. To suppress cross-talk artefacts resulting from the propagation of activity features into attenuation maps and vice versa, and more importantly the scaling issue of the MLAA algorithm, a constrained Gaussian mixture model is used. The GMM prior favours an attenuation map whose statistical distribution follows a distribution parameterized over a patient population. This model is based on the observation that the distribution (histogram) of linear attenuation coefficients of 511-keV attenuation maps can be modelled as a mixture of known Gaussian functions with means, standard deviations and mixture proportions calculated from a large number of typical CT datasets.

Since MRI data provide additional tissue type information, the GMM was spatially unmixed using a tissue prior map obtained from T1- and T2-weighted MRI images. This map indicates the membership of the attenuation voxels to three known tissue classes, namely, soft-tissue, fat and background air, and an unknown tissue class that contains bones, internal air and susceptibility artefacts. For voxels belonging to the known tissue classes, single Gaussians with the known means and standard deviations corresponding to each tissue are employed, while for voxels in the unknown tissue class a mixture of Gaussians is used. The constrained prior penalizes large deviations of attenuation estimation from their expected values (mean LACs) in each tissue class, especially soft-tissue and therefore substantially suppresses noise, cross-talk artefacts and the unknown scaling of the attenuation maps. Fat and background air tissue classes of the tissue prior map were obtained in a similar way as the 3-class attenuation map described in section 2.2.1. The soft-tissue class was defined as the complement of fat, background air and unknown tissue classes. The unknown class corresponds to the regions that have low MR intensity due to short T2 relaxation time and low proton density such as bones and air cavities. We employed T2-weighted images as they complete the signal intensity of T1-weighted images over tissues showing low MR intensity due to low T1 relaxation time, such as the cerebrospinal fluid, ventricles and eyes. This enables to correctly include them into the soft-tissue class. The unknown tissue class was therefore obtained by segmentation of superimposed T1- and T2-weighted images (which in fact resemble proton-density weighted MR images) using a heuristically-adjusted thresholding technique.

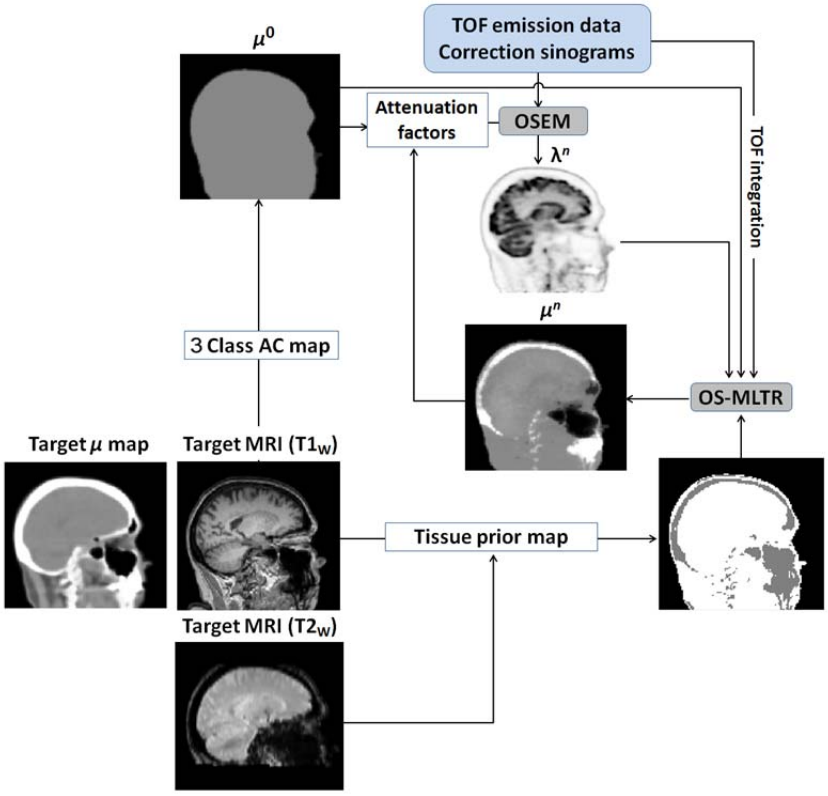

Figure 2. Flowchart of the MLAA-AC algorithm used in this work. This algorithm alternates between an OSEM activity reconstruction and a constrained OS-MLTR transmission reconstruction. The attenuation estimation is guided by an MRI-derived tissue prior map. The algorithm is initialized by a 3-class MRAC attenuation map which is iteratively updated toward the final solution.

The proposed MLAA algorithm was implemented for image reconstruction in the native geometry of the mCT scanner. The PET component of the scanner consists of a total number of 32448 LSO crystals, each 4 × 4 × 20 mm^3 in dimension, accommodated in 4 rings of 48 detector blocks. Time-of-flight PET data were acquired using a coincidence window width of 4.06 ns with an effective TOF timing resolution of 580 ps and sorted into 13 TOF bins with a maximum ring difference of 49 planes. The algorithm was initialized using a uniform activity map and the 3-class attenuation map obtained from tissue classification of T1-weighted images. Scatter sinograms were obtained from TOF single-scatter simulation with the 3-class attenuation maps using the Siemens e7 tools. The activity and attenuation maps were reconstructed using 40 global iterations and 2 and 3 sub-iterations for activity and attenuation, respectively. The regularization parameters of the applied priors were experimentally optimized for 2 clinical studies and used for the rest of patients.

II.C. Image Reconstruction and Data Analysis

For each patient, 4 PET image reconstructions were performed using different attenuation maps, including reference CTAC, 3class-AC, MLAA-AC and atlas-AC. The image were reconstructed using Siemens VG50 e7 tool with an OP-OSEM algorithm with point spread function (PSF) modelling and TOF information with 3 iterations and 21 subsets. All data corrections (scatter, random, dead-time, decay, attenuation, and normalization) were included in the reconstruction procedure. The image matrix size is 400 × 400 × 109 with 2 × 2 × 2 mm^3 voxels.

The accuracy of bones delineation using MLAA-AC and atlas-AC methods was assessed based on bone extraction criteria including the Dice similarity coefficient (DSC), relative volume difference (RVD) and Jaccard similarity (JC) with respect to reference CTAC maps. For each patient, the above-mentioned metrics were calculated as follows:

$$DSC(A,M) = \frac{2|A \cap M|}{|A| + |M|} \tag{8}$$

$$RVD(A,M) = 100 \times \frac{|A| - |M|}{|M|} \tag{9}$$

$$JC(A,M) = \frac{|A \cap M|}{|A \cup M|} \tag{10}$$

where A and M are reference CT-derived and predicted bones, respectively.

The Hermes BRASS analysis tool (Hermes medical solutions AB, Sweden) was used for quantitative evaluation of brain PET data. The BRASS software wraps input PET images to the spatial coordinates of an ^{18}F-FDG PET template obtained by averaging PET images of 12 normal subjects. The tracer activity quantification is then performed over 63 distinct brain regions located in the left and right hemispheres. In this work, we merged left and right regions, thus reducing the total number of regions to 32. Supplemental figure 1 shows the region map used in our quantitative analysis. Quantification errors or bias with respect to reference CTAC PET images were calculated for each region and individual voxels according to the following equation:

$$B_i = \frac{(SUV_m)_i - (SUV_{CTAC})_i}{(SUV_{CTAC})_i} \tag{11}$$

where SUV stands for standardized uptake value of the tracer, i indicates region's label number or voxel number and m the method of attenuation correction. Since the PET images were registered to BRASS template's space, we further calculated the mean (m) and standard deviation (σ) of the bias across all 14 patients resulting in atlas bias maps according to the following equations [6]:

$$m_i = \frac{\sum_{P=1}^{N} B_i^p}{N}, \qquad \sigma_i = \sqrt{\frac{\sum_{P=1}^{N} \left(B_i^p - m_i\right)^2}{N-1}} \tag{12}$$

where B_i^p is the bias in voxel i for patient p according to Eq. (11). Note that the BRASS software employs a normalized mutual information criterion for robust registration of patient PET images to the PET template. The accuracy of the registration was qualitatively controlled based on the generated temple isocontour to minimize errors induced by miss-alignments.

The correlation between CTAC-PET uptake values and those produced by the studied attenuation correction methods were determined on scatter plots for each of the 32 regions using Pearson correlation analysis. Bland-Altman plots were also used to calculate the concordance between the SUVs and determine the systematic bias introduced by the AC methods. The statistical differences in quantitative performance of the AC methods were calculated using the paired-sample t-test. The differences were considered statistically significant for a p-value less than 0.05.

III. Results

Figure 3 shows the reference CTAC and T1-weighted MR images of two representative patients and compares patient-specific attenuation maps obtained by conventional segmentation-based, emission-based and atlas registration-based AC methods. For these patients, the tissue prior maps calculated to implement the MLAA-AC method are also shown. The unknown tissue classes, corresponding to MRI voxels with low intensity, are displayed in white colour, while known soft and fat tissue classes are displayed in gray. As shown, the MLAA-AC algorithm can reliably differentiate air cavities from bone/soft-tissues residing in unknown tissue classes. However, this algorithm fails to completely and homogenously estimate bony structures, especially in the temporoparietal regions of the skull. The visual inspection of atlas-AC maps reveals that the atlas-registration method predicts bones more accurately over all regions of the skull compared to the MLAA-AC method. However, it cannot predict well the air cavity's shape, especially in the top-panel patient dataset. The accuracy of bone extraction using these algorithms was objectively evaluated based on metrics defined in Eqs. (8-10). Table 1 summarizes the mean and standard deviation of DCS, RVD and JC metrics calculated for all 14 clinical studies. Consistent with the qualitative results (figure 3), the quantitative analysis demonstrates that the atlas-AC method outperforms the MLAA-AC method in terms of deriving bones, particularly reflected by an increase of the mean DSC value from 0.79 to 0.92. The atlas-AC algorithm also improves both RVD and JC metrics as indicators to detect failed segmentation. Figure 4 compares the mean of bone attenuation values of the various attenuation maps per patient. It can be observed that the mean LAC values predicted by the atlas-AC method are

generally very close to CTAC reference values, while those predicted by the MLAA-AC method are substantially underestimated. The results show that the means and standard deviations of bone LACs in CTAC, atlas-AC, MLAA-AC and 3-class MRAC maps are, on average, 0.138 ± 0.012, 0.134 ± 0.02, 0.107 ± 0.014, 0.097 ± 0.005 cm^{-1}, respectively. The mean ± SD of bone LACs for individual patients are provided in supplemental Table 1. Note that the attenuation maps were smoothed using an isotropic 4 mm Gaussian filter, therefore the bone LACs of 3-class AC method show some variations.

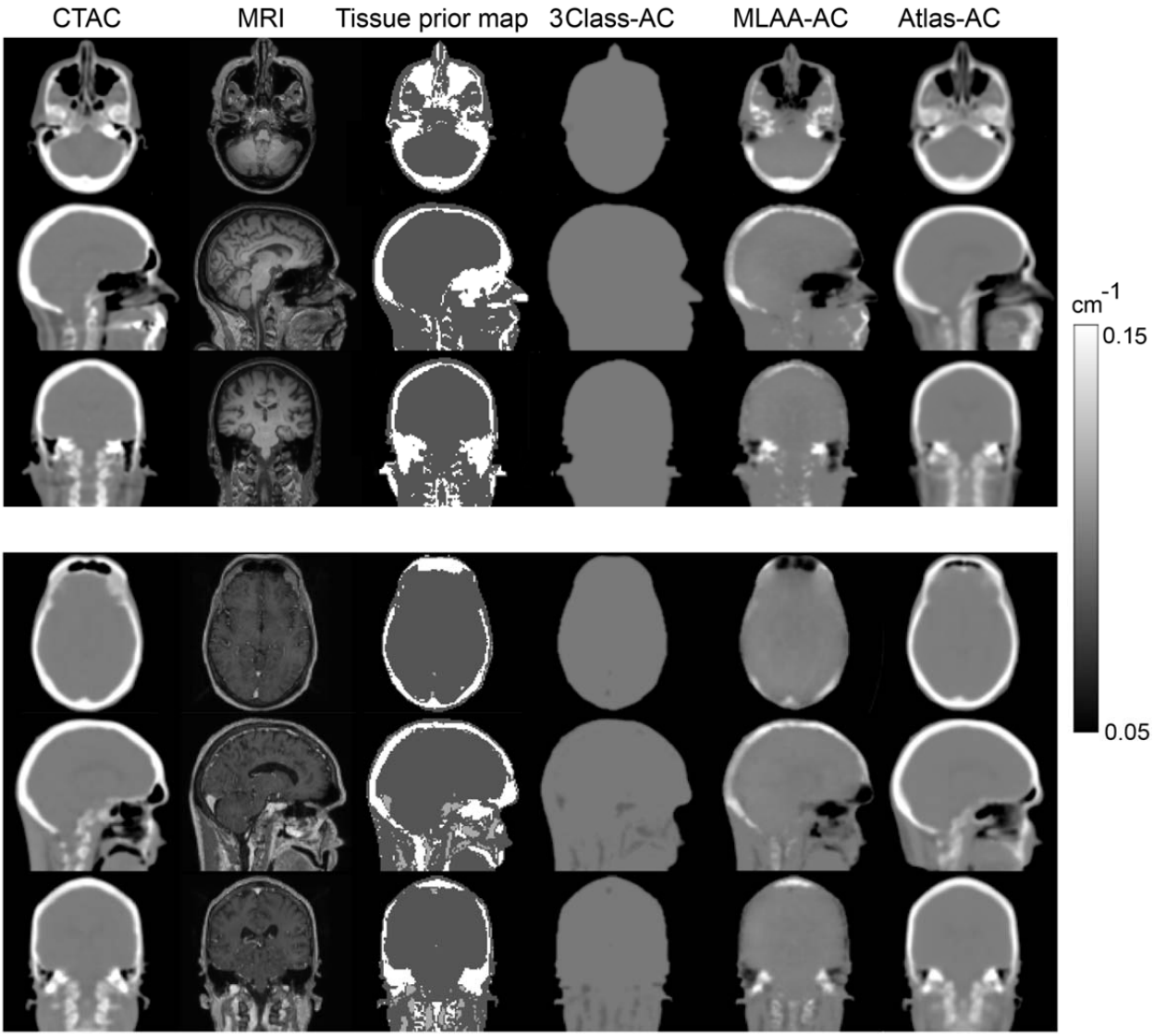

Figure 3. Comparison of the attenuation maps for two representative patients generated by the different attenuation correction techniques together with the reference CTAC map, the target MRI image and MR-based tissue prior map used for the MLAA algorithm.

Table 1. Quantitative accuracy of the estimated bone tissues by the MLAA-AC and atlas-AC methods over 14 patients (mean ± standard deviation).

Methods	DSC	RVD(%)	JC
MLAA-AC	0.79 ± 0.02	–15.6 ± 2.8	0.64 ± 0.03
Atlas-AC	0.92 ± 0.02	–9.0 ± 2.1	0.85 ± 0.03

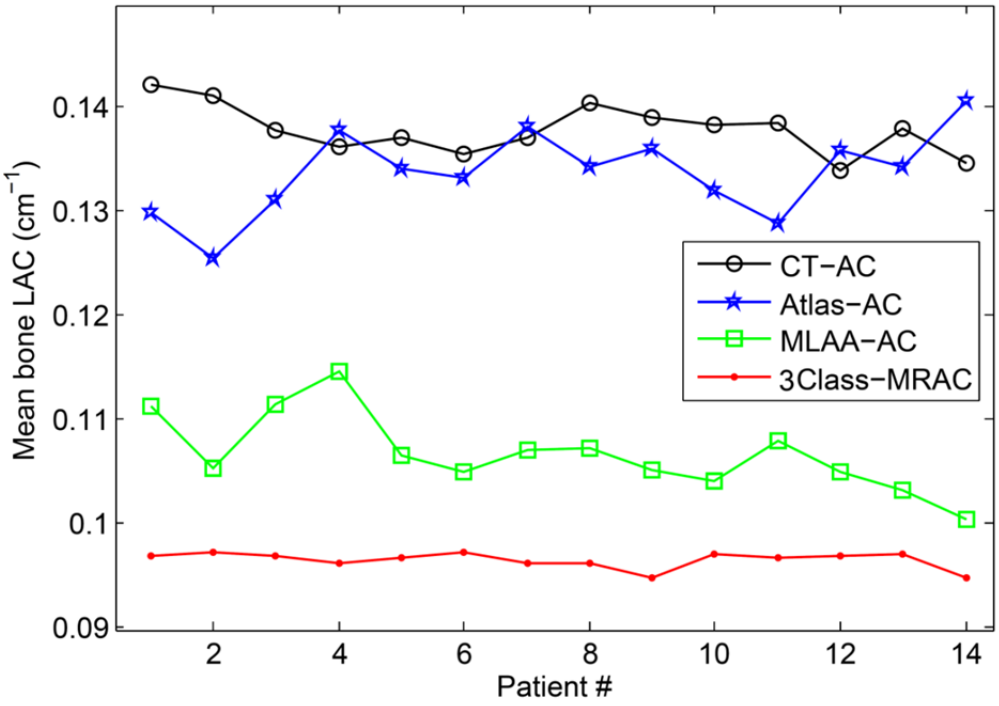

Figure 4. Mean bone linear attenuation coefficients calculated for each patient for different attenuation correction methods.

Table 2. Percentage (%) of PET quantification errors for the different AC methods in 32 regions of the brain with respect to the reference CTAC-PET data.

Region	**3-Class-AC**	**MLAA-AC**	**Atlas-AC**
Cerebellum	–18.0 ± 3.5	–14.2 ± 3.1	–0.3 ± 5.4
G.frontalis superior	–17.9 ± 2.7	–14.2 ± 2.8	1.0 ± 3.1
G.frontalis medius	–17.3 ± 2.3	–14.3 ± 2.3	1.4 ± 2.6
G.frontalis inferior	–15.4 ± 1.9	–12.7 ± 2.1	1.1 ± 2.7
G.front.sup.pars med.	–16.2 ± 2.2	–13.0 ± 2.2	1.2 ± 2.3
G.precentralis	–17.6 ± 2.3	–14.4 ± 2.1	1.1 ± 2.6
Lobulus paracentralis	–11.1 ± 6.6	–10.0 ± 6.6	2.1 ± 4.4
G.rectus	–12.4 ± 4.8	–9.7 ± 5.0	0.6 ± 4.9
G.orbitalis	–16.0 ± 2.2	–13.5 ± 2.9	0.7 ± 2.5
G.temporalis superior	–15.6 ± 2.7	–12.0 ± 2.4	0.8 ± 3.0
G.temporalis medius	–15.8 ± 2.4	–12.8 ± 1.9	0.9 ± 2.9
G.temporalis inferior	–16.5 ± 3.0	–13.7 ± 2.6	0.7 ± 4.4
G.postcentralis	–17.1 ± 2.6	–13.9 ± 2.3	1.9 ± 2.9
Lobulus par.inf.	–17.3 ± 2.6	–14.8 ± 2.6	1.4 ± 2.9
G.supramarginalis	–18.6 ± 2.6	–16.0 ± 2.2	1.1 ± 2.8
G.angularis	–18.8 ± 2.7	–15.8 ± 2.3	0.9 ± 2.9
Lobulus par.sup.	–17.5 ± 4.1	–14.4 ± 3.5	1.0 ± 2.7
G.occipitalis sup.	–19.4 ± 2.8	–15.8 ± 2.1	0.9 ± 2.7
G.occipitalis medius	–19.5 ± 3.0	–15.7 ± 2.1	0.9 ± 3.0
G.occipitalis inf.	–18.2 ± 4.5	–13.8 ± 3.6	0.9 ± 6.2
Cuneus	–16.2 ± 3.2	–13.2 ± 2.7	1.3 ± 2.8
Precuneus	–16.5 ± 2.7	–13.3 ± 2.2	1.2 ± 2.5
Uncus	–13.5 ± 3.7	–12.2 ± 3.7	1.2 ± 6.4
Hippocampus	–15.2 ± 2.9	–12.7 ± 3.0	0.6 ± 3.6
G.occipitotemp. lat.	–15.8 ± 2.4	–12.0 ± 1.9	0.4 ± 3.6
G.occipitotemp. med.	–16.0 ± 3.3	–11.7 ± 2.6	0.8 ± 3.2
G.cinguli	–15.2 ± 2.2	–12.2 ± 2.0	1.6 ± 2.3
Thalamus	–14.8 ± 3.4	–13.0 ± 3.4	0.9 ± 2.7
Putamen	–14.1 ± 1.9	–11.7 ± 2.4	1.0 ± 2.7
Caput nuclei caudati	–15.5 ± 3.9	–13.3 ± 4.1	1.4 ± 4.2
Brain stem	–14.6 ± 4.1	–12.9 ± 4.1	0.7 ± 4.9
Insula	–13.5 ± 2.6	–10.7 ± 2.5	1.5 ± 2.5
Total	–16.2 ± 3.6	–13.3 ± 3.3	1.0 ± 3.4

The quantitative performance of the different AC methods was further evaluated in comparison with the CTAC method using region-based analysis of PET images warped to fit with the BRASS template space. Table 2 summarizes the mean and SD of quantification errors (bias) induced by the 3-class AC, MLAA-AC and atlas-AC methods in 32 regions of the brain over all patients. Figure 5 illustrates the mean of the bias for each region and AC method. The results clearly demonstrate that the atlas-AC method results in a mean positive error <2%, while the 3-class AC and MLAA-AC methods both show high negative errors and thus tracer underestimation over all regions in the brain. It was found that the 3-class AC, MLAA-AC and atlas-AC methods result, on average, in a total bias of -16.2 ± 3.6%, -13.3 ± 3.3% and 1.0 ± 3.4%, respectively. This magnitude of the bias could be predicted from the mean of the bone LACs shown in figure 4, where both 3-class- and MLAA-AC methods underestimate the bone attenuation coefficients, which is of prime importance in brain PET quantification. As reported in [8], the activity concentration in brain regions close to the skull such as occipital gyri and cerebellum is more underestimated by the 3-class AC method.

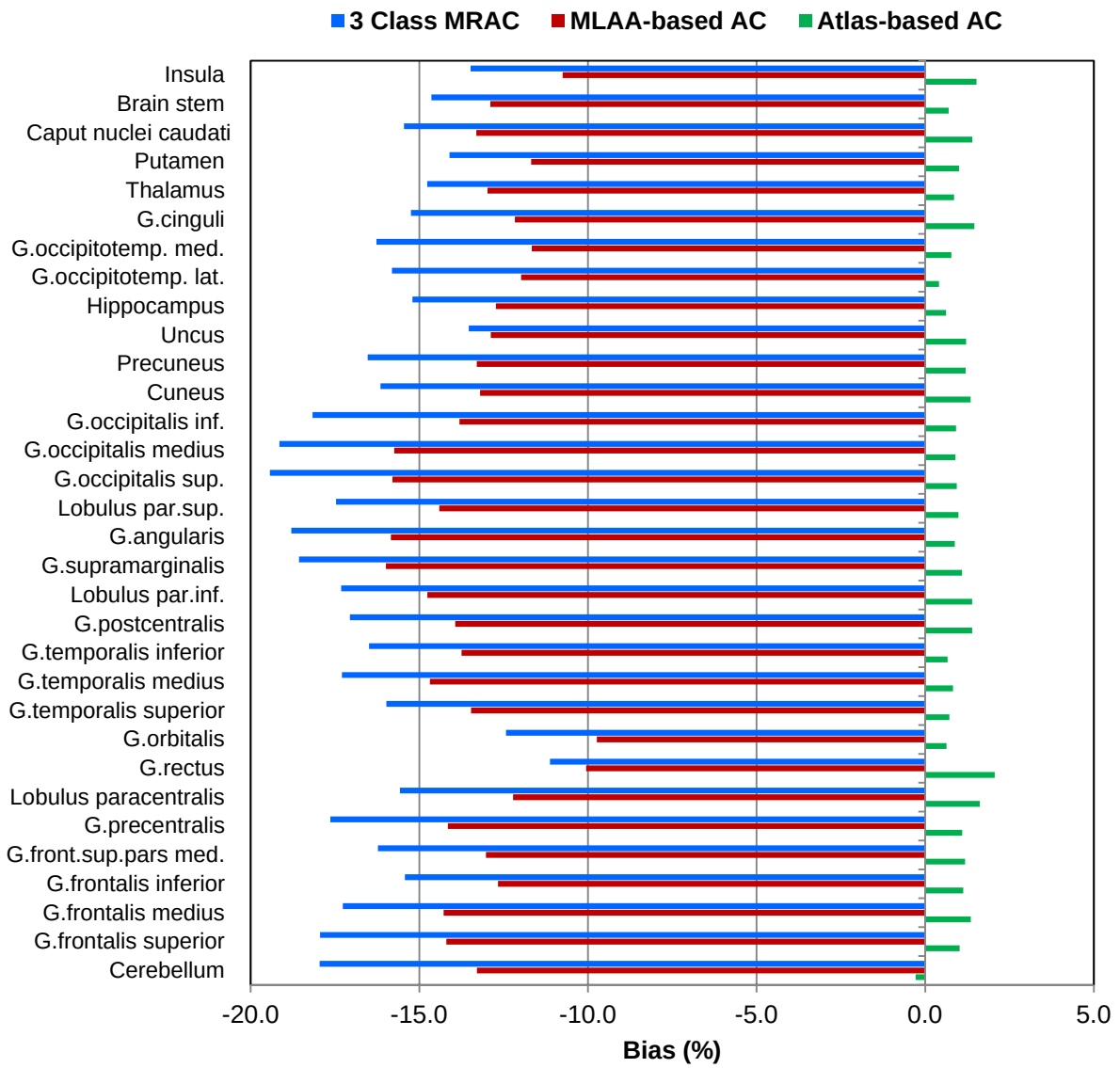

Figure 5. Mean of the PET quantification errors in 32 brain regions calculated over all patients for the different AC methods with respect to reference CTAC.

Figure 6 shows the voxel-wise mean and standard deviation of an atlas bias map calculated for all patients according to Eq. (12). It represents the magnitude and spatial distribution of quantification errors among the studied datasets in axial and sagittal views. The results further support the outperformance of the atlas-AC

method by reducing the mean errors especially in or close to bones. However, as also shown in figure 5, this AC method resulted in a slight over-estimation of the tracer concentration in all regions. It can be seen that the MLAA-AC method has slightly improved performance compared to the 3-class AC method. The statistical analysis showed that there is significant difference between the performance of the MLAA-AC and 3-class AC methods over most brain regions, except a few regions far from bones such as the precuneus and gyrus rectus ($p < 0.001$). Similar evaluation between the performance of atlas-AC and the other two methods showed a statistically significant difference. Figure 7 shows linear regression plots illustrating the correlation between the tracer uptake of the different AC methods and the reference CTAC method. The results show that the atlas-AC PET uptake values are highly correlated to CTAC PET values over all 32 brain regions ($R^2 = 0.99$). The scatter plots of the 3-class AC and MLAA-AC PET images show reduced R^2 correlation coefficients of 0.98 and 0.985 and tend to underestimate the uptake values since the slope of the regression line is less than 1.

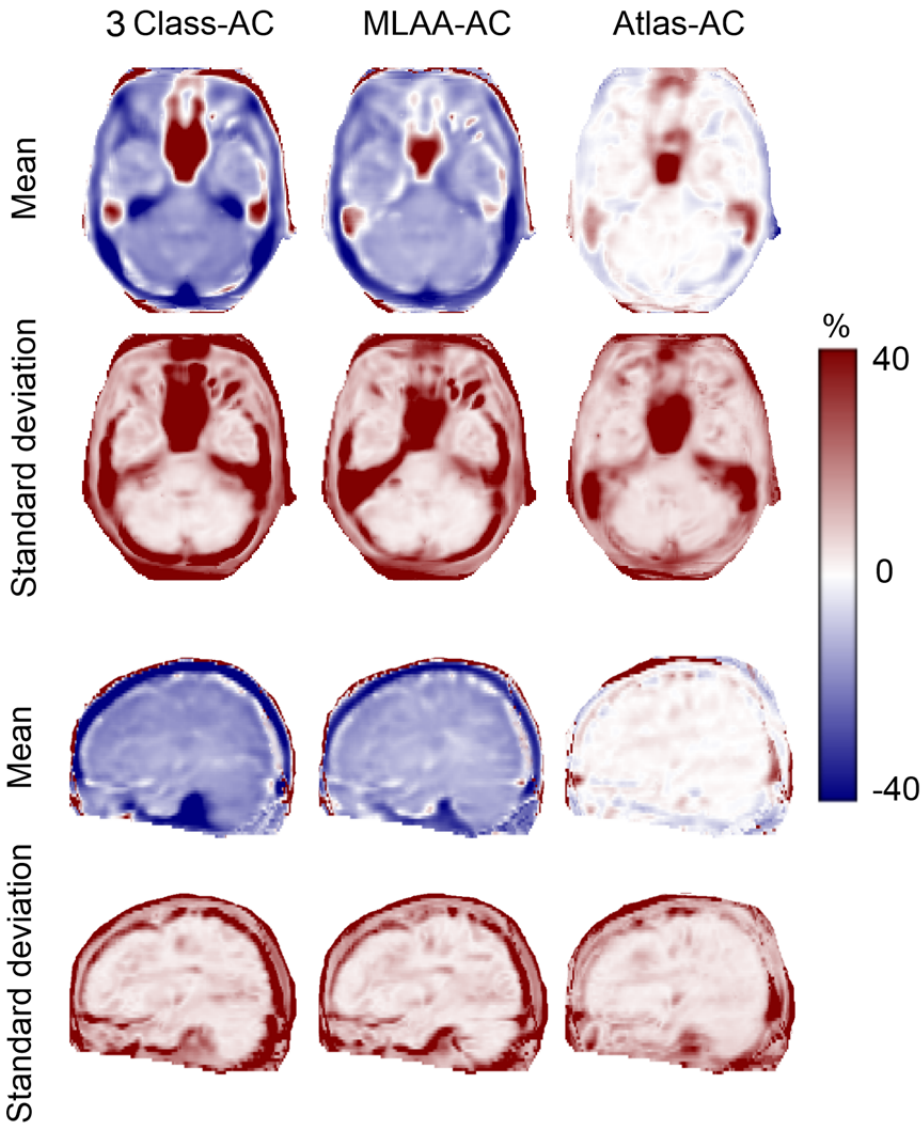

Figure 6. Mean and standard deviation of atlas bias maps calculated over all patients for the different attenuation correction methods displayed in transaxial and coronnal planes.

Figure 8 shows the results of Bland-Altman concordance analysis. As can be seen, both 3-class and MLAA-AC methods give rise to a high systematic bias in tracer uptake quantification compared to the atlas-AC method. The mean-difference horizontal lines indicating the estimated bias, however, show that the atlas-AC method results in a slight overestimation, as also reflected in pervious results.

IV. Discussion

Accurate MRI-guided attenuation correction in PET/MRI has been a major challenge since the introduction of this clinical hybrid imaging technology [38]. Since then, a number of strategies have been proposed to derive patient-specific attenuation maps either from MR images and PET emission data or co-registered MR/CT datasets. The development of novel AC methods enabling particularly to account for bone attenuation is of importance in PET brain imaging since a large proportion of cortical bone is accommodated in the skull [18]. To provide a clear picture of the performance and cost-effectiveness of these AC methods, we compared the quantitative performance of the standard segmentation-based and state-of-the-art emission- and atlas registration-based AC methods in brain PET/MR imaging.

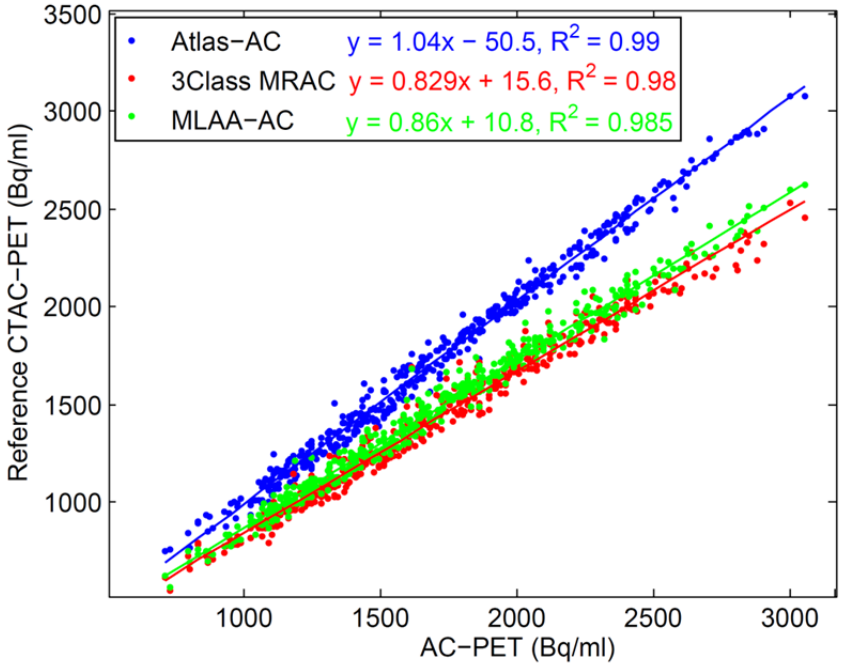

Figure 7. Scatter and linear regression plots between the tracer uptake in PET images reconstructed using reference CTAC maps and those reconstructed using the different AC maps.

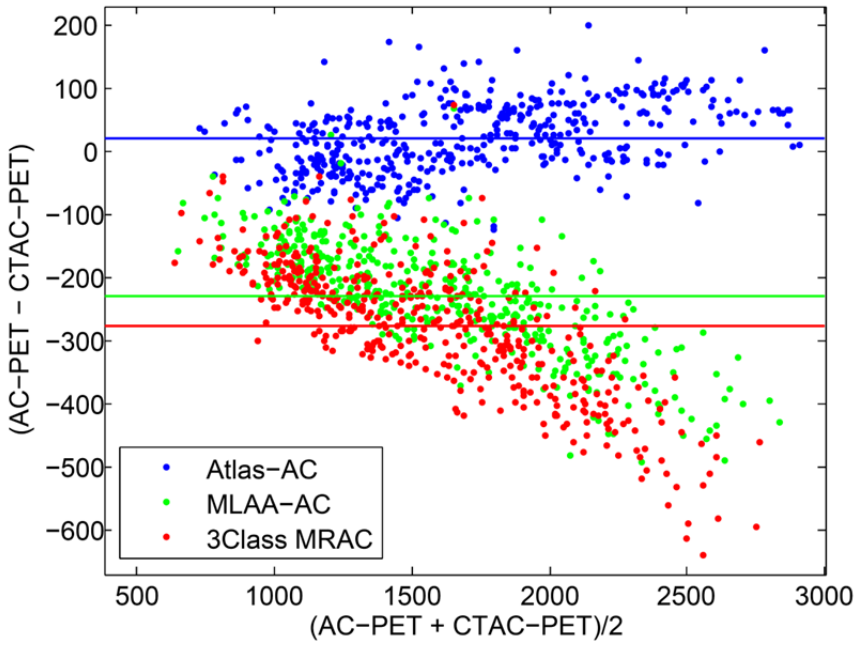

Figure 8. Bland–Altman concordance plots for PET data corrected for attenuation using reference CTAC, 3-class MRAC, MLAA-AC and atlas-AC methods.

The results demonstrate that the exclusion of the bones in 3-class AC methods results in a significant underestimation of tracer uptake, ranging from 13% to 19% in various regions of the brain. Consistent with our findings, Dickson *et al.* also reported underestimations in range of 10-21% using 25 clinical studies based on a similar regions-wise analysis using SPM templates [9]. More importantly, our results showed that in the cortical regions of the brain, such as the cerebellum and frontal gyri, the 3-class AC method results in about –19% bias (Table 1), while Dickson *et al.* reported–21% bias on average for these regions. These results among others reported in the literature [21, 23], clearly justify the need for more accurate AC methods that account for bones.

Atlas registration-based methods have therefore been proposed as a viable attenuation correction technique for the prediction of bones from a patient population. In this work, we evaluated the performance of a new multi-atlas registration AC method, which exploits a local weighting atlas fusion strategy. The results of this study showed that this algorithm reduces the bias to 1.0 ± 3.4%, on average, which is considered as an insignificant error from a clinical perspective. Izquierdo-Garcia *et al.* also reported that their atlas-registration method resulted in an error of 0.75 ± 1.6% using 16 subjects administered with ^{18}F-FDG and ^{18}F-FET radiotracers [23]. Likewise, Burgos *et al.* evaluated their improved atlas-AC method for attenuation correction of 22 patients who have undergone ^{18}F-FDG and ^{18}F-florbetapir scans [39]. The authors reported that their method resulted in relative mean errors of <0.6% for FDG and <0.1% for Florbetapir, on average, with a standard deviation of 1% for both tracers. This study demonstrated that this multi-atlas registration technique outperforms the single-atlas registration AC method proposed by Izquierdo-Garcia *et al*.

In spite of promising results, atlas-AC methods have some limitations as their performance depends strongly on the accuracy of the applied registration algorithm, especially in whole-body imaging. In brain PET/MRI, the registration errors are inherently lower than in whole-body imaging owing to the high morphological similarity of the brain among different subjects. In addition, the predictive performance of these algorithms depends considerably on how accurately the atlas dataset used for registration and training can represent the morphological variability and pathological abnormalities of the target subject. In other words, the representativeness of the atlas dataset is another key to the success and performance of this category of AC techniques. Due to the limited number of MRI/CT pair datasets in most studies proposing and evaluating atlas-registration based methods, a leave-one out cross-validation approach is used to generate a template or to train the predictive model. However, a limitation of these studies, including the present work, is that the performance assessment of the atlas-AC method on the same datasets used during LOOCV might obscure the actual predictive accuracy of these methods when using different datasets. Therefore, there is a high demand for large-scale evaluation of atlas-AC methods in the clinic. The initial promising results of this category of methods in brain PET/MRI has encouraged their adoption on state-of-the-art commercial systems, such as the GE SIGNA TOF PET/MRI scanner, providing an opportunity to validate their robustness and predictive accuracy over a large number of datasets. Recently, Yang *et al.* compared the performance of the standard atlas-AC method implemented on the commercial scanner with the conventional segmentation-based AC method using 20 clinical studies [40]. Their initial results demonstrated that the atlas-AC method reduces the average quantification error of the segmentation-based AC method in 8 regions of the brain to less than 5% (from 9.27 ± 2.91% to 4.11 ± 1.68%).

In this work, we evaluated the performance of the nascent emission-based AC methods in TOF PET/MRI brain imaging. We employed our previously proposed MLAA-AC algorithm which exploits MRI anatomical and CT statistical information to improve the performance of the original MLAA technique particularly in terms of quantification bias and cross-talk artefacts. Overall, the performance of the MLAA algorithm depends highly on the TOF timing resolution and biodistribution of the PET tracer. The TOF resolution is of particular importance in brain PET imaging. With the current TOF timing resolution (e.g. 580 ps on the Siemens mCT scanner used in this study), most of the detected counts are distributed in a small number of TOF bins. As the TOF resolution improves (e.g. <400 ps for the GE PET/MR scanner), the data are further separated in a larger number of TOF bins and therefore the ability of the MLAA algorithms to derive the attenuation experienced by emission data is improved. The results of this study indicate that emission-based methods present a high potential in terms of differentiating air from bone and metallic implants from soft-tissues. However, as shown in Figures 4 and 5, the MLAA-AC algorithm failed to completely estimate bone attenuation and thus to substantially improve the 3-class AC method. However, this category of approaches is in their infancy and still requires more research and development efforts.

In our initial evaluation of the proposed MLAA-AC algorithm with non-TOF brain PET data (not shown here), we noticed that this algorithm is not only incapable of increasing the value of voxels whose underlying LACs is bone but also reduces their initial soft-tissue values toward air or lung LACs. This can mainly be ascribed to the instability of the non-TOF version of the algorithm despite the precisely-defined MRI/CT constraints. Given that with the current nominal TOF timing resolution of 580 ps the TOF-MLAA algorithm showed promising trends, we expect a substantial improvement of this algorithm on future generation TOF PET/MRI scanners with improved TOF resolution. The performance of the applied MLAA algorithm in deriving bone is somewhat close to what is achieved by UTE-based algorithms since the accuracy of bone segmentation from UTE images is limited by the spatial resolution MR images, which in turn is conditioned by the data acquisition time. Some studies have shown that UTE-segmented bones are usually incomplete and underestimated. Therefore, PET quantification errors are not considerably reduced compared to conventional 3-class MRAC methods [9, 22]. For instance, Dickson *et al.* showed that UTE-based AC reduced the quantification errors in the brain from 17% (for the 3-class MRAC method) to 12%, on average. Our results follow the same trend since the errors of the 3-class AC method were reduced by the MLAA-AC method from about 16% to 13%. As mentioned above, the performance of emission-based AC methods also depends on the biodistribution and support provided by the PET tracer. In this work, we included ^{18}F-FDG PET studies which is the most widely used tracer for brain imaging in nuclear medicine departments. To demonstrate the influence of the tracer distribution, we analysed one ^{18}F-fluoro-ethyl-tyrosine (^{18}F-FET) scan. This tracer does not have significant uptake in normal brain tissue but presents with an uptake in the skin and neoplasms such as gliomas. Figure 8 compares the results of the MLAA-AC algorithm for an ^{18}F-FDG scan with those of a ^{18}F-FET scan. As can be seen, bone attenuation coefficients are more accurately estimated in the ^{18}F-FET study compared to the ^{18}F-FDG scan. These results are in agreement with our previous observations in brain imaging using ^{18}F-FCH [28]. Therefore, these observations call for further evaluation of emission-based AC methods with non-FDG tracers.

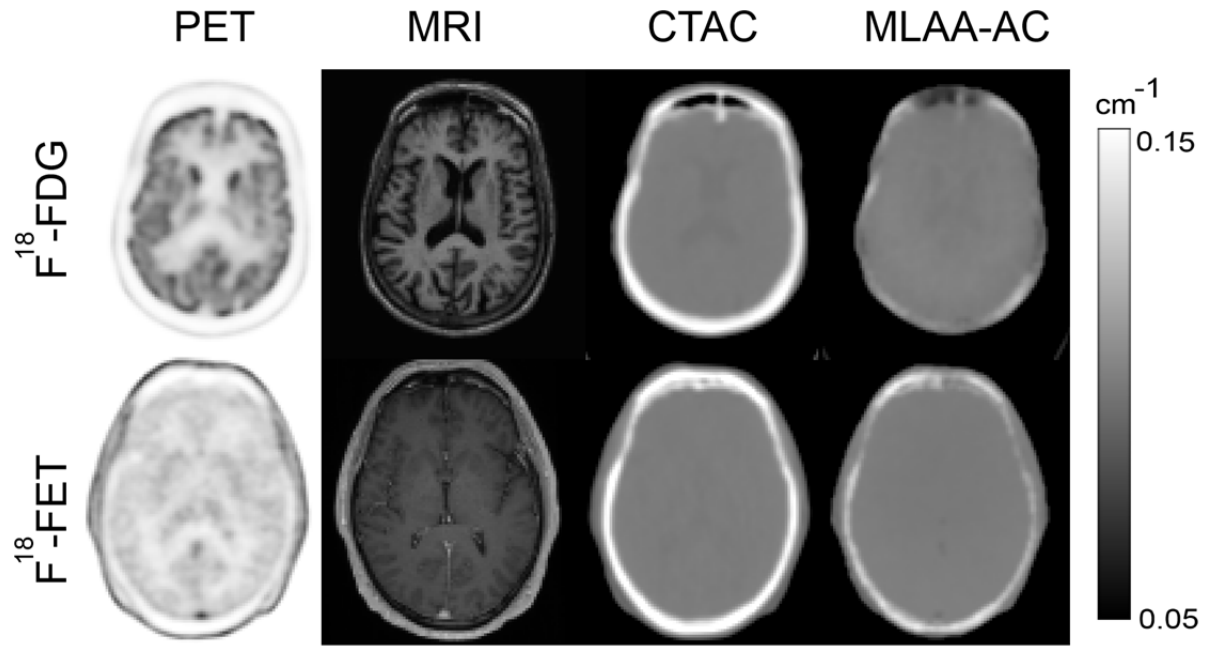

Figure 9. The impact of tracer distribution on the performance of the MLAA-AC algorithm. Note that this algorithm estimate more accurately the bone LACs from the ^{18}F-FET emission data.

One of the limitations of this study is the quantitative analysis of different attenuation correction techniques based on only the relative change of activity concentration (SUV) with respect to reference CTAC-PET data. In neurological studies, it is common practice to normalize PET images with respect to a reference region in the brain, such as the pons (located in brainstem) [41]. Therefore, in addition to SUV analysis, one can also evaluate the AC methods based on the resulting regional SUV (SUVr). In this work, we focused on SUV and absolute tracer quantification metrics, which are widely used in neuro-oncology. Furthermore, the MRI/CT datasets used

in this study are chosen out of a large patient population, where patients presenting with highly abnormal anatomy (i.e. due to craniectomy, traumatic brain injury and etc.) or with severe metallic artefacts in dental regions were excluded. Therefore, further investigation is required to scrutinize the performance of atlas- and MLAA-AC algorithms on subjects presenting with pathologies and abnormalities. It should however be noted that in the case of moderate dental metal-susceptibility artefacts, our results showed that both MLAA- and atlas-AC methods are able to reasonably recover high-valued LACs of dental fillings. For instance, the MRI/CT dataset used in Figures 1 and 2 showed moderate metal artefacts in both CT and MR images. As can be seen in these figures, both atlas- and MLAA-AC methods exquisitely estimated the metal's LAC values. The capability of atlas-AC methods should be attributed to the fact that the employed CT/MRI atlas dataset is representative of patients presenting with metal artefacts, since most of the CT images in this dataset were contaminated with metal artefacts. In contrast, the MLAA algorithm recognizes high-valued LACs purely based on the attenuation experienced by emission data along lines of response passing through the metallic objects. Another limitation of this study lies in the biased average age of the included patients toward the elderly (on average 65 years). Most of the patients referred to our institution suffer from dementia, which occurs frequently at advanced age. Therefore, it is also necessary to evaluate the AC algorithms for different age groups. In particular, the development of age-dependant MRI/CT atlas dataset is of paramount importance for atlas-based pseudo-CT generation in paediatric patients, whose body features different shape and anatomy compared to adults [42].

V. Conclusion

In the present study, the quantitative performance of three generic attenuation correction methods was evaluated in the context of brain TOF PET/MRI imaging. It was found that the segmentation-based AC method results in a signification underestimation of PET tracer uptake in both cortical and sub-cortical regions of the brain. Our recently developed MRI-guided emission-based AC method, which attempts to estimate bone attenuation values and differentiate them from air cavities, showed promising but limited success in reducing quantification errors. In contrast, the proposed atlas-AC method is capable of predicting more accurate patient-specific attenuation maps, thereby significantly reducing maximum regional quantification errors to about 2%. This work suggests the need for further development of the emission-based AC method for current TOF timing resolution of PET scanners using, for example, empirical functions that promote the derivation of bones. Further evaluation of atlas-registration AC methods using a large clinical database, which includes patients from different age groups with different pathological indications is guaranteed.

Acknowledgements

This work was supported by the Swiss National Science Foundation under Grant SNSF 31003A-149957 and the Indo-Swiss Joint Research Programme ISJRP-138866.

Supplementary material

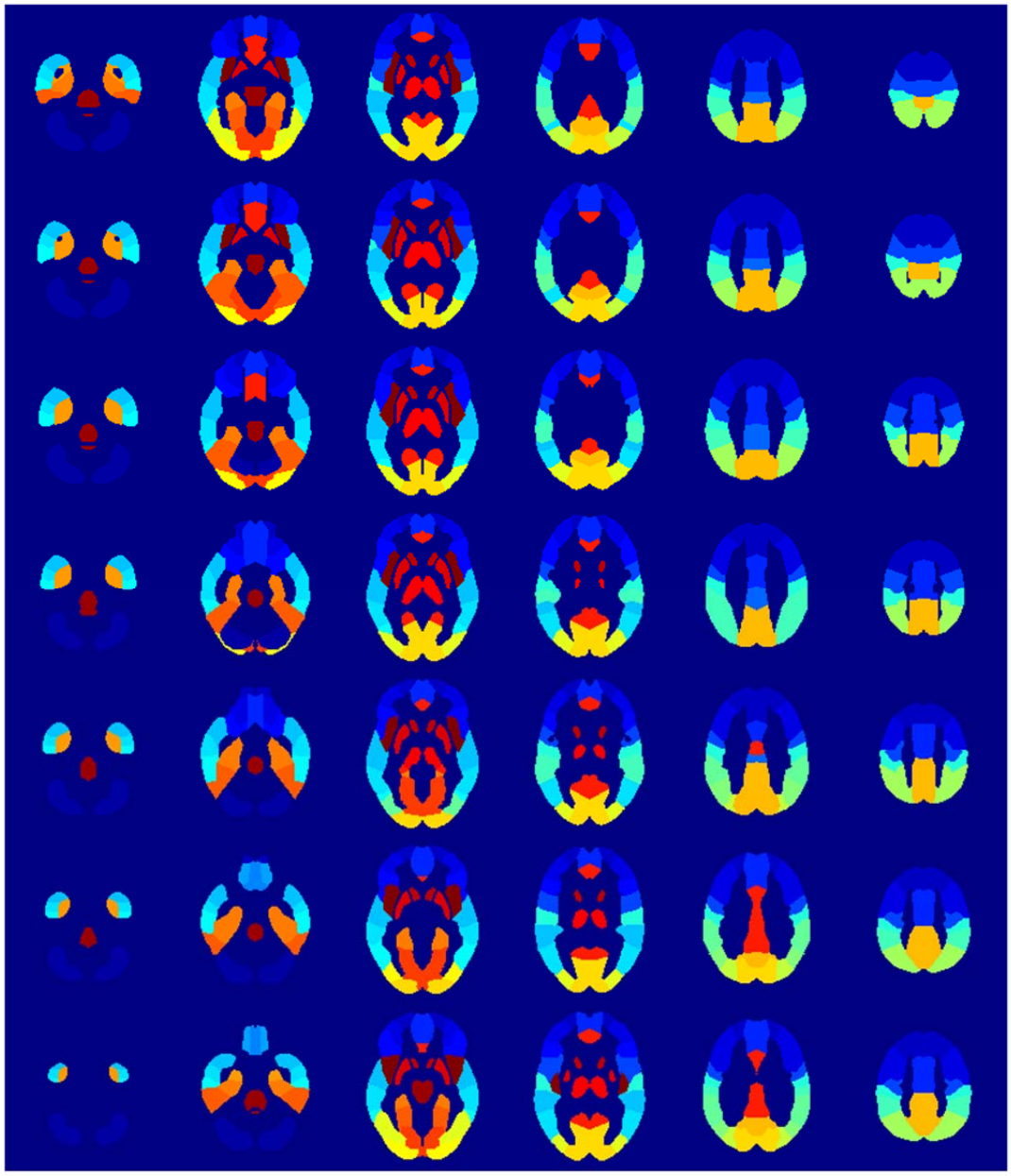

Figure 1S. The region map of the BRASS template consisting of 63 left and right brain regions (Hermes BRASS software, Nuclear Diagnostics AB, Sweden).

Table 1S. Mean and standard deviation of bone linear attenuation coefficients for each of the 14 included patients.

Patient No.	CTAC	Atlas-AC	MLAA-AC	3-Class-AC
1	0.142 ± 0.015	0.130 ± 0.014	0.111 ± 0.019	0.097 ± 0.005
2	0.141 ± 0.015	0.125 ± 0.028	0.105 ± 0.014	0.097 ± 0.002
3	0.138± 0.014	0.131± 0.022	0.111± 0.022	0.097± 0.003
4	0.136 ± 0.010	0.138 ± 0.013	0.115 ± 0.011	0.096 ± 0.006
5	0.137 ± 0.010	0.134± 0.023	0.106 ± 0.013	0.097 ± 0.004
6	0.135 ± 0.010	0.133 ± 0.025	0.105 ± 0.010	0.097 ± 0.003
7	0.137 ± 0.011	0.138 ± 0.016	0.107 ± 0.013	0.096 ± 0.005
8	0.140 ± 0.013	0.134 ± 0.017	0.107 ± 0.015	0.096 ± 0.005
9	0.139 ± 0.012	0.136 ± 0.015	0.105± 0.016	0.095 ± 0.008
10	0.138 ± 0.012	0.132 ± 0.020	0.104 ± 0.016	0.097 ± 0.004
11	0.138 ± 0.012	0.129 ± 0.032	0.108 ± 0.012	0.097 ± 0.004
12	0.134 ± 0.010	0.136 ± 0.019	0.105 ± 0.015	0.097 ± 0.004
13	0.138 ± 0.012	0.134 ± 0.023	0.103 ± 0.010	0.097 ± 0.004
14	0.135 ± 0.010	0.140 ± 0.013	0.100 ± 0.014	0.095 ± 0.007

References

[1] V. Garibotto, S. Heinzer, S. Vulliemoz, R. Guignard, M. Wissmeyer, M. Seeck*, et al.*, "Clinical applications of hybrid PET/MRI in neuroimaging.," *Clin Nucl Med,* vol. 38, pp. e13-e18, Jan 2013.

[2] A. H. Jacobs, L. W. Kracht, A. Gossmann, M. A. Ruger, A. V. Thomas, A. Thiel*, et al.*, "Imaging in neurooncology," *NeuroRx,* vol. 2, pp. 333-47, Apr 2005.

[3] C. Catana, A. Drzezga, W. D. Heiss, and B. R. Rosen, "PET/MRI for neurologic applications," *J Nucl Med,* vol. 53, pp. 1916-25, Dec 2012.

[4] H. Zaidi, "Is MRI-guided attenuation correction a viable option for dual-modality PET/MR imaging?," *Radiology,* vol. 244, pp. 639-642, September 1, 2007 2007.

[5] A. Martinez-Möller, M. Souvatzoglou, G. Delso, R. A. Bundschuh, C. Chefd'hotel, S. I. Ziegler*, et al.*, "Tissue classification as a potential approach for attenuation correction in whole-body PET/MRI: evaluation with PET/CT data," *J Nucl Med,* vol. 50, pp. 520-526, 2009.

[6] J. Ouyang, C. Se Young, Y. Petibon, A. A. Bonab, N. Alpert, and G. El Fakhri, "Bias atlases for segmentation-based PET attenuation correction using PET-CT and MR," *IEEE Trans Nuc Sci,* vol. 60, pp. 3373-3382, 2013.

[7] A. Akbarzadeh, M. R. Ay, A. Ahmadian, N. Riahi Alam, and H. Zaidi, "MRI-guided attenuation correction in whole-body PET/MR: assessment of the effect of bone attenuation.," *Ann Nucl Med,* vol. 27, pp. 152-162, Feb 2013.

[8] F. L. Andersen, C. N. Ladefoged, T. Beyer, S. H. Keller, A. E. Hansen, L. Hojgaard*, et al.*, "Combined PET/MR imaging in neurology: MR-based attenuation correction implies a strong spatial bias when ignoring bone," *Neuroimage,* vol. 84, pp. 206-16, Jan 1 2014.

[9] J. C. Dickson, C. O'Meara, and A. Barnes, "A comparison of CT- and MR-based attenuation correction in neurological PET," *Eur. J. Nucl. Med. Mol. Imag,* vol. 41, pp. 1176-89, Jun 2014.

[10] A. Samarin, C. Burger, S. Wollenweber, D. Crook, I. Burger, D. Schmid*, et al.*, "PET/MR imaging of bone lesions – implications for PET quantification from imperfect attenuation correction," *Eur. J. Nucl. Med. Mol. Imaging,* vol. 39, pp. 1154-1160, 2012/07/01 2012.

[11] H. Arabi, O. Rager, A. Alem, A. Varoquaux, M. Becker, and H. Zaidi, "Clinical assessment of MR-guided 3-class and 4-class attenuation correction in PET/MR.," *Mol Imaging Biol,* vol. 17, pp. 264-276, 2015.

[12] V. Keereman, Y. Fierens, T. Broux, Y. De Deene, M. Lonneux, and S. Vandenberghe, "MRI-based attenuation correction for PET/MRI using ultrashort echo time sequences," *J Nucl Med,* vol. 51, pp. 812-8, 2010.

[13] C. Catana, A. van der Kouwe, T. Benner, C. J. Michel, M. Hamm, M. Fenchel*, et al.*, "Toward implementing an MRI-based PET attenuation-correction method for neurologic studies on the MR-PET brain prototype.," *J Nucl Med,* vol. 51, pp. 1431-1438, Sep 2010.

[14] F. Wiesinger, L. I. Sacolick, A. Menini, S. S. Kaushik, S. Ahn, P. Veit-Haibach*, et al.*, "Zero TE MR bone imaging in the head.," *Magn Reson Med,* p. *in press*, Jan 16 2015.

[15] G. Delso, F. Wiesinger, L. I. Sacolick, S. S. Kaushik, D. D. Shanbhag, M. Hüllner*, et al.*, "Clinical evaluation of zero-echo-time MR imaging for the segmentation of the skull," *J Nucl Med,* vol. 56, pp. 417-422, March 1, 2015 2015.

[16] L. B. Aasheim, A. Karlberg, P. E. Goa, A. Haberg, S. Sorhaug, U. M. Fagerli*, et al.*, "PET/MR brain imaging: evaluation of clinical UTE-based attenuation correction.," *Eur J Nucl Med Mol Imaging,* vol. 42, pp. 1439-1446, Aug 2015.

[17] G. Delso, M. Carl, F. Wiesinger, L. Sacolick, M. Porto, M. Hüllner*, et al.*, "Anatomic evaluation of 3-dimensional ultrashort-echo-time bone maps for PET/MR attenuation correction," *J Nucl Med,* vol. 55, pp. 780-785, May 1, 2014 2014.

[18] H. Zaidi, M.-L. Montandon, and S. Meikle, "Strategies for attenuation compensation in neurological PET studies.," *Neuroimage,* vol. 34, pp. 518-541, 2007.

[19] E. R. Kops, G. Wagenknecht, J. Scheins, L. Tellmann, and H. Herzog, "Attenuation correction in MR-PET scanners with segmented T1-weighted MR images," presented at the IEEE Nuclear Science Symposium Conference Record (NSS/MIC), 2009.

[20] M.-L. Montandon and H. Zaidi, "Atlas-guided non-uniform attenuation correction in cerebral 3D PET imaging.," *Neuroimage,* vol. 25, pp. 278-286, 2005.

[21] M. Hofmann, F. Steinke, V. Scheel, G. Charpiat, J. Farquhar, P. Aschoff*, et al.*, "MRI-based attenuation correction for PET/MRI: a novel approach combining pattern recognition and atlas registration," *J Nucl Med,* vol. 49, pp. 1875-1883, 2008.

[22] N. Burgos, M. Cardoso, K. Thielemans, M. Modat, J. Schott, J. Duncan*, et al.*, "Attenuation correction synthesis for hybrid PET-MR scanners: Application to brain studies.," *IEEE Trans Med Imaging,* vol. 33, pp. 2332-2341, Jul 17 2014.

[23] D. Izquierdo-Garcia, A. E. Hansen, S. Forster, D. Benoit, S. Schachoff, S. Furst*, et al.*, "An SPM8-based approach for attenuation correction combining segmentation and nonrigid template formation: application to simultaneous PET/MR brain imaging," *J Nucl Med,* vol. 55, pp. 1825-30, Nov 2014.

[24] A. Salomon, A. Goedicke, B. Schweizer, T. Aach, and V. Schulz, "Simultaneous reconstruction of activity and attenuation for PET/MR," *IEEE Trans Med Imaging,* vol. 30, pp. 804-813, 2011.

[25] J. Nuyts, P. Dupont, S. Stroobants, R. Benninck, L. Mortelmans, and P. Suetens, "Simultaneous maximum a posteriori reconstruction of attenuation and activity distributions from emission sinograms," *IEEE Trans Med Imaging,* vol. 18, pp. 393-403, 1999.

[26] M. Defrise, A. Rezaei, and J. Nuyts, "Time-of-flight PET data determine the attenuation sinogram up to a constant," *Phys Med Biol,* vol. 57, pp. 885-899, Feb 2012.

[27] A. Rezaei, M. Defrise, G. Bal, C. Michel, M. Conti, C. Watson*, et al.*, "Simultaneous reconstruction of activity and attenuation in Time-of-Flight PET," *IEEE Trans Med Imaging* vol. 31, pp. 2224-33, 2012.

[28] A. Mehranian and H. Zaidi, "Joint estimation of activity and attenuation in whole-body TOF PET/MRI using constrained Gaussian mixture models.," *IEEE Trans Med Imaging,* vol. 34, pp. 1808-1821, 2015.

[29] A. Mehranian, H. Arabi, and H. Zaidi, "Vision 20/20: Magnetic resonance imaging-guided attenuation correction in PET/MRI: Challenges, solutions, and opportunities.," Med Phys, vol. 43, pp. 1130-1155, 2016.

[30] I. Bezrukov, F. Mantlik, H. Schmidt, B. Scholkopf, and B. J. Pichler, "MR-Based PET attenuation correction for PET/MR imaging," *Semin Nucl Med,* vol. 43, pp. 45-59, Jan 2013.

[31] S. Klein, M. Staring, K. Murphy, M. A. Viergever, and J. P. Pluim, "elastix: a toolbox for intensity-based medical image registration," *IEEE Trans Med Imaging,* vol. 29, pp. 196-205, Jan 2010.

[32] J. P. Carney, D. W. Townsend, V. Rappoport, and B. Bendriem, "Method for transforming CT images for attenuation correction in PET/CT imaging.," *Med Phys,* vol. 33, pp. 976-983, Apr 2006.

[33] N. J. Tustison, B. B. Avants, P. A. Cook, Z. Yuanjie, A. Egan, P. A. Yushkevich*, et al.*, "N4ITK: Improved N3 Bias Correction," *Medical Imaging, IEEE Transactions on,* vol. 29, pp. 1310-1320, 2010.

[34] A. Akbarzadeh, D. Gutierrez, A. Baskin, M. R. Ay, A. Ahmadian, N. Riahi Alam*, et al.*, "Evaluation of whole-body MR to CT deformable image registration.," *J Appl Clin Med Phys,* vol. 14, pp. 238-253, 2013.

[35] P. Kovesi, "Phase congruency: A low-level image invariant," *Psychological research,* vol. 64, pp. 136-148, 2000.

[36] C. G. Ortiz and A. Martel, "Automatic atlas-based segmentation of the breast in MRI for 3D breast volume computation," *Medical physics,* vol. 39, pp. 5835-5848, 2012.

[37] A. Mehranian and H. Zaidi, "Clinical assessment of emission- and segmentation-based MRI-guided attenuation correction in whole body TOF PET/MRI.," *J Nucl Med,* vol. 56, pp. 877-883, 2015.

[38] J. A. Disselhorst, I. Bezrukov, A. Kolb, C. Parl, and B. J. Pichler, "Principles of PET/MR imaging," *J Nucl Med,* vol. 55, pp. 2S-10S, 2014.

[39] N. Burgos, M. J. Cardoso, K. Thielemans, M. Modat, J. Dickson, J. M. Schott*, et al.*, "Multi-contrast attenuation map synthesis for PET/MR scanners: assessment on FDG and Florbetapir PET tracers," *Eur. J. Nucl. Med. Mol. Imag,* vol. 42, pp. 1447-58, Aug 2015.

[40] J. Yang, Y. Jian, M. Tohme, S. Behr, D. Vigneron, S. Majumdar*, et al.*, "Impact of atlas-CT-based bone anatomy compensation on MR-based attenuation correction for brain PET imaging in a time-of-flight PET/MRI system: A direct comparison to a patient-CT-based approach," in *Proceedings of the 4th PSMR Conference on PET/MR and SPECT/MR*, Eleba, Italy, 2015.

[41] S. Minoshima, K. A. Frey, N. L. Foster, and D. E. Kuhl, "Preserved pontine glucose metabolism in Alzheimer disease: a reference region for functional brain image (PET) analysis," *J Comput Assist Tomogr,* vol. 19, pp. 541-7, Jul-Aug 1995.

[42] I. Bezrukov, H. Schmidt, S. Gatidis, F. Mantlik, J. F. Schafer, N. Schwenzer*, et al.*, "Quantitative evaluation of segmentation- and atlas-based attenuation correction for PET/MR on pediatric patients," *J Nucl Med,* vol. 56, pp. 1067-74, Jul 2015.

Chapter 9

Whole-body bone segmentation from MRI for PET/MRI attenuation correction using shape-based averaging

Hossein Arabi and Habib Zaidi

Medical Physics, Vol. 43, No. 11, pp 5848-5861 (2016)

Abstract

Purpose: We evaluate the performance of shape-based averaging (SBA) technique for whole-body bone segmentation from MRI in the context of MRI-guided attenuation correction (MRAC) in hybrid PET/MRI. To enhance the performance of the SBA scheme, we propose to combine it with statistical atlas fusion techniques. Moreover, a fast and efficient shape comparison-based atlas selection scheme was developed and incorporated into the SBA method.

Methods: Clinical studies consisting of PET/CT and MR images of 21 patients were used to assess the performance of the SBA method. In addition, we assessed the performance of simultaneous truth and performance level estimation (STAPLE) and the selective and iterative method for performance level estimation (SIMPLE) combined with SBA. In addition, a local shape comparison scheme (L-Shp) was proposed to improve the performance of SBA. The SIMPLE method was applied globally (G-SIMPLE) while STAPLE method was employed at both global (G-STAPLE) and local (L-STAPLE) levels. The evaluation was performed based on the accuracy of extracted whole-body bones, fragmentation, and computation time achieved by the different methods. The majority voting (MV) atlas fusion scheme was also evaluated as a conventional and commonly used method. MRI-guided attenuation maps were generated using the different segmentation methods. Thereafter, quantitative analysis of PET attenuation correction was performed using CT-based attenuation correction as reference.

Results: The SBA and MV methods resulted in considerable underestimation of bone identification (Dice≈0.62) and high factitious fragmentation error of contiguous structures. Applying global atlas selection or regularization (G-STAPLE and G-SIMPLE) to the SBA method enhanced bone segmentation accuracy up to a Dice=0.66. The best results were achieved when applying the L-STAPLE method with a Dice of 0.76 and the L-Shp method with a Dice of 0.75. However, L-STAPLE required up to fivefold increased computation time compared to L-Shp method. Moreover, both L-STAPLE and L-Shp methods resulted in less than 3% SUV mean relative error and 6% SUV mean absolute error in bony structures owing to superior bone identification accuracy. The quantitative analysis using joint histograms revealed good correlation between PET-MRAC images using the proposed L-Shp algorithm and the corresponding reference PET-CT images.

Conclusion: The performance of SBA was enhanced through application of local atlas weighting or regularization schemes (L-STAPLE and L-Shp). Bone recognition, fragmentation of the contiguous structures and quantitative PET uptake recovery improved dramatically using these methods while the proposed L-Shp method significantly reduced the computation time.

I. Introduction

Image segmentation and anatomical regions delineation, aiming at classifying a subject image into volumes of interest and background, play a major role in medical image processing. In many situations, such as bone segmentation from magnetic resonance images (MRI), non-ideal image quality or lack of contrast challenges the segmentation task. Due to the high demand for (semi-) automated segmentation techniques, multi-atlas based framework has attracted considerable attention because of its promising performance, robustness and flexibility [1]. Technically, multi-atlas refers to a set of images, preferably from the same body region of the test image together with approved target segmentation information. Multi-atlas based segmentation typically entails the following steps: (i) individual registration of atlas images to the test image followed by propagation (using the obtained deformation fields) of the corresponding label information to the test subject coordinates, and (ii) final decision on labeling of test image through atlas fusion schemes. Inclusion of multiple atlases is considered to be an effective procedure, which has been found to be more accurate than any of the individual atlases.[1, 2]

The atlas fusion task is typically carried out using voxel-wise decision merging techniques, such as majority voting (MV) [3] or assigning likelihoods to each of outcome possibilities via Bayesian classifiers [4]. Moreover, the information provided by each of the raters can be preferably assessed and weighted according to performance and relevance to enhance the effectiveness of the atlas fusion task [5]. To achieve the best possible accuracy, this task is commonly carried out locally or at the voxel level, which might lead to undesirable fragmentation of the structures owing to local noise and spatial uncertainty [6]. To address this issue, shape-based averaging (SBA), which exploits the natural distance relationship between the voxels to combine different raters decisions based on the signed distance maps of the atlas label maps, was introduced [7]. Basically, the SBA technique relies on the Euclidean distance transform, which assigns the distance from the nearest boundary of the target object to each voxel of the label map. The decision about the final segmentation is made by computing the average of all distance maps calculated on rater label maps.

Atlas fusion SBA performed as well as or even slightly better than MV in terms of segmentation accuracy and object identification on human brain MRI data [7]. Besides, SBA resulted in less specious fragmentation, which led to significantly more natural and contiguous structures compared to the popular majority voting approach [6]. Moreover, SBA exhibited more robustness to poor resolution and small number of input atlases [7]. Robitaille *et al.* [8] compared a number of effective atlas fusion schemes, namely SBA, simultaneous truth and performance level estimation (STAPLE) [9] and MV for brain MRI segmentation using datasets from the International Consortium for Brain Mapping (ICBM) [10]. In almost all simulated and studies involving segmentation of 2D and 3D neuroanatomical structures, the SBA atlas fusion scheme outperformed the other methods in terms of recognition rate.

The outstanding merit of SBA, in addition to its robustness to noise and homogeneity of output labeling, is thought to be the good performance on a small number of input atlases. In this regard, we chose the SBA method for bone volume identification from whole-body MR images with the aim to incorporate bone in the derivation of attenuation maps for attenuation correction in hybrid PET/MRI. Correcting the PET emission data for attenuation is still a major challenge in PET/MRI owing to the lack of direct correlation between MRI signal and attenuation properties of biological tissues [11]. The complexity and variability of the human anatomy combined with the high level of noise and partial volume effect make the segmentation of bone from MRI a challenging task. In addition, application of dedicated MR sequences enabling to delineate bony structures, such as ultra-short echo time (UTE)[12] or zero time echo (ZTE)[13], in whole-body imaging is not yet clinically feasible owing to the long acquisition time and susceptibility to artifacts when using a large field-of-view. As such, the use of atlas-based methods for identification of bone tissue is common practice in MRI-guided attenuation generation in brain[14-17] and more importantly in whole-body imaging.[18-20]

Despite promising potential reported in the literature, we observed that the SBA technique tends to underestimate bone volume identification in a comparative assessment of common atlas-based bone segmentation techniques from MRI using a set of MR/CT image pairs [21]. Although SBA exhibited poor performance compared to other techniques, its best performance was achieved on a relatively small number of input atlases.

In this work, we aim to propose the SBA method for whole-body bone segmentation from MRI motivated by its remarkable merits, in particular robustness to a small number of input atlases and minimal factitious fragmentation of contiguous structures. These features could be appealing to PET/MRI attenuation map

generation, thus allowing the derivation of artifact free attenuation maps using gender/body/posture-specific atlas dataset, which may contain only few atlas images. The main contribution of this work is the combination of the promising SBA atlas fusion scheme with state-of-the-art statistical atlas selection/weighting methods, such as STAPLE[9] and selective and iterative method for performance level estimation (SIMPLE)[22], to adapt the SBA technique and enhance its performance for the purpose of whole-body bone segmentation from MRI. In addition, a simple atlas weighting scheme based on shape similarity with a competitive performance was proposed for incorporation within the SBA technique. The performance of different atlas fusion schemes were evaluated in terms of whole-body bone extraction and PET attenuation correction accuracy.

II. Materials and methods

II.A. Data acquisition

The study population comprised 21 patients who underwent whole-body ^{18}F-FDG PET/CT and MRI scanning for staging of head and neck malignancies. The study protocol was approved by the institutional ethics committee and the patients signed written informed consent. PET/CT imaging was performed on a Biograph 64 True Point scanner (Siemens Healthcare, Erlangen, Germany). CT images were acquired for attenuation correction using an unenhanced low dose CT scan (120 kVp, 60 mAs, 24×1.5 collimation, pitch of 1.2 and 1 s per rotation) after a localization scout scan. PET data acquisition started 146.2±20 min post-injection of ^{18}F-FDG (371±23 MBq) with 3 min per bed position for a total of 4-5 beds, resulting in a total acquisition time of 15-18 min. MRI examinations were performed on the Ingenuity TF PET/MR (Philips Healthcare, Cleveland, USA) [23] using a whole-body MRI Dixon volumetric interpolated T1-weighted sequence [24] using the following parameters: flip angle 10°, TE_1 1.1 ms, TE_2 2.0 ms, TR 3.2 ms, 450×354 mm^2 transverse FOV, 0.85×0.85×3 mm^3 voxel size, and a total acquisition time of 2-3 minutes. The slight time difference is due to different axial coverage depending on patients' length. Some patients underwent one or two more bed-positions acquisition. The in-phase image generated by the MRI Dixon sequence was used for the segmentation process. Due to temporal shift between MRI and CT acquisitions, the in-phase MR image of each patient was non-rigidly registered to the corresponding CT image to ensure spatial alignment of MR and CT image pairs. The segmented bone from CT images (produced by applying an intensity threshold of 140 HU) can be considered as the ground truth bone label map for corresponding MR images. The MR and CT image pairs after registration had 512×512 matrix resolution in 207 axial slices.

Fast whole-body MRI protocols acquired for attenuation map generation suffer from a relatively high level of noise, corruption due to the low frequency bias field and inter-patient intensity inhomogeneity.[25-27] To remove or minimize these effects, in-phase MR images of all patients underwent the following corrections: (i) gradient anisotropic diffusion filtering [28] for statistical noise removal using a conductance = 4, number of iterations = 10 and time step = 0.01, (ii) N4 bias field correction [29] for cancelling out intra-subject intensity inhomogeneity using B-spline grid resolution = 400, iteration number = 200 (at each grid resolution), convergence threshold = 0.001, B-spline order = 3, spline distance = 400, number of histogram bins = 256 and shrink factor = 3, (iii) histogram matching [30] to minimize inter-subject intensity non-uniformity using a histogram level = 512 and match points = 64.

II.B. MRI image segmentation algorithms

1) Shape-based averaging

In principle, the combination of multiple atlas information or segmentations would result in a more accurate outcome than any of the individual segmentations. Unlike other segmentation fusion schemes, SBA exploits a natural distance relationship between the voxels of an image to achieve the segmentation fusion task. Usually, this distance relationship is expressed in terms of signed Euclidean distance maps of the bone label in each of the input atlas images. Let us suppose that $L_j(x_i)$ stands for the label map of atlas (j) at voxel (x_i), for instance with a value of 0 for the background (BKG) and 1 for bone, and $O_j(x_i)$ denotes its corresponding signed Euclidean distance of voxels (x_i) from the nearest voxel with the bone label in L_j. $O_j(x_i)$ is positive inside bone volume, negative outside and equal to zero if and only if the voxel resides on the surface of bony structures. In other words, each voxel in the bone label map is weighted based on its distance from the surface of the bony

structures. The voxels deep inside the bony structures receive higher positive weights and voxels further outside the bony structures receive higher negative weights ($O_j(x_i)$).

In the first step, the distance maps of all structures in all input atlases/segmentations are computed ($O_j(x_i)$) and then, the average distance (D_{ave}) of voxel (x_i) from nearest bone label is defined as:

$$D_{ave}(x_i) = \frac{1}{A} \sum_j O_{ji} \quad (1)$$

where A indicates the number of input atlas images. Thereafter, the segmentation outcome for each voxel $T(x_i)$ is determined through minimization of the average distance from combined label maps. Equation 2 tends to assign labels (bone or BKG) to each voxel, such that it minimizes the average distance map (D_{ave}) to the assigned labels.

$$T(x_i) = arg\ \min_{Bone\ or\ BKG} D_{ave}(x_i) \quad (2)$$

This minimization problem can be iteratively solved by applying algorithm 1 below.

Algorithm 1. Shape-based averaging algorithm.[7]

1. **For** all x — Initialization: loop over all voxel
   $T(x_i) = unknown$ — Unknown label for target label map
   $D_{aux}(x_i) = \infty$ — Auxiliary distance map
   End

2. **For** all labels — Main loop: over all labels
   For all x
   $D_{ave}(x_i) = \frac{1}{A} \sum_j O_j(x_i)$ — Average distance map for a specific label
   If $D_{aux}(x_i) < D_{ave}(x_i)$
   $T(x_i) = bone$
   $D_{aux}(x_i) = D_{ave}(x_i)$
   End
   End
   End

Compared to other atlas fusion schemes, SBA produces smoother, more regular and natural looking output segmentations as well as comparable recognition rate [7, 8]. However, the SBA method resulted in dramatic underestimation of bone recognition in our previous study [21]. This stems from the complexity of structures and the relatively large number of fragmentations of whole-body bone tissue. Figure 1 depicts an example of the SBA fusion scheme, in which three atlas images contributed to the segmentation task while atlas No. 3 exhibited poor performance. Since in the SBA scheme, the fusion task is performed based on distance maps, the poor performance of atlas No. 3 is also magnified in the corresponding distance map at the indicated point, consequently leading to underestimation of the segmentation despite the fact that the majority of the atlases voted differently. Due to the large anatomical variability, different body postures, non-rigid motion and far from perfect accuracy of atlas registration in whole-body imaging (compared for instance to brain imaging), this issue is very likely to occur in multi-atlas whole-body segmentation when applying the SBA method.

Motivated by the remarkable advantages of the SBA technique, we aimed to improve its performance in the context of whole-body bone segmentation through incorporation of SIMPLE and STAPLE procedures. To this end, the SBA scheme was combined with SIMPLE and STAPLE methods at both local and global levels. Moreover, a simple but effective atlas selection procedure based on shape comparison was proposed. In the following, we elaborate on the mathematical foundations and algorithmic implementation of the proposed methods.

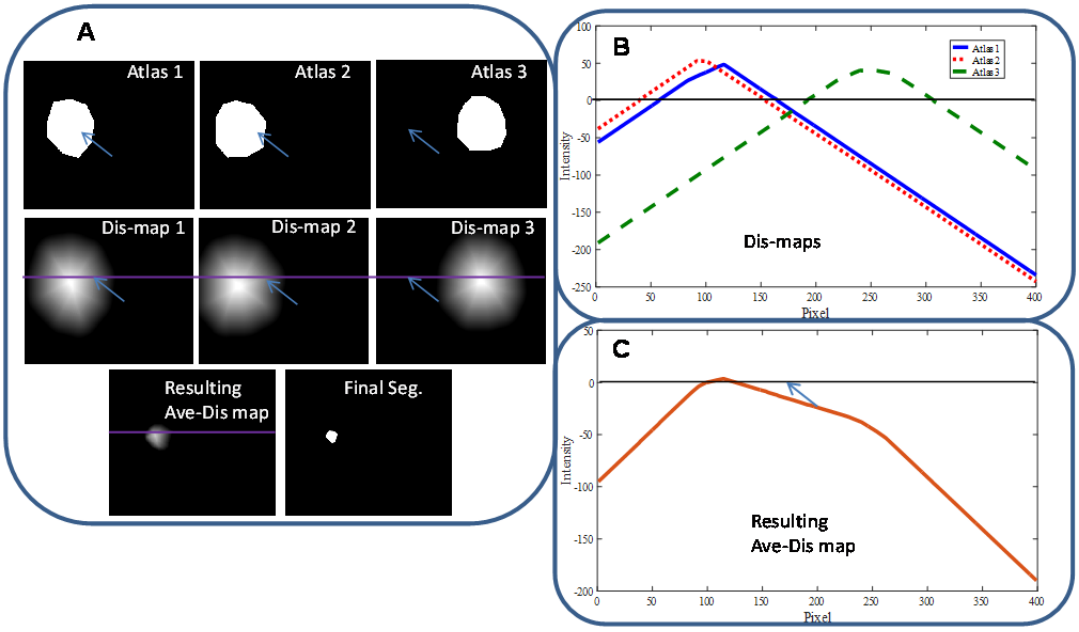

Figure 1. Illustration of shape-based averaging (SBA) atlas fusion framework. The top left panel (A) depicts three binary label images generated by three different atlases and the middle row shows the corresponding distance maps. The lower row presents the combined distance map together with the final labeling result. The right panel depicts the profiles of distance maps corresponding to the lines indicated on the atlases (B) and resulting (C) distance maps. The poor performance of one of the raters (here atlas 3) led to signification underestimation of the segmentation output.

2) Global SIMPLE

The selective and iterative method for performance level estimation (SIMPLE) employs an atlas selection scheme after registration through iterative performance estimation and uses this performance as a weight in the label fusion process [22]. Poorly performing atlases act as noise in the SBA scheme as illustrated in figure 1. At each iteration, SIMPLE discards badly performing atlases such that they no longer contribute to the final segmentation. In the first step, all registered atlases are combined (here using the SBA scheme) to create a rough estimation of the ground truth segmentation (T^0).

In the next step, the performance of each atlas ($\emptyset_j = f(L_j, T^k),\ j \in Sl^k$) can be estimated via binary overlap measures (such as $Dice = \frac{2|L_j \cap T^k|}{|L_j|+|T^k|}$ or $SP = \frac{TPR(L_j,T^k)+TNR(L_j,T^k)}{2}$) where Sl^k indicates the selected atlases at the k^{th} iteration, *TPR* (true positive rate) and *TNR* (true negative rate) indicate sensitivity and specificity, respectively, and *SP* indicates a binary overlap measure composed of the average of sensitivity and specificity (see Eq. 3 below). The estimated performance of the atlases is used to identify and discard poor performing ones in the next iteration to generate (T^{k+1}), which in turn enhances the accuracy of the new estimated segmentation. This process repeated iteratively to optimize the selection of atlases (algorithm 2). In algorithm 2, we propose to combine the SIMPLE atlas selection/weighting method with the SBA atlas fusion scheme.

Algorithm 2. Global SIMPLE algorithm (G-SIMPLE).

1. Segmentation (T^k) using the SBA scheme weighted by estimated performances ($\emptyset_j = f(L_j, T^{k-1})$) using the selected atlases ($j \in Sl^k$).

2. Performance assessment of each input atlas ($\emptyset_j = f(L_j, T^k),\ j \in Sl^k$).

3. A set of atlases is determined (Sl^k) for the next segmentation provided $j \in Sl^k\ if\ \emptyset_j > \theta$ (atlas selection threshold)

To ensure that an atlas image is not excluded prematurely in the first few iterations (here we used 3), all atlas images contribute to the segmentation. Technically, the atlas selection threshold (Θ) plays a key role as it

determines both the convergence rate and performance of the algorithm. To find the optimal value of Θ, we employed the procedure described in Ref.[22] where the atlas selection threshold is determined as a function of the mean ($\overline{\emptyset}^k$) and standard deviation (σ^k) of the performance of all atlases ($j \in Sl^k$): $\theta^k = \overline{\emptyset}^k - c\sigma^k$. The free parameter ($c$) produced the best results when defined as an increasing function of the number of selected atlases ($c/Num(Sl^k)$) because in early iterations a larger number of atlases should be discarded and as the algorithm proceeds, the selection threshold should decrease to discard atlases less quickly. At the end of each iteration, the estimation of the ground truth segmentation is achieved by applying the SBA fusion scheme on the selected atlas images. The binary overlap measures (such as *Dice* and combination of sensitivity and specificity introduced earlier) between atlas images and the estimated ground truth segmentation (T^k) is used to discard poor atlases. In our experiments, the sensitivity performed slightly better than *Dice*. Therefore, we selected it as the similarity measure for threshold selection. The binary overlap measure used to estimate the performance of atlases is estimated globally (whole image). We call this approach G-SIMPLE (global SIMPLE).

3) Global STAPLE

Simultaneous truth and performance level estimation (STAPLE) considers a set of label maps, provided by atlas registration, and computes a probabilistic estimate of the ground truth segmentation as well as a criterion of the performance level achieved by each of the atlases [9]. The task of probabilistic estimate of the ground truth segmentation is carried out through combining an optimal subset of the atlases (or label maps) weighted by the estimated performance level. Here, we consider $Y(x_i)$ as the target MR image with unknown label map $T(x_i)$ containing N voxels. Given A atlas images or label maps ($L(x_i)$) registered to the target image (Y), the D_{ij} matrix of size $N \times A$ can be formed where the rows (D_j) represent L_j. Assuming an estimate of the ground truth segmentation (T) is available, the sensitivity and specificity of each atlas can be calculated using:

$$\begin{aligned} Sensitivity\ (true\ positive\ ratio): TPR &= TP/(TP+FN) \\ Specificity\ (true\ netative\ ratio): TNR &= TN/(TN+FP) \\ p_j &= Probability(D_{ij}=1|T(x_i)=1) \\ q_j &= Probability(D_{ij}=0|T(x_i)=0) \end{aligned} \quad (3)$$

where TP and FN are the true positive and false negative rates, respectively. Then, the sensitivity $P=(p_1, p_2, \ldots, p_A)^T$ and specificity $Q=(q_1, q_2, \ldots, q_A)^T$ matrices can be generated where the elements p and q indicate the sensitivity and specificity of one of the atlas images, respectively. Given a matrix D containing all the atlas label maps and hidden true target label map T, the probability mass function of the complete data would be $f(D,T|P,Q)$, where the goal is to estimate the performance level parameters of the atlases characterized by P or Q, which maximize the log likelihood function of the complete data.

$$(\hat{P},\hat{Q}) = arg\max_{P,Q}\ \log(f(D,T|P,Q)) \quad (4)$$

Based on the assumption that atlas label maps are all conditionally independent, given the estimated ground truth segmentation and performance level parameters, a version of the expectation-maximization (EM) algorithm was employed to estimate the solution of the maximization problem. A detailed description of the employed EM algorithm is provided in Ref.s [9] and [31]. In the *expectation-step* an estimation of the unknown target label map is derived through computation of the conditional probability at each voxel:

$$w_i^k \equiv f(T(x_i)=1|D_i,P^k,Q^k) = \frac{a_i^k}{b_i^k+a_i^k} \quad (5)$$

where w_i indicates the probability of the true target segmentation at voxel (i) subject to

$$if\ w_i \geq 0.5\ \ then\ T(x_i)=1\ (bone)\ else\ T(x_i)=0\ (BKG) \quad (6)$$

To merge the SBA atlas fusion scheme and STAPLE atlas selection method, the signed Euclidean distance map of all atlas labels were computed (O_{ij}) considering positive values inside bony structures and negative values outside. Then, the calculated distance map was incorporated into the conditional probability (Eq. 5) as a weighting factor for each voxel:

$$a_i^k \equiv f(T(x_i)=1)\ \prod_{j:D_{ij}=1} O_{ij} \times p_j^k\ \prod_{j:D_{ij}=0} \frac{1}{|O_{ij}|+1} \times (1-p_j^k)$$

$$b_i^k \equiv f(T(x_i)=0)\ \prod_{j:D_{ij}=0} |O_{ij}| \times q_j^k\ \prod_{j:D_{ij}=0} \frac{1}{O_{ij}+1} \times (1-q_j^k) \quad (7)$$

Here, $f(T(x_i)=1)/f(T(x_i)=0)$ serves as prior knowledge for the presence/absence of bone in the target image, where a constant value of 1 is considered for all voxels. Equation 7 differs from the original STAPLE method in the sense that it is weighted with signed distance map of bone label.

In the *Maximization-step,* given the estimated weight variables (w_i), performance level parameters that maximize the conditional expectation of the complete data log likelihood function can be computed considering:

$$p_j^{k+1} = \frac{\sum_i w_i^k D_{ij}}{\sum_i w_i^k}$$

$$q_j^{k+1} = \frac{\sum_i (1-w_i^k)(1-D_{ij})}{\sum_i (1-w_i^k)} \quad (8)$$

Regarding Eq. (8), since the sensitivity and specificity of each atlas is estimated using all voxels of the image (as opposed to local estimation) we call this method G-STAPLE (global STAPLE).

4) Local STAPLE

So far, the described approaches (G-SIMPLE and G-STAPLE) combined with the SBA scheme were designed to assign weights to each atlas based on the global measurement of performance level. In this section, the same concept is employed for local assignment of weights based on the atlas performance measured on a subset or small patch of images. The procedure (*expectation-* and *maximization-steps*) is quite similar as the one described in section 2.2.3 but the sensitivity and specificity are computed locally and as such, a spatially varying (voxel-wise) sensitivity-specificity matrix can be formed as described in REF. [32]:

$$\gamma = (p, q)$$

$$\gamma = \begin{bmatrix} \gamma_{11} & \gamma_{21} \cdots \gamma_{A1} \\ \gamma_{12} & \gamma_{22} \cdots \gamma_{A2} \\ \cdots & \cdots \cdots \cdots \\ \gamma_{1N} & \gamma_{2N} \cdots \gamma_{AN} \end{bmatrix} \quad (9)$$

where $\gamma_{ij}(p_{ij},q_{ij})$ indicates the sensitivity and specificity pair measured for the atlas *j* at the voxel *i*. Given matrix γ, the aim is to estimate the voxel-wise performance level parameters of the atlases which maximize the log likelihood function of the complete data.

$$\hat{\gamma} = arg\max_{\gamma}\ \log(f(D,T|\gamma)) \quad (10)$$

In a way similar to the one described previously, the *expectation-step* deals with an estimation of the unknown target label map derived from the computation of the conditional probability at each voxel:

$$w_i^k \equiv f\left(T(x_i)=1 \middle| D_i, \gamma_i^k\right) = \frac{a_i^k}{b_i^k + a_i^k} \quad (11)$$

$$if\ w_i \geq 0.5\ \ then\ T(x_i)=1\ (bone)\ else\ T(x_i)=0\ (BGK)$$

The SBA atlas fusion scheme is then combined with spatially varying STAPLE approach via incorporation of the signed Euclidean distance map (O_{ij}) into the conditional probability (Eq. 11) as a weighting factor:

$$a_i^k \equiv f(T(x_i)=1)\ \prod_{j:D_{ij}=1} O_{ji} \times p_{ji}^k\ \prod_{j:D_{ij}=0} \frac{1}{|O_{ji}|+1} \times (1-p_{ji}^k)$$

$$b_i^k \equiv f(T(x_i)=0)\ \prod_{j:D_{ij}=0} |O_{ji}| \times q_{ji}^k\ \prod_{j:D_{ij}=0} \frac{1}{O_{ji}+1} \times (1-q_{ji}^k) \quad (12)$$

These equations differ from the original spatially varying STAPLE algorithm since they are weighted with the signed distance map of bone label. The *Maximization-step* computes the performance level parameters that maximize the conditional expectation of the complete data log likelihood function:

$$p_{ji}^{k+1} = \frac{\sum_{m \in R_i} w_m^k D_{jm}}{\sum_{m \in R_i} w_m^k}$$

$$q_{ji}^{k+1} = \frac{\sum_{m \in R_i} (1 - w_m^k)(1 - D_{jm})}{\sum_{m \in R_i} (1 - w_m^k)} \tag{13}$$

By employing the spatially varying or local STAPLE (L-STAPLE) approach, a new parameter is introduced (R), which represents the window size centered at the target voxel (i) for local measurement of the atlas performance.

5) Local shape comparison

The methods described so far tend to improve the quality of the segmentation outcome through iterative refinement of the atlas selection task. The iterative nature of these methods makes them computationally demanding, particularly when implemented locally (voxel-wise). To address this issue, a robust and computationally efficient similarity measure is proposed based on local shape comparison (L-Shp). In this approach, the average distance map of the SBA scheme is computed through voxel-wise weighting of the atlases according to their similarity to the others:

$$D_{ave}(x_i) = \frac{1}{A} \sum_j (aw_{ji})^{-\beta} \, O_{ji} \tag{14}$$

To calculate the weighting factor $(aw_{ji})^{-\beta}$, the distance map of the bone label should be created for all atlas images. Thereafter, the weight for atlas (j) at voxel (i) is obtained from:

$$aw_j^2(x_i) = \frac{1}{A} \sum_s^A \sum_{i \in patch_i} (O_{ji} - O_{si})^2 \frac{hO_{ji} + hO_{si}}{2}$$

$$hO_j = \frac{H(O_j)}{\sum_{patch_i} H(O_j)} \tag{15}$$

where $H(:)$ denotes the Heaviside step function [33]. In a similar manner to L-STAPLE, a local window centered at the target voxel ($patch_i$) is defined to calculate the local weights. This procedure implicitly defines the weights based on MV since the value of weights not only depends on the shape similarity but also on the number of similar atlases in the dataset.

II.C. Parameter optimization

The methods described in previous sections contain free parameters that need to be optimized to reach optimal performance. The atlas selection threshold in the G-SIMPLE method plays a crucial role since a conservative threshold will discard fewer atlases at each iteration, which results in slow convergence rate. On the other hand, fast convergence can be achieved by choosing a strict threshold at the risk of unjustly excluding atlases. As mentioned earlier, the atlas selection threshold (θ^k) was determined as a function of the mean and standard deviation of the performance of all atlases $\theta^k = \overline{\emptyset}^k - c\sigma^k$. The best results were achieved when the free parameter (c) was set as an increasing function of the number of selected atlases (ranging from 0.5 to 1.8) and updated after each second iteration. On average, 12 iterations were used for each data set while in the 3 first iterations no thresholding was applied.

For methods tending to refine atlas selection locally, the most influential parameter is the similarity window size (R for L-STAPLE and *patch* for L-Shp). These free parameters were optimized through a leave-one-out cross-validation (LOOCV) scheme. In the first step, for each individual patient, all the remaining (N-1) MR images were deformably registered to the target image. Therefore, for each subject, the remaining 20 patients act as atlas data set. The registration process was performed between in-phase MR images of the target and atlas data set. Thereafter, the obtained transformation matrices were used to transform the corresponding atlas CT images to the spatial coordinate of the target MR image. The registration process was carried out through a combination of affine and non-rigid alignment based on the advanced Mattes mutual information[34] implemented in the Elastix package[35] as described in previous studies.[36, 37] The following parameters were adopted: interpolate: Bspline, optimizer: standard gradient descent, image pyramid schedule: (16 8 4 2 2), grid spacing schedule (32.0 16.0 8.0 4.0 2.0), maximum number of iterations (4096 4096 2048 1024 512), number of histogram bins: 32. The sizes of R and *patch* windows were optimized by varying the window size from 4 to 30

mm. The resulting bone segmentation was then evaluated in terms of *Dice* similarity coefficient. This procedure was repeated for the whole dataset and the optimal sizes of *R* and *patch* windows were chosen for the rest of the study (figure 2).

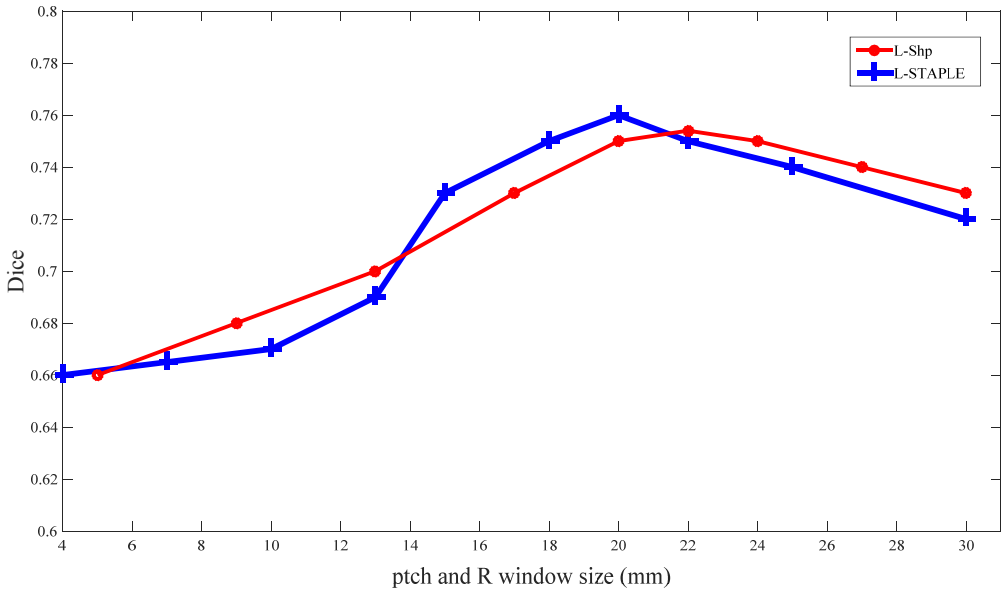

Figure 2. Optimization of *R* window size for local atlas performance assessment in L-STAPLE method (top) and *patch* window size for local shape similarity assessment in the L-Shp method (bottom).

II.D. Quantitative evaluation

Bone segmentation was carried out for the 21 clinical studies on a PC equipped with Intel Xeon CPU (2.3 GHz) running Matlab (The MathWorks, Inc., Natick, MA). For each patient, the segmentation was repeated 5 times using the different methods, namely SBA, G-STAPLE, G-SIMPLE, L-STAPLE, L-Shp. Moreover, MV was considered as a conventional atlas fusion scheme. The assessment of the accuracy of the extracted bones was performed through comparison with bone segmented from the corresponding reference CT images. Bone segmentation from CT images was performed by applying an intensity threshold of 140 HUs. The validation of bone segmentation ass reported using seven volume/distance-based metrics: *Dice* similarity,[38] relative volume difference (*RVD*),[39] Jaccard similarity (*JC*),[40] sensitivity (*S*),[41] mean absolute surface distance (*MASD*),[42] Hausdorff distance (*HD*) [43] and distance error (*DE*).[44]

$$Dice(RefB,T) = \frac{2|RefB \cap T|}{|RefB|+|T|}$$

$$RVD(RefB,T) = 100 \times \frac{|T|-|RefB|}{|RefB|}$$

$$JC(RefB,T) = \frac{|RefB \cap T|}{|RefB \cup T|}$$

$$S(RefB,T) = \frac{|RefB \cap T|}{|T|}$$

$$MASD(RefB,T) = \frac{d_{ave}\ (S_{RefB},S_T) + d_{ave}\ (S_T,S_{RefB})}{2}$$

$$DE(RefB,T) = \frac{1}{bp}\sum_{p=1}^{bp} mindist(RefB_p,T_p)$$

$$HD(RefB,T) = \max_{RefB}\{\min_T\{d(RefB,T)\}\} \quad (16)$$

where *RefB* is the bone segmented from the reference CT image and *T* denotes the extracted bone from the target MRI. $d_{ave}(S_{RefB},S_T)$ is the average direct surface distance from all points on the reference bone surface S_{RefB} to the segmented bone surface S_T. The distance error is equal to the minimum distance from each boundary point of the source region ($RefB_p$) to the entire set of points of the target region [45] averaged across the T_p boundary points. The Hausdorff distance measures the maximum distance one would need to move the boundaries of the source region (*RefB*) to completely cover the target region (*T*).

To assess the sensitivity of the different methods to the number of input atlases, the accuracy of bone segmentation and computation time were also evaluated for varying number of input atlases. In addition to bone extraction accuracy, fragmentation of bony structures was evaluated by computing the number of connected regions in the bone label maps. To this end, face-edge-vertex connectivity (two pixels are considered connected provided they share at least one vertex in the pixel grid) was employed to calculate the number of fragments in the target label maps compared to the reference obtained from CT images.

We further extended our validation through quantitative analysis of PET images corrected for attenuation using the bones segmented from MRI (PET-MRAC). To this end, the segmented bone from the target MRI was superimposed onto the MRI-guided 3-class attenuation map implemented on the Philips Ingenuity TF PET/MR scanner. The latter is obtained by segmenting MR images into surrounding air, lung and soft-tissue followed by assigning pre-defined attenuation coefficient to each tissue class (air: 0 cm^{-1}, lung: 0.022 cm^{-1}, soft-tissue: 0.098 cm^{-1}) [23, 36, 46]. The 3-class attenuation maps with inserted bony structures from reference CT images were taken as the reference in PET attenuation correction analysis (PET-CT). The described segmentation methods generate target bone label maps in binary format. However, a bone label map with continuous linear attenuation coefficients is desired for PET attenuation correction. To this end, we generated continuous valued bone map for each method. The described methods generate the final bone label map through weighted average of the atlas' votes. The obtained weights were multiplied by the values of the original atlas CTs in HUs (instead of binary votes) to recalculate continuous valued bone maps.

PET image reconstruction was performed by means of the e7 tool (Siemens Healthcare, Knoxville, TN)[47] using the ordinary Poisson ordered subset-expectation maximization (OP-OSEM) iterative reconstruction algorithm and default parameters (4 iterations, 8 subsets, and a post-processing Gaussian kernel with a FWHM of 5 mm). The differences between bone segmentation techniques were quantified in terms of change in the standardized uptake value (SUV). The SUVs were calculated by dividing the activity concentration by the injected activity divided by body weight. The impact of whole-body bone segmentation on PET attenuation correction accuracy was assessed through calculation of the relative mean SUV error (Eq. 17) and relative mean absolute SUV error (Eq. 18) in bony structures (voxel-wise evaluation) and lesions in/near bony structures (region of interest-based evaluation). The relative errors of SUV estimates from PET-MRAC images are calculated relative to the SUV measured on PET-CT images used as reference. The relative absolute error (Eq. 18) gives information about reconstruction errors and deviations from the expected values, whereas the relative error (Eq. 17) reflects the inherent bias in the methodology. The regions of interests (ROI) were manually drawn on malignant lesions located inside bony structures or in close proximity such that their activity recovery can be affected by bones.

$$Relative\ error\ (\%) = \frac{MRAC\ (SUV) - Reference\ (SUV)}{Reference\ (SUV)} \times 100\% \tag{17}$$

$$Relative\ absolute\ error\ (\%) = \frac{ABS[MRAC\ (SUV) - Reference\ (SUV)]}{Reference\ (SUV)} \times 100\% \tag{18}$$

In addition to the calculated SUV bias, linear regression analysis was performed on joint histograms of PET-MRAC and PET-CT images in bony structures for each segmentation method.

III. Results

Figure 3 depicts a representative sagittal slice of the segmented whole-body bones from Dixon in-phase MRI together with reference CT image and bone label map. Visual inspection revealed superior bone identification when using locally regularized methods (L-Shp and L-STAPLE).

Table 1 summarizes the quantitative analysis of bone identification accuracy using seven standard volume/distance-based metrics. In agreement with figure 3, considerable bone detection enhancement was achieved using L-Shp and L-STAPLE methods compared to original SBA and MV methods based on the results achieved using 21 patients. Since the implemented methods exhibited different convergence rates in terms of number of input atlases, the representative segmented bones (figure 3) and the quantitative evaluation (Table 1) show the best outcomes for each method. Figure 4 depicts the convergence trend of the different methods based on the *Dice* metric as the number of input atlases vary between 3 and 20.

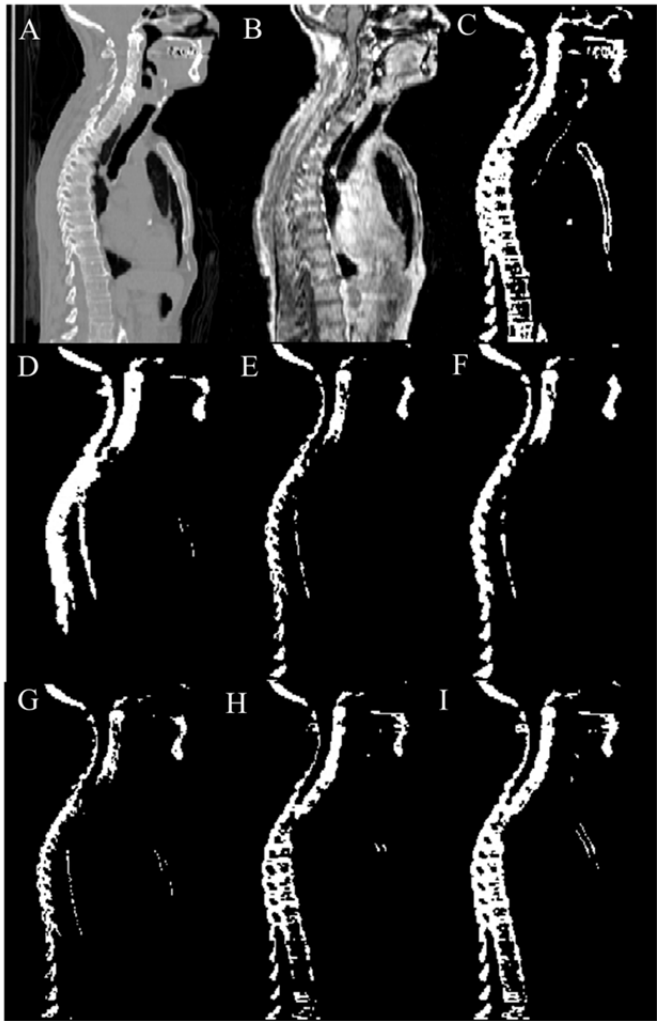

Figure 3. Representative sagittal slice of whole-body bone segmentation using the different methods. A) Reference CT, B) Target in-phase MR image, C) Reference bone map obtained from CT shown in (A), D) SBA, E) MV, F) G-STAPLE, G) G-SIMPLE, H) L-Shp and I) L-STAPLE.

In addition to the evaluation of the convergence rate, the required computation time for performing whole-body bone segmentation was assessed for different methods as a function of the number of input atlases (varying between 3 and 20). Figure 5 (top) shows the processing time (min) for the SBA and globally regularized methods where most of the computation time is taken by the calculation of the signed Euclidean distance maps on bone labels. Similarly, figure 5 (bottom) presents the processing time for the locally regularized methods where most of the processing time is taken by local iterative performance estimation (for L-STAPLE) and local similarity measurement (for L-Shp).

Table 1. Comparison of bone segmentation accuracy (mean±SD) between the different approaches using the selected evaluation metrics, including the Dice, relative volume distance (RVD), Jaccard similarity (JC), sensitivity (S), mean absolute surface distance (MASD), Hausdorff distance (HD), distance error (DE).

	SBA	MV	G-STAPLE	G-SIMPLE	L-STAPLE	L-Shp
Dice	0.62±0.07	0.63±0.08	0.66±0.06	0.66±0.06	0.76±0.05	0.75±0.05
RVD (%)	-31.8±9.1	-31.0±9.2	-30.0±8.2	-29.8±8.4	-25.5±6.5	-25.2±6.9
JC	0.38±0.06	0.39±0.06	0.41±0.05	0.40±0.06	0.47±0.05	0.46±0.06
S	0.42±0.10	0.42±0.11	0.44±0.08	0.45±0.09	0.55±0.07	0.54±0.08
MASD (mm)	6.94±3.10	6.51±2.82	4.46±2.15	5.56±2.21	3.24±1.95	3.17±2.01
HD (mm)	14.5±4.70	13.4±3.95	11.6±3.64	11.3±3.70	07.3±3.10	07.2±3.22
DE (mm)	02.5±1.70	02.2±1.61	02.0±1.55	02.1±1.61	01.3±1.33	01.2±1.40

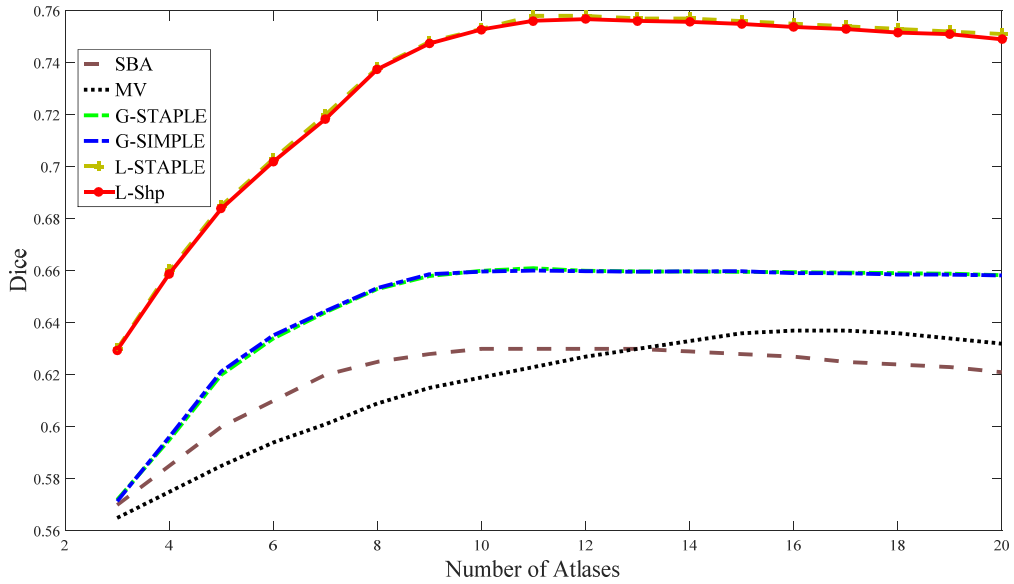

Figure 4. Performance evaluation of the different segmentation methods based on the *Dice* metric as a function of the number of input atlases.

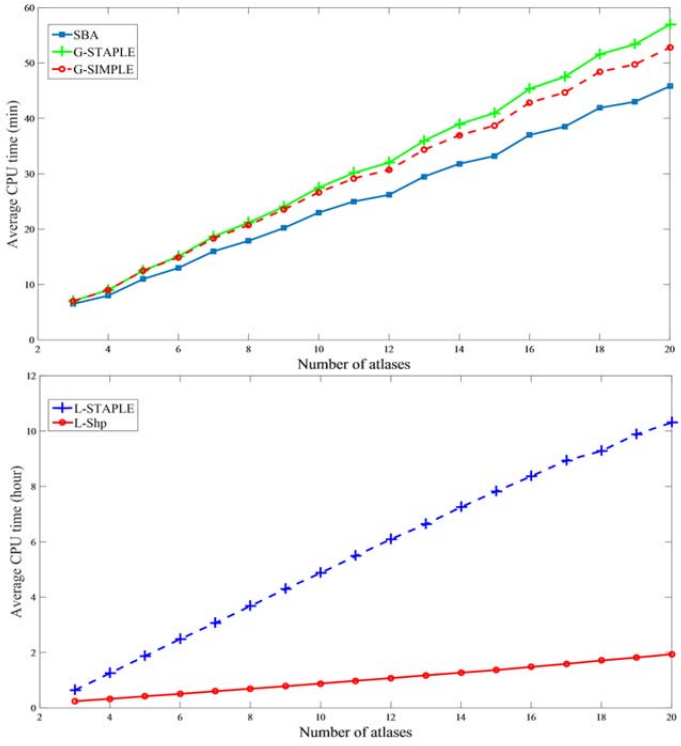

Figure 5. Average computation time for performing whole-body bone segmentation Top) for SBA, G-STAPLE and G-SIMPLE methods (minute). Bottom) for L-STAPLE and L-Shp methods (hour) measured at varying number of input atlases.

The fragmentation of contiguous structures is one of the major performance measures used in this study to evaluate the efficacy of different methods. The number of connected regions in the segmented images is plotted in figure 6, where those obtained from the target CTs are taken as reference. The number of connected regions achieved by MV is substantially higher than the other methods while application of local regularization makes the number of connected regions following nicely the reference values.

Table 2 (top) summarizes the relative SUV_{mean} errors measured on PET images corrected for attenuation using the six different whole-body bone segmentation methods (PET-MRAC). The errors were measured voxel-

wise for all voxels in bony structures as well as in ROIs within high uptake regions in and near bone tissue. Similarly, the SUV_{mean} relative absolute errors are shown in Table 2 (bottom) averaged over 21 patients.

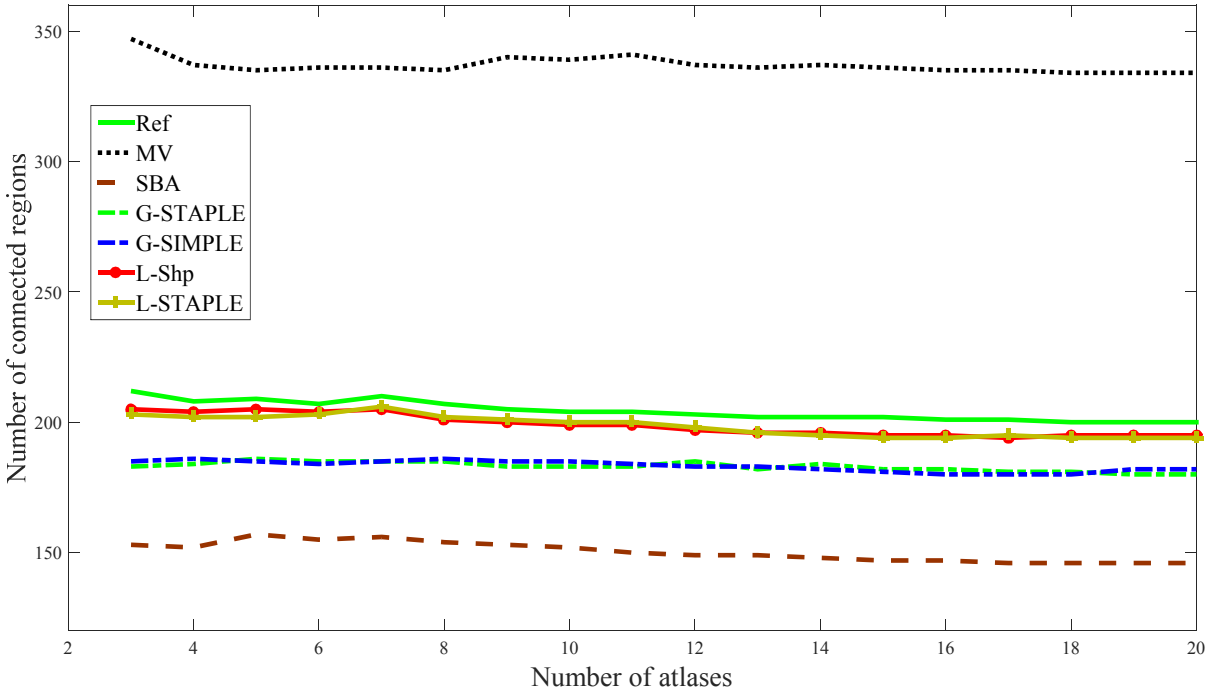

Figure 6. Performance of the different segmentation methods in terms of number of connected regions vs. the number of input atlases. *Ref* indicates the number of connected regions obtained from reference CT images.

Figure 7 depicts the joint histogram graphs obtained by plotting the correlation between PET images corrected for attenuation using the different bone segmentation methods (PET-MRAC) and the reference PET-CT image. The joint histograms are plotted by taking only voxels corresponding to bony structures into account. The L-STAPLE and L-Shp schemes yielded the best correlation for bone tissue y=1.01x +0.05 with R^2= 0.99 and y=1.02x +0.08 with R^2= 0.99, respectively, while the SBA method deviated from the identity line (y=0.87x +0.10 with R^2= 0.97). Figure 8 shows the error maps (relative bias) between reference PET-CT images and PET-MRAC images corrected for attenuation using the six different segmentation methods for one representative clinical study together with attenuation bias maps.

Table 2. Mean relative and absolute errors (bias) between SUV_{mean} estimated using the different PET-MRAC methods and PET-CT images in bony structures and lesions located in and near bone tissue.

Relative error	**Bony structures**	**Lesions in/near bony structures**
PET_SBA	-09.3±7.2	-05.3±5.3
PET_MV	06.1±6.9	04.4±5.0
PET_G-STAPLE	-04.2±5.9	-03.3±4.2
PET_G-SIMPLE	-04.1±4.9	-03.5±4.0
PET_L-STAPLE	02.7±4.3	01.4±3.8
PET_L-Shp	02.8±3.9	01.5±3.5
Relative absolute error	**Bony structures**	**Lesions in/near bony structures**
PET_SBA	15.9±6.2	12.1±5.0
PET_MV	12.3±6.0	10.5±4.8
PET_G-STAPLE	09.8±3.5	08.8±3.2
PET_G-SIMPLE	09.6±3.2	08.3±3.0
PET_L-STAPLE	06.1±2.9	05.6±2.8
PET_L-Shp	05.9±2.5	05.5±2.7

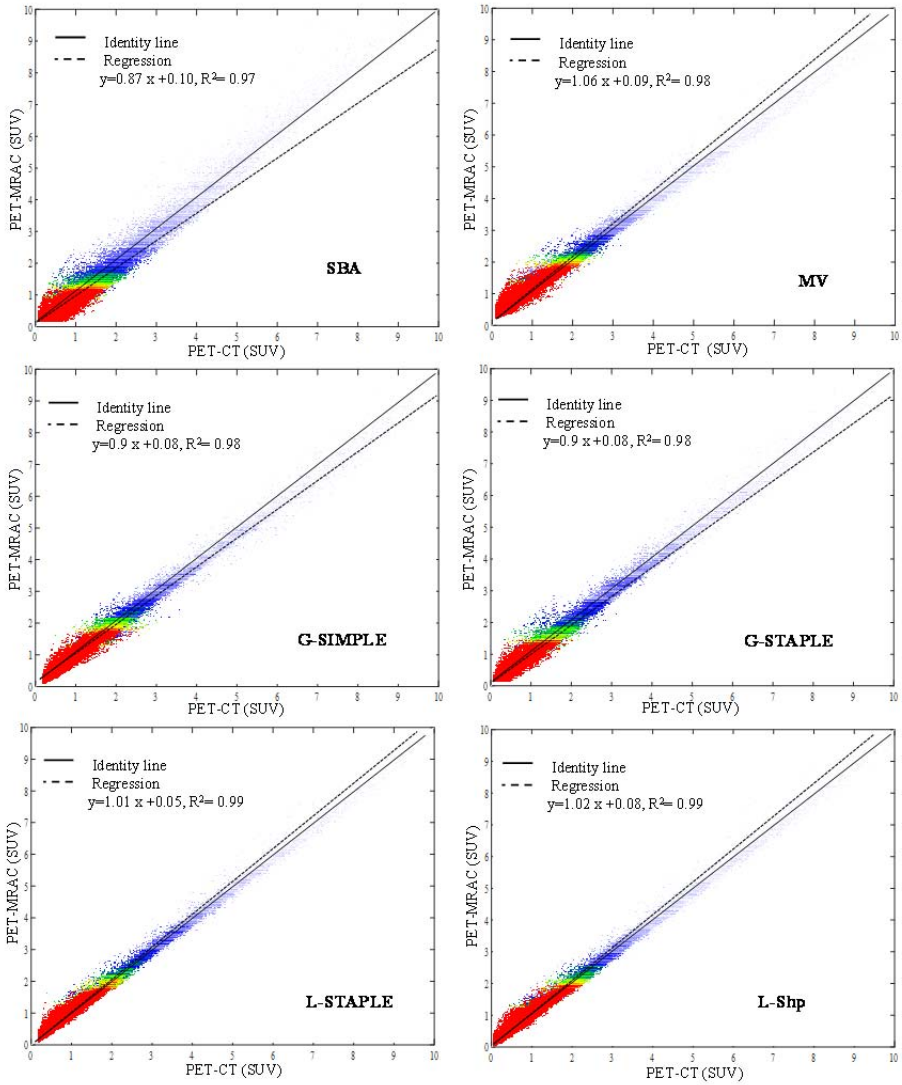

Figure 7. Joint histograms correlating tracer uptake values in bony structures from PET-MRAC images using the different whole-body bone segmentation methods with CT-based attenuation correction (PET-CT).

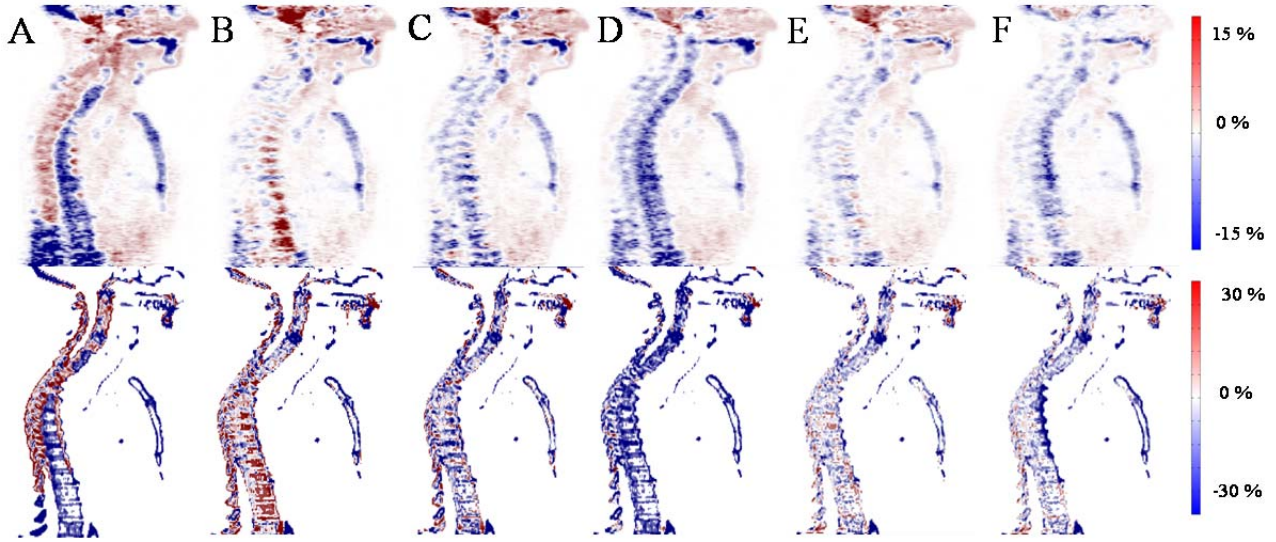

Figure 8. SUV bias maps between PET-CT and PET-MRAC images (top row) and attenuation error maps (bottom row) between reference CT images and attenuation maps generated by (A) SBA, (B) MV, (C) G-STAPLE, (D) G-SIMPLE, (E) L-STAPLE, and (F) L-Shp methods.

IV. Discussion

We assessed the performance of the SBA atlas fusion scheme for whole-body bone segmentation from Dixon MR images. Despite the promising performance reported in the literature [6, 8], the SBA method significantly underestimated bone identification in the context of whole-body imaging, even compared to MV atlas fusion scheme (Table 1 and figure 3). Due to the complexity of anatomical structures, large number of bone fragments, considerable anatomical variations across patients and greater likelihood of gross registration errors in whole-body imaging (compared to prostate segmentation), the performance of the SBA technique in whole-body bone identification is challenged.

The bone identification accuracy did not exceed 0.63 in terms of *Dice* metric when applying either the SBA or MV methods. SBA tended to overlook small fractions of bone tissues whereas the MV scheme led to dramatically increased factitious fragmentation (artificially disconnected regions in the resulting bone segmentation) (figures 3 and 6). The MV technique operates solely on binary label maps and reaches a conclusion based on the consensus of the atlas' votes, while SBA implicitly ignores the consensus of the raters by incorporating the labels' distance map (figure 1). As such, in the SBA method, one atlas might have greater impact than the combination of several other atlases, which can result in underestimation/missing of a small fraction of the target segmentation. Fragmentation of the continuous structures plays a minor role in the task of PET attenuation correction considering the processing steps applied to generate attenuation maps (downsampling, Gaussian smoothing). However, this performance measure is an important factor in other applications requiring bone segmentation, such as vertebral fracture and morphometric analysis of the osteochondral elements. Despite sub-optimal performance, the SBA method exhibited better convergence rate in terms of the number of input atlases, particularly compared to the MV method.

We proposed to combine the SBA scheme with an atlas selection/refinement technique to enhance the performance of the SBA method and at the same time sustain its superior convergence rate. To this end, the STAPLE method was chosen owing to its proven efficiency [25]. Moreover, the SIMPLE method exhibited similar performance when applied globally (G-SIMPLE) with relatively simpler implementation and lower computational complexity. However, the STAPLE method performed better when applied locally (L-STAPLE) compared to local SIMPLE, thus justifying to report only the results achieved by L-STAPLE. In addition, the proposed local shape-based similarity measure (L-Shp) substantially reduced the computation time by up to five times (figure 5) while enhancing the performance of the SBA method. The L-Shp method employed local atlas refinement scheme based on the measurement of the structure/shape similarity across the atlas label maps. In the L-STAPLE method, the atlas performance should be updated after each iteration and the whole algorithm takes on average 11 iterations to converge (in this study), while the L-Shp method computes the inter-atlas similarity matrix only once to generate weights to be inserted into the SBA atlas fusion scheme. In addition to the improved recognition rate when applying local regularization, the number of connected regions in the resulting label maps follows the reference true values, independent of the number of input atlases. Considering figure 4, combining local regularization methods (L-STAPLE and L-Shp) with the SBA scheme sustained the convergence rate of the original SBA to some extent.

The quantitative evaluation of the SUV bias demonstrated a similar trend to that of bone segmentation accuracy while PET images showed less sensitivity to errors in bone identification owing to lower spatial resolution and higher level of noise. Both L-STAPLE and L-Shp methods resulted in less than 3% SUV mean relative and less than 6% mean absolute errors in bony structures due to superior bone identification. The joint histogram plot and regression analysis also support the voxel-wise and ROI analysis of activity recovery. In this work, we used the 3-class MRI segmentation-based attenuation map for all methods followed by superimposition of only the bone tissue obtained using the different methods. The same 3-class attenuation map with bone tissue derived from reference CT was taken as reference attenuation map. However, a small SUV bias was observed in soft-tissue regions (even far from bony structures). This may be partially due to differences in scatter correction and the inherent smoothing during the generation of attenuation maps.

The results presented in this work demonstrate that the developed methods are promising and can potentially be used in the clinic. However, atlas-based segmentation techniques consist of some key steps where each step plays a critical role in the quality of the ultimate outcome. The first step is the creation of the atlas data set that should cover a reasonably wide variability of the human anatomy, with a sufficient number of samples for each category based for instance on gender, pathology, body weight and length, body mass index, sitting

height/stature ratio,…etc. The richness of the atlas data set greatly influences the quality of outcomes since it increases the likelihood of finding an atlas similar to the target subject. The registration algorithm and optimization of their associated free parameters are also important determining factors. The final step is the atlas fusion task, which determines the segmentation output while trying to minimize the non-systematic errors arising from the previous steps. In this light, atlas-based methods entail many steps and free parameters that need to be optimized prior to potential use in the clinic. These issues question the robustness of the atlas-based techniques to be utilized as the method of choice. Therefore, despite the superior performance of atlas-based methods, as reported in this study and numerous previous works, the shift toward clinical implementation of these techniques is only gradual.

It's the intention of the authors to make the algorithms presented in this work available to the research community under the terms of the GNU Lesser General Public License version. This also applies to the CT/MRI atlases provided approval from our institution/IRB is secured.

V. Conclusion

In this work, we evaluated the performance of the SBA atlas fusion scheme in the context of whole-body bone segmentation from MR images. The SBA technique exhibited sub-optimal performance compared to conventional MV atlas fusion scheme. To enhance the performance of the SBA method, the technique was combined with STAPLE and SIMPLE atlas selection (refinement) methods. Local (voxel-wise) application of the STAPLE method led to dramatic improvement of bone fragmentation and recognition accuracy despite the high computation time. Moreover, a shape comparison based atlas weighting scheme (L-Shp) was proposed, which achieved similar results to L-STAPE while considerably diminishing the computational burden. The quantitative SUV analysis revealed good correlation between PET images corrected for attenuation using both L-STAPLE and L-Shp methods and the corresponding reference CT images. The technique is promising for potential application in MRI-guided attenuation correction in whole-body PET/MRI.

Acknowledgments

This work was supported by the Swiss National Science Foundation under grant SNFN 31003A-149957 and the Swiss Cancer Research Foundation under Grant KFS-3855-02-2016.

References

[1] T. Rohlfing, R. Brandt, R. Menzel, and C. R. Maurer Jr, "Evaluation of atlas selection strategies for atlas-based image segmentation with application to confocal microscopy images of bee brains," *NeuroImage,* vol. 21, pp. 1428-1442, 4// 2004.

[2] X. Artaechevarria, A. Munoz-Barrutia, and C. Ortiz-de-Solorzano, "Combination Strategies in Multi-Atlas Image Segmentation: Application to Brain MR Data," *Medical Imaging, IEEE Transactions on,* vol. 28, pp. 1266-1277, 2009.

[3] T. Rohlfing and C. R. Maurer, "Multi-classifier framework for atlas-based image segmentation," *Pattern Recognition Letters,* vol. 26, pp. 2070-2079, 2005.

[4] J. Kittler, M. Hatef, R. P. W. Duin, and J. Matas, "On combining classifiers," *Pattern Analysis and Machine Intelligence, IEEE Transactions on,* vol. 20, pp. 226-239, 1998.

[5] P. Aljabar, R. A. Heckemann, A. Hammers, J. V. Hajnal, and D. Rueckert, "Multi-atlas based segmentation of brain images: Atlas selection and its effect on accuracy," *NeuroImage,* vol. 46, pp. 726-738, 7/1/ 2009.

[6] T. Rohlfing and C. R. Maurer Jr, "Shape-based averaging for combination of multiple segmentations," in *Medical Image Computing and Computer-Assisted Intervention–MICCAI 2005*, ed: Springer, 2005, pp. 838-845.

[7] T. Rohlfing and C. R. Maurer, Jr., "Shape-Based Averaging," *Image Processing, IEEE Transactions on,* vol. 16, pp. 153-161, 2007.

[8] N. Robitaille and S. Duchesne, "Label fusion strategy selection," *International journal of biomedical imaging,* vol. 2012, 2012.

[9] S. K. Warfield, K. H. Zou, and W. M. Wells, "Simultaneous truth and performance level estimation (STAPLE): an algorithm for the validation of image segmentation," *Medical Imaging, IEEE Transactions on,* vol. 23, pp. 903-921, 2004.

[10] J. C. Mazziotta, A. W. Toga, A. Evans, P. Fox, and J. Lancaster, "A probabilistic atlas of the human brain: theory and rationale for its development the international consortium for brain mapping (ICBM)," *Neuroimage,* vol. 2, pp. 89-101, 1995.

[11] A. Mehranian, H. Arabi, and H. Zaidi, "Vision 20/20: Magnetic resonance imaging-guided attenuation correction in PET/MRI: Challenges, solutions, and opportunities.," *Med Phys,* vol. 43, pp. 1130-1155, 2016.

[12] V. Keereman, Y. Fierens, T. Broux, Y. De Deene, M. Lonneux, and S. Vandenberghe, "MRI-based attenuation correction for PET/MRI using ultrashort echo time sequences.," *J Nucl Med,* vol. 51, pp. 812-818, May 2010.

[13] G. Delso, F. Wiesinger, L. Sacolick, S. Kaushik, D. Shanbhag, M. Hullner*, et al.*, "Clinical evaluation of zero echo time MRI for the segmentation of the skull.," *J Nucl Med,* vol. 56, pp. 417-422, Feb 12 2015.

[14] N. Burgos, M. Cardoso, K. Thielemans, M. Modat, J. Schott, J. Duncan*, et al.*, "Attenuation correction synthesis for hybrid PET-MR scanners: Application to brain studies.," *IEEE Trans Med Imaging,* vol. 33, pp. 2332-2341, Jul 17 2014.

[15] S. D. Wollenweber, S. Ambwani, G. Delso, A. H. R. Lonn, R. Mullick, F. Wiesinger*, et al.*, "Evaluation of an atlas-based PET head attenuation correction using PET/CT & MR patient data.," *IEEE Trans Nucl Sci,* vol. 60, pp. 3383-3390, 2013.

[16] D. Izquierdo-Garcia, A. E. Hansen, S. Forster, D. Benoit, S. Schachoff, S. Furst*, et al.*, "An SPM8-based approach for attenuation correction combining segmentation and nonrigid template formation: Application to simultaneous PET/MR brain imaging.," *J Nucl Med,* vol. 55, pp. 1825-1830, Nov 2014.

[17] A. Mehranian, H. Arabi, and H. Zaidi, "Quantitative analysis of MRI-guided attenuation correction techniques in time-of-flight brain PET/MRI," *NeuroImage,* vol. 130, pp. 123-133, 2016.

[18] H. Arabi and H. Zaidi, "Magnetic resonance imaging-guided attenuation correction in whole-body PET/MRI using a sorted atlas approach.," *Med Image Anal,* vol. 31, pp. 1-15, 7, 2016.

[19] H. Arabi and H. Zaidi, "One registration multi-atlas-based pseudo-CT generation for attenuation correction in PET/MRI.," *Eur J Nucl Med Mol Imaging,* Vol. 43, No. 11, pp 2021-2035, 2016.

[20] M. Hofmann, I. Bezrukov, F. Mantlik, P. Aschoff, F. Steinke, T. Beyer*, et al.*, "MRI-based attenuation correction for whole-body PET/MRI: Quantitative evaluation of segmentation- and Atlas-based methods.," *J Nucl Med,* vol. 52, pp. 1392-1399, Sep 2011.

[21] H. Arabi and H. Zaidi, "Comparison of atlas-based bone segmentation methods in whole-body PET/MRI," *IEEE Nuclear Science Symposium & Medical Imaging Conference,* vol. Seattle, USA, 2014.

[22] T. R. Langerak, U. A. Van Der Heide, A. N. Kotte, M. A. Viergever, M. Van Vulpen, and J. P. Pluim, "Label fusion in atlas-based segmentation using a selective and iterative method for performance level estimation (SIMPLE)," *Medical Imaging, IEEE Transactions on,* vol. 29, pp. 2000-2008, 2010.

[23] H. Zaidi, N. Ojha, M. Morich, J. Griesmer, Z. Hu, P. Maniawski*, et al.*, "Design and performance evaluation of a whole-body Ingenuity TF PET-MRI system.," *Phys Med Biol,* vol. 56, pp. 3091-3106, Apr 20 2011.

[24] W. T. Dixon, "Simple proton spectroscopic imaging.," *Radiology,* vol. 153, pp. 189-194, Oct 1984.

[25] J. M. Lotjonen, R. Wolz, J. R. Koikkalainen, L. Thurfjell, G. Waldemar, H. Soininen*, et al.*, "Fast and robust multi-atlas segmentation of brain magnetic resonance images.," *Neuroimage,* vol. 49, pp. 2352-2365, Feb 1 2010.

[26] Y. Zhuge, J. K. Udupa, J. Liu, and P. K. Saha, "Image background inhomogeneity correction in MRI via intensity standardization," *Computerized Medical Imaging and Graphics,* vol. 33, pp. 7-16, 2009.

[27] L. G. Nyúl, J. K. Udupa, and X. Zhang, "New variants of a method of MRI scale standardization," *Medical Imaging, IEEE Transactions on,* vol. 19, pp. 143-150, 2000.

[28] J. Weickert, *Anisotropic diffusion in image processing* vol. 1: Teubner Stuttgart, 1998.

[29] N. J. Tustison, B. B. Avants, P. A. Cook, Y. Zheng, A. Egan, P. A. Yushkevich*, et al.*, "N4ITK: improved N3 bias correction.," *IEEE Trans Med Imaging,* vol. 29, pp. 1310-1320, Jun 2010.

[30] M. J. McAuliffe, F. M. Lalonde, D. McGarry, W. Gandler, K. Csaky, and B. L. Trus, "Medical Image Processing, Analysis and Visualization in clinical research," in *14th IEEE Symposium on Computer-Based Medical Systems, 2001. CBMS 2001. Proceedings*, 2001, pp. 381-386.

[31] A. P. Dempster, N. M. Laird, and D. B. Rubin, "Maximum likelihood from incomplete data via the EM algorithm," *Journal of the royal statistical society. Series B (methodological),* pp. 1-38, 1977.

[32] A. J. Asman and B. A. Landman, "Formulating spatially varying performance in the statistical fusion framework," *Medical Imaging, IEEE Transactions on,* vol. 31, pp. 1326-1336, 2012.

[33] D. Cremers, S. J. Osher, and S. Soatto, "Kernel density estimation and intrinsic alignment for shape priors in level set segmentation," *International Journal of Computer Vision,* vol. 69, pp. 335-351, 2006.

[34] D. Mattes, D. R. Haynor, H. Vesselle, T. K. Lewellen, and W. Eubank, "PET-CT image registration in the chest using free-form deformations.," *IEEE Trans Med Imaging,* vol. 22, pp. 120-128, Jan 2003.

[35] S. Klein, M. Staring, K. Murphy, M. A. Viergever, and J. P. W. Pluim, "elastix: A toolbox for intensity-based medical image registration.," *IEEE Trans Med Imaging,* vol. 29, pp. 196-205, 2010.

[36] H. Arabi, O. Rager, A. Alem, A. Varoquaux, M. Becker, and H. Zaidi, "Clinical assessment of MR-guided 3-class and 4-class attenuation correction in PET/MR," *Mol Imaging Biol,* vol. 17, pp. 264-276, 2015.

[37] A. Akbarzadeh, D. Gutierrez, A. Baskin, M. R. Ay, A. Ahmadian, N. Riahi Alam*, et al.*, "Evaluation of whole-body MR to CT deformable image registration.," *J Appl Clin Med Phys,* vol. 14, pp. 238-253, 2013.

[38] L. R. Dice, "Measures of the amount of ecologic association between species.," *Ecology,* vol. 26, pp. 297-302, 1945.

[39] T. Heimann, B. van Ginneken, M. A. Styner, Y. Arzhaeva, V. Aurich, C. Bauer*, et al.*, "Comparison and evaluation of methods for liver segmentation from CT datasets.," *IEEE Trans Med Imaging,* vol. 28, pp. 1251-1265, Aug 2009.

[40] D. L. Collins and J. C. Pruessner, "Towards accurate, automatic segmentation of the hippocampus and amygdala from MRI by augmenting ANIMAL with a template library and label fusion.," *Neuroimage,* vol. 52, pp. 1355-1366, Oct 1 2010.

[41] Y. Xia, J. Fripp, S. S. Chandra, R. Schwarz, C. Engstrom, and S. Crozier, "Automated bone segmentation from large field of view 3D MR images of the hip joint.," *Phys Med Biol,* vol. 58, pp. 7375-7390, 2013.

[42] G. Gerig, M. Jomier, and M. Chakos, "Valmet: A New Validation Tool for Assessing and Improving 3D Object Segmentation," presented at the Proceedings of the 4th International Conference on Medical Image Computing and Computer-Assisted Intervention, 2001.

[43] W. R. Crum, O. Camara, and D. L. Hill, "Generalized overlap measures for evaluation and validation in medical image analysis," *Medical Imaging, IEEE Transactions on,* vol. 25, pp. 1451-1461, 2006.

[44] A. Klein, J. Andersson, B. A. Ardekani, J. Ashburner, B. Avants, M.-C. Chiang*, et al.*, "Evaluation of 14 nonlinear deformation algorithms applied to human brain MRI registration," *Neuroimage,* vol. 46, pp. 786-802, 2009.

[45] J. Zaknun, C. Bal, A. Maes, S. Tepmongkol, S. Vazquez, P. Dupont*, et al.*, "Comparative analysis of MR imaging, Ictal SPECT and EEG in temporal lobe epilepsy: a prospective IAEA multi-center study.," *Eur J Nuc Med Mol Imaging,* vol. 35, pp. 107-115, 2008/01/09/ 2008.

[46] V. Schulz, I. Torres-Espallardo, S. Renisch, Z. Hu, N. Ojha, P. Börnert*, et al.*, "Automatic, three-segment, MR-based attenuation correction for whole-body PET/MR data.," *Eur J Nucl Med Mol Imaging,* vol. 38, pp. 138-152, 2011.

[47] J. P. Carney, D. W. Townsend, V. Rappoport, and B. Bendriem, "Method for transforming CT images for attenuation correction in PET/CT imaging.," *Med Phys,* vol. 33, pp. 976-983, 2006.

Chapter 10

Conclusions and future perspectives

I. Conclusions

The synergy given by combining PET and MRI imaging systems has offered new opportunities for improving the diagnostic confidence of PET findings as well as enhancing the patient treatment precision. Despite great advantages of new PET/MR hybrid imaging systems, new techniques and innovative solutions are required to coup with their associated challenges and drawbacks in instrumentation, data acquisition and quantitative performance. For maximum realization of the hybrid PET/MR imaging potentials, the key limiting factors should be properly addressed to facilitate its research and clinical applications. This dissertation aimed at evaluation and development of new algorithms that are designed to offer robust and practical solutions for the key challenges and major limitations of quantitative procedures and data analysis in the hybrid PET/MR imaging. The main contributions achieved during this dissertation are summarized in the following:

1. The quantitative accuracy of MRI-based attenuation correction techniques being used in clinical practice were compared using a dataset of clinical cases. The evaluated methods consist of two most frequently used techniques in clinical practice, namely the 3-class attenuation map implemented on the Ingenuity TF PET/MRI and the 4-class attenuation map similar to the approach used on the Siemens mMR PET/MR. These two scanners were chosen for this study because they are widely used in clinic and the evaluation of their performances allows us for further improvement of these strategies and offering new effective solutions. Considerable underestimation of activity accumultion was observed in bone ti The accurate bias assessment and quantitative anaylsis of the available AC methods allowed us to address their shortcomings and potentials source of errors in our future studies.

2. The PET/MR attenuation correction strategies being used in clinics for whole-body imaging suffer from a separate bone tissue class which leads to significant underestimation of activity recovery in PET images. In addition, patient-specific lung attenuation estimation was lacking in most of the available strategies. Thus, a new pseudo-CT generation approach was proposed for accurate extraction of bones and estimation of lung attenuation properties. The presented approach aimed to improve the Gaussian process regression (GPR) kernel proposed by Hofmann et al. (J Nucl Med 2011). The atlas dataset was sorted on the basis of local normalized cross-correlation to select the most similar image in the atlas dataset for each voxel. For lung tissue, the existing correlation between lung volume and corresponding attenuation properties of lung was utilized to predict patient-specific lung attenuation coefficients. Moreover, abnormal anatomical variations were addressed by segmentation of the lesions on PET images followed by assignment of soft-tissue attenuation coefficient. The proposed technique showed better overall PET quantification accuracy than both Hofmann's and the 3-class approaches owing to the more accurate extraction of bones and better prediction of lung attenuation coefficients.

3. Due to the fact that bony structures play key role in accuracy of whole-body attenuation map, an extensive performance comparison of whole-body bone identification from MR images were conducted exploiting a number of atlas-based segmentation methods. The promising approaches were then employed for the purpose of MR-derived PET attenuation map generation. To this end, a variety of atlas-based segmentation strategies, which are commonly used in the field of medical image segmentation and pseudo-CT generation, were implemented and evaluated using a clinical dataset of whole-body MR images. Despite promising performance of local weighted atlas-based segmenation methods, one of the major challenges of these approaches is the long processing time taken by atlas registration. Therefore, to address this issue, a novel method was proposed that consists of only one online registration between the target and reference images, regardless of the number of atlas images (N), while for the remaining atlas images, the pre-computed transformation matrices to the reference image are used to align them to the target image. The quantitative analysis revealed a good correlation between PET images corrected for attenuation using the proposed pseudo-CT generation approach and the corresponding CT images. The computational time is reduced by a factor 1/N (number of atlas images) at the expense of a modest decrease in quantitative accuracy, thus introduced new apportunity for using large data set of atlas image for generation of whole-body attenuatin maps.

4. Generation of μ-map from MR images not only can be used for the task of PET/MR attenuation correction but also for MR-alone radiation therapy planning. Radiation therapy treatment planning is challenged by the lack of a direct link between MRI voxel intensities and electron density. A novel two-step (segmentation and fusion) atlas-based algorithm was proposed for accurate bone tissue identification on a dataset of pelvis images. The aim was to generate μ-map for the purpose of radiation therapy planning for treatment of prostate and rectum cancers. First, the bone segmentation of the target image is optimized through local weighted atlas voting then the obtained bone map is used to assess the quality of deformed atlases to perform voxel-wise weighted atlas fusion. A dosimetric evaluation of volumetric modulated arc therapy photon treatment plans proved promising performance of the purposed method to be used in MR-only radiatin therapy planning.

5. An extensive and comperhensive review of major researches performed during the last decade was accomplished dealing with solutions and addressing the major limitations in deriving PET/MR attenuation maps. Generally, the MRAC techniques were categorized in to three major groups of segmentation-, atlas registration- and emission-based methods. Then, the characteristics, key performance parameters and recent advances of the described method were elaborated. The outlook section of the work dealt with prospective development in this field. The most promising attenuation correction methods are expected to be achieved through hybrid techniques benefiting from added advantages of the different categories of MRAC methods to avoid or minimize shortcoming of each individual method. Moreover, technological advances in PET detector designs and electronics are expected to dramaticly improve the timing resolution of the PET scanners leading to ever more accurate TOF PET imaging. Concerently, the MR imaging technology, in particular U/ZTE sequences, will steadly continue to advance creating new opportunities to address the issue of attenuation correction in PET/MR imaing and might finally put an end to the researches in this field.

6. Despite extensive evaluation and analysis of each individual MR-guided AC algorithms, there was a need to objectively compare the accuracy different strategies using a common ground in order to put into prespective the merits and negative aspects of each approach. To this end, a number of strategies (which are considered as the most promising and common approahes) have been developed for MRI-guided attenuation correction were quantitatively evaluated and compared. These methods include three generic attenuation correction methods of standard 3-class MR segmentation-based (segmentation-based approach), advanced atlas-registration-based (atlas-based approach) and emission-based approaches (simultaneous activey and attenuation estimation approach) in the context of brain time-of-flight (TOF) PET/MRI. Considering the accuracy of bone identification and quantification of PET tracer uptake, 3-class attenuation map led to significant underestimation of the PET tracer uptake, while the proposed MLAA-AC methods were unable to remarkably reduce quantification errors. On the other hand, the atlas-AC method provided the most accurate attenuation maps in terms of bone prediction accuracy, and thus the lowest quantification bias. For brain imaging atlas-based methods can generate adequately accurate attenuation map leading to minimal PET quantification errors.

7. For whole-body bone segmenation, we proposed and evaluated the Shape-based averaging (SBA) method with is a promising scheme of atlas fusion. The performance of SBA method was improved through incorporation of local regularisation to maximize bone segmentation accuracy. The outstanding advantage of the improved SBA method is its ability to generate robust whole-body segmentation through exploiting small number of input atlases as well as minimal fragementation errors compared to other conventional atlas fusion methods.

II. Future perspectives

The studies conducted in this dissertation addressed the multimodal molecular imaging in particular hybrid PET/MR imaging. The day in day out advancement in instrumentation, data acquisition procedure and signal processing has introduced great opportunities to realize the synergy associated with multimodal imaging and complementary structural and molecular information. Logically, prospective researches in this field would deal with further development, evaluation and commercialization of the proposed algorithms and methods to enhance the performance of current dual-modality PET/MR imaging systems and upgrading existing systems for the next generation.

The quantitative accuracy of existing MRI-based attenuation correction techniques being used in clinical practice gave us precious insight into how to prevent or minimize quantification biases and to eliminate potential sources of artifacts and errors in the whole-body PET imaging. Despite the fact that the average biases observed in most of the tissues/organs/lesions happened to fall within the clinically acceptable range error (10%), remarkable artifacts and significant biases were observed in some patients, which might adversely influence the diagnostic confidence. Although there are a large number of evaluation studies, future work might also include more extensive evaluation of attenuation correction techniques in clinical practice not only in whole-body imaging but also for brain, pelvis and breast imaging employing reasonably large dataset of clinical cases to examine the robustness and detect the drawbacks of the available methods. Considering the so far published results, lack of separate bone class, non-patient-specific lung attenuation value, presence of the abnormal anatomy and segmentation errors would attract most of the future investments and research efforts in order to boost the robustness of current techniques and enhance the confidence of the PET findings.

In this dissertation, we conducted three comprehensive researches dealing with whole-body bone segmentation from MR images. The motivation behind these studies was the fact that ignorance of bone tissue in PET attenuation maps has been considered to be the primary cause of errors in radiotracer uptake recovery. Moreover, high level of noise, low quality of the dedicated MR sequence for generation of PET attenuation map and presence of remarkable partial volume effects, have made the bone segmentation from MR images a major challenge not only in PET/MR AC but also in MR-alone radiation therapy and patho-anatomical conditions analysis. Among various segmentation techniques, atlas-based methods, particularly in whole-body imaging, exhibited promising performance and superior outcomes in terms of bone segmentation accuracy. However, in case of gross anatomical abnormality or presence of metallic implants these algorithms failed to fully identify the correct volume of the bony structures and artificial inserts. A possible direction for future research in this field would be through integration of the other state-of-arts segmentation algorithms in order to cover the shortcomings of the atlas-based methods. On the other hand, creating large database of atlas images representing a wide range of anatomical difference, body poses and ages would enable us to perform more versatile and accurate atlas-based segmentations. Despite promising performance of the atlas-based method to identify the bone volume, yet patient-specific bone attenuation value estimation warrants special consideration. Perfect bone identification with wrong or non-patient specific attenuation value would lead to significant quantification biases. In this regard, there are some works trying to establish a link between MR intensity and bone density/linear attenuation coefficient. However, their performances are not yet validated using large number of patients or different MR sequences. Combining the great performance of atlas-based method in bone volume identification with patient-specific estimation of bone attenuation value would minimize radiotracer recovery errors in PET/MR images.

In brain imaging, there is a possibility to identify bone volume using the dedicated MR sequences such as UTE/ZTE in order to generate PET/MR attenuation map with a distinct bone tissue class. However, in whole-body imaging this possibility is not yet available due to prohibitive long acquisition time. Therefore, atlas-based pseudo-CT generation methods play key role to develop MR-guided attenuation maps containing distinct bone tissue in whole-body imaging. Similar to atlas-based bone segmentation from MR images, whole-body atlas-based pseudo CT generation suffers from rare anatomical variations, particularly when the atlas dataset lacks any similar cases. In our proposed methods, we tried to minimize this effect through employing advanced image processing techniques to find the best matches within the atlas dataset. This strategy significantly enhanced the performance of the atlas-based pseudo-CT generation; however this issue is still an open research area. Creating and employing of large database of atlas images classified based on patients´ sex, age, specific pathology and body posture can help the advanced atlas-based methods to effectively identify rare anatomical variations

leading to flawless pseudo-CT generation. The other challenge in whole-body pseudo-CT generation, apart from large anatomy variations, is patient-specific estimation of attenuation value particularly for the lung tissues. Although applying the advanced atlas-based methods equipped with techniques of image similarity measurement led to closer estimation of bone and lung attenuation values, this issue could be the topic of future works. Exploiting the advantages of the other AC methods, such as simultaneous emission and activity estimation and UTE/ZTE MR sequences together with atlas-based methods can offer desirable solutions for this issue.

One of the major drawbacks of atlas-based methods is considerably high computation time taken by the process of atlas registration, particularly in whole-body imaging where larger field of view and higher size of the images add to this problem. In this dissertation, we proposed a novel approach to address this issue, which tremendously reduced the computational time of the atlas-based methods. This approach enables us to utilize larger database of atlas images covering wide range of anatomical variation and body posture without increasing the complexity of problem or burdening the computation process. Even though this approach introduced non-negligible compromise between accuracy of outcome and the processing time, employing advanced registration algorithm or developing dedicated image alignment approaches for this purpose can minimize the adverse effect of the proposed method.

MRI-only radiation therapy has been developed to reduce non-therapeutic radiation exposure. Radiation therapy consists of a series of procedures, namely therapy planning, treatment delivery, and therapy adaptation during the course of treatment. Since CT imaging provides accurate electron-density map of body, it has not yet been replaced with MRI due to technical challenges to derive electron density information from MR images, in particular for bony tissue, required for dose calculations. Nevertheless, many research centers and institutes have been focusing on developing new workflow and demonstration of fully integrated MRI solution for radiation therapy. The prospective advantages of such a concept would to be improved tissue contouring due to superior soft-tissue contrast of MRI, enhanced precision in soft-tissue therapy setup, use of biological information at treatment planning and imaging of therapy response. Besides, eliminating the x-ray imaging from the radiation therapy chain introduces additional benefit of the “out-of-target dose” reduction. To generate electron density map solely based on MRI, we proposed a novel pseudo-CT generation approach based on the conventional MR images for the radiation treatment planning dealing with prostate and rectum cancers. The proposed method significantly improved the accuracy of surrogate CT prediction in pelvis imaging leading to acceptable treatment planning and dose measurement. A prospective application of the proposed method could be in the real-time MRI-guided radiotherapy, which will become available for clinical practices using a hybrid MRI-linac modality. MR-based techniques seem to play key role in providing adaptive radiation treatments in the future provided the hurdle of the electron density estimation based on only MR data is overcome. The proposed method can be easily applied to other body regions, such as the brain, and even to whole-body PET/MR imaging.

In the comparison study conducted in this dissertation, a number of methods were developed and implemented for MRI-guided attenuation correction. These methods belong to different generic AC strategies evaluated separately showing different degrees of success in terms of quantitative PET imaging. These methods are either used in clinical practice or are considered as the state-of-the-art in the field of PET/MR AC, consisting of standard 3-class MR segmentation-based, advanced atlas-registration-based and emission-based approaches in the context of brain time-of-flight (TOF) PET/MRI. The quantitative performance of three generic attenuation correction methods was evaluated using a dataset of brain images acquired from TOF PET/CT and MR imaging. It was found that the segmentation-based and emission based AC methods results in a signification underestimation of PET tracer uptake, in contrast, the advanced atlas-AC method was able to predict more accurate patient-specific attenuation maps. There is a need for further development of the emission-based AC method for the current TOF timing resolution of PET scanners, since this method has the outstanding merit of patient-specific metallic implant detection, anatomical abnormality prediction and patient-specific attenuation value estimation. Further evaluation of atlas-registration AC methods, in comparison with other generic methods, using a larger clinical database for example with patients from different age groups and pathological indications is warranted. Since this study was conducted in brain imaging, PET/MR AC methods which employ the UTE or ZTE sequences could also have been involved in order to give a comprehensive insight into MR-guided attenuation correction (at least in brain imaging).

Acknowledgements

Undertaking this PhD has been a truly life-changing experience for me and it would not have been possible to do without the support and guidance that I received from my supervisor and colleagues. During this thesis period, there are many people who have supported me in many ways to the realisation of this thesis. I extremely acknowledge my deep gratitude and appreciations to all of them. Hence, I would like to take this opportunity to acknowledge all of them.

I would like to first say a very big thank you to my supervisor Prof. Habib Zaidi for all the support and encouragement he gave me during my PhD program. Without his guidance and constant feedback, this PhD would not have been achievable. Over these years, he encouraged me to have initiative in conducting the projects and to develop the necessary skills for becoming an independent early-stage researcher. Habib has been supportive and has given me the freedom to pursue various projects without objection. I am also very grateful to Habib for his scientific advice and knowledge and many insightful discussions and suggestions.

I would like to extend my gratitude to Prof. Sviatoslav Voloshynovskiy, my thesis co-advisor, for continuous encouragements and taking the administrative measures of my thesis and examinations. I am really impressed by his friendly and kind interaction with his students. Again, I am sincerely grateful for all his supports.

I would like to thank Prof. Mohammad Reza Ay, my former boss at PNP company, who believed in my abilities and encouraged me to follow a PhD program at PinLab.

I am grateful to the members of the jury, Profs. R. Boellaard, S. Ziegler, H. Ammari and K. Lovblad for examining my thesis. I am highly honored by the presence these high profile academic people, celebrated experts in the field of medical physics and nuclear medicine, as the members of jury.

I also would like to mention and thank to my entire colleagues and friends at the department of nuclear medicine and PinLab, Abolfazl Mehranian, Fotis Kotasidis, Nikolaos Karakatsanis, Tianwu Xie, Giulia Di Domenicantonio, Jan Perhac, Sara Trombella and David Garcia for providing support and friendship that I needed.

My appreciation also goes to the reviewers of my journal articles for their constructive criticisms and suggestions that undoubtedly improved the overall quality of my work. Several reviewers of various scientific journals are especially thanked for their constructive comments and suggestions that improved the scientific sspect of my journal articles.

I thank the Swiss National Science Foundation and Geneva Cancer League for financial support.

I also would like especially thank to all the staff of the department of nuclear medicine at HUG for being warm, cordial, supportive and creating friendly environment in the department.

Last but not least, I would like to express my deepest gratitude to my parents for their support, encouragement and devotion.

Hossein Arabi

09 Sep 2016
Geneva

List of publications

Peer-reviewed journals

1. Arabi H, Rager O, Alem A, Varoquaux A, Becker M and Zaidi H "Clinical assessment of MRI-guided 3-class and 4-class attenuation correction in PET/MR" **Mol Imaging Biol** Vol. 17, No. 2, pp 264-276 (2015).

2. Mehranian A, Arabi H and Zaidi H "Magnetic resonance imaging-guided attenuation correction in PET/MRI: Challenges, solutions and opportunities" **Med Phys** Vol. 43, No. 3, pp 1130-1155 (2016).

3. Arabi H and Zaidi H "MRI-guided attenuation correction in whole-body PET/MRI using a sorted atlas approach" **Med Imag Anal** Vol. 31, No. July, pp 1-15 (2016).

4. Mehranian A, Arabi H and Zaidi H "Quantitative analysis of MRI-guided attenuation correction methods in time-of-flight brain PET/MRI" **Neuroimage** Vol. 130, No. April, pp 123-133 (2016).

5. Arabi H and Zaidi H "One registration multi atlas-based pseudo-CT generation for attenuation correction in PET/MRI" **Eur J Nucl Med Mol Imaging** Vol. 43, No. 11, pp 2021-2035 (2016).

6. Arabi H, Koutsouvelis N, Rouzaud M, Miralbell R and Zaidi H "Atlas-guided generation of pseudoCT images for hybrid PET-MRI and MR-only based radiotherapy treatment planning" **Phys Med Biol** Vol. 61, No. 17, pp 6531-6552 (2016).

7. Arabi H and Zaidi H "Whole-body bone segmentation from MRI for PET/MRI attenuation correction using shape-based averaging" **Med Phys** Vol. 43, No. 11, pp 5848-5861 (2016).

8. Arabi H and Zaidi "Comparison of atlas-based techniques for whole-body bone segmentation" **Med Image Anal** Vol. 36, pp 98–112 (2017).

9. Arabi H, Kamali-Asl AR, Ay MR and Zaidi H "Monte Carlo-based assessment of the trade-off between spatial resolution, field-of-view and scattered radiation in the variable resolution x-ray CT scanner" **Phys Med** Vol. 31, No. 5, pp 510-516 (2015).

10. Sajedi S, Zeraatkar N, Moji M, Farahani M H, Sarkar S, Arabi H, Teymoorian B, Ghafarian P, Rahmim A, Ay M R "Design and Development of a High Resolution Animal SPECT Scanner Dedicated for Rat and Mouse Imaging" **Nucl. Instr. Meth. Phys**. **Res** Vol. 741, No. March, pp 169–176 (2014).

11. Zeraatkar N, Sajedi S, Farahani M H, Arabi H, Sarkar S, Ghafarian P, Rahmim A, Ay M R "Resolution-recovery-embedded image reconstruction for a high-resolution animal SPECT system" **Physica Medica** Vol. 30 No.7, pp 774–781 (2014).

Conferences proceedings and abstracts

1. Arabi H and Zaidi H "Comparison of atlas-based bone segmentation methods in whole-body PET/MRI" **IEEE Nuclear Science Symposium & Medical Imaging Conference**, Seattle, USA, 8 – 15 November 2014, pp 1-4.
2. Arabi H and Zaidi H "MRI-based pseudo-CT generation using sorted atlas images in whole-body PET/MRI" **IEEE Nuclear Science Symposium & Medical Imaging Conference**, Seattle, USA, 8 – 15 November 2014, pp 1-4.

3. Arabi H and Zaidi H "Fast atlas-based MRI-guided PET attenuation map generation in whole-body PET/MR imaging" **IEEE Nuclear Science Symposium & Medical Imaging Conference**, San Diego, USA, 31 October – 7 November 2015, pp 1-4.
4. Arabi H, Rager O, Alem A, Varoquaux A, Becker M and Zaidi H "Comparison of MRI-guided attenuation correction strategies in PET/MRI" **60th SNMMI Annual Meeting**, Saint-Louis, USA, 7–11 June 2014, J Nucl Med, Vol. 55, Suppl. 1, pp 648.